Coloured, photocatalytic coatings for self-cleaning and architectural glazing applications

Precursors and processes for the aerosol-assisted chemical vapour deposition of functional coatings on glass

Stanton, David

Award date:
2016

Awarding institution:
University of Bath

Coloured, photocatalytic coatings for self-cleaning and architectural glazing applications;

Precursors and processes for the aerosol-assisted chemical vapour deposition of functional coatings on glass

David Stanton

A Thesis Submitted for the Degree of Doctor of Philosophy

University of Bath

Department of Chemistry

September 2015

Copyright notice

D. C. Stanton

Contents

Declarations

The work described in this thesis was conducted by the author at the University of Bath between October 2011 and March 2015. It represents the author's original and independent work, except where specific reference is made to the contrary. This thesis does not exceed the prescribed limit, including tables, references and appendices.

Acknowledgements

First and foremost, I would like to thank my supervisors, Professors Kieran Molloy, Mike Hill and Dr Andy Johnson. I am truly lucky to have had the continued support of these remarkable characters for so many years. Fantastic teachers all, they have been inspirational throughout my entire time at Bath.

For technical support I thank John Mitchells of the microscopy and analysis suite here at the University of Bath. Thanks also to Drs Anna Colley and Troy Manning of Pilkington-NSG for their guidance and supervision. Mark Farnworth, Alex Abbot and the rest of the surface analysis division of Pilkington Group LTD also receive my thanks.

I would also like to thank Drs Anna Robinson (née Sudlow!) and Jeff Hamilton, not only for their tremendous assistance in the lab, but their continuing and valuable friendship – I do not know if I would have made it without you both.

Boys - Joe, Andy and Jamie, what a ridiculous office. Thank you for the concerted, daily morale-boosting. So too to past and present members of my group, Amanda, Mat, Niall, Ibbi, Pete, Coshform, Pugh, Wildy and Robbo.

Heather, thanks for the creative musical outlet when the chemistry just got too much, and Beige, you're a great friend and flatmate. Also away from the lab, Beanie, and Dave J, you've made my time at Bath better, thank you.

A big thank you goes to Lauma for being the light at the end of the tunnel. Thanks also to Geoff, Grandma, Grandad, Mormor and Opa whose memories are forever cherished. And lastly, I owe so much to Mum, Dad, Rich, Andy, and Em for your limitless love and support. Thank you – this thesis is for you.

List of abbreviations

AACVD	Aerosol-Assisted Chemical Vapour Deposition
CFSE	Crystal Field Stabilisation Energy
CFT	Crystal Field Theory
CSD	Chemical Solution Deposition
CVD	Chemical Vapour Deposition
Diglyme	1-Methoxy-2-(2-methoxyethoxy)ethane
Dpm	2,2,6,6-tetramethylheptane-3,5-dione
EDS	Energy Dispersive [X-ray] Spectroscopy
FWHM	Full Width at Half Maximum
HEC	Hydroxyethyl Cellulose
Hfac	1,1,1,5,5,5-Hexafluoro-2,4-pentanedione
IM	Instrument Magnification
Low-E	Low Emissivity
MU	N-methylurea
NNDMU	N,N'-Dimethylurea
PXRD	Powder X-Ray Diffraction
tbaoac	*t*-butylacetoacetato
TFT	Thin Film Transistor
Thd	2,2,6,6-tetramethyl-3,5-hepadionate
ToF-SIMS	Time of Flight – Secondary Ion Mass Spectroscopy
XPS	X-Ray Photoelectron Spectroscopy
XRD	X-Ray Diffraction

List of Figures, Tables and Schemes

Chapter 1 Introduction

Chapter 2 Blue, photocatalytic films

Chapter 3 AACVD of tin oxide and fluorine-doped tin oxide.

Chapter 4 Spinels and ceria

Abstracts

There are a number of “smart” coatings that can be applied to glass. These include self-cleaning coatings based on titanium diioxide, and low-E coatings based on fluorine-doped tin oxide. Products are often more desirable with colour options such as Pilkington Activ Blue™. There are currently no alternatives to body tinting glass to achieve colour which is a time-consuming and expensive procedure. The work in this project details a number of coloured coatings via the AACVD or combustion processing of metal nitrate/urea precursors.

Chapter 1: Introduction

The introduction provides an overview of the float glass industry and the relevance of Pilkington-NSG to this project. The application of functional coatings on glass via CVD routes are explored, and the common precursors that are used in industry are described. Common characterisation techniques for thin-films are also detailed.

Chapter 2: Blue, photocatalytic coatings.

The chapter details the production of several blue, photocatalytic coatings based on the AACVD of a colour layer of copper or copper oxide and subsequent coating of anatase titania. Samples show photoactivity similar to commercially available Pilkington Activ™. The chapter also attempts to explain the deposition of metallic Cu and Ni thin films, as well as providing a process for depositing thin films of Cu, Cu_2O,and CuO from the same precursor. Samples were analysed by a variety of characterisation techniques including SEM, XRD, Raman, EDS, XPS, ToF-SIMS, and UV/Vis. Photoactivity was measured using the resazurin redox active ink.

Chapter 3: AACVD of tin oxide and fluorine-doped tin oxide.

The work in this chapter details the invention of a novel process for the deposition of SnO_2 and FTO from the AACVD of an *in-situ* generated Sn(II)-nitrate precursor. The process has shown to generate highly conductive, transparent films of FTO from precursors in both ethanol and water solvents. The work has now formed the main part of a joint-patent application between the University of Bath and Pilkington-NSG for the low temperature AACVD of various metal oxides.

Chapter 4: Spinels and ceria.

Utilizing the concept of combustion processing of metal nitrates, a number of coloured and functional metal oxide thin films have been deposited. These include the spinel-type materials $CoAl_2O_4$, $CoCr_2O_4$ and $CoTiO_3$, which have all yielded green thin films. The deposition of CeO_2 coatings has also been successfully deployed through a spin-coating route.

Chapter 5: Experimental

The general experimental procedures are detailed in this section, including the deposition conditions for all thin-film samples, and characterisation techniques.

Chapter 6: Appendices

Additional data including crystallographic refinement and XRD data are included here. Photographic images of selected films are also included.

Chapter 1:

Introduction

1.1. An overview of the flat-glass industry

€ 23 billion is the estimated figure given to the value of the global flat glass industry.[1] It becomes easier to justify this sum by looking at the tonnage of flat glass produced annually. In 2011, 56 million tonnes were produced which equates to roughly 5.5 billion m^2 of glass – 50% of which comes from Chinese markets, reflecting their growing economy and increased foreign investment. Together with Europe and North America, they account for over three quarters of the world's demand for flat glass.

The remaining demand is distributed across the globe as shown in figure 1.1.

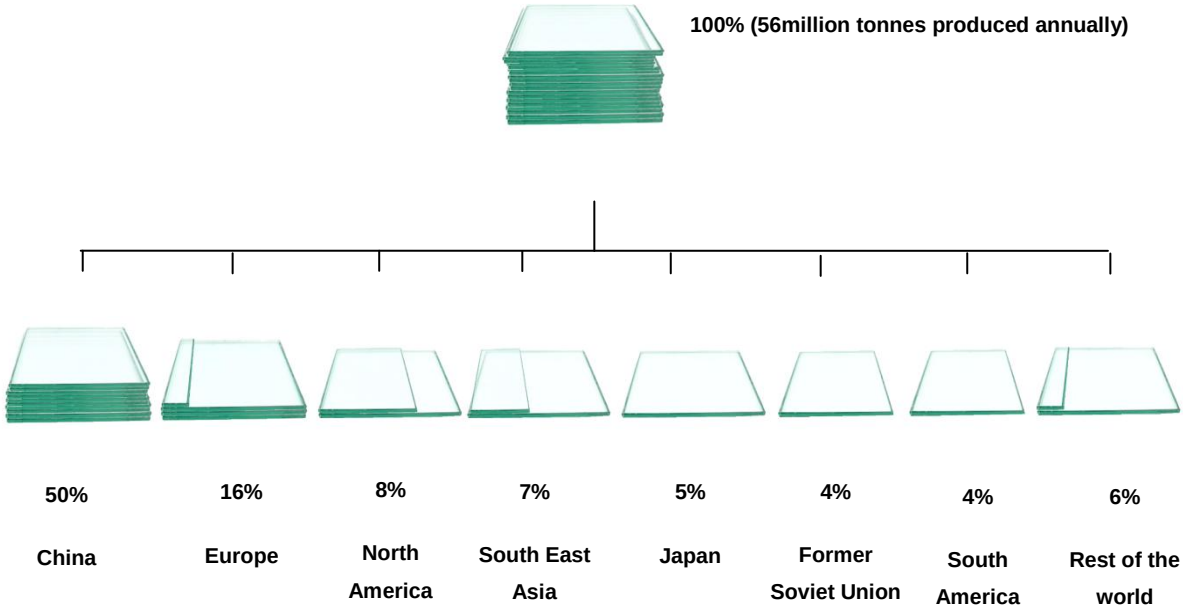

Figure 1.1: Global demand for flat glass.

Glass products broadly fall into three main areas of development: architectural, automotive, and technical applications. The float-glass process is at the heart of this industry.

1.2. Pilkington NSG and the float-glass process

Developed in 1959 by Pilkington LTD, the float-line process revolutionised the flat-glass industry. Historically, flat glass was made by spreading the melt onto a plate where it subsequently cooled and was polished. Later, in the early 1900s it was realised that the molten glass could be drawn off from a reservoir and either spread, or rolled. Such methods were crude and often resulted in glass with poor optical quality and defects such as bubbles or warping. The modern float-glass process solves these issues by producing a constant ribbon of high-quality glass by floating the material on a bath of molten tin. Capable of producing 6000 km of glass per year, the float-glass process now accounts for over 90% of the world's flat glass manufacture.[2]

The float-glass process consists of 6 key stages, a diagram of which is shown in figure 1.2.

1 - Raw materials feed

Typical soda glass consists of 60 – 70% silica (sand), 15 – 20 % soda (a mixture of sodium and potassium carbonates) and 10 – 20 % lime (calcium carbonate), hence "soda-lime" glass. Silica is exceptionally durable, but has a very high melting temperature – in excess of 1700°C. Energy costs can be lowered by the addition of "flux", in this case sodium oxide, which lowers the temperature of the melt by disrupting the silica structure.[3] Other raw materials include magnesium oxide which delays crystallisation while the glass is in the float bath, aluminium oxide to increase durability and iron oxide to add a required level of green colouration for the customer. It is at this stage where colour (body tinting) can be added such as cobalt oxide for production of blue glass for which there is a large European market. The fact that currently there exists no "switch-on, switch-off" alternative to body tinting glass will be elaborated on later.

2 - Melting

Materials are mixed in the desired stoichiometries before being introduced into the furnace where large gas burners heat the mixture to around 1500°C. At this temperature CO_2 is evolved from the carbonates to give sodium, potassium and calcium oxides which react with silica to form soda-glass.[4]

$$Na_2CO_3 + SiO_2 \xrightarrow{1500ºC} Na_2SiO_3 + CO_2$$

$$Na_2SiO_3 + x\,SiO_2 \xrightarrow[\text{Digestion}]{Na_2SO_4} (Na_2O)(SiO_2)_{(x+1)}$$

3 - The float bath

The molten glass flows onto a bath of molten tin where it spreads out – much like oil on water, and flows along the surface to make an incredibly flat sheet (1 nm variance typically). The temperature of the tin bath is kept at 1000°C to ensure any defects melt. As the glass flows further down the line, it cools to around 600°C and over the lip of the bath where large rollers draw the ribbon out. By varying the speed of the rollers, the glass can be slowed and thickened to 20 mm or sped up to reduce thickness to as low as 4 mm. The atmosphere within the tin bath is nitrogen with 10% hydrogen which prevents oxidation of the tin metal, and the reducing atmosphere also ensures any oxygen evolved from the glass is removed. This environment is ideal for the application of functional coatings by chemical vapour deposition (CVD). These so called “on-line” coatings must have extremely high growth rates owing to the fast movement of the glass ribbon and therefore the high temperatures within the tin bath can aid this process. This remains the largest scale application of CVD in industry which is described in more detail in section 1.5.

4 - Cooling/annealing

The glass enters the annealing lehr where it cools sequentially down to around 40°C. This annealing stage removes some internal stress within the glass, allowing for cutting without damaging the product. Coatings can also be applied within the lehr, although temperatures are significantly lower than in the tin bath, so coatings requiring higher growth rates are applied at the hotter end of the process.

5 – Quality control

Before cutting and packing, the glass is thoroughly inspected to assess for defects or variation in thickness. If glass is of unsuitable quality e.g. unacceptable levels of haze, or a non-uniform coating has been deposited, feedback tells the process engineers where to locate and correct the problem.

6 – Cutting/stacking

After quality control method, the glass is now cool enough at the end of the 0.5 km long process to be cut and stacked ready for shipping to the customer. The entire process is completely automated and designed to run throughout the 10 – 15 year lifespan of the factory.

A diagram of the float line process is shown below:

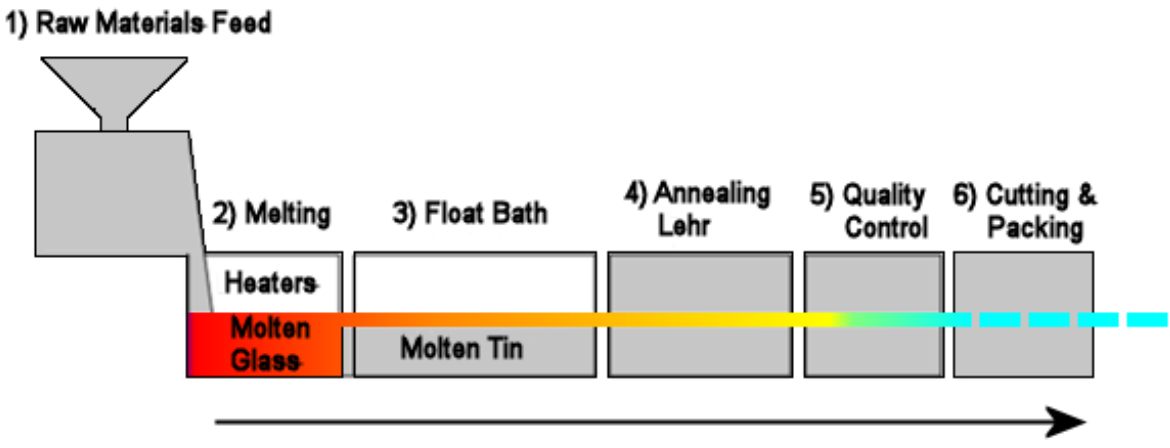

Figure 1.2: The Pilkington Float-Line process, adapted from source.[5]

Today Pilkington are equal to Asahi glass in scale, and are the most profitable company in flat glass. They have ownership or interest in 49 float lines worldwide which produce 9 million tonnes of glass annually. This supplies a large automotive customer base as well as building companies and employs 30,000 people. A yearly research and development budget of around ¥10 billion (€73 million) reflects the necessity of the company to stay up to date with current technologies.

Pilkington LTD now form part of the larger Japanese group NSG who part-fund this project, and have an interest in a wide variety of “smart” coatings for glass.

1.3. Glass Coatings and their Syntheses

“Smart” coatings can give a seemingly simple product such as glass an impressive array of unique properties and functions.[6] Such function might include anti-reflection, anti-fogging or scratch resistant glass which has obvious uses in the automotive industry. Others may involve anti-microbial coatings, or surfaces for solar energy generation. The focus of this project will be geared primarily toward self-cleaning (photocatalytic) and low emissivity coatings, with the conductivity of some explored.

Whilst some coatings can be applied to glass post-manufacture (off-line coatings), the majority are deposited on-line by CVD methods.

1.3.1 Glass and SiCO

Glass is an amorphous material consisting of a random organised network of corner-sharing SiO_4 units. The Si^{4+} atom is surrounded by four covalently bonded O^{2-} atoms form the incredibly strong $[SiO_4]^{4-}$ unit known as orthosilicate.[7] The shape of these units is tetrahedral, and complex silicate structures are formed by a linking of units between oxygen atoms. While amorphous, glass structures can be represented by chains and rings sharing vertices bridged by oxygen atoms, see Figure 1.3.

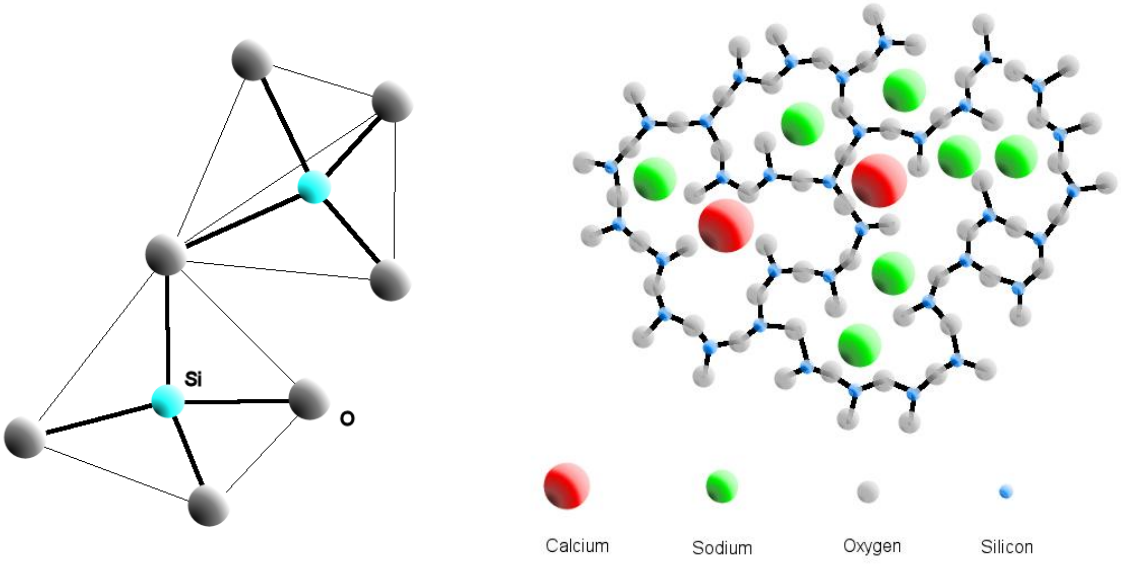

Figure 1.3: The structure of two corner-sharing orthosilicate octahedra (left) and a portion of the structure of soda-lime silicate glass (right)

Glass sheets can be manufactured continuously in the float plant and can be up to 3 metres wide. As well as sodium and calcium, glass contains many other ions such as magnesium, aluminium and iron which can leach into applied coatings with detrimental effect to its function. To negate this, float glass is coated with a thin layer of a silicon oxide coating with high carbon content “SiCO”. At thicknesses of around 20 nm thick, this acts not only as a barrier layer to prevent ion migration into the glass, but also as a colour-suppressant to nullify unwanted interference effects. As a further advantage, SiCO undercoat provides a more uniform surface on which to seed further coatings. The SiCO coating can be seen underneath a layer of fluorine-doped tin oxide (FTO) in figure 1.4.

1.3.2 Solar control coatings

K-glass^{TM} is a product with energy saving functionality with applications in both domestic and commercial glazing. The glazing unit is based on IR-reflective technology and works to limit solar heat gains into a building to keep it cool during summer months, and prevent heat loss to keep interiors warm during the winter months. It consists of a base SiCO barrier layer onto which a layer of fluorine-doped tin oxide is deposited. FTO offers IR reflectivity, and can be applied on the inner face of a double-glazed unit where it is less prone to weathering and

hydrolysis. An SEM image of an FTO layer on SiCO coating is shown in figure 1.4. Solar control coatings based on FTO are examined in more detail in chapter 3.

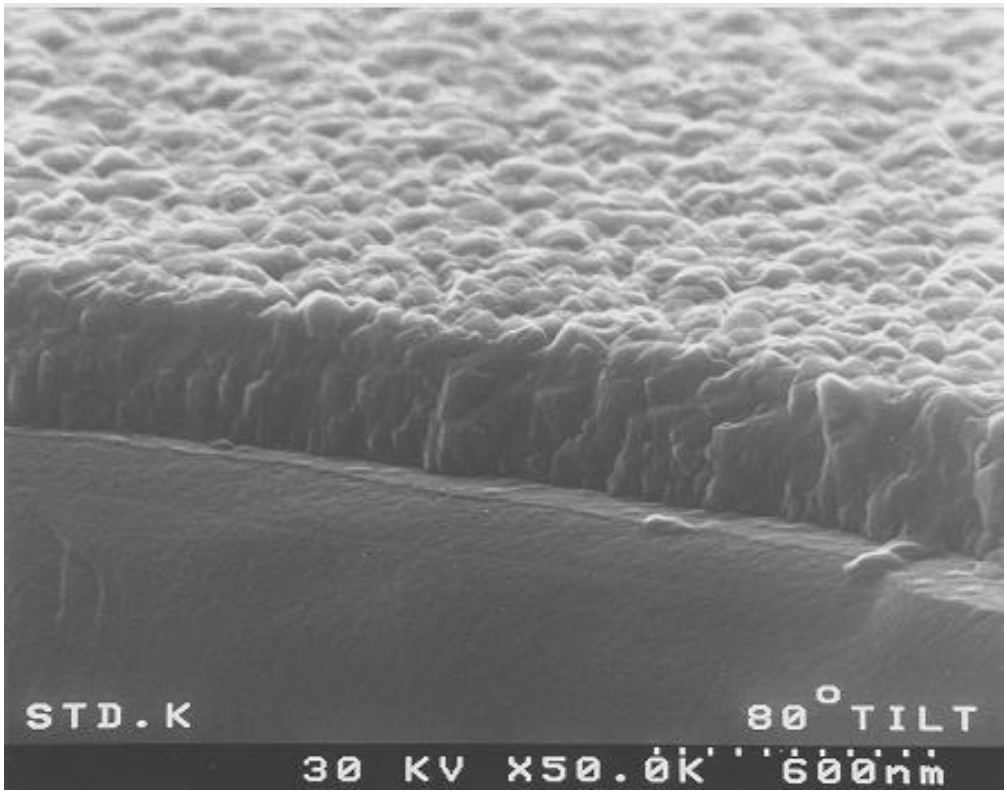

Figure 1.4: Electron micrograph image of FTO on SiCO glass at 80° tilt.[8]

1.3.3 Self cleaning coatings

Pilkington Activ™ is a second generation coating with self-cleaning functionality based on the semiconductor titanium dioxide, a front-runner in photocatalysis. The anatase polymorph has a fairly wide band gap of 3.2 eV (320 nm) corresponding to UV light. When exposed to sunlight or other sources of UV, electron-hole pairs are generated which oxidise organic material on the surface of the glass. UV light also induces superhydrophilicity on the surface, reducing the contact angle of water to a negligible value. This process, known as sheeting, easily directs the water off the surface of the glass, washing away any oxidised material on the surface. Deposited as a thin film, titania is a cheap, non-toxic and transparent coating which offers self-cleaning ability. This allows the glass to retain its primary function as a window. Activ™ has a visible reflectance of around 7%, and absorbs roughly 20% of solar UV radiation. The product is extremely

robust and resistant to abrasion, resulting in functionality for the lifetime of the window frame. In conjuction with a layer of FTO, the glass becomes a truly "smart" product. The nature of TiO_2 and its role in industry is explored in chapter 2.

1.3.4 Copper and nickel thin films

Metallic thin films form a crucial part of integrated circuits (ICs) by acting as the conductive wire that connects all components together. Few people in a modern, westernised society will ever be far from the kind of integrated circuitry found in smart-phones, tablets, computers and televisions. The highly conductive material which interconnects all components together makes up the majority of an IC's mass.[9]

Metals are ideal candidates for these interconnecting materials owing to their typically high conductivities. Aluminium is one such metal that has been used for this particular application, being of low resistivity and good adherence to SiO_2, but suffers from electron migration problems when thinned – a knock-on effect of device miniaturisation.[10]

Copper is an obvious choice in place of aluminium as it suffers far less from electron migration problems while still retaining an excellently low resistvity of 2.81 μΩ cm.[11] Copper is also still relatively cheap compared with the other coinage metals at 5.5 $/kg compared with 497.0 and 37,169.5 $/kg for silver and gold respectively. One disadvantage of using copper, is that of its poor adhesion to silicon. The application of an adhesion aid layer on which copper can seed such as Ni will combat this problem.[14] Copper is also known for its ability to diffuse into materials such as SiO_2 which can be remedied by application of a barrier layer such as TaN or TiN.[12]

Metallic nickel thin films also find applications in spin-electronic or "spintronic" devices such as magnetoresistive random access memory (MRAM).[13]

1.3.5 Ceria

Cerium oxide (CeO_2) is an important material with a variety of applications including as a catalyst for the oxidation of carbon monoxide,[14] gas sensing,[15] solid oxide fuel cells,[16] and as a photocatalyst either in the pure form, or doped within a matrix such as TiO_2.[17] Another intriguing use of ceria, is for the self-cleaning of oven glass by oxidation of accumulated organic deposits.[18]

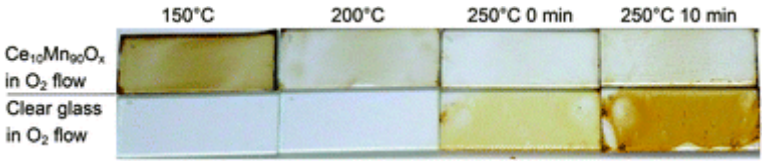

Figure 1.5: Self-cleaning behaviour of Ce-doped MnO coated glass.[18]

Cerium dioxide is a *n*-type semiconductor with a wide band-gap of between 2.9 and 3.2eV.[19] Pure CeO_2 is thermally unstable and can be reduced to Ce_2O_3 with heat. Deposited as a thin film, CeO_2 coatings on the inside of ovens are able to decompose organic residue from the cooking process at temperatures less than 350 °C. This is energetically and therefore more economically favourable to other cleaning methods such as pyrolysis whereby organic deposits are carbonised at temperatures in excess of 450 °C.

$$CeO_2 \xrightarrow{\Delta\ 300^oC} Ce_2O_3$$

Scheme 1.1: The redox couple of Ce^{4+} / Ce^{3+}.

A recent study has concluded that some composite CeO_2 impregnated TiO_2 films have shown photoactivities a factor of ten greater than that of commercially available Activ^{TM}.[20]

Table 1.1: Highlighting some select materials, their applications as thin films and selected CVD precursors.

Material	Application	Selected precursors
TiO_2	Gas sensing, photocatalysis, water splitting, [21] photovoltaic devices, [22] self-cleaning coatings.	$TiCl_4$*, $Ti(O^iPr)_4$,[23] $Ti(dpm)_2(OiPr)_2$[24], $Ti(NO_3)_4$,[25]
SnO_2, F:SnO_2	Low-E glazing, transparent conducting oxide (TCO)	$SnCl_4$*,[26] $Sn(Bu)_2(ac)_2$, $Sn(Bu)_2(ac)_2$ and CCl_3CF_3,[27] $Sn(CF_3CO_2)_2$,[28] $Sn(Me)_4$* and CF_3Br, [29,30] $SnCl_4$* and NH_4F, [31,32] $SnCl_4$* and F_2 [33] SnR_4, where R = various perfluoroalkyls,[34] (Bu)$SnCl_3$ and NH_4F.[35]
CeO_2	Self-cleaning oven coatings, gas sensors	$Ce(thd)_4$,[36] $Ce(hfac)_3(diglyme)$[37], $Ce(OR)$[38] $Ce(NO_3)_3.6H_2O$. [20]
Cu	Integrated circuit connection	Cu(hfac)(vtms),[39] $Cu(amd)_2$,[40] $Cu(tbaoac)_2$,[41] Cu(hfac)(mhy),[42] $Cu(hfac)_2$[43] $Cu(NO_3)_2.2.5H_2O$,[44]
Ni	Spintronic device, adhesion layers, Integrated circuit connections, catalysis	$Ni(CO)_4$,[45] $NiCp_2$,[46] $Ni(amd)_2$,[47] $Ni(acac)_2$,[48] NiCp(allyl),[49]

*Requires oxygen source

dpm	=	2,2,6,6-tetramethylheptane-3,5-dione	thd	=	2,2,6,6-tetramethyl-3,5-hepadionate
hfac	=	1,1,1,5,5,5-Hexafluoro-2,4-pentanedione	amd	=	$[RNRCNR]^-$
diglyme	=	1-Methoxy-2-(2-methoxyethoxy)ethane	tbaoac	=	*t*-butylacetoacetato

1.3.6 Coloured glass dilemma

In addition to the product Activ^{TM}, a self-cleaning coating applied to clear glass, there also exists a blue counterpart Activ Blue^{TM}.[50] As the name implies, the product offers the same self-cleaning ability as Activ, but is an aesthetically pleasing blue colour. A large market for this blue glass exists in European countries where it is most widely used for conservatory window glazing.

As mentioned previously, colour can be achieved by changing the base composition of the glass which almost always involves the incorporation of metal oxides to the mix. Body-tinting glass and ceramics this way has been explored across the ages and resulted in some of the most stunning art and symbology from every culture.[4] Blue glass can be produced on a float line by addition of large amounts of the transition metal cobalt, in the form of cobalt oxide. Transition metals often exhibit strong colour both in the solid state or in solution arising from *d-d* orbital transitions. Table 1.2 lists some of the most common glass colours achieved by body-tinting with transition metals.

3d transition metals can exist in a variety of valencies which have incompletely filled d-orbitals. A number of criteria based on quantum mechanical considerations will dictate the observed colour and intensities of a M^{n+} ion with a particular 3d configuration. The spin selection rule states that the incident radiation cannot change the relative orientations of the spins of electrons in a complex.

E.g. a singlet (S = 0) cannot undergo a transition to a triplet state (S = 1). This can be summarised as:

$\Delta S = 0$ for spin-allowed transitions

$\Delta S \neq 0$ for spin-forbidden transitions

Where S = spin momentum. The rule can be relaxed in certain cases, such as coupling of spin and orbital angular momenta of electrons, though this is more prominent for heavier atoms.

The Laporte selection rule states that "*In a centrosymmetric ion or molecule, the only allowed transitions are those which are accompanied by a change in parity"*

Hence s-s, p-p and d-d transitions are forbidden, but s-p and p-d transitions are allowed. This can be summarised as:

$\Delta l = \pm 1$

Where l = angular momentum. Centrosymmetric molecules have inversion centres and include octahedral, tetragonal, cubic, square planar and linear molecules. So, transitions between *g* and *u* terms are permitted but *g* – *g* and *u* – *u* are parity forbidden. In centrosymmetric molecules, d-d transitions are $\Delta l=0$ and *g-g* and therefore both parity and orbitally forbidden. This is the reason that octahedral complexes are generally weakly coloured.

The Laporte selection rule can be relaxed in a number of ways, such as a distortion of perfect centrosymmetry, from Jahn-Teller type distortions or asymmetric vibrational modes.

Cobalt is in group 9 of the periodic table and has the electronic configuration $[Ar]4s^2 3d^7$. Upon complexation, the d orbitals are stabilised due to metal-ligand bonding. Co^{2+} complexes often exhibit a tetrahedral geometry owing to its high spin d^7 electronic configuration and are typically intensely coloured. In an octahedral environment, colour is usually less intense owing to a higher degree of symmetry and therefore violating the Laporte selection rule of changing parity.[51] A CFT diagram of a Co^{2+} ion in octahedral and tetrahedral environments are shown in figure 1.6.

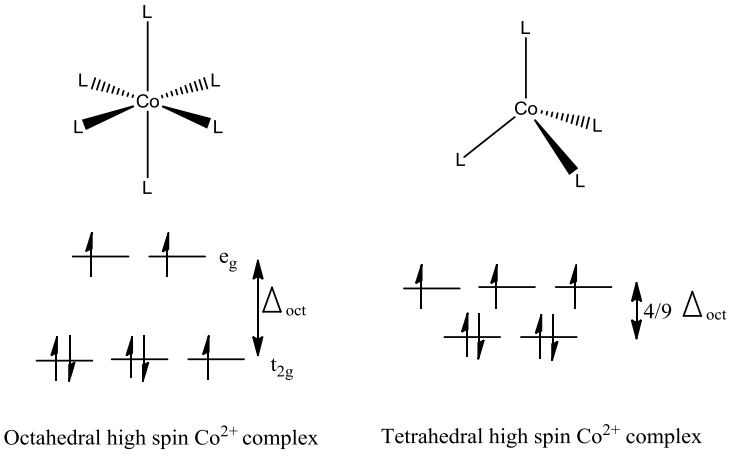

Figure 1.6: CFT diagram of Co^{2+} ions in octahedral and tetrahedral environments.

The paramagnetic nature of these complexes with unpaired electrons leads to complications in the acquisition of NMR spectra. Co^{2+} imparts a blue tint at concentrations of parts per million, which when increased to around 1000 ppm forms the characteristic “cobalt-blue” colour. Standard Pilkington float glass is actually tinted slightly green, the origin of which can be traced back to levels of iron oxide contamination in the silica deposits around Lancashire. The iron oxide is now deliberately added in to the process to give the product its signature colour. Indeed the Pilkington logo is a shade of green for this very reason.[4]

Table 1.2: Glass colour achieved from transition metal body-tinting, adapted from source.[52]

	Transition metal ions	
Configuration	**Ion**	**Colour**
d^0	Ti^{4+}	Colourless
	V^{5+}	Faint yellow
	Cr^{6+}	Faint yellow
d^1	Ti^{3+}	Violet-purple
	V^{4+}	Blue
	Mn^{6+}	Colourless
d^2	V^{3+}	Yellow-green
d^3	Cr^{3+}	Green
d^4	Cr^{2+}	Faint blue
	Mn^{3+}	Purple
d^5	Mn^{2+}	Light yellow
	Fe^{3+}	Faint yellow
d^6	Fe^{2+}	Blue-green
	Co^{3+}	Faint yellow
d^7	Co^{2+}	Blue-pink
d^8	Ni^{2+}	Brown-purple
d^9	Cu^{2+}	Blue-green
d^{10}	Cu^{+}	Colourless
f^2	U^{4+}	Yellow-green

Unfortunately body tinting for coloured glass is extremely expensive both in terms of time and cost. Introduction of additional colour sources in the form of metal oxides requires a complete shutdown of the float line process while raw materials are changed – a process designed to operate non-stop for a decade. The correct hue of glass must be carefully monitored, producing massive quantities of glass that cannot be recycled back into the furnace. Furthermore, after the batch of coloured glass is produced, every trace of colourant must be removed or risk contaminating later products. This requires a shutdown of the furnace which can take a week to cool, and another week to bring back to temperature. Such a long period of downtime amounts to an exorbitant loss of revenue, as much as £1 million per day.

Problems continue when it is realised that the main area for production of blue glass is in North America, where little market for the product exists. The coloured glass must then be shipped to Europe at great cost. It therefore stands to reason that a "switch-on, switch-off" process for a coloured coating is desirable, and CVD offers a feasible opportunity for such a process. [53] Efforts to produce a coloured thin-fim via CVD for purely aesthetic reasons have been sparse, though there are contributions from University College London and the University of Bath[54, 55] At present, there are no coloured glass products that have been produced solely by CVD as opposed to body-tinting.

1.3.7. The need for improved coating systems

A review by Mol *et al* has highlighted the necessity for improvements on large scale CVD float-line coating systems.[56] The reasoning behind this is that industrial processes are typically engineered by trial and error, rather than scientific approaches. This leads to a fundamental lack of understanding of the basic mechanisms of the CVD processes on such a large scale.

For example, the best yield of a tin oxide-coated flat glass deposited by CVD was only around 70% but can be as low as 50%. In the absence of a coating the glass yield is around 75%, signifying a reduction in productivity of the process when coatings are applied. This is problematic as rejected glass must be crushed and re-melted, a hugely energy-intensive endeavour estimated at 4×10^{10} kJ / year globally.[57] Furthermore, precursor efficiency on a float-line can be as low as 10%,

requiring costly incinerators and scrubbing units. Such low efficiency also results in the landfill of around 1000 tonnes of waste per year.

1.4. Chemical vapour deposition

1.4.1 Basics of CVD

The coatings described previously are examples of the largest scale applications of chemical vapour deposition. CVD has long been used to produce thin films of materials including metals, metal oxides, metal nitrides and metal carbides with a staggering range of potential applications. These include but are by no means limited to microelectronics, photovoltaic-, thermoelectric- and thermochromic device and *p*- or *n*-type semiconductors. The list goes on.

To be described as a chemical vapour deposition, as opposed to a physical process, there must be some chemical reaction of vapour-phase precursors. In general terms, a solid material is deposited on an activated surface (conventionally heated), from the chemical reaction of clearly-defined molecular precursors.[58] A physical process such as sputtering or spin-coating can involve a molecule to be adsorbed onto a surface without subsequent chemical reaction taking place. During a CVD process, the precursor is vaporised and transported to the substrate by some carrier gas whereupon it decomposes to form the desired material.[59] Growth of material can occur in three ways, Volmer-Weber “island growth”, [60] Frank - van der Merwe “layer growth” or Stranski – Kastanov - mixed layer and island growth. Volatile by-products of the reaction are removed by a carrier gas or vacuum along with any solvent that may be present, see figure 1.7.

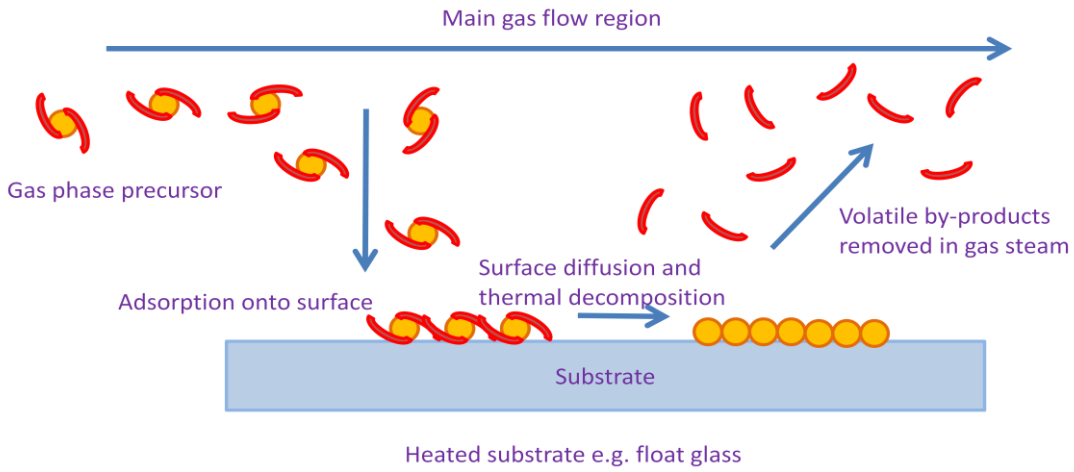

Figure 1.7: Diagram of a conventional CVD process[60]

One early application of CVD is the Mond process for the purification of nickel metal from its ore. This involved passing carbon monoxide over impure metallic nickel at 50°C to form the extremely toxic $Ni(CO)_4$ complex in gaseous form. This was subsequently decomposed at 230°C releasing four equivalents of CO, leaving pure nickel deposits. [61]

1.4.2. Variations of CVD

As technology has advanced and new materials discovered, so too has the CVD process evolved. CVD is an excellent route to investigating new materials, as precursors can easily be synthesised in a laboratory and tested on a small scale with relatively simple apparatus. If successful, scale up can be facilitated by companies such as Pilkington-NSG who are ideally suited to test new processes on large area substrates.[6] The great source of heat on an industrial float line is inherently a prime location for large area CVD of functional coatings.[62] There are now a bewildering amount of prefixes ascribed to CVD, often to differentiate between methods of activating the substrate, but also the process by which the precursor is transported there.

The first stage that a precursor undergoes is its vaporisation and there are numerous ways in which this can be achieved. Some precursors are highly volatile or even gaseous to begin with, and therefore room temperature vapour pressure is sufficient to transport controllable concentrations into the reactor and substrate surface.[62] The precursor can also be gently heated to increase the

vapour pressure if room temperature is not sufficient. This type of process is typically given the prefix of atmospheric pressure, or AP-CVD. This type of CVD is ideal if the precursor can be designed to be sufficiently volatile, as other activation methods can be expensive, or involve scale-up challenges such as plasma-enhanced- (PE) CVD.

To affect a good deal of control over the flow rates of precursor, stainless steel bubblers can be used, such as those used at Pilkington group Ltd laboratories.[63] A known quantity of precursor is introduced into the bubbler, above the level of the dip-tube, but below the gas-out tube (figure 1.8). The clamp and O-ring form an airtight seal, and the bubbler can be heated to the required temperature for vaporisation. This has the added advantage of being able to be filled with volatile, toxic, flammable or otherwise hazardous precursor and transport it from an inert atmosphere environment to the CVD equipment.

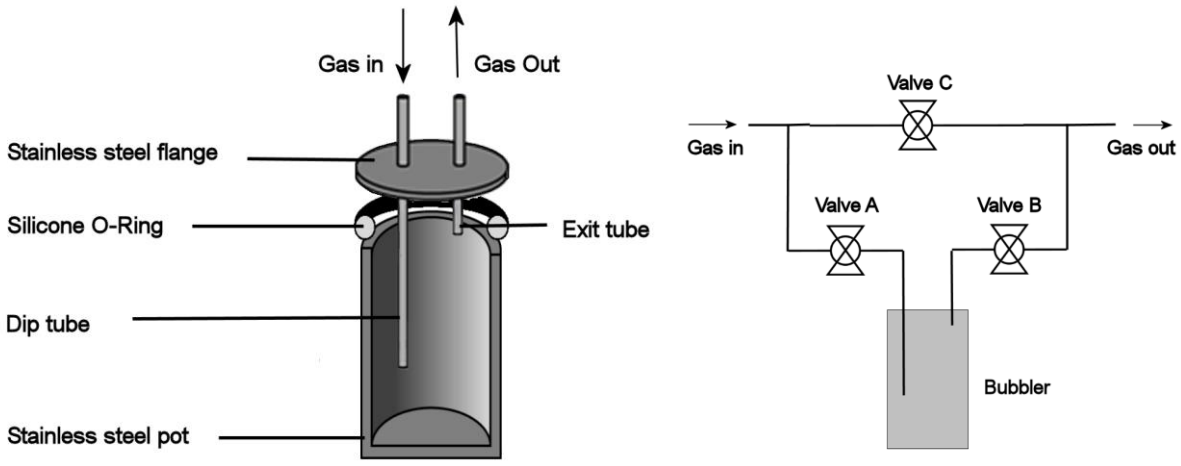

Figure 1.8: Cross sectional and line diagram of stainless steel bubbler for introduction of precursors for CVD experiments.

Precursor flow is regulated by valves A, B and C either manually or with automated mass-flow controllers. Valve C acts as a bypass of the precursor vessel, allowing a purge of the entire system both pre- and post-deposition. This is essential to ensure an oxygen and moisture-free atmosphere.

If the precursor is not sufficiently volatile to produce an appreciable vapour pressure, even when heated, a vacuum can be applied across the whole system in a process known as low pressure CVD (LPCVD).[64] This is preferable to excessive heating of a precursor both for safety and practical reasons. Often when testing a new precursor, excessive heating results in premature decomposition which can heavily contaminate lines for future runs, which then require thorough and time-consuming cleaning. It goes without saying that this is impossible to scale up to large-scale operations such as a float line as the entire system needs to be enclosed.[64] However, the method can still have applications in smaller-scale, off-line coatings.

An alternative to LPCVD is direct liquid injection (DLICVD) whereby a liquid precursor (or dissolved if sufficiently soluble) is introduced at constant flow rate by a syringe driver.[64] Upon injection into the system, the precursor flash evaporates and is carried to the substrate. Similarly, for dissolved precursors, flash evaporation results in immediate aerosolisation and subsequent transport to

the substrate. This method is often used for a source of oxygen, such as ethyl acetate used in conjunction with the highly volatile $TiCl_4$ in the CVD of TiO_2. A particular advantage when dealing with liquids is that control and measurement of flow rates and concentrations of precursor used is much easier. Conversely, if a dissolved precursor is used, flash evaporation can result in condensation and build-up of precursor onto the hot-spot. This results in an unknown amount of precursor entering the reactor, and deposits of decomposed by-products which must be cleaned.

Where a precursor is not volatile enough for LPCVD, but *is* soluble in common solvents, the precursor can also be introduced via an aerosol. A large amount of the work in this project focuses on the use of precursors for aerosol-assisted CVD (AACVD). The method removes the common requirement for volatility of the precursor allowing a much greater range of ligands and complexes to be tested. There are two typical ways of generating an aerosol, the first utilising an ultrasonic actuator to generate micron- and submicron-sized particles, and the other a high pressure nebulisation of precursor solution through a nozzle or pin hole based on Bernoulli's principle.[65]

During the ultrasonic generation of aerosols, a metal diaphragm at the base of a water bath vibrates at ultrasonic frequency. These vibrations are transmitted through the water and into a glass nebulising vessel containing a solution of a known quantity and concentration of dissolved precursor. The ultrasonic vibrations cause positive and negative oscillations by rarefaction and compression which momentarily cavitate the solution into a fine mist. These tiny particles of solution are easily transported by the carrier gas into the reactor. This process clearly offers advantages over delivery systems that require vacuum, or precursors which have extremely low volatility or decomposition pathways.

Where a pinhole-type aerosol generator is used, compressed carrier gas expands through an orifice to form a high-velocity jet. Liquid is drawn up through a vertical tube and is subsequently atomised by the jet. Larger droplets impact the wall opposite the jet and condense back down into the precursor solution to be reused, while fine spray leaves the atomiser through the top. Through this method, submicron diameter droplets are achieved in a much more uniform way

than the ultrasonic counterpart. This process has the advantage that the typical stainless steel bubbler set-up can effectively be reversed, with the dip-tube being the outlet, figure 1.9.

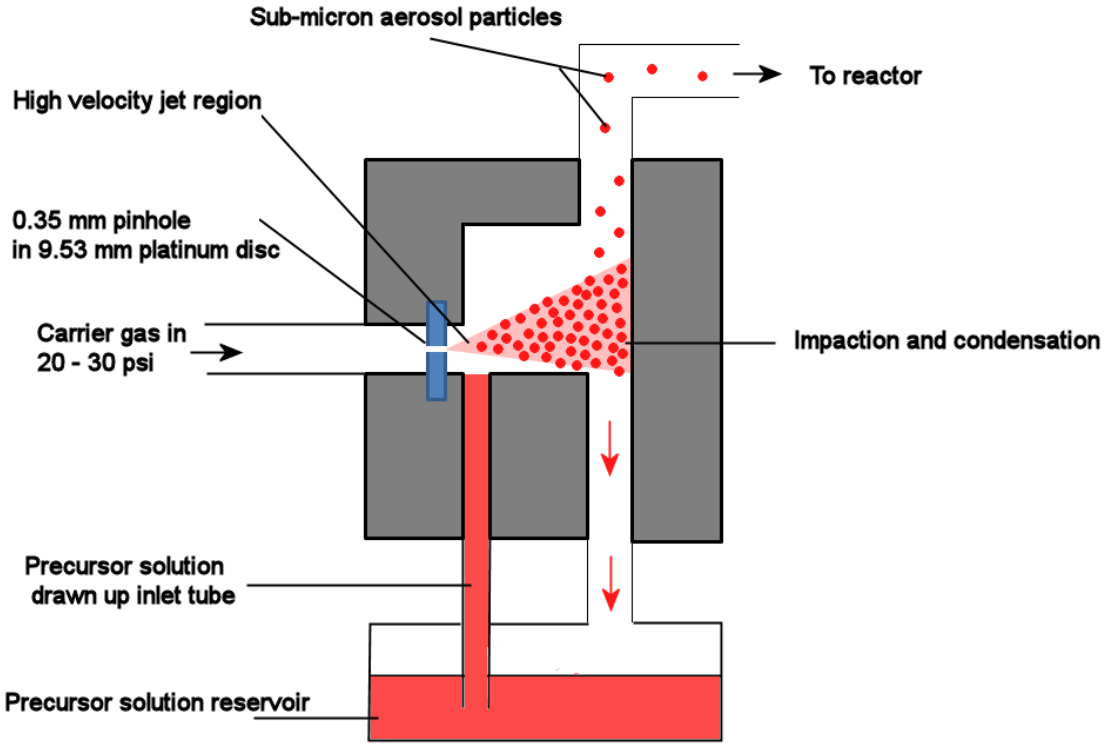

Figure 1.9: Diagram of aerosol generation from a constant-output atomizer.

Once above the heated substrate, solvent evaporates releasing the precursor into the gas phase where subsequent CVD occurs.[66] The deposition phase is the same regardless of aerosol generation method, the one variation being the size of the particles generated. As long as concentrations and volumes of precursor solutions are known prior to deposition experiments, flow rates can be calculated and therefore reaction efficiency. A diagram of the AACVD equipment used in this project is shown in figure 1.10 while a photographic image of the kit can be found in appendix 6.12.

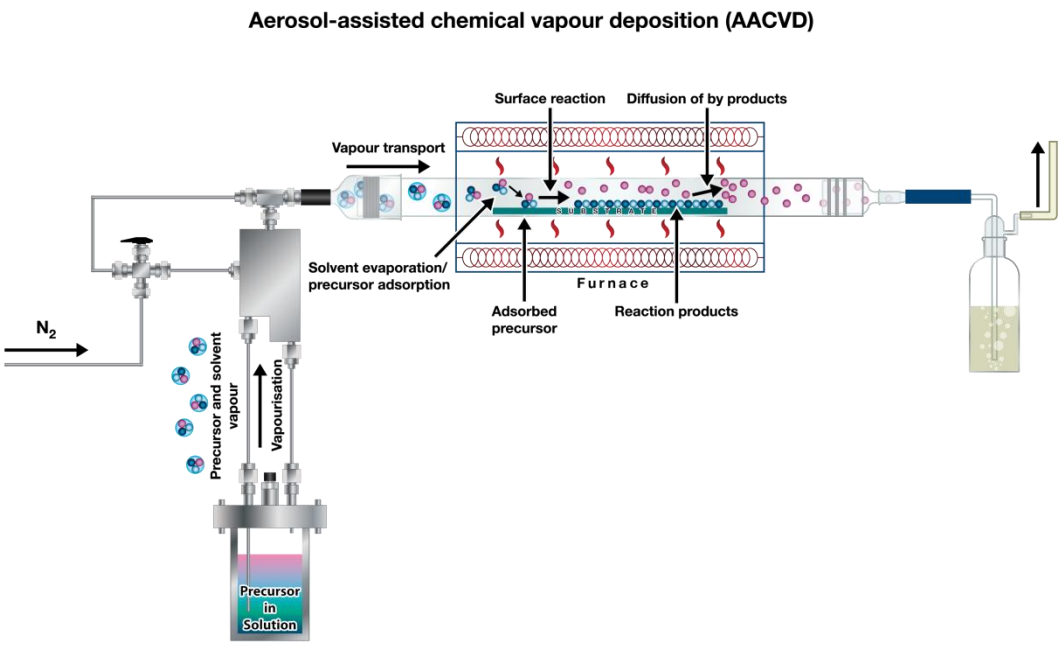

Figure 1.10: Diagram of AACVD equipment used throughout this project

The aforementioned CVD techniques have all required thermal activation of the substrate. The thermal properties of the substrate dictate the limits of the activation energy that can be applied. For instance, soda-lime glass can be heated to a maximum of 650°C, although significant warping and structural change of the glass is likely to occur anywhere between 650°C and 500°C. It is still possible to successfully deposit films between these temperatures, however, above this range the glass will deform and melt. This can also lead to problems where annealing steps are required. As will be seen in chapter 4, the colourful spinel $CoAl_2O_4$ requires heating to above 700°C to acquire the characteristic cobalt-blue colour. Substrates with a higher tolerance to heat include quartz and silicon wafers which are crystalline and can withstand temperatures in excess of 1000°C – although such conditions are impractical and hazardous.

Increasingly, research focuses on the synthesis of materials at lower temperatures for economical and environmental reasons. Additionally, some coatings find use when applied on surfaces like plastics which have significantly lower melting points than ceramic materials. PECVD offers a work-around for these substrates, requiring very mild heating. This involves the generation of a plasma from discharge between two electrodes in the reactor. The activated precursor is adsorbed onto the substrate and decomposes to form the desired

material.[64] An oxygen plasma can therefore be expected to provide oxide-materials on substrates at relatively low temperatures. Unfortunately, despite the low temperatures involved, plasma is still a very high energy process. Within the plasma-precursor mix, a number of extremely reactive molecules and atoms exist, many of which contribute to the film growth, while many may also affect the film detrimentally. For this reason the process is exceptionally hard to control, and a large number of variables can affect the film growth, such as temperature, RF power, pressure, choice of gas, deposition time, reactor shape etc. Therefore a high-quality and uniform film may take many experiments to perfect parameters with no guarantee of scale-up being possible. Indeed, since most plasma generation requires a vacuum, scale up to something similar to a float-line becomes an impossible task. There is an emerging type of PECVD reactor which does not require a vacuum, but this offers additional problems in terms of increased variety of reactive species within the chamber. [67]

For a more detailed discussion on the variants of the CVD process, the reader is directed to the following literature.[68, 69]

Table 1.3: Some of the more common variants of CVD.

Thermal CVD methods	**Activated CVD methods**
Atmospheric Pressure – APCVD	Combustion/Flame – CCVD
Low Pressure – LPCVD	Plasma Enhanced - PECVD
Metalorganic – MOCVD	Laser Assisted – LACVD
Aerosol Assisted - AACVD	Microwave Assisted – MWCVD

1.4.3 Precursor Design

With the variants discussed previously, it is apt to summarise the desired properties of a CVD precursor. Clearly, there are a number of variations within a CVD process so it is important to identify appropriate precursors when planning a material deposition.

Perhaps the most important requirement is that all elements of the desired material must be present in the precursor (or precursors if dual- or multi-source).

The choice of precursor depends heavily on the type of material being deposited. For example for a metallic film, O-containing ligands or solvents to the system should be kept to a minimum to avoid deposition of the corresponding metal oxide.

Secondly, the precursor should be sufficiently volatile (unless for use in AACVD) to provide an adequate vapour pressure for facile introduction into the reactor system. Ideally this should be at moderate or room-temperature to avoid process problems with premature decomposition.[62]

Volatility can be achieved by careful choice of ligands. Intermolecular forces such as Van der Waals forces, π- and H-bonding interactions play a large part in oligomerisation of monomeric species to form dimers or polymeric complexes.[62] Saturating the coordination sphere of a metal is a typical way of limiting these influences and is often achieved with bi- or polydentate ligands or monodentate ligands that are sufficiently bulky.

It may seem counter-intuitive to state that the precursor should also be somewhat thermally stable. Of course, the precursor should decompose when activated, however it must be sufficiently robust to survive vaporisation, transport and early stages of decomposition. Failing to add this property results in major wastage of precursor, and limited or even total absence of film growth.[70] It is therefore important to allow a substantial temperature window to decomposition which can be achieved by careful consideration of the ligand sphere. Common metal-oxide precursors include β-diketonate complexes owing to their superior ligand sphere saturation over analogous alkoxide counterparts, see figure 1.11.

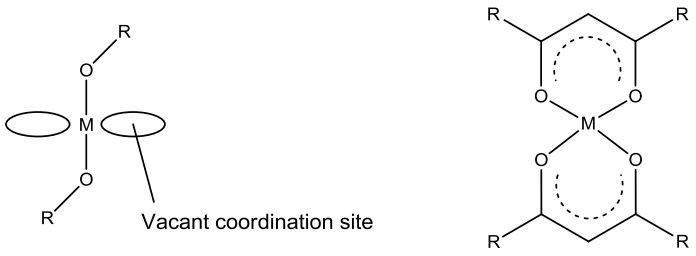

Figure 1.11: A divalent metal alkoxide showing vacant coordination sites compared to a metal β-diketonate with enhanced ligand sphere saturation.

Metal alkoxides and β-diketonates have been extensively studied as precursors for CVD of metal oxide materials. β-diketonate ligands often coordinate to metal centres bidentate fashion, helping to saturate the coordination sphere of the metal.[71] Acetylacetonate (acac) is an example of one such ligand, but steric hindrance and therefore volatility can be increased by increasing the steric bulk of substituent groups.

Another method of preventing oligomerisation is through the coordination of spectator ligands which take no part in the formation of the deposited material. Such ligands are often non-ionic Lewis-bases such as tetramethyl-ethlyenediamine (TMEDA). This ligand coordinates to the metal centre in a bidentate fashion via the lone pairs on the nitrogen atoms of the two amino groups. Once the precursor molecule reaches the substrate, the spectator ligand effectively dissociates and is removed in the gas stream, without contaminating the film with carbon or nitrogen.[71]

The chelate-effect is often observed for these type of ligands, for example a bi- or tridentate ligand is entropically more stable than two or three equivalents of a monomeric ligand. This has been observed, for example in the formation of some lead sulphide precursors, where tridentate pentamethyldiethylenetriamine (PMDETA) and TMEDA adducts of the lead xanthate $Pb(S_2COEt)_2$ were isolable, but monodentate analogues decomposed immediately,[72] see figure 1.12.

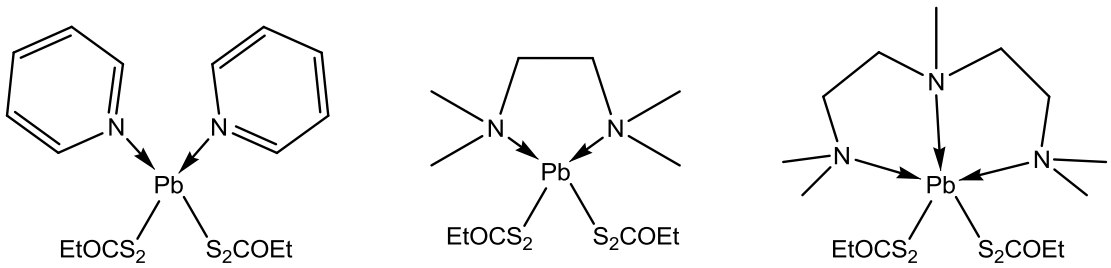

m.p. Dec. RT

$Pb(S_2COEt)_2.2pyr$

m.p. 102°C

$Pb(S_2COEt)_2.TMEDA$

m.p. 94°C

$Pb(S_2COEt)_2.PMDETA$

Figure 1.12: Lead (II) xanthate precursors with mono-, bi- and tridentate spectator ligands.[72]

A precursor that is able to reach the substrate (either by sufficient volatility or solubility) must then effect an appropriate and ideally clean decomposition at an

accessible temperature to yield the desired material. Metal β-diketonate complexes are often “go-to” single-source precursors to deposit a particular material owing to their generation of metal oxide by β-hydrogen elimination, shown in scheme 1.2.

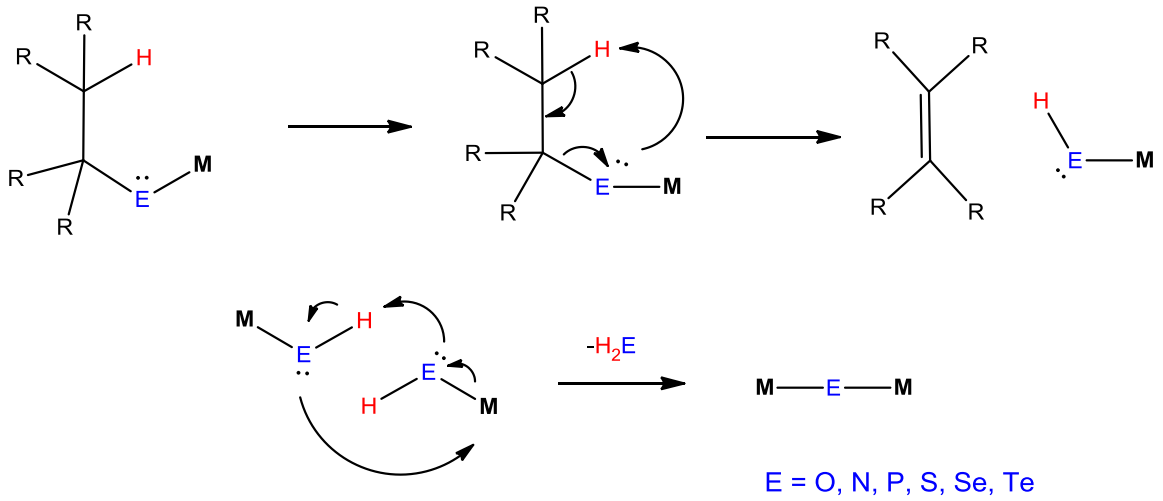

Scheme 1.2: General β-hydrogen elimination mechanism.[73]

Indeed, this mechanism can hypothetically occur with any metal complex with a hydrogen atom that is β to any non-carbon heteroatom which connects it to the metal. The mechanism produces an alkene by-product which is usually volatile enough to pass through the reactor and be exhausted. The as formed metal hydroxide species undergo condensation reactions to yield thin-films of the desired material.

Other precursors may require an external source of oxidant, such as oxygen gas, water or ethyl acetate. Although the process is referred to as “dual-source”, depending on the complexity of the material, this may require further, or multi-source precursor in-puts. An example of a dual-source process has already been described in the deposition of TiO_2 from $TiCl_4$ and EtOAc. Its single-source counterpart, the deposition from $Ti(OiPr)_4$ may seem a more elegant and logical choice until it is realised that the incredible high growth rates required (20 nm in ~2s) can only be achieved by the former system. This is largely due to the vast differences in vapour pressures of the two precursors at room temperature, limiting the single-source precursor to LPCVD applications.[24]

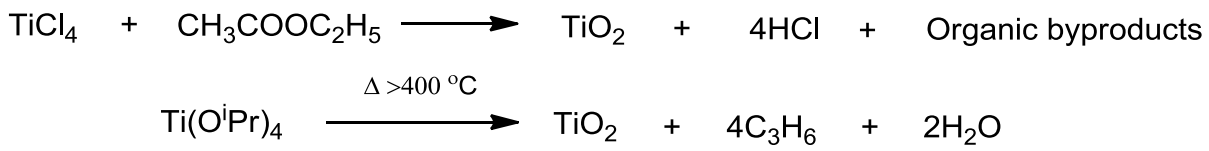

Scheme 1.3: Single- and dual-source precursor routes to TiO_2 thin-films

When a CVD process is scaled up to something comparable to a float line, operating costs are inherently huge. To be of realistic use in industry, therefore, the precursor must be economically viable. Furthermore, the large quantities of precursor involved also carry increased risks in terms of storage and transport of large amounts of volatile, toxic or flammable chemicals. It is therefore preferential to use a precursor with limited negative environmental impact.

The necessary and desirable qualities of a CVD precursor are summarised below: [74, 75]

- Volatility/solubility;
- Elements for desired material present in precursor(s);
- Thermal stability for decomposition window;
- Clean deposition pathway;
- Economically viable;
- Preferably non toxic;

1.5. Materials from metal nitrates

1.5.1 Chemical solution deposition (CSD)

Solution-processing of inorganic materials is certainly not a new concept. Formation of silica-gel from hydrolysed silicon alkoxides can be dated back as far as the mid-nineteenth century,[76] in what we now term sol-gel processing. There now exist a variety of solution-processing techniques for production of inorganic materials, such as spin-, dip-, and spray coating, doctor blading, spray pyrolysis, evaporation and inkjet printing. It is worth mentioning for project relevance that sol-gel techniques have been used to apply a number of optical coatings onto glass.[77] For a full review of the various techniques for solution processing of inorganic materials the reader is directed to the following literature.[78, 79] Figure 1.13 shows a diagram of a typical chemical solution deposition (CSD) process.

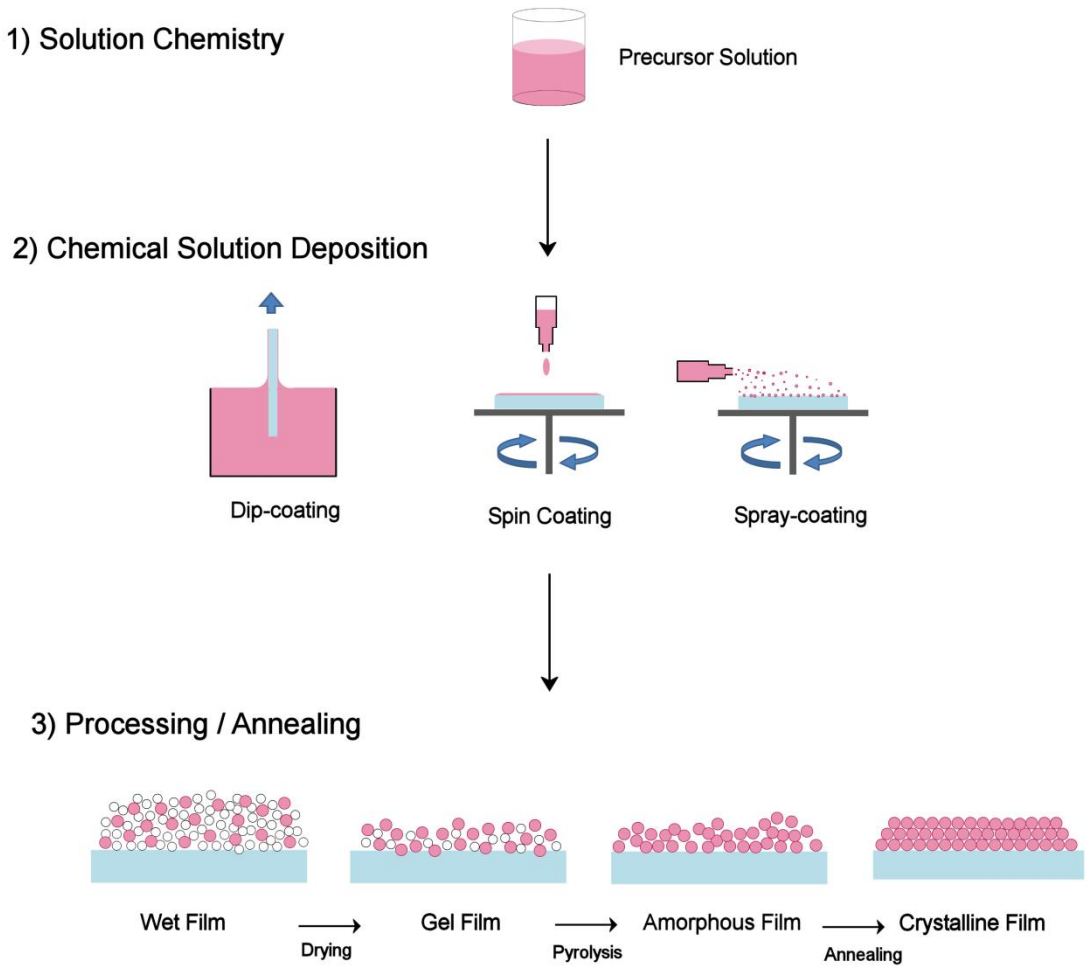

Figure 1.13: Diagram of a typical CSD process, adapted from source.[79]

As with a CVD process, CSD precursors require certain properties to achieve desired results, namely:

- Solubility of precursor(s) in solvent to for a one-pot solution;
- Long-term stability of the precursor solution, one month minimum;
- Adequate solution properties for application (e.g. viscosity for inkjet printing nozzles and spin-coating will be different);
- Wettability of substrate;
- Homogeneity retained during the process;
- Cracking and other defects of subsequent film kept to a minimum;
- Minimal diffusion of constituent elements between film and substrate;
- Minimal degradation of substrate throughout the process;

1.5.1 Combustion processing of metal nitrates

Typically, simple metal alkoxides and oxalates are popular choices for CSD. However precursor solutions containing simple salts such as metal-halides, -sulphates and -nitrates are finding increased usage. The attraction of a commercially available source of the metal, free from any carbon whatsoever has been exploited for a wealth of materials, and from such a variety of techniques that they simply cannot be documented here. The majority of work in this project has involved the use of metal nitrates as precursors to functional materials. Marks *et al* have reported the low-temperature combustion synthesis of a number of metal oxide materials from solutions of corresponding metal nitrate/urea systems.[80]

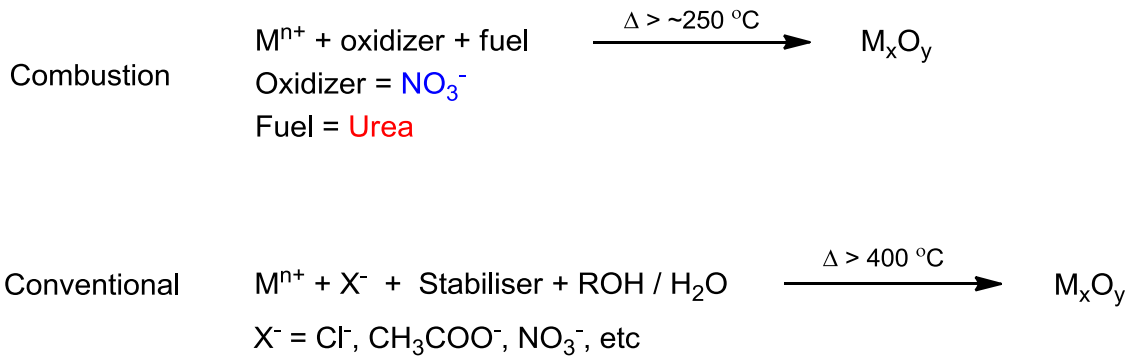

Figure 1.14: Two approaches to metal oxide materials

Materials are generated on the basis that a conventional pyrolysis requires a greater activation energy in the form of heat, whereas a precursor with an oxidiser and fuel component i.e. nitrate and urea will require far lower temperatures.

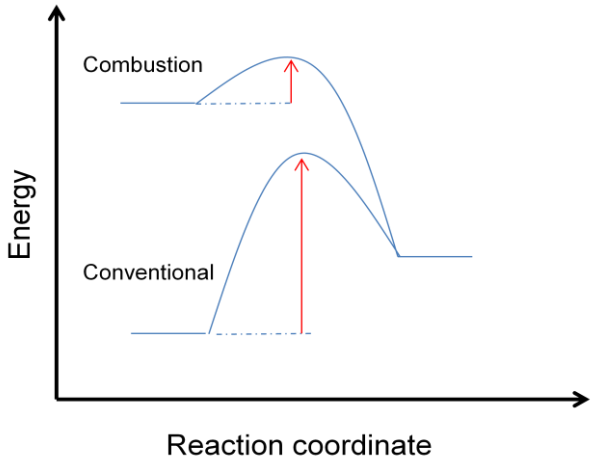

Figure 1.15: General energetics of combustion based synthesis versus conventional methods.

Metal-nitrates are very well characterised materials, commercially available in large quantities and relatively cheap. Furthermore, the overwhelming majority of metal nitrates are extremely soluble in common laboratory solvents such as water and ethanol. A few metal oxide thin-films relevant to this project that have been synthesised from a metal nitrate precursor are listed in table 1.4.

A localized energy supply is effectively generated by the heat of combustion, eliminating the need for external high processing temperatures. This enables formation of materials potentially at temperatures as low as 200°C. The formation of zinc oxide (ZnO) is shown in scheme 1.4 by way of example.

Scheme 1.4: Combustion synthesis of ZnO from $Zn(NO_3)_2.6H_2O$ and urea.

Table 1.4: Selected project-relevant thin-film materials that have been synthesised from a metal nitrate source

Metal Nitrate(s)	**Material fabricated**	**Temperature range (°C)**	**Applications**	**Deposition method**
$Zn(NO_3)_2.6H_2O$	ZnO	300 - 700	Microsensors, Memory transistors	Spin-coating [81]
$Zn(NO_3)_2.6H_2O$, $Sn(NO_3)_2$*	$ZnSnO_3$ (ZTO)	200 - 400	Thin film transistors (TFTs),	Spin-coating [80]
$Sn(NO_3)_4$	SnO_2	400	Solar control coatings, transparent conducting oxides (TCOs)	LPCVD[82]
$In(NO_3)_3$	In_2O_3	180 - 325	TCOs, TFTs,	Spin-coating [83]
$In(NO)_3$, $Sn(NO_3)_2$*	Sn : In_2O_3 (ITO)	200 - 500	TCOs, TFTs, LCD screens, photovoltaic devices.	Spin-coating [83]
$Ti(NO_3)_4$	TiO_2	230 - 330	Gas sensing, photocatalysis, water splitting, [21] photovoltaic devices, [22] self-cleaning coatings.	LPCVD [84]
$Al(NO_3)_3$	Al_2O_3	200	Adhesion layers, High-κ dielectrics	Dip-coating [85]
$Co(NO_3)_2$	CoO, Co_3O_4	300 - 500	Heterogeneous catalysis, solar absorbers, solid-state sensors	Spin-coating[86]

*$Sn(NO_3)_2$ species synthesised *in situ* from $SnCl_2$ and NH_4NO_3

CSD techniques such as spray- or spin-coating are wasteful, with much precursor-containing solution unused. Inkjet printing techniques are more sophisticated and offer potential to maximise precursor efficiency. Furthermore, thin-film synthesis is typically a two-step process - the deposition of the precursors and then a subsequent activation or annealing step. Another unfortunate consequence of a moving substrate (either spinning or vertical dipping) is that of an inherent non-uniformity in the resulting thin films compared to a CVD process. But perhaps the biggest disadvantage of spin-, dip- or spray-coating techniques is that of substrate size limitation. Large area deposition is a requirement for industrial scale operations and this project aims to exploit the middle-ground offered by an AACVD process.

Whilst not significantly volatile, the overwhelming majority of metal nitrates are extremely soluble and therefore can be explored as aerosol-assisted CVD precursors. Despite being one of the simplest precursors available, the amount of work achieved relating to AACVD of pure metal nitrates is extremely limited.

1.6. Analysis of solid state materials

1.6.1. Physical appearance

1.6.1.1. Scanning Electron Microscopy (SEM)

SEM is one of the most common techniques for thin-film analysis and is able to generate data including film thickness, crystallite size, surface morphology/topography and elemental composition. A beam of high energy electrons generated from a tungsten filament, dissipate into a sample producing a variety of emissions. These include secondary electrons, backscattered electrons, X-rays, visible light, and IR radiation, see figure 1.16. Images of surface morphology and topography are commonly collected from secondary electron detection, usually in the accelerating voltage region of 2 – 10 kV. X-rays yield information about elemental composition (see 1.6.2.2 EDS). [87]

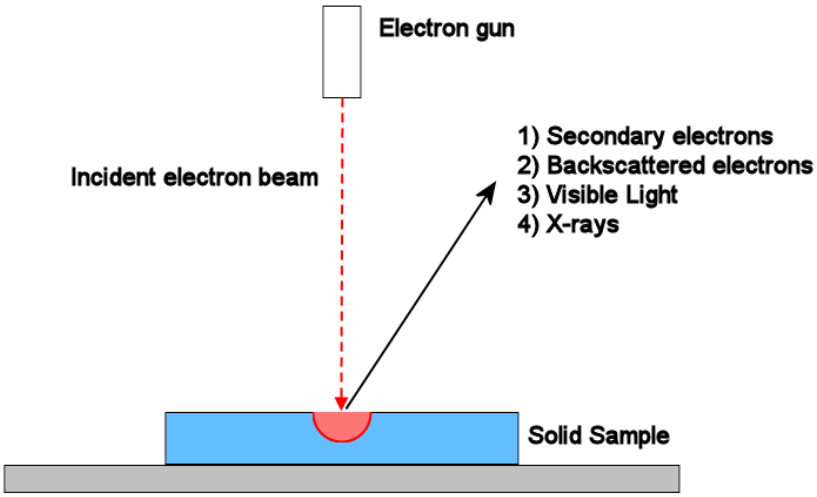

Figure 1.16: Different types of emitted radiation from a sample within a scanning electron microscope.[87]

The microscope works on similar principles to a light microscope, except the lenses are focussing the beam of electrons as opposed to visible light. These electrons must be able to dissipate through the sample – necessitating a conducting sample, or, coating of an insulating (or semiconducting) sample with a conductive material such as gold or chromium. Once coated in a conducting layer, accurate elemental analysis of a material becomes impossible due to the contaminating overcoat.

1.6.1.2. UV-visible spectroscopy

The optical properties of coatings on glass are integral to the product. A self-cleaning window must still fulfil its primary function, i.e. have high optical transparency. Other coatings may serve anti-reflection or decorative purposes. It has already been mentioned that colour can arise from specific transitions of metals in certain environments so UV-vis spectroscopy is important when measuring some of these optical properties.

In flat-plate mode, the spectrometer is capable of recoding transmitted, absorbed, and reflected light.

1.6.2. Chemical composition

1.6.2.1. X-ray diffraction

The majority of thin-film characterisation in this project has relied on X-ray diffraction (XRD), Energy Dispersive X-ray Spectroscopy (EDS or EDX) and X-ray photoelectron spectroscopy (XPS). Each of these techniques offers unique information about the material and when used in conjunction with other characterisation methods are powerful sources of data.

A thin-film of a material can be analysed in much the same way as a powder, and will generate a similar diffraction pattern as long as the sample is crystalline. The arrangement of ions within a lattice determine where its Miller planes lie, and the spacing between them. Effectively an infinite number of these planes exist which can give rise to diffraction maxima when bombarded by X-rays at a particular diffraction angle.[88] The technique is non-destructive and can quickly determine the crystalline phase or phases of a deposited material. Since a generated pattern is unique to that material, it provides a fingerprint which can be indexed to a database for comparison. Amorphous material will not generate a pattern and therefore other techniques must be used for characterisation.[89]

1.6.2.2. Energy Dispersive Spectroscopy

EDS is both a qualitative and quantitative technique used in conjunction with SEM or TEM. Electrons from the primary beam penetrate into the material and ionise inner electrons of atoms within to excited states. Subsequent relaxation of these excited electrons does so with the emission of X-rays are with discreet energies dependent on the electronic configuration of the parent atom. An energy dispersive detector detects these X-rays and produces a spectrum of the number of counts versus a particular energy. Indexation of the spectrum allows qualitative analysis of the material, while quantitative measurements (such as weight % of a particular atom) can be made by summation of intensities.

Limitations of EDS include the inability to detect elements with $Z < 4$, i.e. H, He, Li and Be. Effective detection limits of an SEM-EDS system is typically in the range 0.1 – 0.5 wt %.[90]

Additionally, in order to receive signal from heavier elements a higher accelerating voltage must be used. This results in deeper penetration of the primary electron beams into the sample and therefore more bulk generation of X-rays relative to sample signal. In some cases this poses a problem, particularly where thin films are concerned, as it becomes harder to resolve surface signal from substrate noise.

EDS is also considered a non-destructive technique as the same sample can be re-analysed many times. In reality samples do suffer some damage under the electron beam, and in some cases severe charging can actually alter the surface due to thermal expansion or oxidation.

1.6.2.3. X-ray photoelectron spectroscopy

XPS is an exceptionally useful technique allowing for qualitative and quantitative analysis of a sample with the added benefit of depth profiling. A sample surface is bombarded by X-rays of known wavelength and photoelectrons are ejected from the top 10 nm of the sample. These photoelectrons are very short-range which makes the technique highly surface specific. A diagram of the basic principles of XPS is shown in figure 1.17.

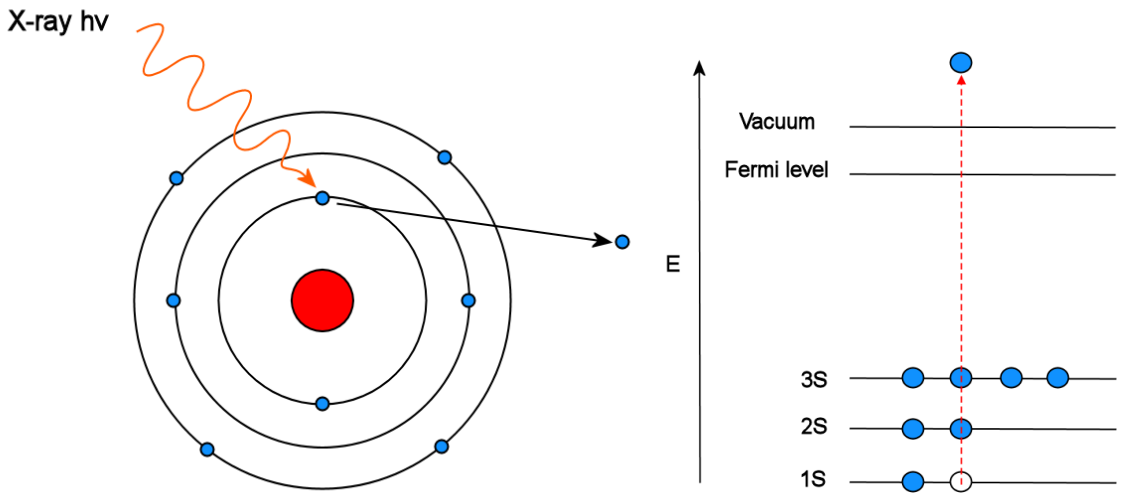

Figure 1.17: Basic principles of XPS showing ejection of core electrons

Since this process is elastic, the kinetic energy of the ejected electrons and therefore the binding energy of the electrons can be measured. These energies are unique to a specific core orbital from a specific element.91 In this way it is possible to differentiate between a C 2p or O 2p electron. Similarly, since electrons experience different environments depending on the oxidation state of a metal, a Cu^{2+} 3d electron will give a different binding energy to that of a Cu^{+} 3d electron.

When combined with an ion beam etcher, the technique becomes dynamic as the surface is etched away. As this occurs, ejected electrons originate from deeper into the bulk of the sample, detecting any changes in composition throughout the film and eventually the substrate beneath. This technique is extremely useful for layered devices and can also give an indication of the thickness of a film.

1.6.3. Photoactivity

It is necessary to have a reliable and quantitative method for measuring the photocatalytic response from a deposited film. Typically where TiO_2 is concerned, the conversion of stearic acid to carbon dioxide and water has been a standard test for photocatalyitc ability. This experiment involves the application of stearic acid from solution onto the surface of the substrate to form a solid, waxy film. UV-light is applied at the correct wavelength, and the destruction of the stearic acid layer is monitored, either by measurement of gas evolution, changes in thickness of the film, or more commonly – the decrease of the infrared absorption in the range $2700cm^{-1}$-$3000cm^{-1}$ with respect to time.[92]

$$C_{17}H_{35}COOH + 26O_2 \xrightarrow{h\nu > E_{bg}} 18CO_2 + 18H_2O$$

One of the drawbacks of this type of experiment, is that little information can be obtained for multiple locations on a film, for example a film with varying thicknesses. The stearic acid test is also too slow to be of use for rapid assessment of photocatalytic films, potentially taking days for full destruction of the layer under constant UV illumination. This has caused researchers to look to dyes which are associated with a colour change when illuminated with UV-light in the presence of a photocatalyst.

Mills *et al* have developed an intelligent ink for the rapid assessment of photocatalytic activity of self-cleaning thin films based on the blue dye rezazurin.[93] The photo-reductive mechanism by which the ink functions involves the sacrificial electron donor glycerol, in a hydroxyethylcellulose polymer solution containing resazurin.[94] The ink is spin coated (or in some cases drawn on with a felt tip pen) onto the titania film. Upon illumination of the TiO_2 coated in ink, photo-generated holes oxidise the sacrificial electron donor effectively, acting as a trap. The photo-generated electrons are then available (free from recombination) to reduce the resazurin dye to resorufin which is pink in colour. This is illustrated in scheme 1.5.

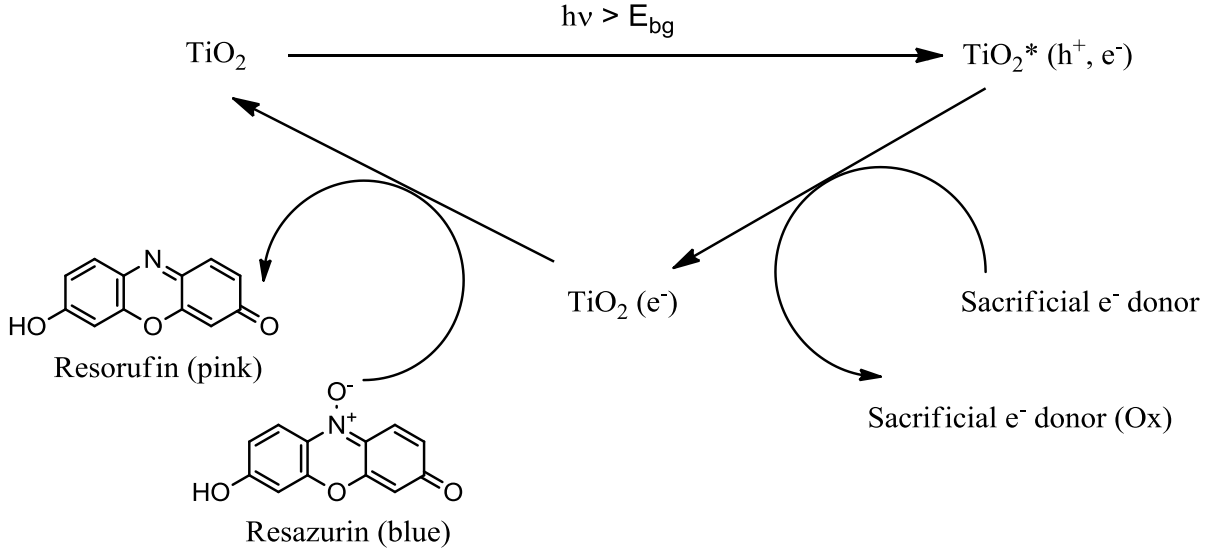

Scheme 1.5:. The reduction of resazurin ink to resorufin in the presence of a sacrificial electron donor, on an irradiated film of titania.[94]

If a baseline spectrum of the underlying substrate plus coating is recorded, the colour change of the dye can then be monitored by conventional UV-Vis spectroscopy at varying intervals. Whilst this technique is excellent for rapid assessment of photocatalytic activity of the films, there is debate as to whether reliable quantitative data can be obtained by this method.

1.7. Project outline

Blue, photocatalytic coatings on glass

It has been discussed that the production of the self-cleaning, coloured glazing product Pilkington Activ Blue^{TM} involves significant challenges to the float glass industry. Not least the requirement for a complete float-line shutdown to change raw materials, but also the transportation of blue glass to countries with relevant markets.

The initial focus of this project is geared toward self-cleaning (photocatalytic) coating on glass for architectural and glazing applications. The coating will ideally be blue and be applied using CVD methods.

The ultimate goal is a precursor, or process using existing precursors for the production of blue, photoactive coatings on glass which can be scaled up for industrial sized applications such as a Pilkington float line.

While other photoactive coatings are known, this project focuses on the use of a thin film of the very well characterised photocatalyst TiO_2. Introduction of colour is explored by the formation of a colour-containing base layer prior to CVD of TiO_2 on top. The resultant thin-films will be thoroughly characterised and assessed for viability as functional coatings on glass.

Novel, low-temperature process for low-E coatings

A secondary aim of the project is to develop a precursor, or process utilising existing precursors for the low-temperature deposition of low-emissivity coatings based on fluorine-doped tin oxide, FTO.

The coating must be applied by CVD methods with the potential to be scaled up for industrial use.

Functional materials from metal-nitrate processing

Metal nitrates offer potential as affordable and soluble precursors to a near-limitless array of materials if the deposition process can be sufficiently controlled. They offer advantages in that there is no carbon present which could potentially contaminate the film, and are often significantly less toxic than their

organometallic counterparts (e.g. the benign $Sn(NO_3)_2$ versus toxic Me_2SnCl_2). Furthermore, the majority of metal nitrates do not require air- or moisture-sensitive handling techniques which can otherwise make scale-up a significant challenge. In this regard, a variety of materials could be produced from basic metal nitrate precursors. More complicated coatings such as mixed-metal oxides will be explored by AACVD from metal nitrates.

References for chapter 1

1. NSG The Glass Industry. http://www.nsg.com/en/about-nsg/whatwedo
2. Ltd., P. B. In *Proceedings of the Royal Society Series A*, The Royal Society of London Series A-Mathematical and Physical Sciences, London, 1969; London, 1969; p 1.
3. Beretto-Lopez, M., *Glass Chemistry*. Springer-Verlag Berlin and Heidelberg GmbH & Co. K: Berlin, 1994.
4. Klein, D.; Ward, L., *The History of Glass*. Illustrated: 2000.
5. Tangram Float Glass Production. http://www.tangram.co.uk/TI-Glazing-Float%20Glass.html
6. Parkin, I. P.; Palgrave, R. G., CVD of Functional Coatings on Glass. In *Chemical Vapour Deposition: Precursors, Processes and Applications.*, Jones, A. C.; Hitchman, M. L., Eds. Royal Society of Chemistry: 2009.
7. Cotton, F. A.; Wilkinson, G., *Advanced Inorganic Chemistry*. 5th ed.; Wiley: New York, 1988.
8. Troy, M., **Flat Glass and Coatings On Glass**. In *Applications of Inorganic Chemistry in Industry*, NSG European Technical Centre: 2011.
9. Tao, J.; Cheung, N. W.; Hu, C., *IEEE Electron Device Lett.* **1993,** *14*, 249-251.
10. Pratt, A., *Overview of the Use of Copper Interconnects in the Semiconductor Industry*. 2004.
11. Rickerby, J.; Steinke, J. H. G., *Chem. Rev.* **2002,** *102*, 1525-1550.
12. Kwon, O.-K.; Kim, J.-H.; Park, H.-S.; Kang, S.-W., *J. Electrochem. Soc.* **2004,** *151*, G109-G112.
13. Sousa, R. C.; Prejbeanu, I. L., *C. R. Phys.* **2005,** *6*, 1013-1021.
14. Renuka, N. K.; Praveen, A. K.; Aniz, C. U., *Microporous and Mesoporous Materials* **2013,** *169*, 35-41.
15. Fang, G.; Liu, Z.; Liu, C.; Yao, K.-l., *Sensors and Actuators B: Chemical* **2000,** *66*, 46-48.
16. Steele, B. C. H., *Ceramics International* **1993,** *19*, 269-277.
17. Qureshi, U.; Dunnill, C. W.; Parkin, I. P., *Applied Surface Science* **2009,** *256*, 852-856.

18. Verhelst, J.; Decroupet, D.; De Vos, D., *Catalysis Science & Technology* **2013,** *3*, 1579-1590.
19. Bamwenda, G. R.; Sayama, K.; Arakawa, H., *Chemistry Letters* **1999,** *28*, 1047-1048.
20. Ismail, A. A.; Bouzid, H., *Journal of Colloid and Interface Science* **2013,** *404*, 127-134.
21. Jitputti, J.; Pavasupree, S.; Suzuki, Y.; Yoshikawa, S., *Journal of Solid State Chemistry* **2007,** *180*, 1743-1749.
22. Oregan, B.; Gratzel, M., *Nature* **1991,** *353*, 737-740.
23. Mills, A.; Elliott, N.; Parkin, I. P.; O'Neill, S. A.; Clark, R. J. H., *Journal of Photochemistry and Photobiology a-Chemistry* **2002,** *151*.
24. Besserguenev, V. G.; Pereira, R. J. F.; Mateus, M. C.; Khmelinskii, I. V.; Nicula, R. C.; Burkel, E., *International Journal of Photoenergy* **2003,** *5*.
25. Colombo, D. G.; Gilmer, D. C.; Young, V. G.; Campbell, S. A.; Gladfelter, W. L., *Chemical Vapor Deposition* **1998,** *4*.
26. Kojima, M.; Kato, H.; Imai, A.; Yoshida, A., *Journal of Applied Physics* **1988,** *64*, 1902-1905.
27. Bélanger, D.; Dodelet, J. P.; Lombos, B. A.; Dickson, J. I., *Journal of The Electrochemical Society* **1985,** *132*, 1398-1405.
28. Maruyama, T.; Tabata, K., *Journal of Applied Physics* **1990,** *68*, 4282-4285.
29. Borman, C. G.; Gordon, R. G., *Journal of The Electrochemical Society* **1989,** *136*, 3820-3828.
30. Ghandhi, S. K.; Siviy, R.; Borrego, J. M., *Applied Physics Letters* **1979,** *34*, 833-835.
31. Fang, T.-H.; Chang, W.-J., *Applied Surface Science* **2003,** *220*, 175-180.
32. Fang, T.-H.; Chang, W.-J., *Applied Surface Science* **2005,** *252*, 1863-1869.
33. Ma, H. L.; Zhang, D. H.; Win, S. Z.; Li, S. Y.; Chen, Y. P., *Solar Energy Materials and Solar Cells* **1996,** *40*, 371-380.
34. Stanley, J. E.; Swain, A. C.; Molloy, K. C.; Rankin, D. W. H.; Robertson, H. E.; Johnston, B. F., *Applied Organometallic Chemistry* **2005,** *19*, 644-657.
35. Noor, N.; Parkin, I. P., *Journal of Materials Chemistry C* **2013,** *1*, 984-996.

36. Becht, M.; Gerfin, T.; Dahmen, K. H., *Chemistry of Materials* **1993,** *5*, 137-144.
37. Malandrino, G. a. N. R. L. a. B. C. a. C. F. a. F. I. L., *Chemical Vapor Deposition* **2000,** *6*, 233--238.
38. Wrench, J. S. a. B. K. a. A. H. C. a. J. A. C. a. B. J. a. C. P. R. a. K. P. J. a. W. M. a., *Chemical Vapor Deposition* **2009,** *15*, 259--261.
39. Petersen, G. A.; Parmeter, J. E.; Apblett, C. A.; Gonzales, M. F.; Smith, P. M.; Omstead, T. R.; Norman, J. A. T., *J. Electrochem. Soc.* **1995,** *142*, 939-944.
40. Krisyuk, V.; Aloui, L.; Prud'Homme, N.; Sarapata, B.; Senocq, F.; Samelor, D.; Vahlas, C., *ECS Trans.* **2009,** *25*, 581-586.
41. Choi, H.; Hwang, S., *Chem. Mater.* **1998,** *10*, 2326-2328.
42. Chen, T. Y.; Vaissermann, J.; Ruiz, E.; Sénateur, J. P.; Doppelt, P., *Chem. Mater.* **2001,** *13*, 3993-4004.
43. Temple, D.; Reisman, A., *J. Electrochem. Soc.* **1989,** *136*, 3525-3529.
44. Crick, C. R.; Parkin, I. P., *Journal of Materials Chemistry* **2011,** *21*, 14712-14716.
45. Mond, L.; Langer, C.; Quincke, F., *J. Chem. Soc.* **1890,** *57*, 749-753.
46. Brissonneau, L.; Vahlas, C., *Chem. Vap. Deposition* **1999,** *5*, 135-142.
47. Lim, B. S.; Rahtu, A.; Gordon, R. G., *Nat. Mater.* **2003,** *2*, 749-754.
48. Maruyama, T.; Tago, T., *J. Mater. Sci.* **1993,** *28*, 5345-5348.
49. Kada, T.; Ishikawa, M.; Machida, H.; Ogura, A.; Ohshita, Y.; Soai, K., *J. Cryst. Growth* **2005,** *275*, e1115-e1119.
50. NSG, P., Pilkington Activ Range Brochure. In 2015.
51. Shriver, D. F., *Inorganic Chemistry*. Oxford University Press: 1999; Vol. Third Edition.
52. Rao, K. J., Chapter 11 - Optical properties. In *Structural Chemistry of Glasses*, Rao, K. J., Ed. Elsevier Science Ltd: Oxford, 2002; pp 429-462.
53. Manning, T.; Sanderson, K., Research Proposal Discussions. In Hill, M. S.; Molloy, K. C.; Johnson, A. L.; Wickham, B. J., Eds. Bath, 2009.
54. Wickham, B. Single-Source Precursors for the CVD of Metal Silicon Oxide Materials. University of Bath, 2012.
55. Hill, M. S.; Johnson, A. L.; Manning, T. D.; Molloy, K. C.; Wickham, B. J., *Inorganica Chimica Acta* **2014,** *422*, 47-56.

56. van Mol, A. M. B.; Chae, Y.; McDaniel, A. H.; Allendorf, M. D., *Thin Solid Films* **2006,** *502*, 72-78.
57. Allendorf, M. D., *Thin Solid Films* **2001,** *392*, 155-163.
58. Jones, A. C.; O'Brien, P., *CVD of Compound Semiconductors*. VCH: 1997.
59. Atkins, P. W.; de Paula, J., *Physical Chemistry*. Oxford University Press: 2003.
60. Jones, A. C. a. H., M. L., Overview of Chmeical Vapour Deposition. In *Chemical Vapour Deposition: Precursors, Processes and Applications* Jones, A. C. a. H., M. L., Ed. Royal Society of Chemistry: 2009.
61. Mond, L.; Langer, C.; Quincke, F., *Journal of Organometallic Chemistry* **1990,** *383*, 1-5.
62. Malik, M. A.; O'Brien, P., Basic Chemistry of CVD Precursors. In *Chemical Vapour Deposition: Precursors, Processes and Applications*, Jones, A. C.; Hitchman, M. L., Eds. 2009.
63. Boer, H. J., *Journal de Physique IV* **1995,** *5*.
64. Krumpdieck, S. P., CVD Reactors, Delivery and Systems Technology. In *Chemical Vapour Deposition: Precursors, Processes and Applications*, Jones, A. C.; Hitchman, M. L., Eds. Royal Society of Chemistry: 2009.
65. Bernoulli, D., *Hydrodynamica - De Viribus et Motibus Fluidorum Commentaril*. 1738.
66. Jones, A. C.; Hitchman, M. L., Overview of Chemical Vapour Deposition. In *Chemical Vapour Deposition: Precursors, Processes and Applications*, Jones, A. C.; Hitchman, M. L., Eds. Royal Society of Chemistry: 2009.
67. Lecouvreur, P.; Pirot, M.; Quoizola, R.; Monna, R.; Madec, A.; Massines, F. In *Comparison between Atmospheric and Low Pressure PECVD SiNx:Hy Coatings for Photovoltaic Applications*, European Photovoltaic Solar Energy Conference and Exhibition, Frankfurt, Gernamy, 2009; Frankfurt, Gernamy, 2009.
68. Jones, A. C., Hitchman, M. L., Chemical Vapour Deposition: Precursors, Processes and Applications. In Royal Society of Chemistry: Cambridge, 2009.
69. Xu, Y., Yan, X. –T., Chemical Vapour Deposition: An Integrated Engineering Design for Advanced Materials. In Springer: London, 2010.

70. Rees, W. S., Introduction. In *CVD of Nonmetals*, Wiley-VCH Verlag GmbH: 2007; pp 1-35.
71. Jones, A. C.; Aspinall, H. C.; Chalker, P. R., Chemical Vapour Deposition of Metal Oxides for Microelectronic Applications. In *Chemical Vapour Deposition: Precursors, Processes and Applications*, Jones, A. C.; Hitchman, M. L., Eds. Royal Society of Chemistry: 2009.
72. Clark, J. M.; Kociok-Kohn, G.; Harnett, N. J.; Hill, M. S.; Hill, R.; Molloy, K. C.; Saponia, H.; Stanton, D.; Sudlow, A., *Dalton Transactions* **2011,** *40*, 6893-6900.
73. Mutin, P. H.; Vioux, A., *Chemistry of Materials* **2009,** *21*, 582-596.
74. Doppelt, P., *Coord. Chem. Rev.* **1998,** *178–180, Part 2*, 1785-1809.
75. Jones, A. C.; Hitchman, M. L., *Chemical Vapour Deposition: Precursors, Processes and Applications*. 1 ed.; Royal Society of Chemistry: Cambridge, 2009.
76. Ebelmen, M., *Ann. Chim. Phys.* **1846,** *16*, 129-166.
77. Aegerter, M. A.; Mennig, M., *Sol-Gel Technologies for Glass Producers and Users*. Springer: 2004.
78. Mitzi, D. B., Solution processing of inorganic materials. John Wiley & Sons, Inc., Publication: 2009.
79. Schneller, T.; Waser, R.; Kosec, M.; Payne, D., *Chemical Solution Deposition of Functional Oxide Thin Films*. Springer-Verlag: 2013.
80. Kim, M.-G.; Kanatzidis, M. G.; Facchetti, A.; Marks, T. J., *Nat Mater* **2011,** *10*, 382-388.
81. Kitazawa, N.; Aono, M.; Watanabe, Y., *Journal of Physics and Chemistry of Solids* **2014,** *75*, 1194-1200.
82. Smith, R. C.; Hoilien, N.; Roberts, J.; Campbell, S. A.; Gladfelter, W. L., *Chemistry of Materials* **2002,** *14*, 474-476.
83. Kim, M. G.; Kanatzidis, M. G.; Facchetti, A.; Marks, T. J., *Nature Materials* **2011,** *10*, 382-388.
84. Gilmer, D. C., *Chemical Vapor Deposition* **1998,** *4*, 9--11.
85. Pal, B. N.; Dhar, B. M.; See, K. C.; Katz, H. E., *Nat Mater* **2009,** *8*, 898-903.
86. Wang, S.; Zhang, B.; Zhao, C.; Li, S.; Zhang, M.; Yan, L., *Applied Surface Science* **2011,** *257*, 3358-3362.

87. Wells, O. C., Scanning Electron Microscopy. In McGraw-Hill, Inc.: 1974; p 421.
88. Weller, M., *Inorganic Materials Chemistry*. Oxford University Press: 1994.
89. Dinnebier, R., *Powder Diffraction: Theory And Practice*. Royal Society of Chemistry: Cambridge, 2008.
90. Garratt-Reed, A.; Bell, D., *Energy-Dispersive X-Ray Analysis in the Electron Microscope*. BIOS Scientific Publishers LTD: Oxford, UK, 2003; p 145.
91. Briggs, D., *Practical Surface Analysis: Auger and X-ray Photoelectron Spectroscopy*. 2nd ed.; Wiley: 1990.
92. Mills, A.; Lepre, A.; Elliott, N.; Bhopal, S.; Parkin, I. P.; O'Neill, S. A., *Journal of Photochemistry and Photobiology a-Chemistry* **2003,** *160*, 213-224.
93. Mills, A.; McFarlane, M., *Catalysis Today* **2007,** *129*.
94. Mills, A.; Wang, J. S.; Lee, S. K.; Simonsen, M., *Chemical Communications* **2005**, 2721-2723.

Chapter 2:

Blue, photocatalytic coatings

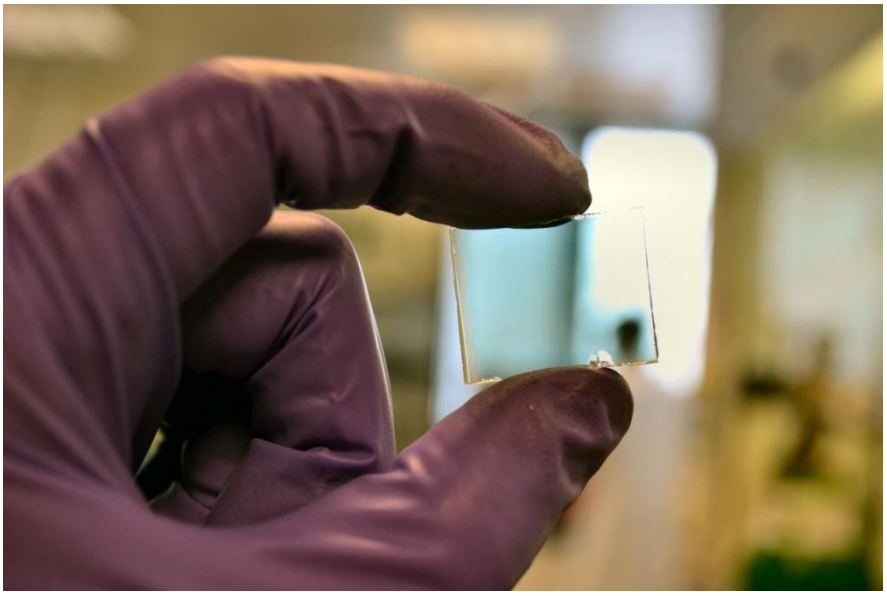

Figure 2.1: A blue, photocatalytic coating on glass based on TiO_2

2.1. Introduction

2.1.1. Titania

In 1929 it was reported that the pigment “Titanium White” (titanium dioxide) was responsible for the bleaching of paintings, giving them a chalky appearance.[1] This initiated a number of studies on the photocatalytic action of TiO_2 which ultimately led to its realisation as a material of huge commercial importance.[2] The high refractive index of titania (2.5-3 for anatase) gave rise to its attraction as an opacifier after it was discovered that by coating the pigment with hydrous silica, the photodegradation of paints was largely eliminated.[3] An estimated 5 million tons of titanium dioxide is produced annually, which reflects the diversity and significance of its industrial applications.[4] These include, but are not limited to, a whitener in paints and plastics, the UV-absorbing component in sunscreen, and even as a food colourant. The photocatalyic ability of anatase TiO_2 has been extensively studied in recent years, with a focus for application in solar cells,[5] water splitting,[6] and significantly in self cleaning surfaces.

It has been discussed in the previous chapter, that TiO_2 deposited as a thin film, has found use in the commercially available Pilkington Activ^{TM} range of self-cleaning products.[7] However, the absorption edge of anatase TiO_2 ($\lambda \leq 385nm$) does not provide a good fit with the solar spectrum and therefore limits utility to the near ultra-violet. There has been significant research by Parkin and Mills among others, into shifting the absorption into the visible light region so as to utilise more of the available energy and thus increase the efficiency of the photocatalytic material.[8] Invariably this involves doping oxygen vacancies in the titania lattice with a range of elements to modify the band gap. CVD has proven to be an ideal route to not only producing uniform films, but also effectively doping titania resulting in improved photocatalytic response.

While most efforts of doping titania are focussed on improving the effectiveness of the material (such as utilisation of indoor lighting for bacteriacidal coatings),[9] there is also another reason why band gap modification is desirable, and that is to change the aesthetic properties of the material. The NSG product Pilkington Activ^{TM} Blue is a self-cleaning blue glass with a main employment in conservatory windows.[7] However, the current Activ^{TM} Blue is produced by depositing a thin

layer (~25nm) of TiO_2 onto blue float glass. Where NSG float lines are employed, production of blue glass requires changing the base composition of the glass itself, usually by adding large quantities of cobalt (II) oxide, (also known as cobalt blue pigment). The changing of raw materials requires around five days of down-time on a line which is designed to be operating non-stop for 10-15 years. Furthermore, Activ^{TM} Blue is currently produced in the US where there exists little market for the product, which requires shipment to European markets.

2.1.2. Photocatalysis in TiO_2

There are three naturally occurring polymorphs of TiO_2; rutile, anatase, and brookite, whose crystal structures are shown in figure 2.2. Rutile is the most thermally stable, and brookite the least stable and rarest form.[10]

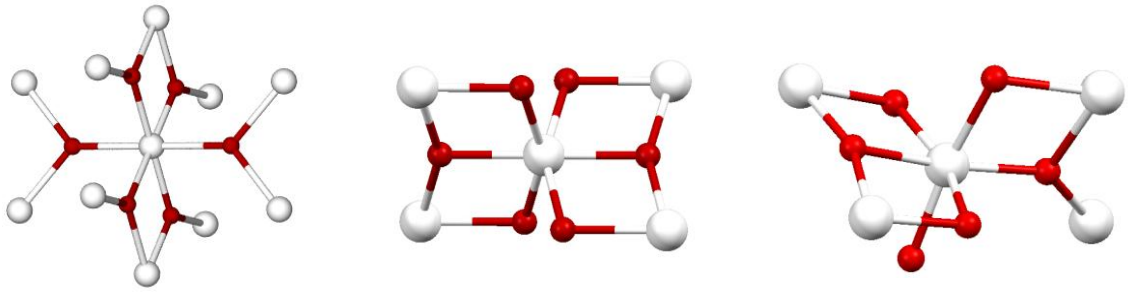

Rutile Anatase Brookite

Figure 2.2: The three polymorphs of titania: rutile, anatase and brookite. Ti (white), Oxygen (red). Adapted from source.11

Rutile[12] and anatase crystallise in tetragonal unit cells, while brookite[13] exists in an orthorhombic cell possessing both edge-sharing and corner TiO_6 units. There are two edge-sharing octahedra in rutile while anatase contains four. TiO_6 symmetry in rutile is D_{2h} rather than O_h due to differences in axial and equatorial Ti-O bond lengths. In anatase, further displacements of oxygen atoms for the equatorial positions result in D_{2h} symmetry again. In brookite, even further distortions from true octahedral are seen as all Ti-O bond lengths differ from one another, leading to C_1 symmetry in the TiO_6 units.[14] The Ti-O bond angles of every TiO_6 octahedron are different in all three structures, and both anatase and brookite will convert irreversibly to rutile upon heating.[15] By looking at the trigonal-planar-like Ti_3O units, it can be seen that the oxide centres in the rutile phase

take on a Y-shaped geometry. In anatase these units appear as more T-shaped, whereas in brookite, both T- and Y-shaped units exist.

Titanium dioxide is a wide band gap semiconductor, with band gaps of 3.2 and 3.0 eV for anatase and rutile respectively.[16] This is the key feature which enables photocatalysis to take place. It is worth noting that brookite remains relatively unexplored in terms of its photocatalytic ability due to its rarity and difficulty in preparation. When light of equivalent or greater energy than the band gap is absorbed by the semiconductor, an electron e^- is promoted from the valence band to the conduction band, resulting in the generation of a hole h^+ in the valence band (see figure 2.3). While rutile has the narrower band gap compared to anatase, the latter is preferred for photocatalysis due to its slower rate of electron-hole pair recombination compared to its rutile counterpart. [17]

The term “photocatalysis” can be misleading, as it implies a reaction is taking place that is catalysed by light. In fact this is not the case, as argued by Suppan:

“In a photochemical reaction, light always acts as a reactant, never as a catalyst…...light is absorbed and its energy is used to make electronically excited molecules; it will not come out and cannot be used after the reaction, so by definition light is not a catalyst and the concept of ‘light catalysed’ reaction is fundamentally incorrect.”[18]

It is actually more appropriate to think of a photocatalytic reaction as an accelerated photo-activated reaction in the presence of a catalyst, in this case TiO_2. The band gap for anatase falls into the UV region of the electromagnetic spectrum and the generation of reactive species under UV radiation has been exploited for the photocatalytic oxidation of organic pollutants,[19] viruses,[20] and for self cleaning applications.[21] An illustration of the main processes that occur in a particle of titania after photo-excitation is shown in figure 2.3.

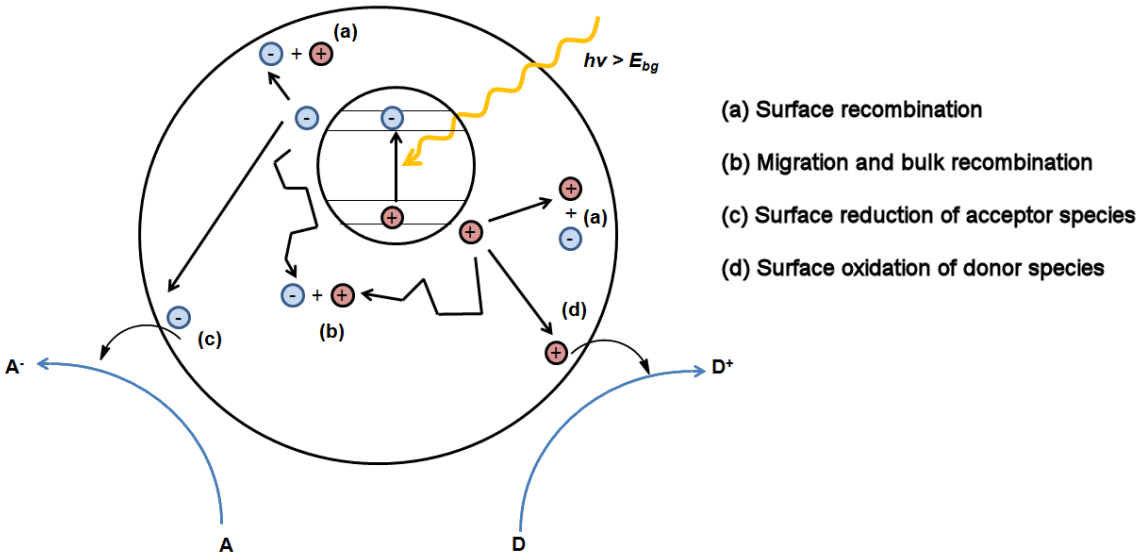

Figure 2.3: Processes upon photoexcitation within a particle of titania. Recombination of electron-hole pairs at the surface (a) and in the bulk (b). Photo-generated electrons can reduce electron acceptors A (c) and holes can oxidise electron donors D (d) at the surface. Adapted from source.[22]

Photo-generated electrons and holes migrate through the bulk of the particle to the surface where they become trapped temporarily. Any local electron donors such as water, can react with the trapped holes to form very reactive radical species (reaction (d) in figure 2.3). Conversely, nearby electron acceptors will react to form other reactive species, e.g. O_2 reacting to form O_2^- (reaction (c) in figure 2.3). It is these highly reactive molecules which can oxidise other organic molecules in the vicinity, into CO_2, H_2O and mineral acids. A summary of reactions (c) and (d) can be shown in equation (1)

$$A + D \xrightarrow[\text{Light} > E_{bg}]{TiO_2} A^- + D^+ \qquad \textbf{(1)}$$

A number of factors affect the rate and efficiency of photocatalysis:

- The energy of the semiconductor band gap. Doping of the lattice with various elements can vary the band gap significantly, altering the wavelength of absorbable light;
- Film thickness. Thicker films will have a greater chance to absorb photons, however too thick a film will become opaque;
- Roughness of the film surface. This determines the available surface area on which active sites for radical or superoxide species can be generated, and be in contact with organic material;
- Crystallinity of the film. Different phases have been shown to have different band gaps, but also have different rates of electron-hole pair migration;

The main challenge to overcome is that the band gap falls in the UV region of the electromagnetic spectrum. Considerable efforts have been made to red-shift the band gap into the visible region, so as to utilise more of the available solar energy.[19] Doping with transition metals replaces a Ti^{4+} ion, and has been calculated to add an intra-bandgap energy level between the TiO_2 conduction and valence bands, as illustrated in figure 2.4. Doping with non-metal anions, results in the direct lowering of the bangap itself.

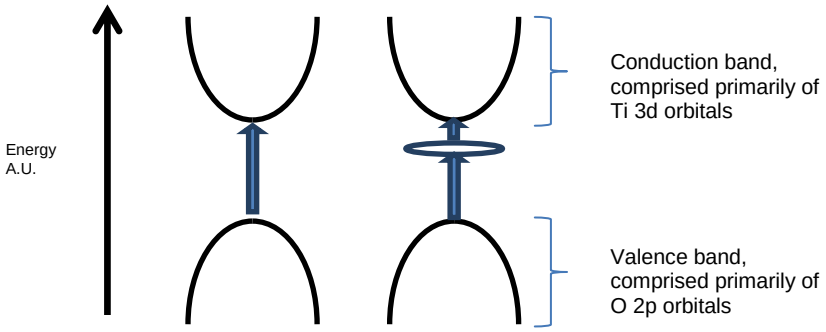

Figure 2.4: Density state diagram for TiO_2 (left) and transition metal-doped TiO_2. Adapted from source.[23]

2.1.3. Doping of TiO_2

The doping of titania for photocatalytic improvement was first seriously studied in 1989 where the effect of substituting Ti^{4+} ions with Cr^{3+} was observed.[24] Since then, various techniques have been employed to dope titania, such as ion implantation,[25] hydrothermal synthesis,[26, 27] and sol-gel formations.[28] It should be observed that the term "doping" can refer to either the direct incorporation of a M^+ cation into the lattice forming a solid solution, or the deposition of small particles of the M_2O_n oxide on the surface of the TiO_2.

A recent review by Parkin covers all of the elements which have been successfully doped into titania films via chemical vapour deposition processes.[8] These include non metals, almost all of the transition metals and a few selected lanthanides. The conclusion made, was that out of all the dopants that have been shown to improve visible light photocatalytic ability of TiO_2, there is no confident candidate for which is best. The reasoning for this lies in the various methods that have been employed to measure photocatalytic activity over the years, which include the stearic acid test, and various colour-changing dyes such as methylene blue and resazurin. It is recommended in the review, that a better understanding of photocatalytic behaviour would be generated if photocatalytic rates were recorded as formal quantum efficiencies (FQE).

Many precursors are known to give colouration in films. This can either be a result of the inherent colour of the deposited molecule, manipulation of the bandgap via doping, or particle size. In titania, it has been observed that nitrogen doping using *t*-butylamine as the nitrogen source gives the film a characterstic yellow-green tint,[29] while doping with tungsten gives a blue tinge to the coating.[23] Yellow coatings could perhaps find use in self-sterilizing surfaces such as hospitals, but are not desirable for glazing applications.

2.1.4. Deposition Strategy

Since there is much literature with regard to doping titania, it was decided to initially deposit a metal oxide which was known to exhibit aesthetically pleasing colour onto float glass with a SiCO barrier layer. A layer of titania is then deposited on top, figure 2.5.

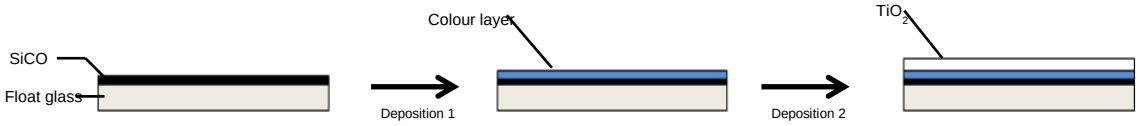

Figure 2.5: Diagram of two-stage deposition for coloured photoactive film.

Previous work in the Hill-Molloy-Johnson group has shown that some copper precursors have decomposed in the presence of oxygen to yield uniform yellow-green films of copper(I) oxide, Cu_2O.

.

2.2. Results and discussion

2.2.1. Synthesis of metal nitrate-urea complexes

Using the concept of combustion synthesis, several copper nitrate compounds were synthesised with differing urea ligands to use as precursors to copper oxide thin films. A general synthetic procedure for metal nitrate-urea complexes is shown in scheme 2.1.

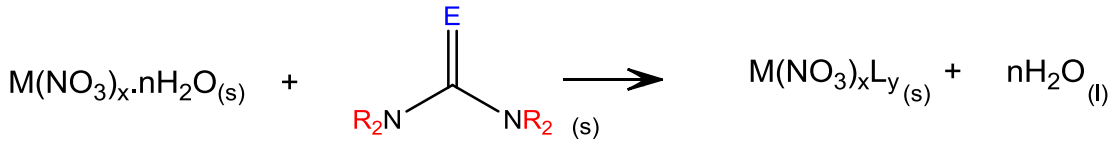

E = O, S, Se
R = H, Me

Scheme 2.1: General synthesis for a metal nitrate-urea complex

A number of Cu(II) nitrate-urea complexes were synthesised by dissolving the hydrated nitrates in ethanol and adding 1 – 6 equivalents of urea ligands. The solution was stirred for 30 minutes and allowed to evaporate and in all cases a tetra-urea product was formed (scheme 2.2).

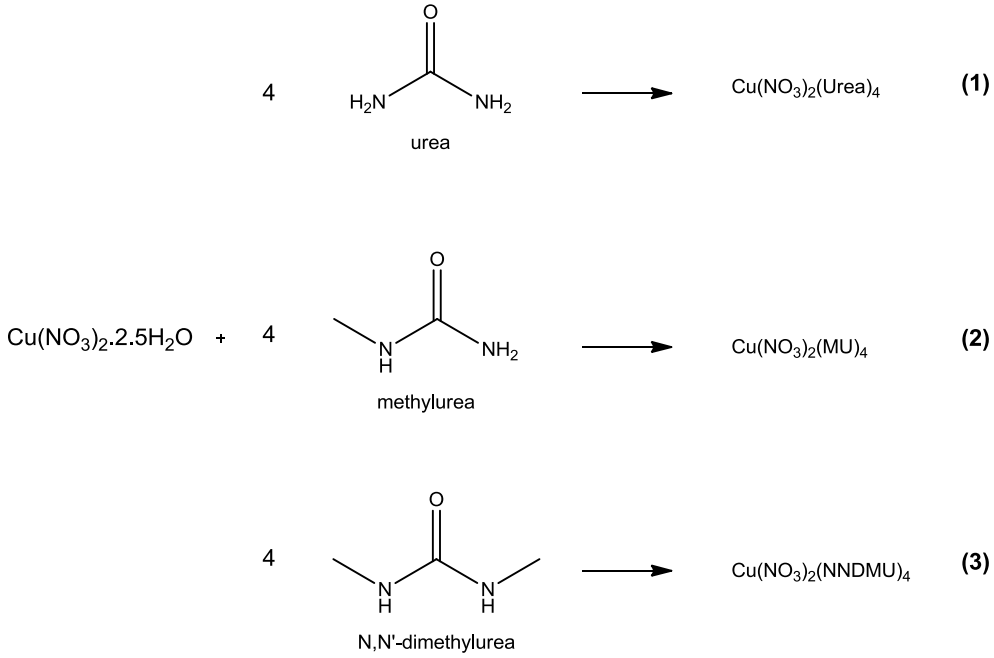

Scheme 2.2: Synthesis of copper nitrate-urea complexes

The structure of **1** is known,[30] but surprisingly **2** and **3** are not found in the literature. Complexes **1 – 3** are pale blue solids and the crystal structure of **3** is shown in figure 2.6. The complex belongs to the triclinic, $P\bar{1}$ space group and features a central copper atom in an octahedral environment surrounded by four equatorial NNDMU ligands and two axial nitrate ions. The NNDMU ligands are coordinated through oxygen, with near-equal bond lengths between 1.952 – 1.957 Å. The nitrate ions were coordinated trans to one another with long Cu – O(3) bond lengths of 2.546 Å. The extended crystal structure reveals H-bonding interactions between peripheral nitrate O(1) atoms and H(1) of distance 2.249 Å. There also exist intermolecular O(5)…H(2) interactions between the dimethylurea O atom and H-N from an adjacent dimethylruea ligand (2.027 Å). C=O bond lengths for the dimethylurea ligands were between 1.274 and 1.282 Å. Selected bond lengths are shown in table 2.1.

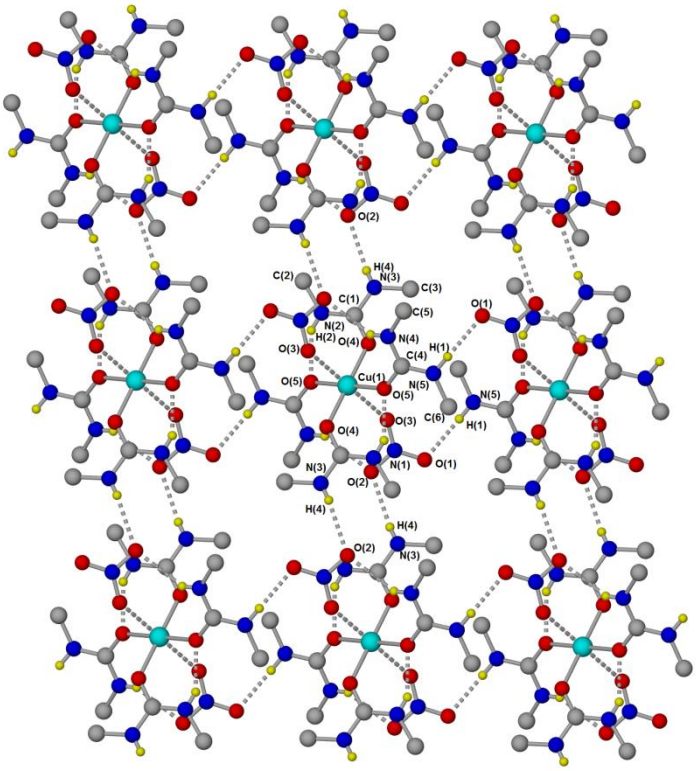

Figure 2.6: Expanded crystal structure of **(3)** showing H-bonding

Table 2.1: Selected bond lengths for **(3)**

Bonding interaction	Bond length (Å)
Cu-O(3)	2.5462(19)
Cu-O(4)	1.9569(16)
Cu-O(5)	1.9522(16)
C(1)-O(4)	1.274(11)
C(4)-O(5)	1.282(16)
O(1)-H(1) *intermolecular*	2.249
O(5)-H(2) *intramolecular*	2.027

In addition to the copper-urea complexes, the analogous reactions to form dimethylurea adducts were undertaken with nickel(II) and cobalt(II) nitrate (scheme 2.3). In neither case were the analogous complexes to **(3)** formed. The only isolatable product from the reaction with $Co(NO_3)_2.6H_2O$ was a hexa-coordinated dimethylurea adduct, whereby the ligand had displaced all water molecules. Interestingly for the reaction with $Ni(NO_3)_2.6H_2O$ there was no displacement of any water molecules, rather a bridging coordination of the NNDMU ligands surrounding the $Ni(H_2O)_6$ units.

$$Co(NO_3)_2.6H_2O + 6\ NNDMU \longrightarrow Co(NO_3)_2(NNDMU)_6 + 6H_2O \quad \textbf{(4)}$$

$$Ni(NO_3)_2.6H_2O + 4\ NNDMU \longrightarrow (NNMU)_4Ni(NO_3)_2.6H_2O \quad \textbf{(5)}$$

Scheme 2.3: Synthesis of cobalt nitrate- and nickel nitrate-urea complexes.

The cobalt complex (4) essentially adopts the same geometry as the hydrated nitrate, with six dimethylurea ligands bonding in an octahedral fashion to the Co centre through O coordination. There was very little difference in equatorial Co-O bond lengths which were between 2.097 - 2.089Å while axial bond lengths were slightly longer at 2.102 Å. Nitrate ions were spectators far from the metal centre. The structure of the nickel complex (5) was unusual in that no displacement of water ligands occurred. Instead, four dimethylurea ligands bridged between octahedral $Ni(H_2O)_6$ centres entirely by H bonding interactions between the O atom on urea, and H atoms on water. Again the nitrate ions were spectators. The crystal structures of complexes (4) and (5) are shown in figures 2.7 - 2.9

respectively. All three complexes are weakly coloured owing to the O_h symmetry at the metal centres.

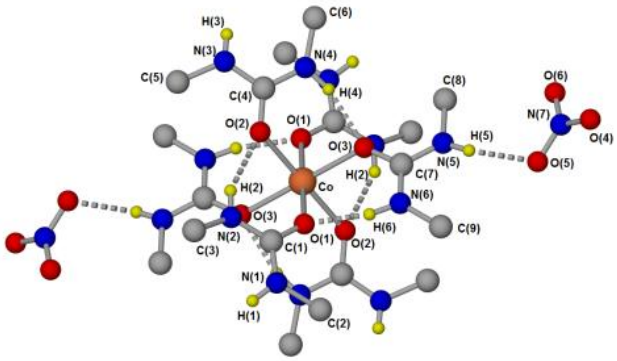

Figure 2.7: Crystal structure of **(4)**, $Co(NO_3)_2$.6NNDMU showing monomeric unit

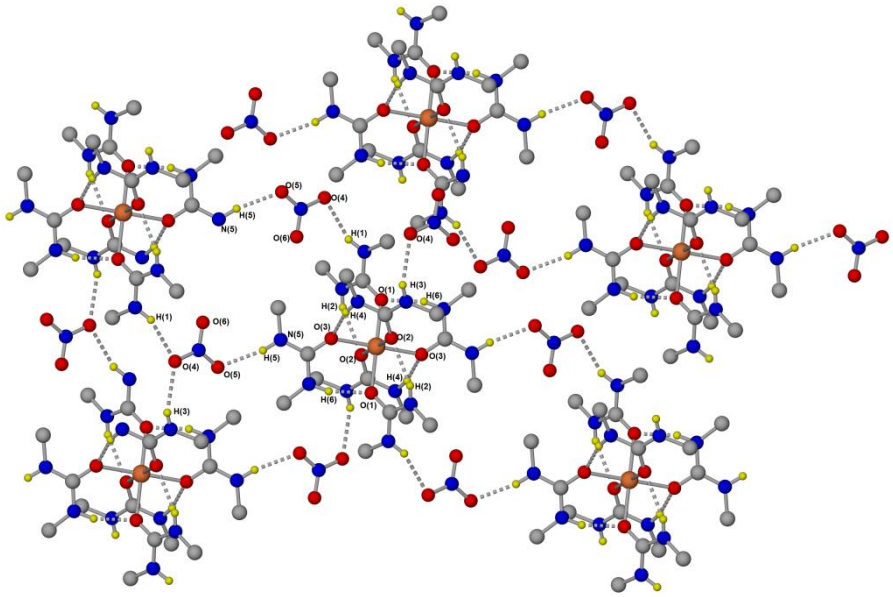

Figure 2.8: Crystal structure of **(4)**, $Co(NO_3)_2$.6NNDMU showing extended structure and H-bonding

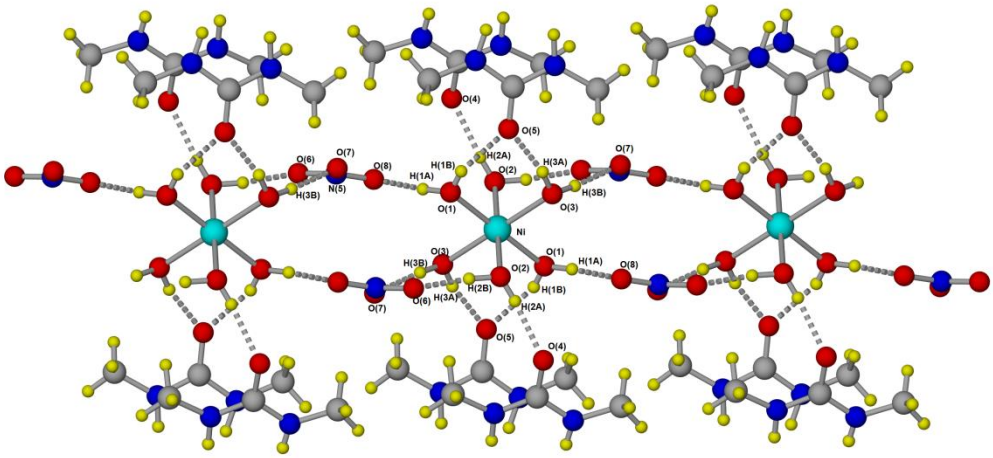

Figure 2.9: Crystal structure of **(5),** $Ni(NO_3)_2.6H_2O.4NNDMU$

2.2.2. Thermogravimetric analysis

Thermogravimetric analysis was performed on compounds **1-3** and $Cu(NO_3)_2.2.5H_2O$ on a Perkin Elmer TGA 4000 under a nitrogen atmosphere and are shown in figure 2.10. Complexes left stable residues of between 10-32% of the original mass, each corresponding to a final residue of CuO. Of these, **2** and **3** provided the sharpest decomposition profiles, with residual masses of 10% and 12% respectively (*cf.* 16 % and 14% expected for CuO), indicating that a small amount of material has been lost from volatilisation.

The decomposition profile for $Cu(NO_3)_2.2.5H_2O$ is significantly less clean than the urea adducts. The decomposition occurs in two main stages over a broad temperature range, with a 43% mass loss occurring between 100 – 200°C which can be attributed to the loss of water. The proposed mechanism for decomposition provides an interesting point of discussion, with the most probable pathway occurring through the formation of a basic metal nitrate $Cu(NO_3)_2.3Cu(OH)_2$.[31] The broad decomposition profile can be attributed to hydrogen bonding, the potential for which is greatly reduced in the urea adducts.

1 exhibits a sharper decomposition than the hydrated nitrate, but still over a relatively broad range between 120 – 250°C. The residue still loses mass until 450°C potentially indicating that complete combustion has not occurred until higher temperatures. **2** and **3** have much sharper single-stage decomposition profiles between 200 - 230°C for both complexes.

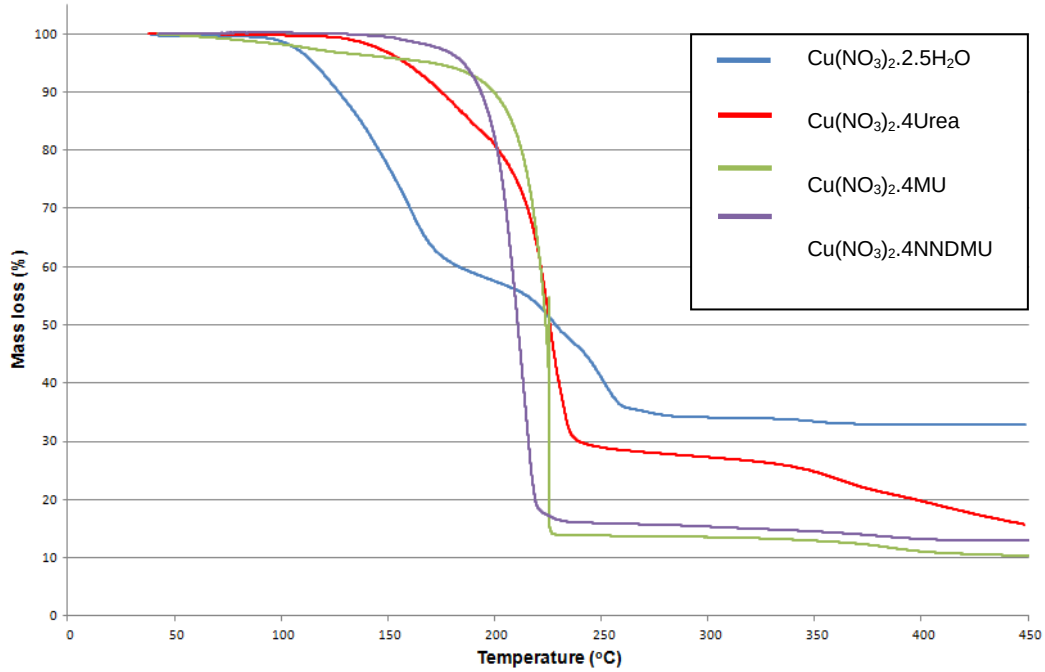

Figure 2.10: TGA analysis of copper nitrate and complexes **1 - 3**

$Cu(NO_3)_2.2.5H_2O$, **1** and **3** were tested as precursors for deposition of copper oxide thin films, however it was soon realised that all precursors deposited the same material. Complexes **(4)** and **(5)** were not tested as precursors due to time constraints.

Table 2.2: List of samples detailed in this chapter

Deposition number	Appearance	Material	substrate	Deposition conditions					Comments
				Precursor	Conc (mol L^{-1})	Solvent	Temp (°C)	Duration (min)	
DS100A		Cu	Glass/Si	$Cu(NO_3)_2.2.5H_2O$	0.1	EtOH	400	30	Unexpected metallic film. Shiny reflectance, blue in transmission. Well adhered.
DS100B	As DS100A	Cu	Glass	$Cu(NO_3)_2.2.5H_2O$	0.1	MeOH	400	30	Copper metal
DS100C	As DS100A	Cu	Glass	$Cu(NO_3)_2.2.5H_2O$	0.1	^{i}PrOH	400	30	Copper metal
DS100D	No deposition	-	Glass	$Cu(NO_3)_2.2.5H_2O$	0.1	H_2O	400	30	No deposition
DS100E	As DS100A	Cu	Glass	**(1)**	0.1	EtOH	400	30	Copper metal
DS100F	As DS100A	Cu	Glass	**(3)**	0.1	EtOH	400	30	Copper metal
DS060		Cu_2O	Glass/Si	$Cu(NO_3)_2.2.5H_2O$	0.1	EtOH	300	30	Yellow, well adhered film.
DS063		CuO	Glass/Si	$Cu(NO_3)_2.2.5H_2O$	0.1	EtOH	500	30	Brown/black film.
DS098		Ni	Glass	$Ni(NO_3)_2.6H_2O$	0.1	EtOH	400	30	Shiny, metallic black. Thin, scratches easily
DS099		NiO	Glass	$Ni(NO_3)_2.6H_2O$	0.1	EtOH	400	30	Ni films annealed in air at 500 °C for 30 minutes. Becomes transparent.

DS053		TiO_2 : Cu	Glass	$Ti(OEt)_4$	0.1	Tol	500	10	Blue colour retained, reflectance disappears
DS054		TiO_2 : Cu	Activ	$Ti(OEt)_4$	0.1	Tol	500	10	Intensely blue, interference fringes observed
DS055		TiO_2:Cu_2O	Glass	$Ti(OEt)_4$	0.1	Tol	500	10	Grey-blue in colour, no yellow colour retained
DS056		TiO_2:Cu_2O	Activ	$Ti(OEt)_4$	0.1	Tol	500	10	Majority of film blue, some areas near the back of the reactor remained yellow and not covered by titania film
DS057		TiO_2:Cu	Si	$Ti(OEt)_4$	0.1	Tol	500	10	Blue-green reflectivity
DS058		TiO_2:CuO	Si	$Ti(OEt)_4$	0.1	Tol	500	10	Blue-green reflectivity, interference fringes seen.

2.3. AACVD of $Cu(NO_3)_2.2.5H_2O$ and urea adducts

Preliminary studies involving the AACVD of $Cu(NO_3)_2.2.5H_2O$, **(1)** and **(3)** were undertaken and it was found that all precursors deposited the same material. The materials deposited in this section give rise to samples DS100A, DS060 and DS063.

2.3.1. Deposition conditions for AACVD of $Cu(NO_3)_2.2.5H_2O$.

Table 2.3: Deposition conditions used for AACVD of $Cu(NO_3)_2.2.5H_2O$

Variable	Value
Substrate temperature	300-500 ^oC
Precursor concentration	0.1 M
Solvent	MeOH, EtOH, ^iPrOH, H_2O
Bulk flow rate (aerosol)	20 ml/hr
Pressure	137.9 kpa
Deposition time	30 minutes
O_2 concentration	0 – 10%

Samples deposited from methanol, ethanol and isopropanol were all unexpectedly metallic, whilst use of a water solvent failed to deposit a thin film. When 10% oxygen was added at 350°C, films were yellow and transparent. When 10% oxygen was added at 500°C, films were brown/black transparent. Metallic films were shiny, brown in reflected light but appeared blue when viewed perpendicular to the film surface (appendix 6.3).

2.3.2. Film analysis

2.3.2.1. Compositional/microstructural analysis

Films grown on glass substrates were analysed by XRD to determine their crystallographic orientation. Figure 2.11 shows an overlay of samples DS100A, DS060, and DS063.

DS100A, deposited at 400°C indexes to cubic copper metal primarily oriented in the (1,0,0) direction with some in the (2,0,0) direction. This is in agreement with the physical metallic appearance of the film, but gives no indication as to the origin of the blue colouration. No other phases are detected within this sample. Sample DS060 which was deposited at the same temperature with the addition of 10% oxygen indexes to cubic Cu_2O with the (1,0,0) peak clearly visible and slight emergence of the (2,0,0).[32] Sample DS063 which was deposited at 500°C with addition of 10% oxygen indexes to CuO, with the (0,0,2), (1,1,1) and (2,0,0) peaks all visible. Patterns indexed to copper oxides were particularly broad, potentially indicating poor crystallinity or very thin films. XRD revealed that all samples contained a single phase.

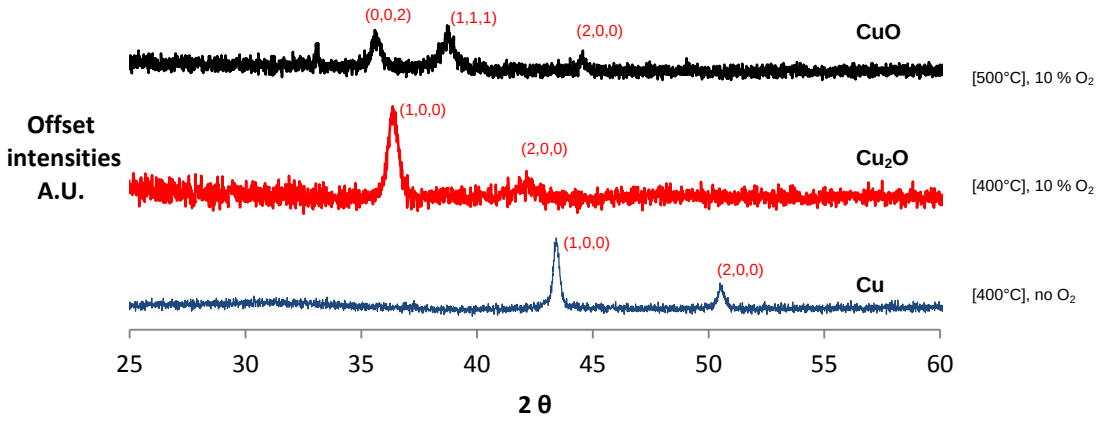

Figure 2.11: An overlay of XRD diffraction patterns for films deposited from $Cu(NO_3)_2.2.5H_2O$

Raman spectroscopy was used for further characterisation of the Cu_2O phase as it has been reported that mixed $Cu/Cu_2O/CuO$ phases can arise from the AACVD of $Cu(NO_3)_2.3H_2O$.[33] Tenorite, Cu_2O is a well characterised material and as such data is available from a number of sources.[34] Signals were detected at 147, 213, 401 and 640 cm^{-1} which correspond to T_{1u} and E_u vibrational modes. The lack of

a strong peak at 300 cm^{-1} indicates that no CuO is present in the sample (figure 2.12). The Raman-inactive copper sample, DS100 was not analysed.

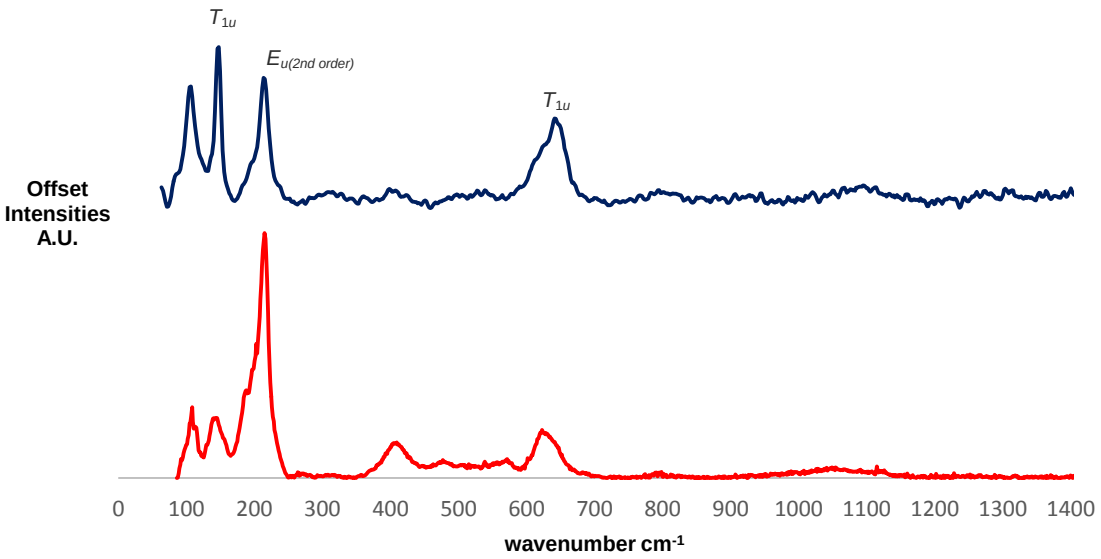

Figure 2.12: Raman spectrum of DS060 – Cu_2O on glass (blue), and literature spectrum of tenorite, Cu_2O (red).

2.3.2.2 Morphological analysis

Cu on glass – DS100A

80° tilt images

The lower magnification images (Figures 2.13-A and -B) showed a coating layer with a few large lumps, and some small lumps, of material at the surface.

Figure 2.14, at an instrument magnification of 50,000x, showed that the coating consisted of closely packed rounded particles, all of a similar size; the thin amorphous SiCO base layer was also seen. Figure 2.13-C, at the same magnification, showed that the small lumps of material were agglomerations of a few of the rounded particles which were slightly larger than the typical particles. Figure 2.13-D (at the same magnification) showed one of the larger lumps which contained some particles that were much larger than the typical coating particles; the lump had a maximum height of approximately 611nm.

90° tilt images

Measurements taken from Figures 2.13-E and -F showed that the coating layer was typically 78 – 86nm thick and the amorphous base layer was approximately 20nm thick; the small lumps (agglomerations) had heights up to 234nm above the surface.

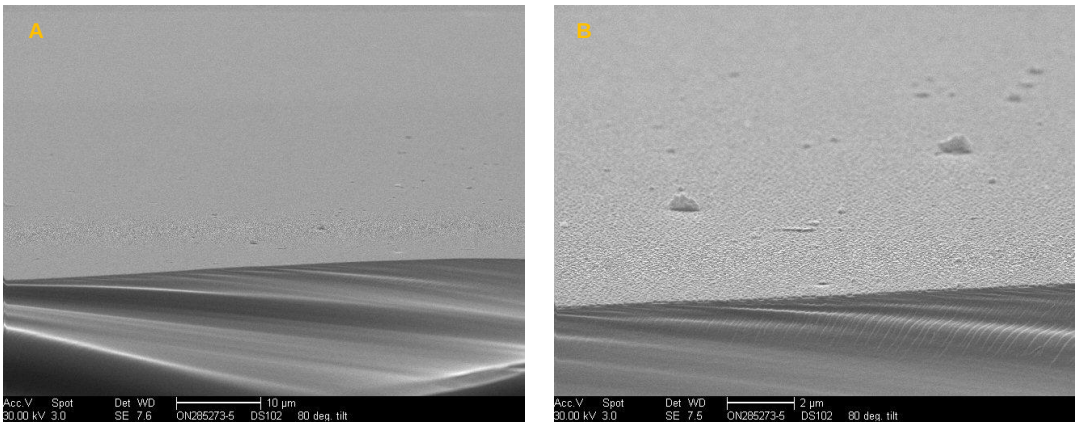

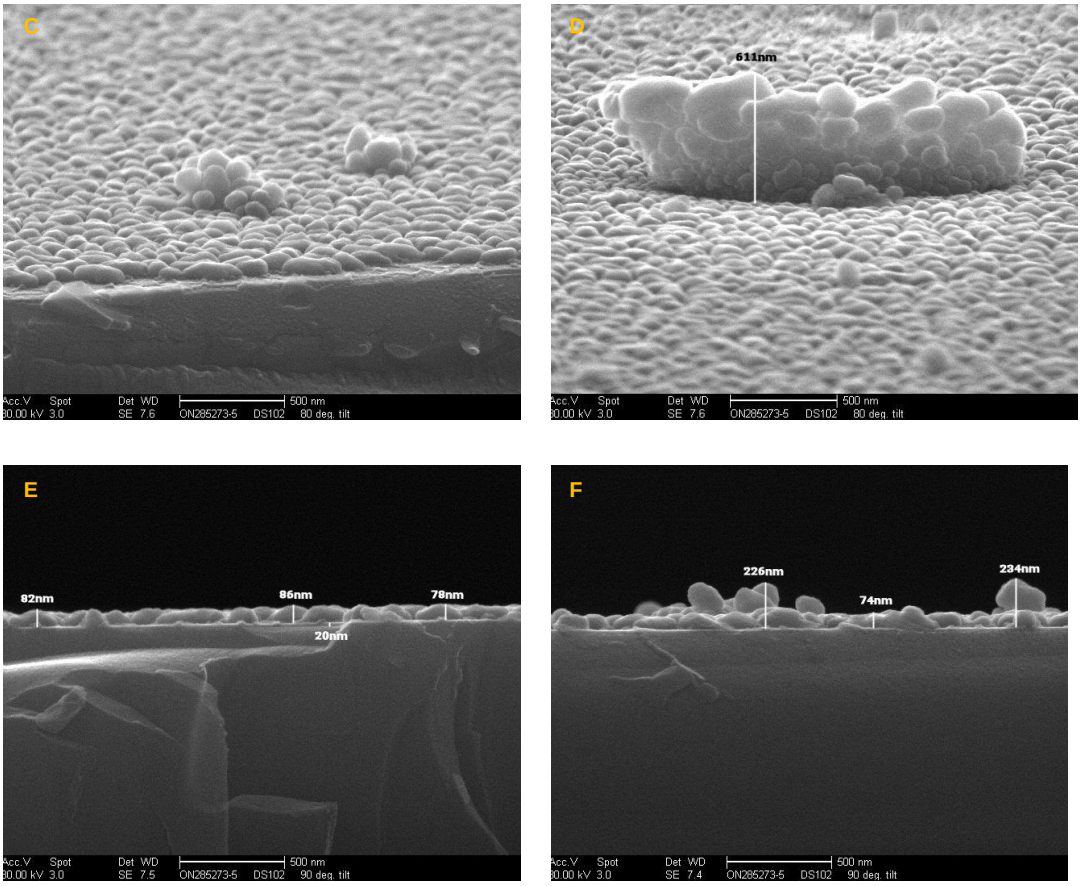

Figure 2.13: SEM micrographs of copper films deposited at 400°C at 2,000 x magnification **(A)**, 10,000 x magnification **(B)** and 50,000 x magnification **(C – F)** at 80 ° tilt **(A – D)** and 90 ° tilt **(E, F).**

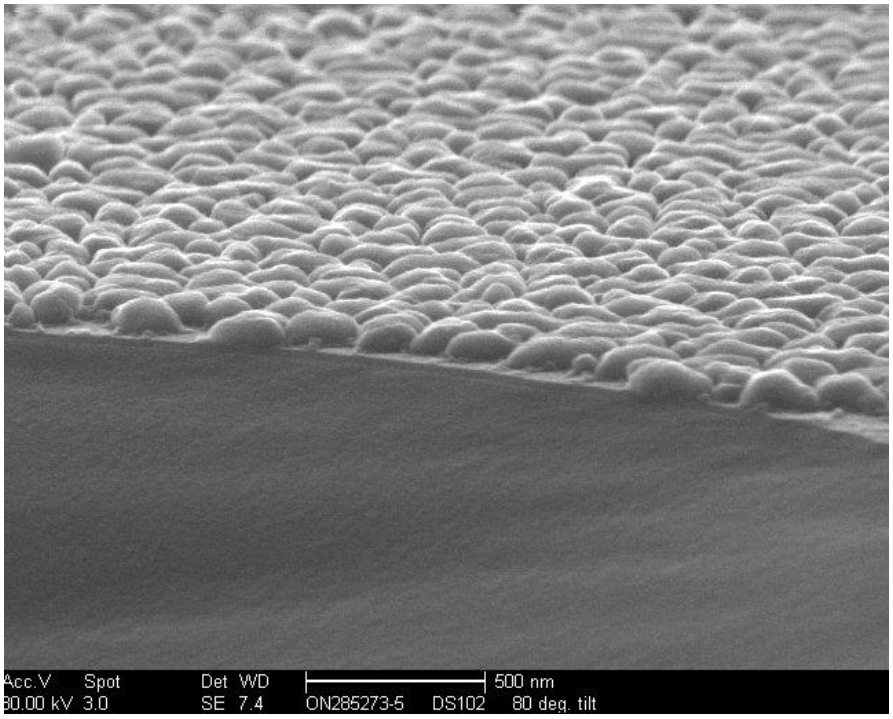

Figure 2.14: SEM micrograph of copper film deposited at 400 °C at 50,000x magnification at 80 ° tilt

CuO on silicon - DS063

80° tilt images

The lower magnification images (Figures 2.15-A and B) showed a coating layer with a few large lumps of material at the surface.

Figure2.15-C, at an instrument magnification of 50,000x showed one of the lumps with a height of 568nm above the surface; Figure 2.15-D, at the same magnification, showed that the copper oxide coating layer consisted of closely packed rounded particles, all of a similar size.

90° tilt images

Measurements taken from Figures 2.15-E and -F showed that the coating layer was typically 66 – 70nm thick with high points of up to 90nm.

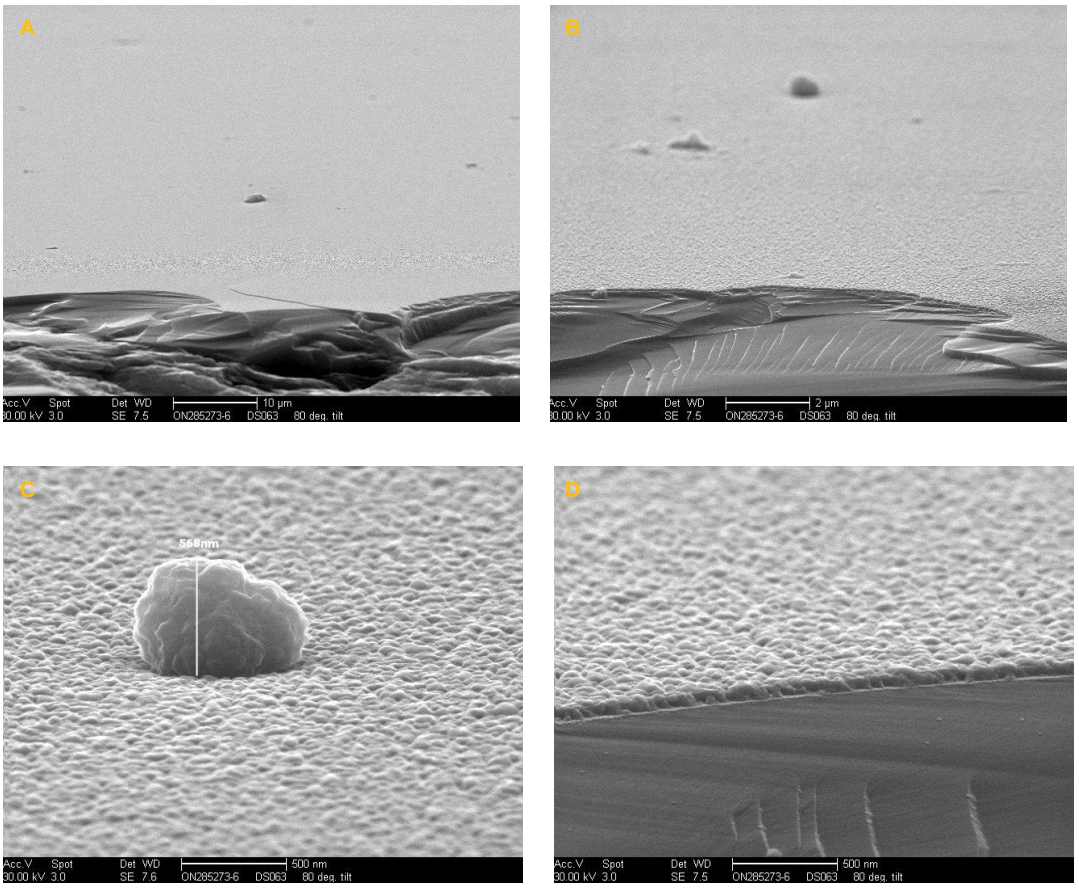

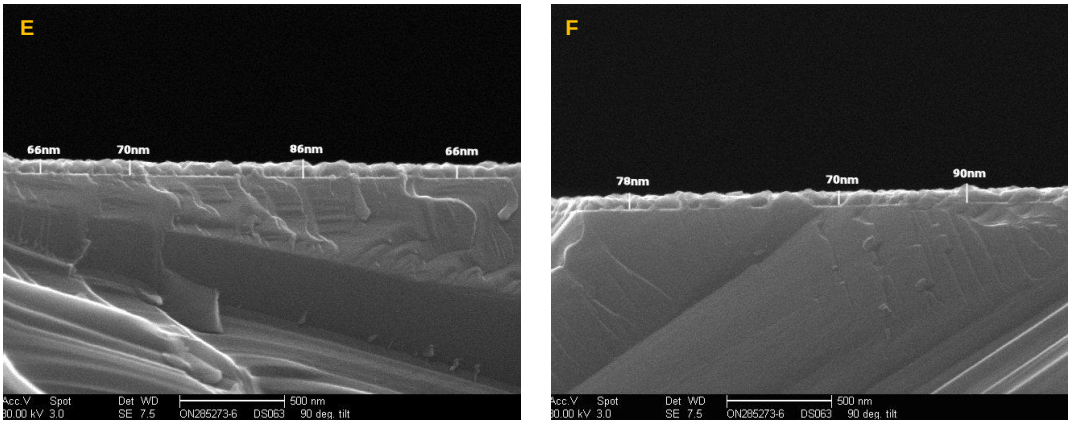

Figure 2.15: SEM micrographs of CuO films deposited at 500°C at 2,000x magnification **(A)**, 10,000x magnification **(B)** and 50,000x magnification (**C-F**) at 80 ° tilt (**A - D**) and 90 ° tilt (**E and F**).

2.3.2.3 Optical properties

The visible light absorbance spectra of DS100 and DS060 were recorded. DS100, a blue film, absorbs strongly between 550 and 750 nm which correspond primarily to the orange, yellow and red parts of the spectrum. Absorbance is low in the 350 – 550nm range, which correspond to the violet, blue and green. This is in good agreement with the observed blue colouration of the copper films. The peak absorbance occurs at 610nm which is very similar to the plasmon resonance observed for copper nanoparticles (619nm).[35] The peak absorbance occurs at an intensity of 44 %, while the majority of other wavelengths are not absorbed strongly - ~4%.

DS060 absorbed more strongly across all wavelengths, with the strongest absorptions occurring between 390 and 490 nm. This corresponds to an absorption of violet, blue and slightly into the green parts of the visible spectrum. Absorption is less strong across the yellow, orange and red wavelengths which results in a yellow colouration of the film.

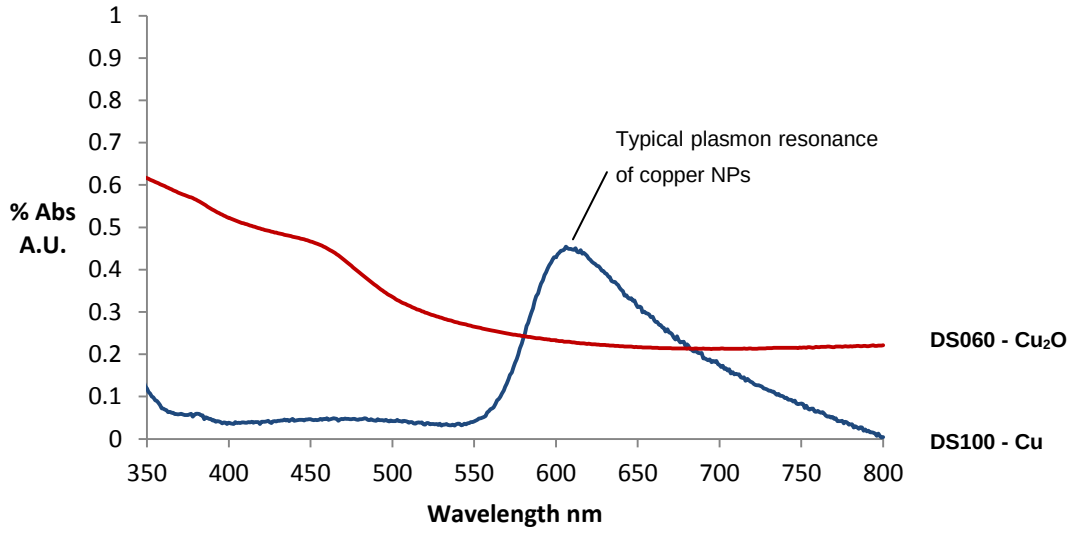

Figure 2.16: Absorption spectrum of Cu on glass - DS100 (blue), and DS060 - Cu_2O on glass (red).

2.4. AACVD of $Ni(NO_3)_2.6H_2O$

With the unexpected deposition of metallic copper films from the hydrated nitrate, the analogous nickel(II) nitrate was investigated. Ethanol was the preferred solvent for the nickel nitrate deposition.

2.4.1. Deposition conditions for AACVD of $Ni(NO_3)_2.6H_2O$.

Table 2.4: Experimental conditions used for AACVD of $Ni(NO_3)_2.6H_2O$

Variable	Value
Substrate temperature	300-500 ^oC
Precursor concentration	0.1 M
Solvent	EtOH
Bulk flow rate (aerosol)	20 ml/hr
Pressure	137.9 kpa
Deposition time	30 minutes

2.4.2. Film analysis

Samples deposited from $Ni(NO_3)_2.6H_2O$ were shiny, metallic black. The film was fairly well adhered to the glass and passed the Scotch tape test. However the film could be easily scratched. Upon annealing for 30 minutes in air at 500°C, the films became transparent.

2.4.2.1. Compositional/microstructural analysis

The nickel film, DS098 was analysed by analysed by XRD to determine the crystallographic orientation (figure 2.17). The pattern could be indexed to cubic nickel metal, with the most intense (1,1,1) reflection visible.

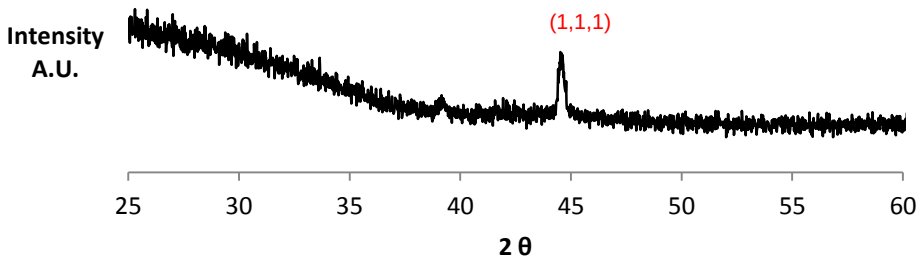

Figure 2.17: XRD pattern of sample DS098, nickel metal on glass deposited from $Ni(NO_3)_2.6H_2O$ precursor at 400°C.

2.4.2.2 Morphological analysis

Nickel on glass - DS098

80° tilt images

Figure 2.18-A, at an instrument magnification (IM) of 1,000x plus Figure 2.18-B (IM – 5,000x) showed some broad lines/scratches at the surface where the coating was missing.

Figure 2.18-C (IM – 50,000x) showed a thin amorphous base layer (arrowed) and the nickel coating which consisted of closely packed, small rounded particles. These were very similar in size and shape to the copper particles deposited previously (DS102). Figure 2.19, at the same magnification showed a “kink” in the nickel coating where it had lifted slightly away from the base layer.

90° tilt image

Measurements from Figure 2.18-D (IM – 50,000x) showed that the thin amorphous base layer was approximately 19nm thick and the nickel layer was typically 62 – 70nm thick with high points up to 93nm.

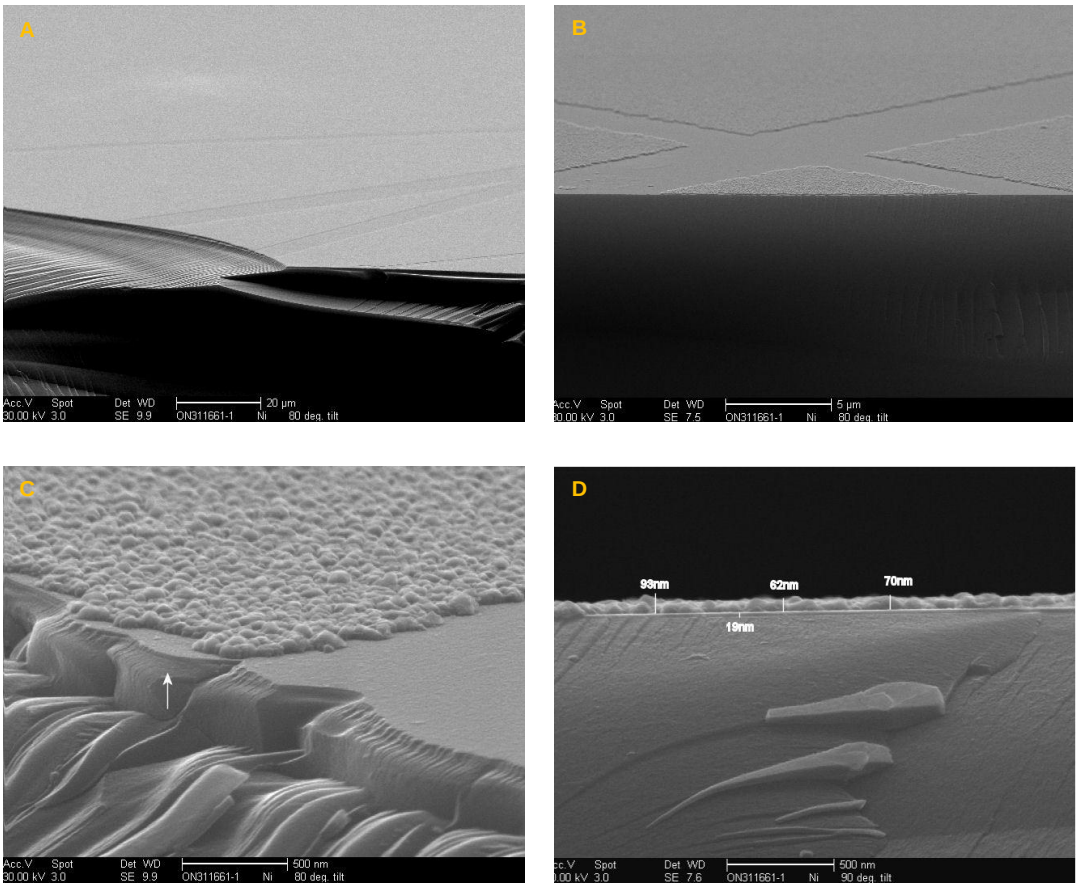

Figure 2.18: SEM micrographs of nickel films deposited at 400°C at 1,000x magnification **(A)**, 5,000x magnification **(B)** and 50,000x magnification **(C, D)** at 80 ° tilt **(A – C)** and 90 ° tilt **(D).**

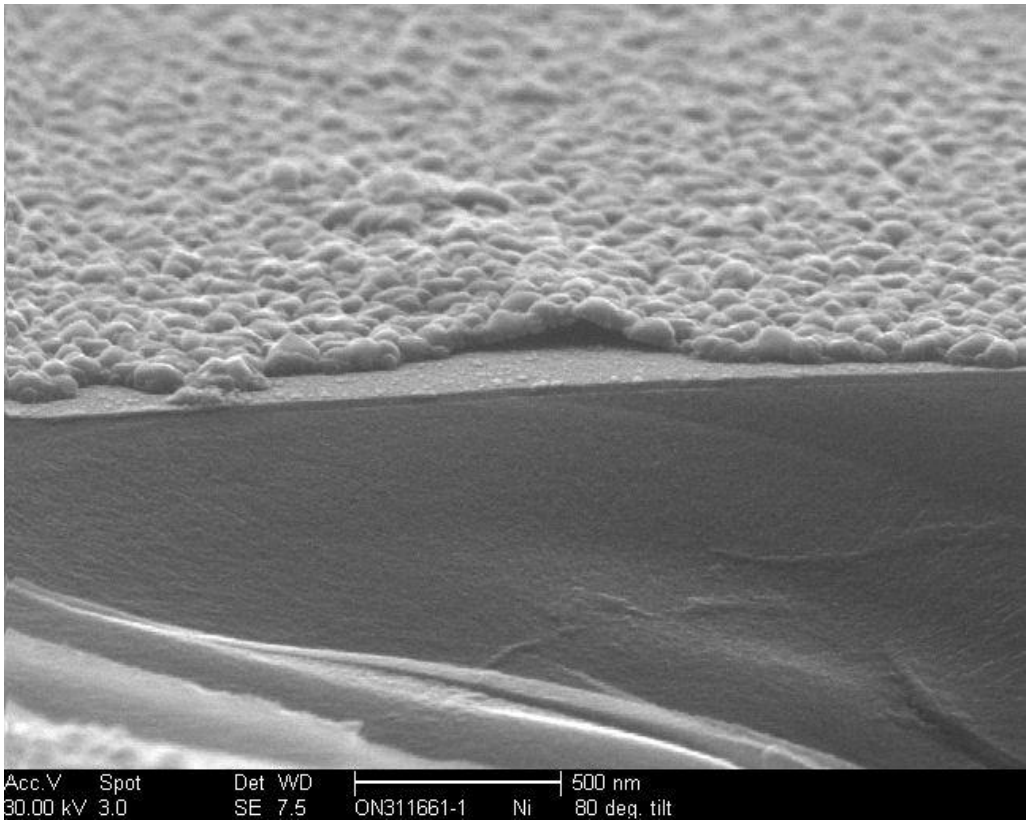

Figure 2.19: SEM micrograph of nickel film deposited at 400°C at 50,000x magnification at 80 ° tilt

NiO on glass - DS099

Figures 2.20-A and -B, at an instrument magnifications of 20,000x and 40,000x respectively showed rounded lumps ranging between 50 – 500 nm in diameter

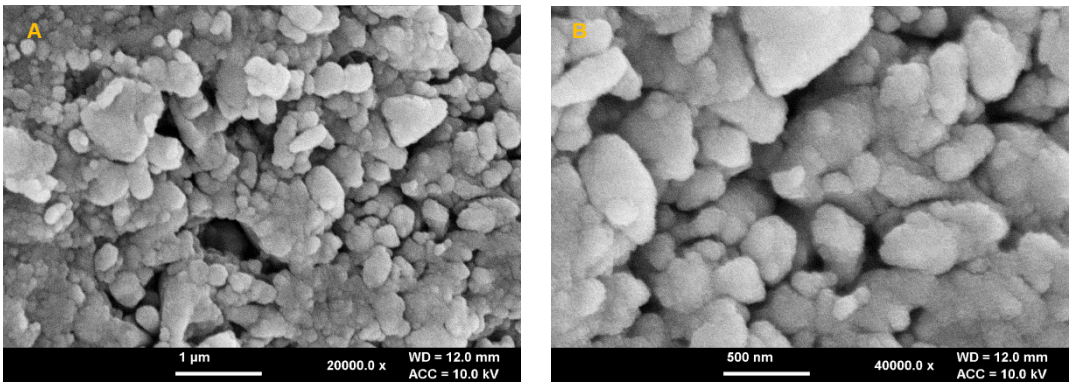

Figure 2.20: SEM micrographs of NiO films deposited at 400°C at 20,000x magnification **(A)** and 40,000x magnification **(B)**.

2.5. AACVD of photoactive TiO_2 layer

A photoactive layer of anatase TiO_2 was deposited on top of the blue copper metallic films, and yellow copper(I) oxide films. The precursor used was a 0.1M solution of titanium ethoxide in toluene. The growth rate of titania is rapid therefore a short deposition time was used. After deposition, samples were left to cool to room temperature under a stream of nitrogen before removal. Upon removal from the reactor, it was noted that for the copper films, the shiny reflectance had disappeared, but a pleasant light-blue colour remained. Interestingly, the yellow copper oxide films also exhibited a faint blue colour. On some samples, interference fringes from different thicknesses of titania were visible. The deposition conditions are detailed in table 2.5.

2.5.1 Deposition conditions for AACVD of $Ti(OEt)_4$

Table 2.5: Experimental conditions used for AACVD of $Ti(OEt)_4$

Variable	Value
Substrate temperature	500^{o}C
Precursor concentration	0.1 M
Solvent	Toluene
Bulk flow rate (aerosol)	20 ml/hr
Pressure	137.9 kpa
Deposition time	10 minutes

2.5.1.1 Morphological analysis

TiO_2:Cu on glass – DS053 (Blue film)

80° tilt images

The low magnification image (Figure 2.21-A) showed a coating layer with a few large lumps and many small lumps of material at the surface.

Figure 2.22 (at an instrument magnification of 50,000x) showed a single coating layer i.e. a clearly defined interface showing a TiO_2 layer on the copper layer was not seen. This image also showed one of the smaller lumps of material which appeared to originate within the coating layer. Another region of the sample, at the same magnification, showed the thin SiCO base layer below the coating (Figure 2.21-B).

90° tilt images

Measurements from Figure 2.21-C showed that the coating layer (Cu and TiO_2) had a typical thickness of 257 – 285nm with high points up to 320nm. Figure 2.21-D showed a region where the amorphous base layer could be seen; it was approximately 20nm thick.

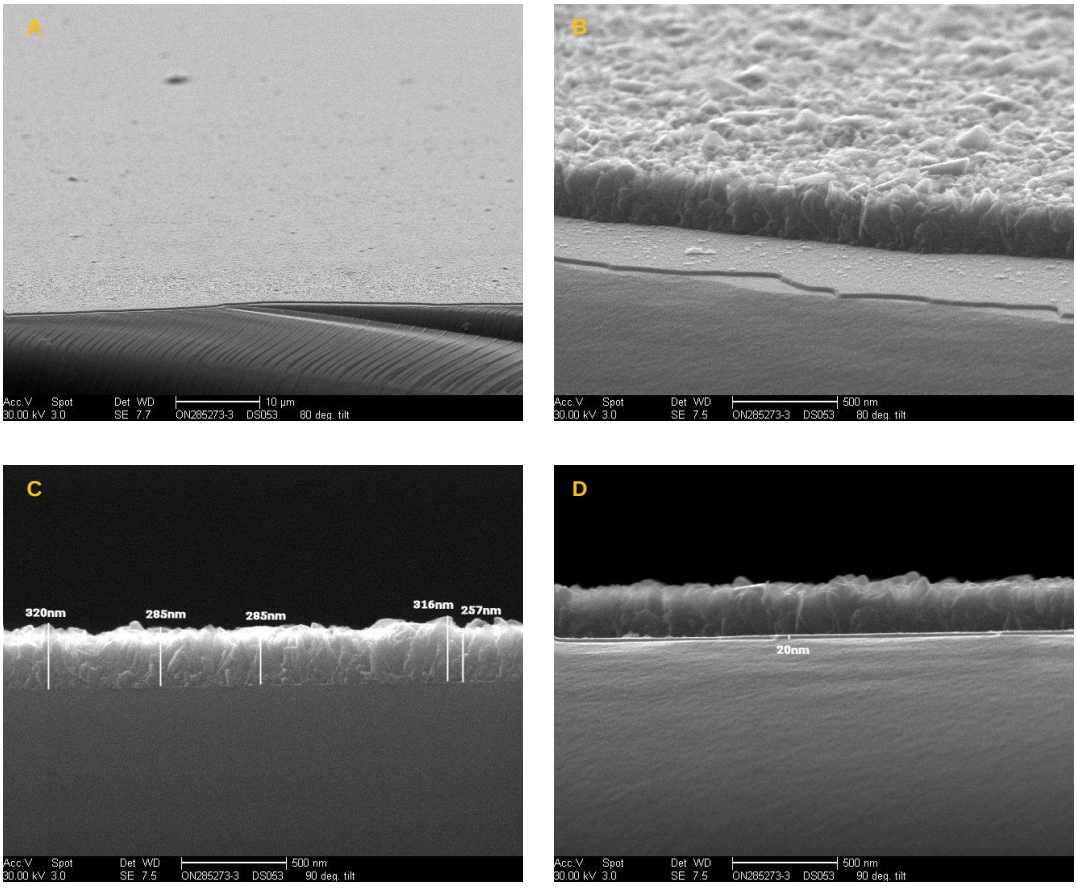

Figure 2.21: SEM micrographs of TiO_2:Cu film deposited at 500°C at 2,000x magnification **(A)** and 50,000x magnification (**B – D**) at 80 ° tilt (**A, B**) and 90 ° tilt (**C, D**)

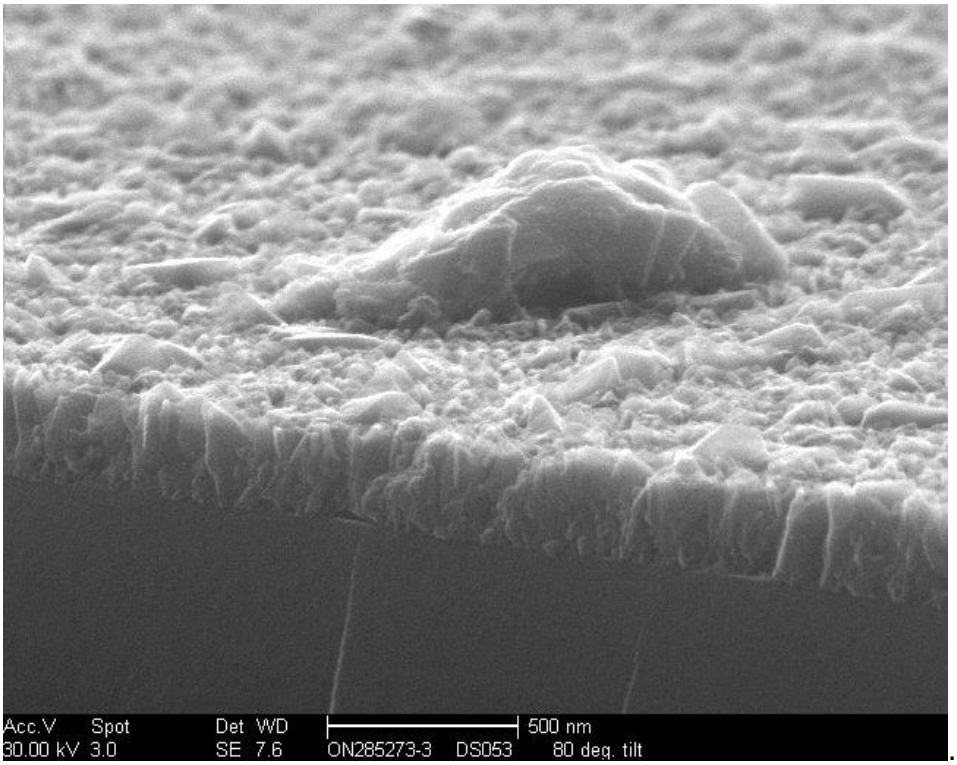

Figure 2.22: SEM micrograph of TiO_2:Cu film deposited at 500°C at 50,000x magnification

TiO_2:Cu_2O on glass – DS055 (Blue-grey film)

80° tilt images

The lower magnification images (Figures 2.23-A and -B) showed a coating layer with several lumps of material at the surface.

Figure 2.23-C (instrument magnification – 50,000x) showed one of the larger lumps of material which appeared to consist of the same material as the coating layer and had a maximum height of 1586nm above the coating surface. Figure 2.23-D (at the same magnification) showed a large particle which appeared to be "sat" on the surface. This probably arose from a gas phase particulate that settled on the surface of the growing film. The same image also shows a smaller particle which appeared to originate from within the coating layer; an interface that showed two layers i.e. a TiO_2 layer on top of the copper layer, was not seen but a thin amorphous base layer was observed.

90° tilt images

Figure 2.23-E showed the same region seen in 2.23-C; the large lump had a maximum height of 507nm above the coating surface.

The coating layer (Cu_2O + TiO_2) had a typical thickness of 265nm with high points of up to 285nm (Figure 2.23-F).

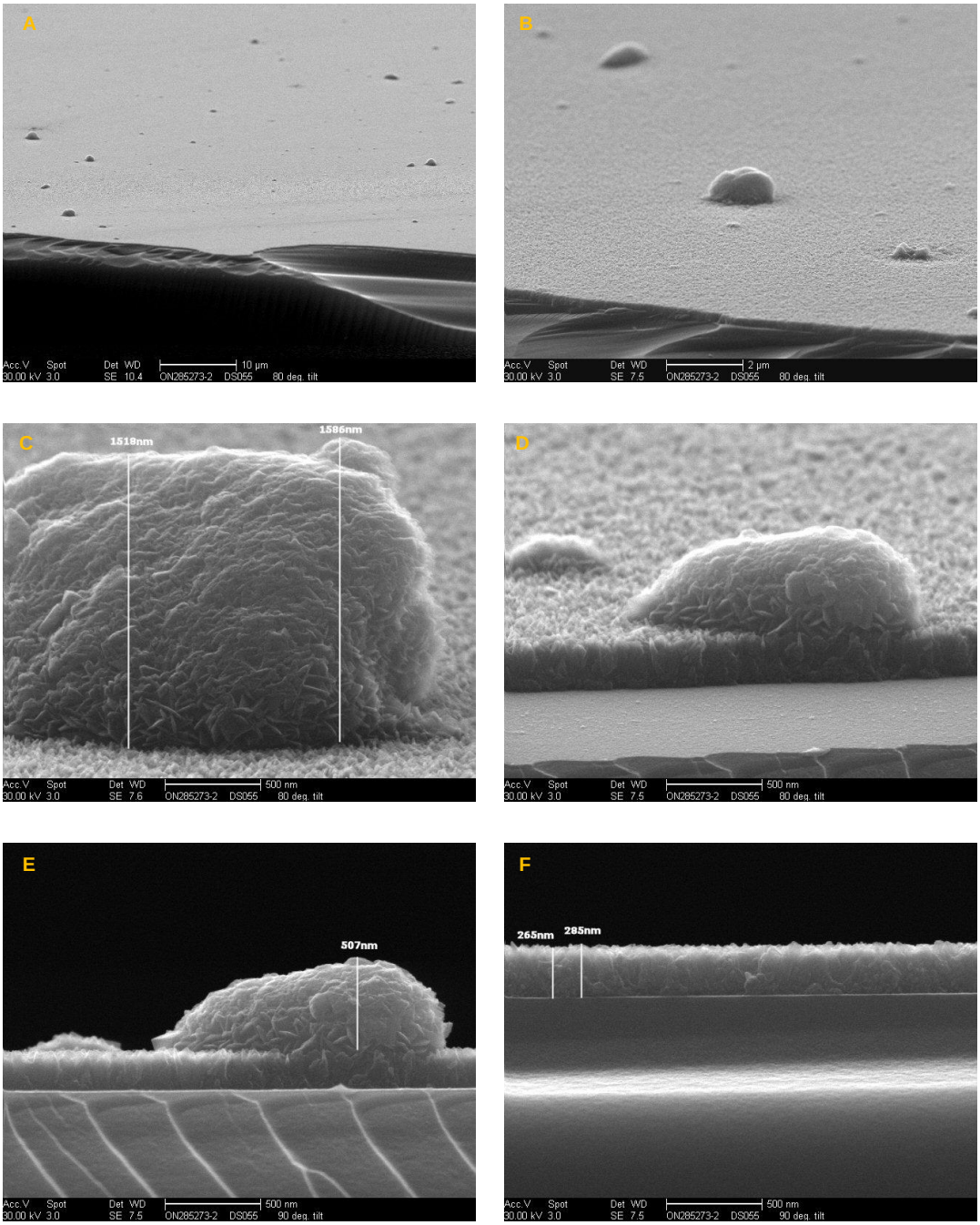

Figure 2.23: SEM micrographs of TiO_2:CuO films deposited at 400°C at 2,000x magnification **(A)**, 10,000x magnification **(B)** and 50,000x magnification (**C-F**) at 80 ° tilt (**A - D**) and 90 ° tilt (**E and F**).

TiO_2:CuO on silicon - DS058

80° tilt images

The low magnification images (Figures 2.24-A and 2.24-B) showed a uniformly rough surface; unlike samples DS053 and DS055 no other lumps of material were seen at the surface.

Images at an instrument magnification of 50,000x (Figures 2.24-C and -D) showed an undulating surface and many circular holes between the silicon substrate and the coating. The holes were below the higher parts of the surface and the rise in the surface was due to the holes below those regions. A clearly defined interface showing a TiO_2 layer on top of the copper oxide layer was not seen.

90° tilt images

Measurements taken from Figures 2.24-E and -F showed that, in the lower parts of the surface, the coating (CuO + TiO_2) had a typical thickness of 304 – 320nm; the higher parts of the surface could be up to 476nm.

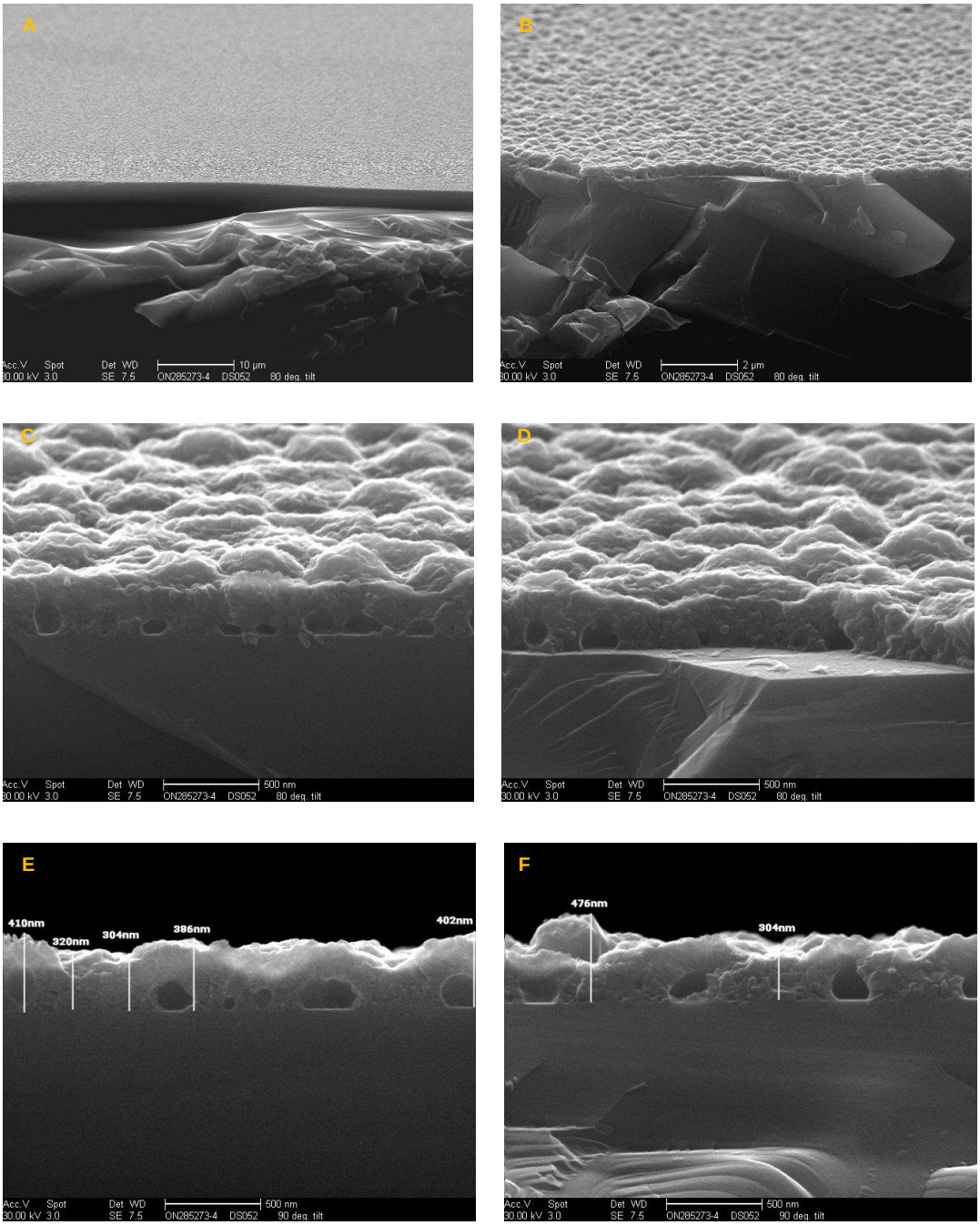

Figure 2.24: SEM micrographs of TiO_2:CuO films deposited at 400°C on silicon substrate at 2,000x magnification **(A)**, 10,000x magnification **(B)** and 50,000x magnification (**C-F**) at 80 ° tilt (**A - D**) and 90 ° tilt (**E and F**).

TiO_2:Cu on Activ – DS054

80° tilt images

The lower magnification images (Figures 2.25-A and -B) show a coating layer with many lumps of material at the surface.

Figure 2.25-C, at an instrument magnification of 50,000x, showed that the lumps appeared to consist of the same material as the coating layer. Figure 2.25-D, at the same magnification, showed the amorphous base layer of the Activ substrate and a single top layer; clearly defined interfaces showing the Activ top layer and the TiO_2 layer on top of the copper layer, were not seen. Figure 2.25-E, also at an instrument magnification of 50,000x, showed that one of the smaller lumps had originated and grown within the coating layer.

90° tilt images

Measurements from Figure 2.25-F showed that the coating layer including the Activ top layer, the copper layer and the TiO_2 top layer was typically 328 – 335nm thick with high points up to 355nm (interfaces for the separate layers were not seen).

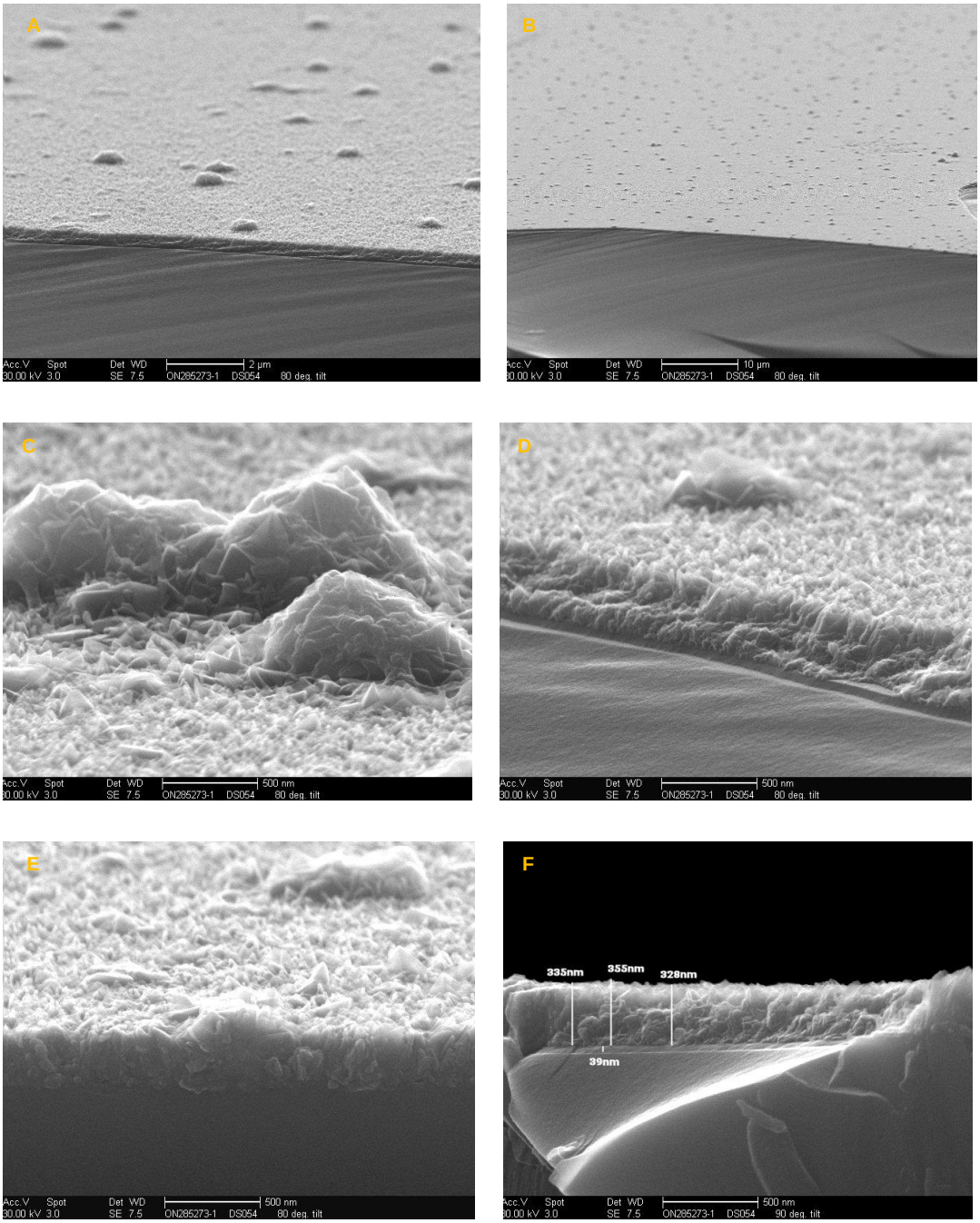

Figure 2.25: SEM micrographs of DS054 - TiO_2:Cu films deposited at 400°C on Activ substrate at 2,000 x magnification **(A)**, 10,000 x magnification **(B)** and 50,000 x magnification (**C-F**) at 80 ° tilt (**A - D**) and 90 ° tilt (**E and F**).

2.5.1.2. Compositional/microstructural analysis

EDS analysis was obtained for selected samples grown on silicon to eliminate unwanted signals from the glass that make quantitative measurements difficult. Pilkington float glass contains significant proportions of Ca, Na, K, Mg, Al, and Fe which can all contribute to noise, especially when looking for lighter elements. Analysis revealed that films grown on silicon wafers at 400°C contained titanium, oxygen and copper as well as silicon which is associated with the substrate. The EDS spectrum of the TiO_2:Cu (DS053) film is shown in figure 2.26

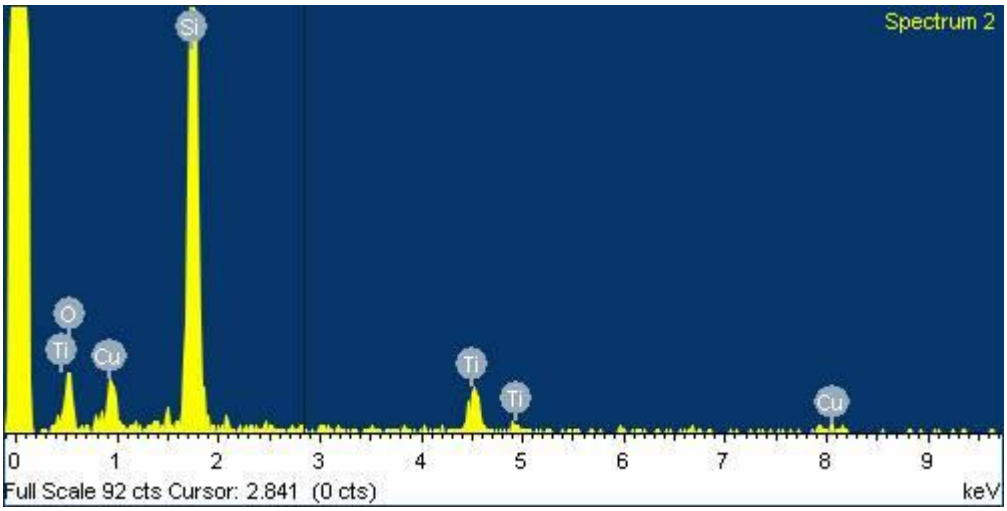

Figure 2.26: EDS spectrum of TiO_2:Cu (DS053) grown at 500 °C on silicon wafer.

Measurements determined that the correct elements were present in the films (table 2.6), however quantitative analysis was not achieved.

Table 2.6: Elements confirmed by EDS

Sample	Material	Elements detected by EDS
DS100A	Cu	Si, Cu,
DS060	Cu_2O	Si, Cu, O
DS063	CuO	Si, Cu, O
DS098	Ni	Si, Ni, C*
DS099	NiO	Si, Ni, O, C*
DS053	TiO_2 : Cu	Si, Ti, Cu, O*, C*
DS054	TiO_2 : Cu	Si, Ti, Cu, O*, C*
DS055	TiO_2:Cu_2O	Si, Ti, Cu, O, C*
DS058	TiO_2:CuO	Si, Ti, Cu, O, C*

*Detected at low concentrations

Micro-X-Ray Diffraction (Micro-XRD) patterns were recorded at Pilkington Technical Centre for the following samples:

DS100A (Cu) [silicon]

DS100A (Cu) [glass]

DS063 (Cu_2O) [silicon]

DS063 (Cu_2O) [glass]

DS053 (TiO_2 on Cu) [glass]

DS055 (TiO_2 on Cu_2O) [glass]

DS058 (TiO_2 on CuO) [silicon]

DS054 (TiO_2 on Cu) [Activ^{TM}]

Peak search-match software was used to identify the crystalline components present in each sample. Patterns for samples DS053, DS055, and DS058 are given in figures 2.27, 2.28 and 2.29 respectively, while the remaining patterns can be viewed in appendix 6.2.

The identified crystalline phases are shown in Table 2.7.

Table 2.7: List of samples and assigned crystallographic phases as determined by micro-XRD

Sample	Database Assignment	Chemical Formula	ICDD Pattern
DS053 (Figure 2.27)	Anatase	TiO_2	01-084-1285
	Copper	Cu	04-002-8854
	Cuprite*	Cu_2O*	04-002-0906*
DS055 (Figure 2.28)	Anatase	TiO_2	01-084-1285
	Copper	Cu	04-002-8854
	Cuprite*	Cu_2O	04-002-0906*
	Silicon (substrate)	Si	01-080-0018
DS058 (Figure 2.29)	Anatase	TiO_2	01-084-1285
	Tenorite	CuO	00-041-0254
	Copper	Cu	04-002-8854

*Due to overlaps with the other phases present it was difficult to accurately identify if a small amount of Cuprite was or was not present in samples DS053.

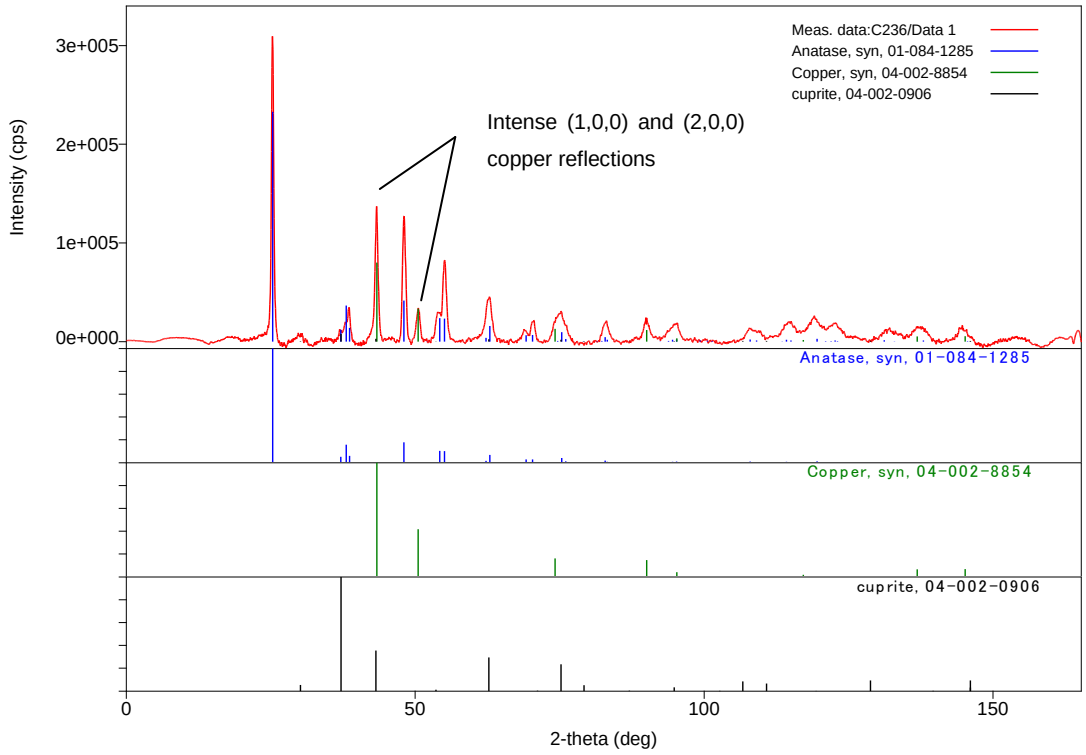

Figure 2.27: XRD pattern for sample DS053, anatase TiO_2 deposited onto a blue thin film copper metal (glass substrate)

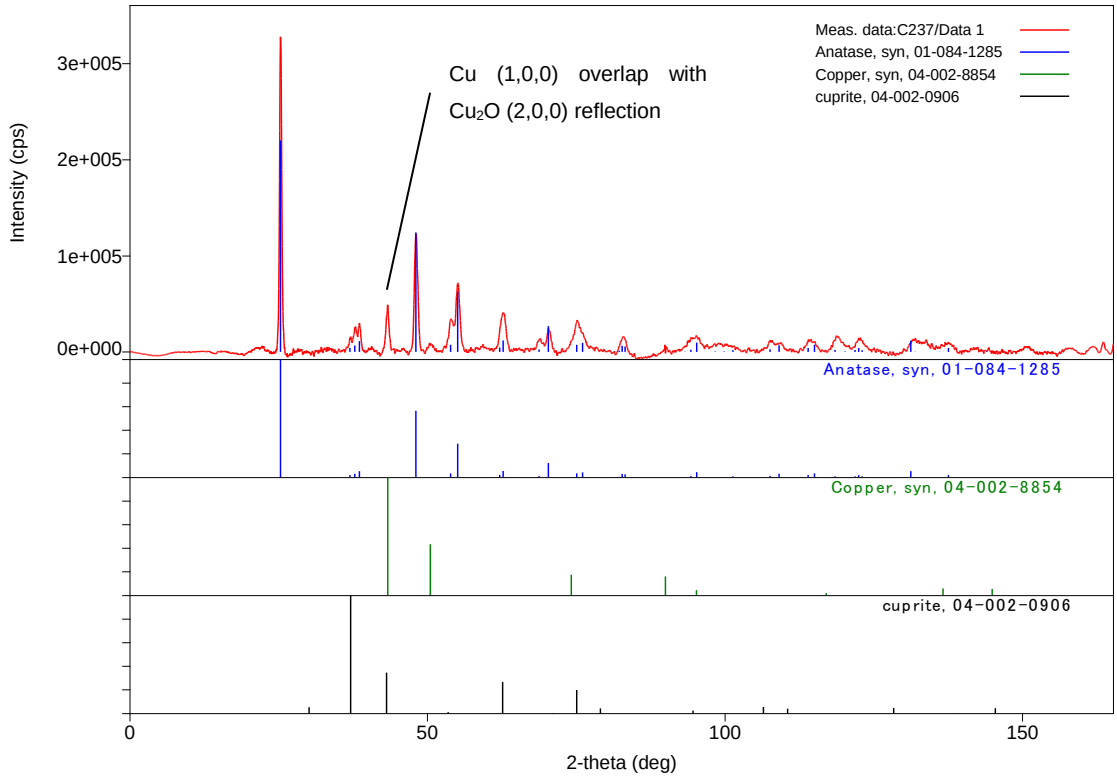

Figure 2.28: XRD pattern for sample DS055 - TiO_2 deposited onto a yellow thin film of Cu_2O (glass substrate)

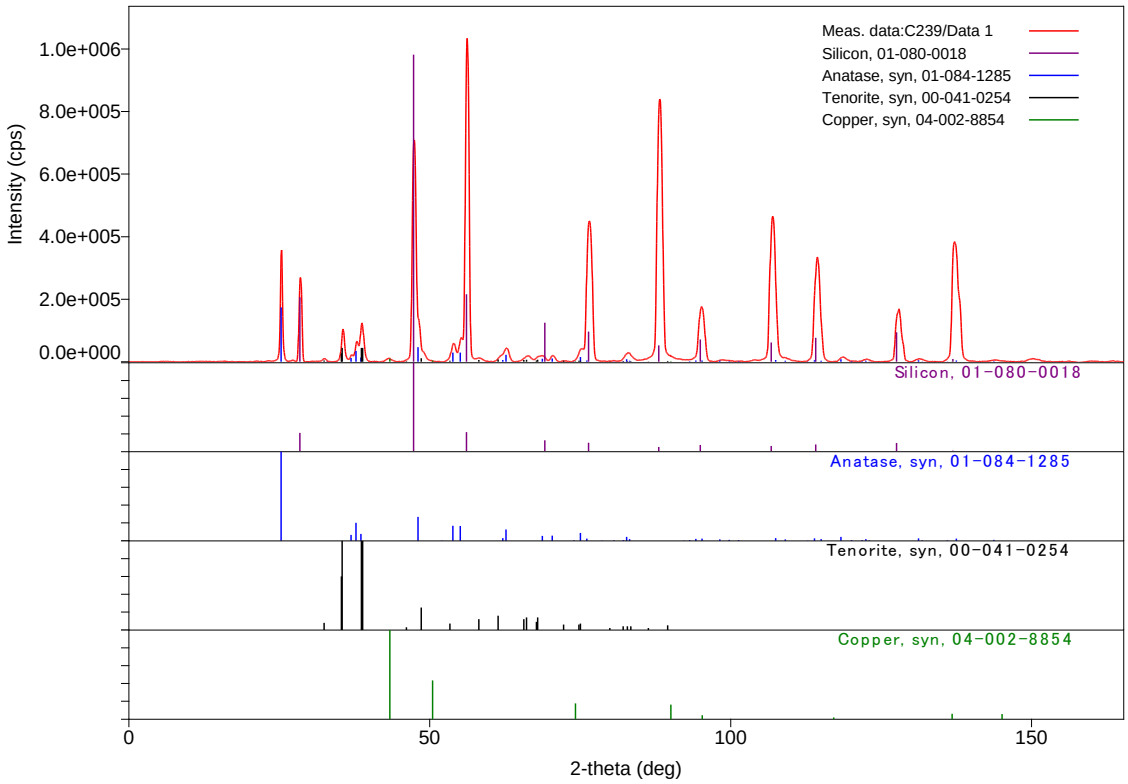

Figure 2.29: XRD pattern for sample DS058 - TiO_2 deposited onto a thin film of CuO (silicon substrate)

Selected samples were also analysed by XPS. Five samples of titania and copper/copper oxide coatings on glass and silicon substrates were submitted for depth profiling by XPS and are detailed in table 2.8.

Table 2.8: Samples analysed by XPS

Sample	Material	Substrate	Figure #
DS053	TiO_2:Cu	glass	2.30
DS055	TiO_2:Cu_2O	glass	2.31
DS057	TiO_2:Cu	silicon	2.32
DS058	TiO_2:CuO	silicon	2.33
DS054	TiO_2:Cu	Activ^{TM}	2.34

All elements associated with the film and substrates were observed across all the samples. DS053 also exhibited a Ti:O ratio over the range 0.5-0.6 through the depth of the coating right up to the copper interface, consistent with TiO_2. The copper was detected at the interface with the glass but reached a maximum at 24 atom.%.

The Ti:O ratio of DS055 was a steady 0.6 throughout the sample. Copper was detected at the interface between the coating and the glass at a maximum concentration of 3.9%.

Samples DS057 and DS058 both had Ti:O ratios that varied between 0.5 and 0.6 through the depth of the coating. Surprisingly in both samples the copper was also detected at the surface of the titania layer. The copper was present in these two samples at levels much greater than those of the other samples deposited on glass/Activ with concentrations of 56% (DS057) and 46% (DS058) respectively.

DS054 had a fairly stable Ti:O ratio of between 0.5 and 0.6 throughout the coating. Copper was again detected at the air and glass interfaces respectively suggesting the presence of an unexpected layer at the very surface. The maximum for the copper at each of these interfaces was 5 atom%.

Due to the significant charging effects of the sample during etching it was not possible to accurately relate the binding energy of the copper peak to a specific oxidation state. The only observation that could be made was that there was a difference in binding energy between the coatings that were on float glass and

those on silicon. It was not clear as to whether this difference was a coating or substrate effect.

The XPS results can be summarised as follows:

- The Ti:O ratio in all the samples was within the range 0.5 - 0.6;
- The samples on silicon had higher atomic % of copper than those on float glass/Activ;
- Samples DS053 and DS055 had titania layers on top of the copper containing film;
- Samples DS057 and DS058 (silicon) did not show a clear layering of copper and titania; rather significant migration of copper was apparent throughout the film.

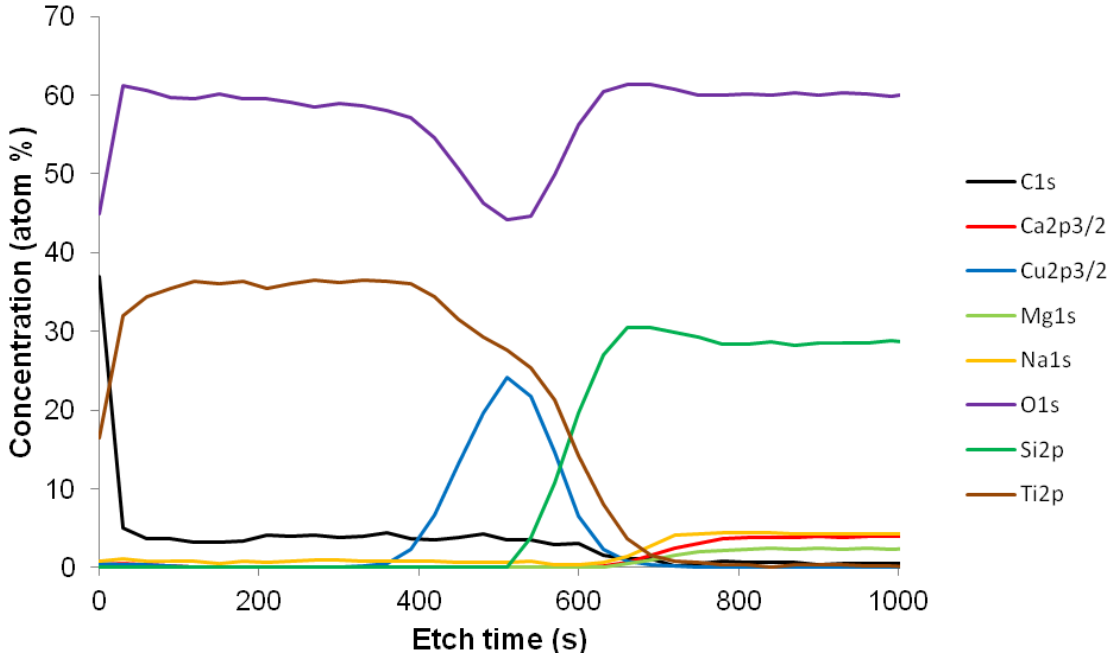

Figure 2.30: XPS depth profile of DS053 - TiO_2:Cu [glass]

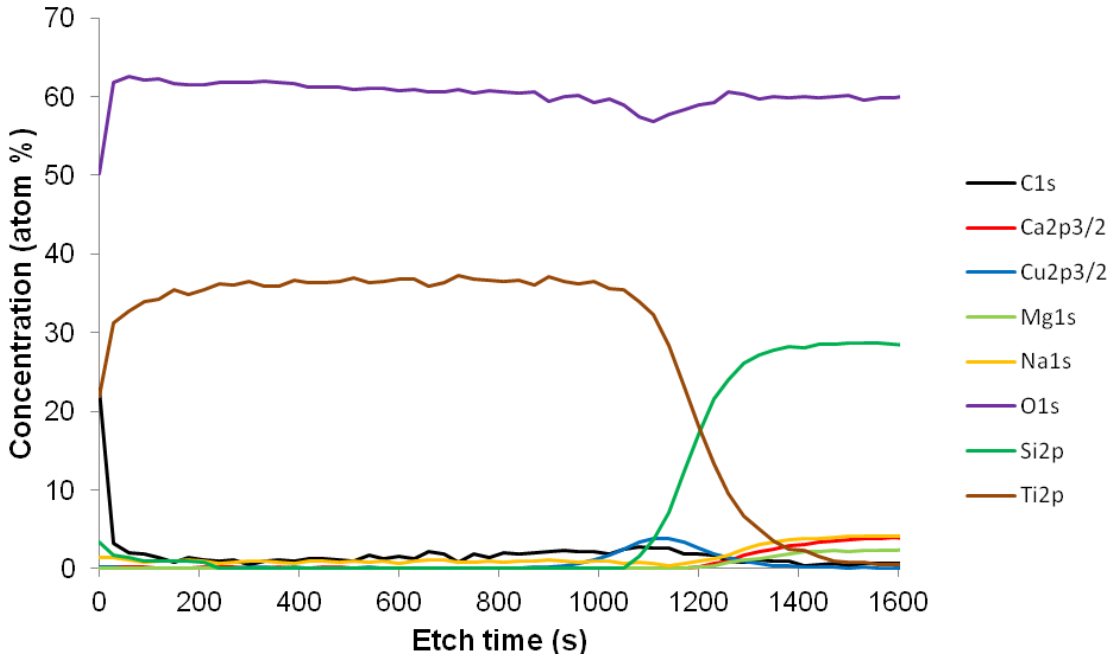

Figure 2.31: XPS depth profile of DS055 - TiO_2:Cu_2O [glass]

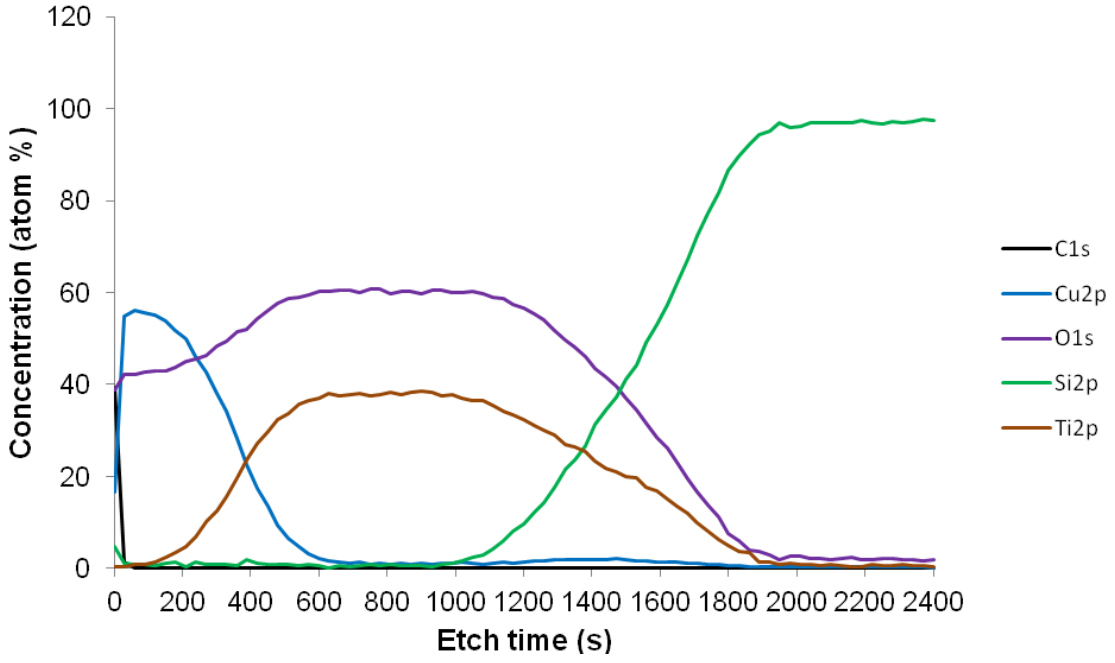

Figure 2.32: XPS depth profile of DS057 – TiO_2:Cu [Silicon]

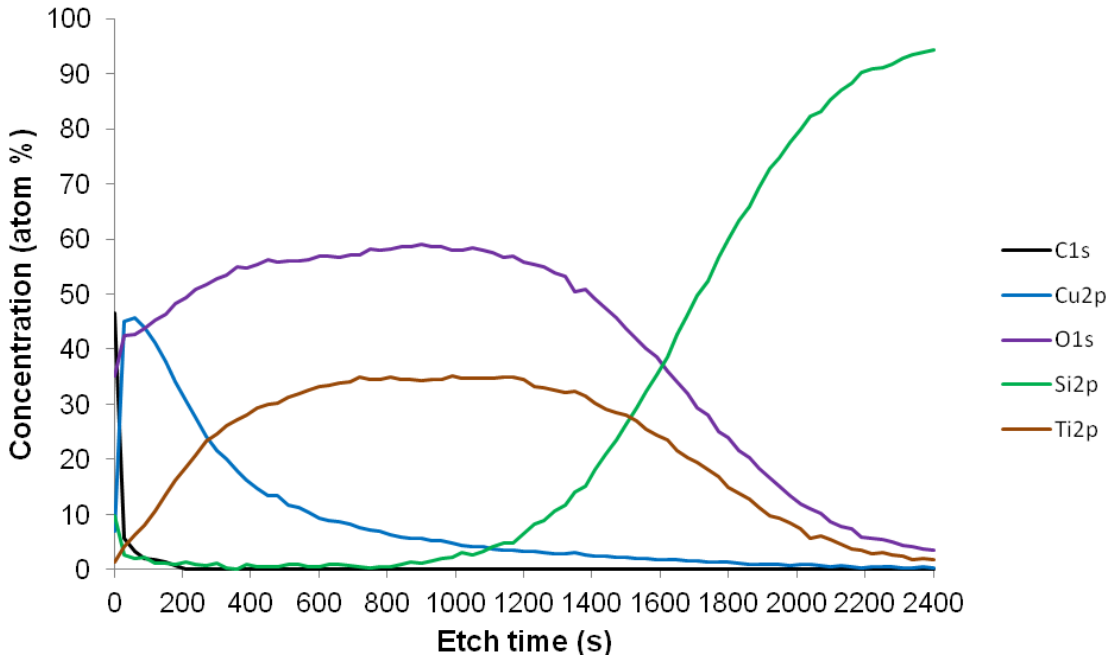

Figure 2.33: XPS depth profile of DS058 – TiO_2:CuO [Silicon]

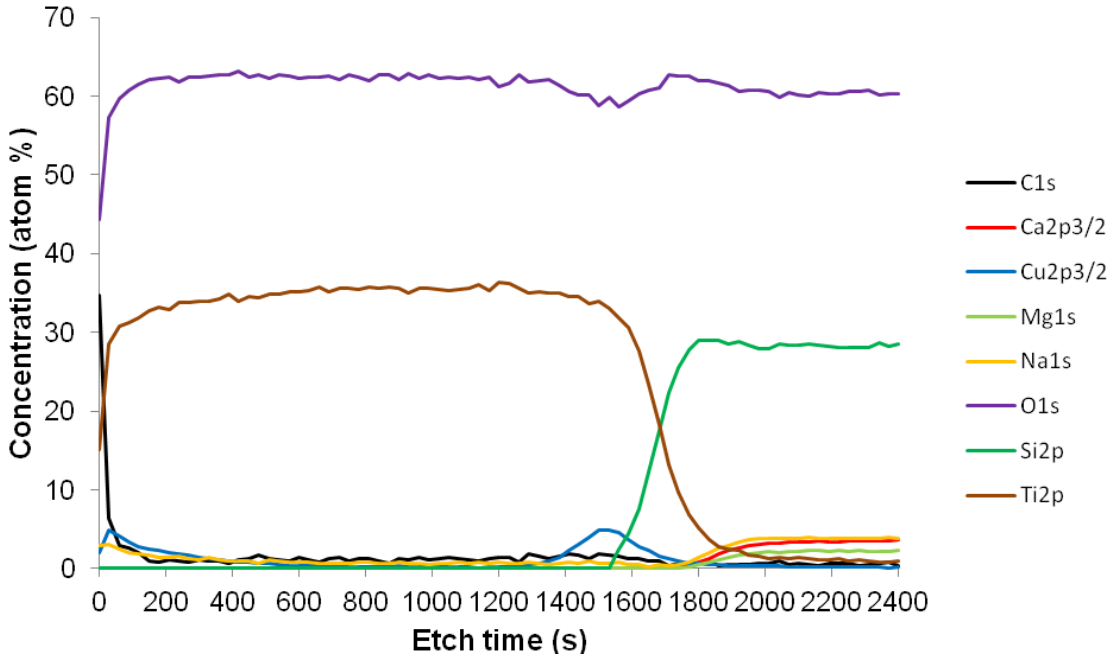

Figure 2.34: XPS depth profile of DS054 – TiO_2:Cu [Activ^{TM}]

Further to the XPS measurements, the most aesthetically pleasing blue film – DS053 a TiO_2:Cu film, was submitted for ToF-SIMS compositional depth profiling.

Examination of the mass spectrum obtained by the summation of all of the mass spectra in the depth profile clearly showed the presence of copper (Figures 2.35 and 2.36).

Figure 2.37 shows the depth profile obtained. As expected, the coating is seen to consist of a titanium-oxygen containing layer on top of a copper containing layer at the surface of the glass. Chlorine was detected in the surface region of the coating and there is evidence for sodium and hydroxyl running through the full thickness of the coating.

Estimated layer thickness is normally calculated from a layer's FWHM in a depth profile, sputter current, sputter yield and sputter beam raster size. Since the coating had been deposited from an aerosol, sputter yields were not available. However, a very approximate calculation of the titania layer thickness using the sputter yield for CVD titania gave a value of 200nm.

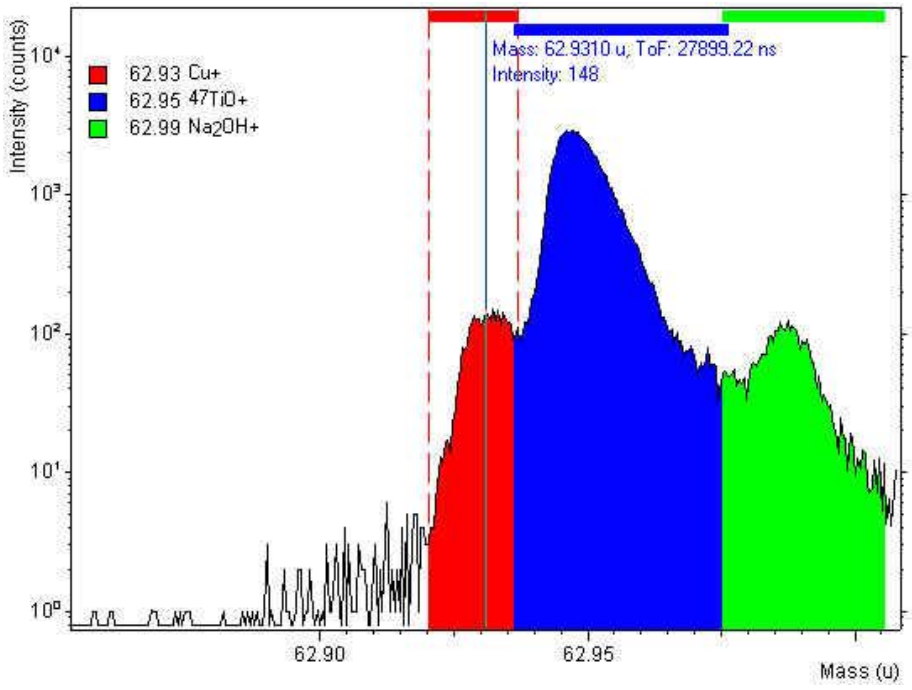

Figure 2.35: ToF-SIMS Copper mass peak (log scale), sample DS053

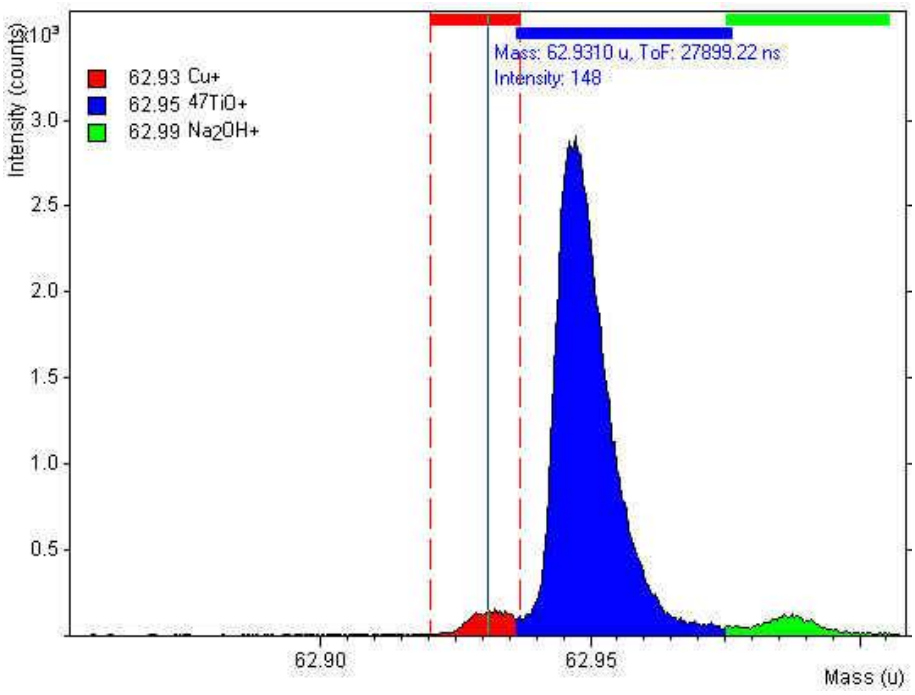

Figure 2.36: ToF-SIMS Copper mass peak (linear scale), sample DS053

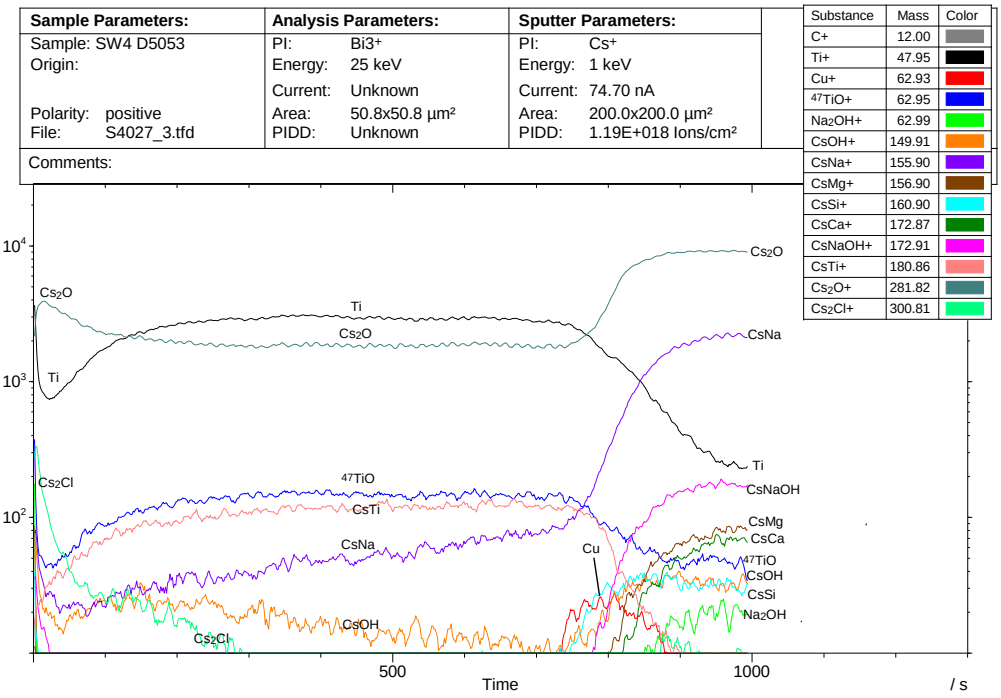

Figure 2.37: ToF-SIMS Positive ion depth profile, sample DS053

2.6. Determination of photoactivity

As discussed in chapter 1, rapid assessment of photoactivity is advantageous over the stearic acid method which can be time consuming. The photocatalytic response was thus determined for selected coloured coatings by measurement of the degradation of resazurin dye which had been applied to the surface under 254 nm UV irradiation. Figure 2.38 shows a typical response for photoactive coatings while under UV irradiation. The blue resazurin dye is reduced to pink resorufin and then colourless organic byproducts. Combined UV-vis absorption spectra for sample DS053 coated with the dye before and after UV irradiation are shown in figure 2.39. Relative concentrations of resazurin dye as a function of irradiation time using the absorption maxima at 610 nm for samples DS053, DS055, Activ^{TM} and blank float glass are given in figure 2.40.

Samples DS053 and DS055 exhibited decreases in the 610 nm absorbance at a similar rate to that of commercially available Activ^{TM} and remained stable after 7 minutes at around 50% intensity. The Activ^{TM} sample however, continued to degrade the dye for 10 minutes whereupon photoactivity stabilised. Blank Pilkington float glass exhibited a very slow but steady decrease in intensity to 90% relative intensity.

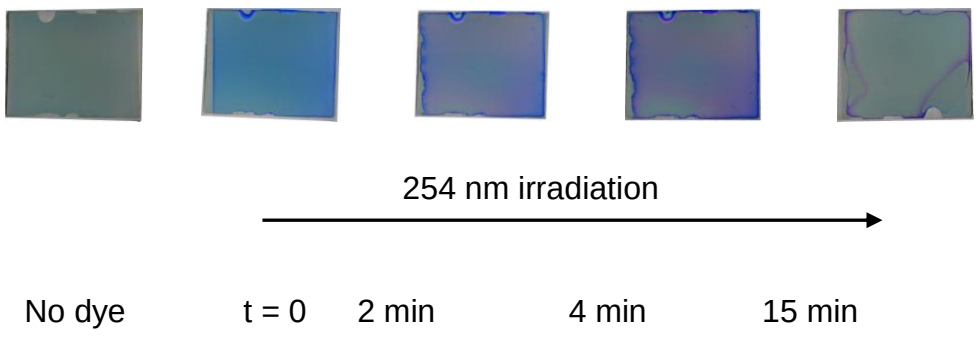

Figure 2.38: Photographic images of sample DS053 at various stages of photoactivity testing using resazurin intelligence ink. Resazurin ink is initially blue, and is reduced to resorufin (pink) under 254 nm UV irradiation before complete reduction to colourless organic species.

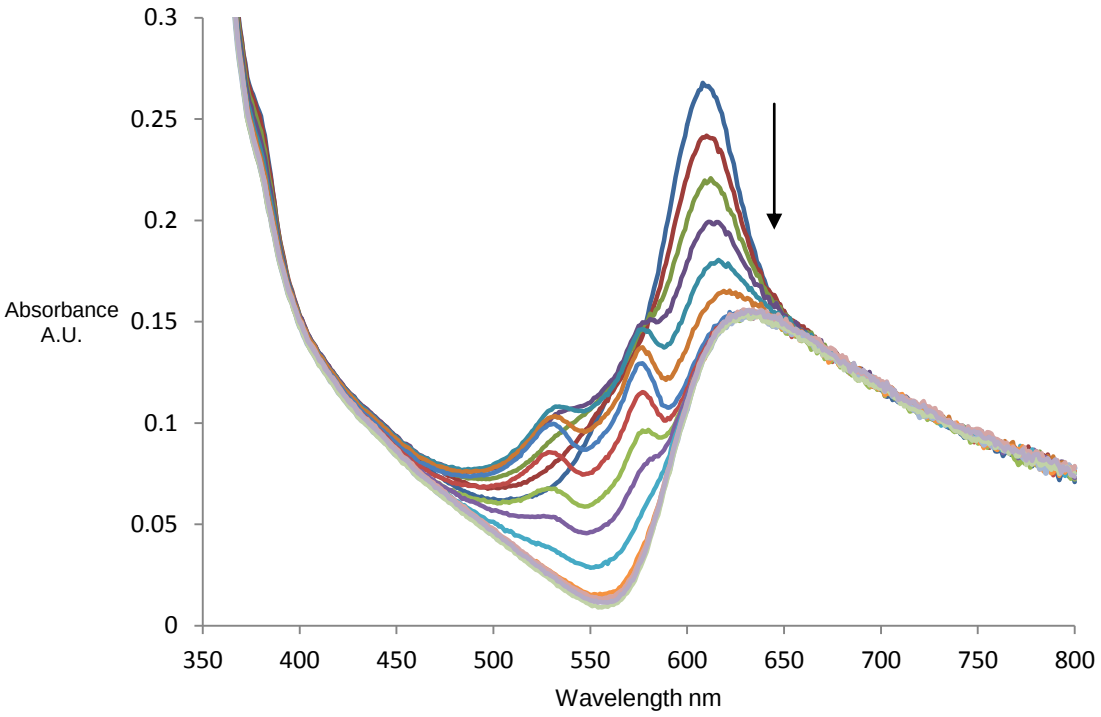

Figure 2.39: UV/Visible absorption spectra of DS053 coated with Rz/glycerol/HEC intelligence ink during UV irradiation at one minute intervals

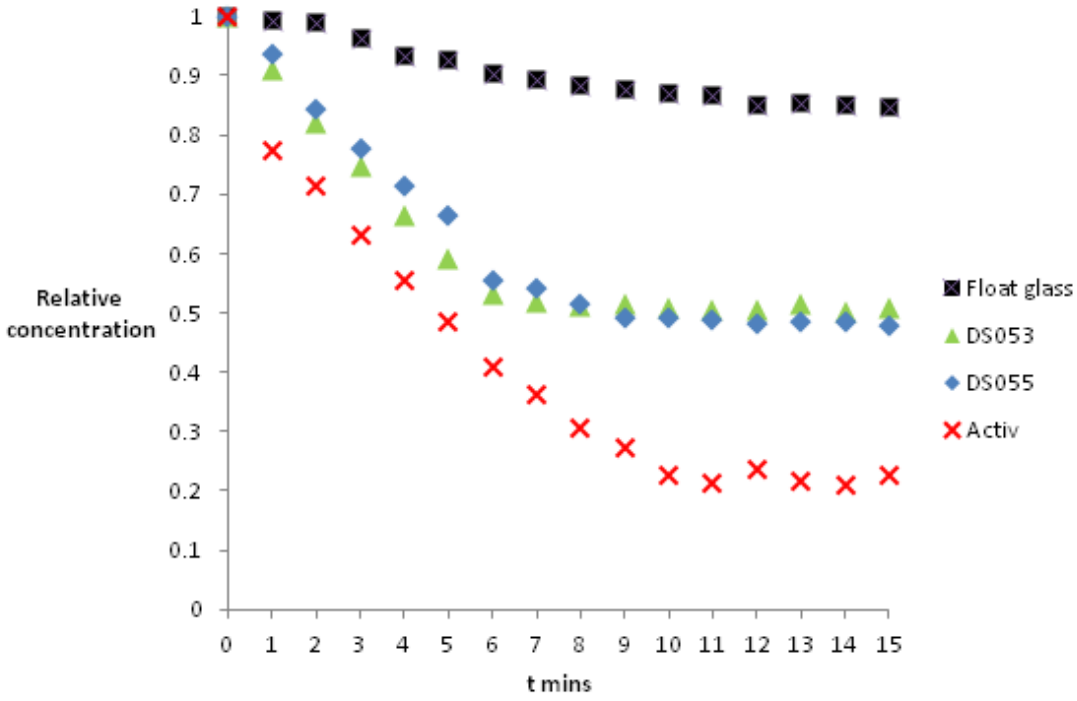

Figure 2.40: Relative concentrations of resazurin dye as a function of irradiation time for coloured coatings DS053 and DS055, Activ™ and blank float glass. Measurements were based on the decrease of the 610 nm absorbance of resazurin dye.

The water contact angles of DS053 and DS055 were measured to give further information on photocatalytic activity. Contact angles were measured before and after 5 minutes of 254 nm UV irradiation with distilled water. Contact angle images for DS053 are shown in figure 2.41 and measurements for selected samples are shown in table 2.9.

Table 2.9: Water contact angles for selected samples

Sample	**Contact angle**	
	Before UV irradiation (°)	**After 254nm irradiation (°)**
DS053 – TiO_2:Cu	82	6
DS055 – TiO_2:Cu_2O	75	5
Activ	71	4
Blank float glass	38	34

Both coloured films exhibited a large reduction in contact angle to around 5°, which is comparable to the UV-induced superhydrophilicty of Activ.[36] Blank float glass exhibited some small reduction in contact angle possibly due to organic hydrophilic contaminants on the surface of the glass.

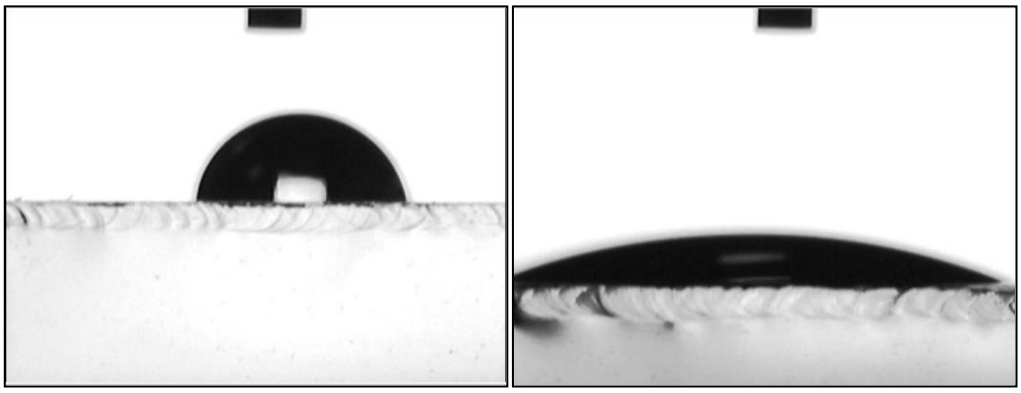

Figure 2.41: Water contact angle images for DS053, TiO_2:Cu coating before (left) and after 5 minutes of 254 nm UV irradiation (right).

2.7. Conclusions

2.7.1. SEM results

The amorphous base layer of the Activ substrate was seen on sample DS054 and the thin amorphous SiCO base layers could be discerned on samples DS100A, DS098, DS053 and DS055 (all glass substrates); an amorphous base layer was not seen on samples DS058 and DS063 that had a silicon substrate.

On all samples that were coated with a TiO_2 layer on top of a copper or copper oxide layer (samples DS053, DS055, and DS058), clearly defined interfaces showing that layer were not seen, interfaces showing the top layer of the Activ substrate on DS054 were also not observed. This means that the thickness measurement of those coatings includes both the TiO_2 layer and the copper or copper oxide layer; the thickness measurement of the coating on DS054 also includes the top layer of the Activ substrate. Thicknesses of the TiO_2 layer were about an order of magnitude greater than those of commercially available Activ indicating a significantly shorter deposition time of the photoactive layer is required.

The coatings on samples DS053, DS054, DS055 and DS058 consisted of sharp edged (pyramidal) coating crystals of TiO_2.

The coatings on samples DS100A, DS063 and DS098 consisted of closely packed, rounded particles. This gives a clear indication of the origin of the blue colour in the metallic copper films as plasmon resonance (PR) is often observed in metallic nanoparticles. While this has been useful in the generation of blue, photoactive coatings, plasmonic materials may have other applications. Indeed colloidal gold has long been used for the staining of glass owing to its unique spectral absorption.[37] Many circular holes were present between the substrate and the coating of sample DS058. The holes originated at the surface of the silicon substrate; possibly suggesting that some gas/vapour was present at the time of coating deposition, although the size of the holes compares well with the size of the original copper nanoparticles. The holes caused the coating surface to undulate so that the coating had a greater surface height above the holes.

On the samples with lumps of material present at the surface (all except sample DS054), the lumps appeared to consist of the same material as the coating layer; sample #1 comprised many lumps at the surface. It is possible that these lumps were seeded by the underlying copper layer, where it had agglomerated into small clusters (as were present in sample DS100A, copper on glass).

2.7.3. XRD

The TiO_2 component deposited across all samples could be indexed to the anatase phase with no indication of the rutile phase present. Where copper metal was the colour layer (DS053), crystalline copper is still present indicating its robustness to oxidation or phase change while deposition of the photoactive titania layer takes place. However, a small amount of cuprite, Cu_2O is present indicating some oxidation may have occurred. Where Cu_2O was used as the base colour layer, Cu_2O was also observed in the final film and, in the case of DS055, a small amount of metallic copper was observed. This is likely due to incomplete oxidation of the original film as opposed to some reduction taking place while depositing the photoactive titania layer.

XPS data are in good agreement with the phases determined by XRD. What is evident is that copper has some degree of mobility within the titania film. Ion migration of Cu(II) as well as Fe(III) and Ni(II) is known to occur within titania matrices.[38] It was also interesting to note that on silicon substrates (DS058 and DS057), the copper signals were far stronger than the glass counterparts. The SiCO layer on float glass should prevent migration of Cu ions into the glass, so it is possible that the increased concentration arises from a faster “entrapment” of copper/copper oxide on the silicon substrate. Since it is much thinner, the silicon is able to cool much more quickly than glass, preventing thermal migration of copper into the titania layer.

ToF-SIMS depth profiling of sample DS053 showed the coating consisted of a titanium-oxygen containing layer on a copper containing layer on glass. The ‘titania’ layer was approximately 200nm thick and the copper layer was very thin in comparison. Due to the absence of a sputter yield for copper, an estimated thickness for the copper underlayer could not be calculated. Sodium and hydroxyl were contaminants in the coating, although the source was not clear.

Figure 2.42 illustrates the final coating.

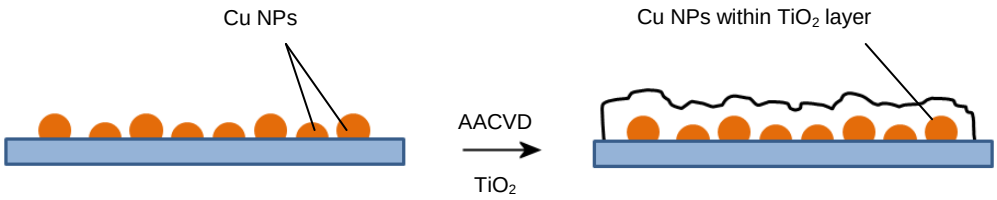

Figure 2.42: Diagram of copper nanoparticles embedded in titania matrix

Copper and copper oxide films (DS100 and DS063) were slow to deposit with growth rates estimated from film thicknesses at 2 nm per minute (c.f. 20 nm in ~2s for conventional CVD of TiO_2). This, however, was at precursor concentrations of 0.1 M so it is likely that increasing the concentration would result in increased growth rates.

Contact angle measurements and photoactive degradation of resazurin dye have shown photocatalytic responses comparable to that of Activ. Whilst Activ and TiO_2:Cu/CuO films (DS053 and DS055) are effectively the same material (anatase TiO_2), surface morphologies are significantly different. The greater thickness and roughness of the coloured coatings will likely result in a better surface interaction with the dye which could account for the faster observed degradation of resazurin.

2.7.4. Oxidation state control within the AACVD process

Work detailed in this chapter has shown that a degree of control over the oxidation state of copper during the AACVD of Cu, Cu_2O and CuO thin films from $Cu(NO_3)_2.2.5H_2O$ precursor, scheme 2.4.

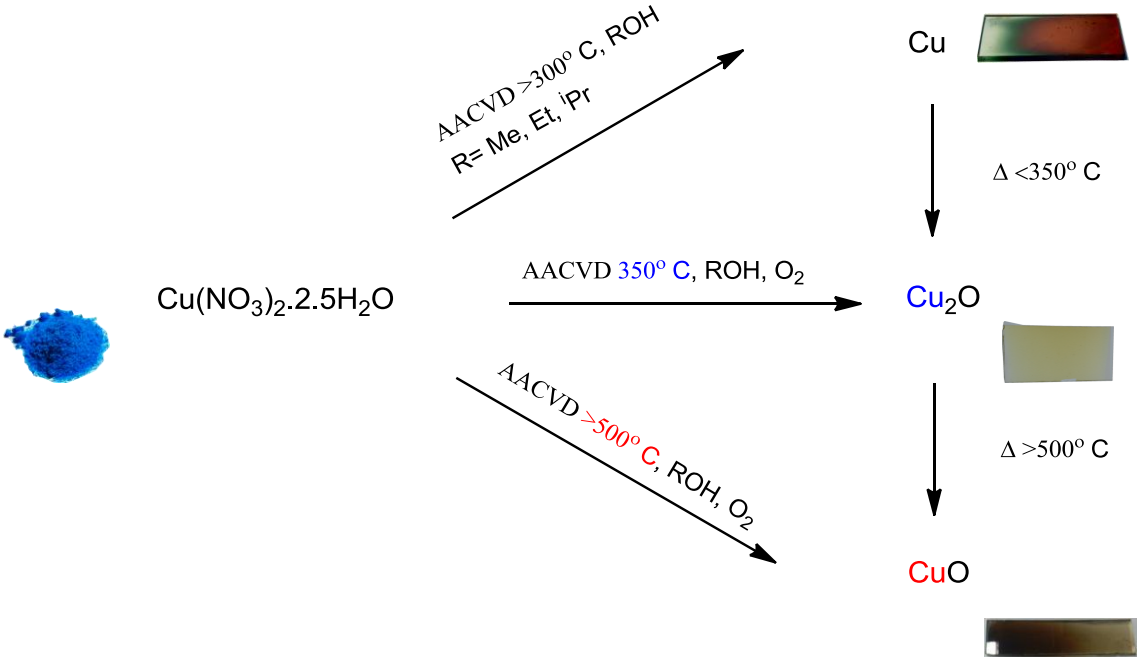

Scheme 2.4: Control of an AACVD process to give phase pure thin films of copper in the 0, +1, or +2 oxidation state.

Cuprous oxide, Cu_2O is a p-type semiconductor with a band gap of 2.2 eV. The earth-abundant material has shown excellent potential for photoelectrochemical water splitting, and type-II multijunction solar cell devices.[39] It has long been problematic to obtain phase-pure thin films of Cu_2O owing to its ready oxidation to the more stable CuO. Current methods toward producing Cu_2O thin films include CVD,[40] plasma evaporation,[41] magnetron sputtering[42] or thermal oxidation of existing copper thin films.[43] The latter method is time consuming, taking care not to exceed temperatures of 300°C and annealing for at least one hour to produce crystalline films. The other methods report some degree of combined growth of Cu_2O and CuO phases. Most recently the electrodeposition of copper oxide has been reported and found to affect control of the deposited material by variation of the applied voltage.[44]

The ability to control the oxidation state of the resultant material by an AACVD process has been explored in this chapter. The precursor is the cheap, non-toxic copper (II) nitrate, $Cu(NO_3)_2.2.5H_2O$ and multiple primary alcohols have been tested as the precursor solvents. Through this method, it is possible to generate thin films of either Cu metal, Cu_2O, or CuO, of copper oxidation states 0, I, and II

respectively, simply by temperature control and addition of O_2 to the deposition process. This method also has the added advantage of reduced carbon contamination owing to the precursor not containing any apart from that which is present in the solvent. This phenomenon of unexpectedly producing metallic and metal oxide films from the AACVD of copper nitrate precursor was reported by Parkin in 2011[33] and more recently in 2014.[45] It is well known that methanol can be used as an oxidising solvent in many depositions. The explanation for the *in situ* reduction of copper (II) to copper (0) was attributed to the formation of a reducing hydrogen atmosphere from the catalytic decomposition of methanol over a copper catalyst.

$$CH_3OH \longleftrightarrow C + H_2 + H_2O \quad \Delta H^0_{298} = -42 \text{ kJ mol}^{-1}$$

$$CH_3OH \longleftrightarrow CO + H_2 \quad \Delta H^0_{298} = 49 \text{ kJ mol}^{-1}$$

However, experiments have shown no difference in deposition rate depending on the choice of alcohol solvent. This also does not address the problem of the need for metallic copper to be present for the initial catalysis to occur. We prefer, therefore, to justify the formation of metallic copper in terms of electrode potential instead of a catalytic process. It is apt to mention that literature data is determined under standard conditions, not necessarily relevant to a deposition environment. In this way E^0 values can be used simply as a figure of merit as opposed to absolute figures.

Solutions of metal nitrates in water or ethanol without a source of 'fuel' e.g. urea or similar variant will deposit the relevant metal oxide if the reduction potential

$$M^{n+} + ne \rightarrow M$$

is less positive than the standard reduction potential for nitrate reduction. i.e. in aqueous solution for a 3 electron reduction in water this will be:

$$NO_3^- + 4H^+ + 3e \rightarrow NO + 2H_2O \qquad +0.96V$$

For Cu^{2+} in aqueous solution:

$$Cu^{2+} + 2e \rightarrow Cu \qquad +0.34V$$

Giving the reduction to Cu metal as E_{cell} = +0.34 – (+0.96) = - 0.62V i.e. endothermic

An interesting case, however, is provided by the same reaction in methanol or ethanol. In this case the vast excess of oxidizable solvent, to formaldehyde and acetaldehyde respectively, must also be taken into consideration.

$$HCHO + 2e + 2H^+ \text{--> } CH_3OH \qquad +0.232V$$

$$CH_3CHO + 2e + 2H^+ \rightarrow CH_3CH_2OH \qquad -0.20V$$

For the reaction of ethanol with nitrate E_{cell} = 0.96 – (-0.20) = + 1.16 V i.e. all the nitrate in solution will be reduced by the solvent (in vast excess) and will, thus, be unavailable to impact on the copper oxide deposition.

In this case, however, with respect to the Cu^{2+}/ethanol system

E_{cell} = +0.34 – (-0.20) = +0.54V with the result that the Cu^{2+} will also be reduced to copper metal (or be able to oxidise the ethanol solvent).

2.7.5. Summary

Simple copper nitrate, $Cu(NO_3)_2.2.5H_2O$ has been dissolved in ethanol and employed as a precursor for the AACVD of metallic copper, cuprite, and tenorite thin films (DS100, DS060 and DS063 respectively). Copper films are shiny and consist of rounded nanoparticles (50 – 80nm) and exhibit strong blue colour owing to plasmon resonance. Cuprous oxide films are yellow and also consist of rounded nanoparticles.

When coated with a layer of anatase TiO_2, also by AACVD, the metallic reflectance disappears but the blue colour remains in the case of metallic copper (DS053). Interestingly the yellow cuprous oxide films also appear blue when covered with a layer of TiO_2 (DS055).

Coatings exhibit good photoactivity comparable with that of commercially available Activ.

2.8. Further Work

There is much that is not understood about the fundamental dynamics of the AACVD process. The ability to control oxidation state of a material depends on many factors including solvent, temperature, atmosphere and substrate. Detailed measurement of aerosol droplet size and flux would yield information on deposition mechanism.

It is recommended that the co-deposition of metal nitrates and titania precursors are investigated. For example, a mixed solution of $Cu(NO_3)_2.2.5H_2O$ and $Ti(O_iPr)_4$ introduced by aerosol in an appropriate solvent may deposit a more uniformly doped material. Since the growth of titania is so much greater than the observed growth rate of copper/copper oxide, the concentration of the titania precursor could be greatly lowered. A much thinner application of a TiO_2 layer may also result in the observation of two distinct layers.

The deposition of metallic copper and nickel also warrants further investigation. Metallic films find a variety of applications and therefore require significant effort into testing precursors for their deposition. Metal nitrate systems offer incredible advantages in terms of cost, toxicity, carbon content and above all simplicity. By selecting appropriate solvents, ligands, deposition temperatures and substrates, there is almost limitless potential for complex material synthesis by an AACVD process.

References for chapter 2

1. Keidel, E., In Furben Zeitung: 1929; Vol. 34, p 1242.
2. Goodeve, C. F.; Kitchener, J. A., *Transactions of the Faraday Society* **1938,** *34*, 570-579.
3. Pappas, S. P.; Fischer, R. M., *Journal of Paint Technology* **1974,** *46*, 65-72.
4. http://www.huntsman.com/pigments
5. Oregan, B.; Gratzel, M., *Nature* **1991,** *353*, 737-740.
6. Jitputti, J.; Pavasupree, S.; Suzuki, Y.; Yoshikawa, S., *Journal of Solid State Chemistry* **2007,** *180*, 1743-1749.
7. http://www.pilkingtonselfcleaningglass.co.uk/.
8. Dunnill, C. W.; Kafizas, A.; Parkin, I. P., *Chemical Vapor Deposition* **2012,** *18*.
9. Dunnill, C. W. H.; Aiken, Z. A.; Pratten, J.; Wilson, M.; Morgan, D. J.; Parkin, I. P., *Journal of Photochemistry and Photobiology a-Chemistry* **2009,** *207*, 244-253.
10. Aiken, Z. A.; Hyett, G.; Dunnill, C. W.; Wilson, M.; Pratten, J.; Parkin, I. P., *Chemical Vapor Deposition* **2010,** *16*.
11. Schmidt, M. L. a. E. R. a. W. G., *Journal of Physics: Condensed Matter* **2012,** *24*, 195503.
12. *Crystal Structures* **1963,** *1*.
13. *Z. Kristallogr.* **1972,** *136*, 273.
14. *Strukturbericht Band II 1928–1932* **1937**.
15. Greenwood; N, N.; A, E., Chemistry of the elements. In Pergamon: Oxford, 1984.
16. Hashimoto, K.; Irie, H.; Fujishima, A., *Japanese Journal of Applied Physics Part 1-Regular Papers Brief Communications & Review Papers* **2005,** *44*.
17. Mills, A.; LeHunte, S., *Journal of Photochemistry and Photobiology a-Chemistry* **1997,** *108*.
18. Suppan, P., *Chemistry and Light*. Royal Society of Chemistry: Cambridge, 1994.
19. Mills, A.; Hill, G.; Crow, M.; Hodgen, S., *Journal of Applied Electrochemistry* **2005,** *35*.

20. Hajkova, P.; Spatenka, P.; Horsky, J.; Horska, I.; Kolouch, A., *Plasma Processes and Polymers* **2007,** *4*.
21. Dunnill, C. W.; Parkin, I. P., *Dalton Transactions* **2011,** *40*.
22. Hoffmann, M. R.; Martin, S. T.; Choi, W. Y.; Bahnemann, D. W., *Chemical Reviews* **1995,** *95*.
23. Kafizas, A.; Parkin, I. P., *Journal of the American Chemical Society* **2011,** *133*.
24. Highfield, J. G.; Pichat, P., *New Journal of Chemistry* **1989,** *13*.
25. Nambu, A.; Graciani, J.; Rodriguez, J. A.; Wu, Q.; Fujita, E.; Sanz, J. F., *Journal of Chemical Physics* **2006,** *125*.
26. Zhu, J. F.; Deng, Z. G.; Chen, F.; Zhang, J. L.; Chen, H. J.; Anpo, M.; Huang, J. Z.; Zhang, L. Z., *Applied Catalysis B-Environmental* **2006,** *62*.
27. Wang, J. P.; Yang, H. C.; Hsieh, C. T., *International Journal of Photoenergy* **2012**, 10.
28. Pomoni, K.; Vomvas, A.; Trapalis, C., *Thin Solid Films* **2008,** *516*.
29. Kafizas, A.; Parkin, I. P., *Journal of Materials Chemistry* **2010,** *20*.
30. Palking, K. K.; Kuz'mina, N. E.; Orlova, V. T., *Russ.J.Inorg.Chem.* **1994,** ***39***, 1133.
31. L'Vov, B. V.; Novichikhin, A. V., *Spectrochimica Acta Part B: Atomic Spectroscopy* **1995,** *50*, 1459-1468.
32. Fu, Z. H., *Journal of Physics D: Applied Physics* **2004,** *37*, 81.
33. Crick, C. R.; Parkin, I. P., *Journal of Materials Chemistry* **2011,** *21*, 14712-14716.
34. Yu, W., *Journal of Raman Spectroscopy* **2013,** *44*, 142--146.
35. Pedersen, D. B.; Wang, S., *The Journal of Physical Chemistry C* **2007,** *111*, 17493-17499.
36. Parkin, I. P.; Palgrave, R. G., *Journal of Materials Chemistry* **2005,** *15*, 1689-1695.
37. Beretto-Lopez, M., *Glass Chemistry*. Springer-Verlag Berlin and Heidelberg GmbH & Co. K: Berlin, 1994.
38. Murakami, N.; Chiyoya, T.; Tsubota, T.; Ohno, T., *Applied Catalysis A: General* **2008,** *348*, 148-152.

39. Messaoudi, O.; Makhlouf, H.; Souissi, A.; Ben assaker, I.; karyaoui, M.; Bardaoui, A.; Oueslati, M.; Chtourou, R., *Journal of Alloys and Compounds* **2014,** *611*, 142-148.
40. Maruyama, T., *Solar Energy Materials and Solar Cells* **1998,** *56*, 85-92.
41. Santra, K.; Sarkar, C. K.; Mukherjee, M. K.; Ghosh, B., *Thin Solid Films* **1992,** *213*, 226-229.
42. Ogwu, A. A.; Bouquerel, E.; Ademosu, O.; Moh, S.; Crossan, E.; Placido, F., *Acta Materialia* **2005,** *53*, 5151-5159.
43. Gong, Y. S.; Lee, C.; Yang, C. K., *Journal of Applied Physics* **1995,** *77*, 5422-5425.
44. Paracchino, A.; Mathews, N.; Hisatomi, T.; Stefik, M.; Tilley, S. D.; Gratzel, M., *Energy & Environmental Science* **2012,** *5*, 8673-8681.
45. Hassan, I. A.; Parkin, I. P.; Nair, S. P.; Carmalt, C. J., *Journal of Materials Chemistry B* **2014,** *2*, 2855-2860.

Chapter 3:
AACVD of tin oxide and fluorine-doped tin oxide thin films

3.1. Introduction

This chapter focuses on the growth of tin-IV oxide (SnO_2) thin films, via the AACVD of a tin(II) nitrate precursor. As discussed in chapter 2, the metal-nitrate solutions yielded unexpected results in the form of metallic films, so it was decided to explore the process further. The work detailed in this chapter has subsequently formed part of patent application “B15003 – Metal Oxide Deposition” which at the time of writing is pending acceptance.

Tin(IV) oxide is a well characterised material with many applications and has a wide band gap of 3.6 eV.[1] SnO_2 is found in nature as the mineral cassiterite and adopts the rutile tetragonal crystal structure, and belongs to the $P4_2/mnm$ space group, shown in figure 3.1.

As a thin film, the material makes up an important part of the transparent conducting oxides (TCOs) when doped with fluorine at concentrations up to around 5%. This fluorine-doped tin oxide (FTO) along with tin-doped indium oxide (ITO), find a variety of applications in microelectronics, displays and solar cells.

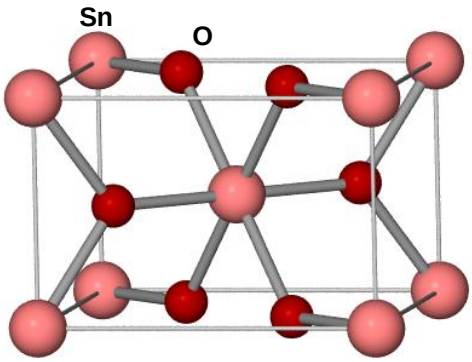

Figure 3.1: Crystal structure of tin(IV) oxide [2]

This F-doped metal oxide is an n-type semiconductor as F^- substitutes for O^{2-} in the SnO_2 lattice allowing an additional electron free to occupy the otherwise empty conduction band i.e.

$$Sn^{4+} + O^{2-}_{2-x} F^-_x e^-_x$$

Through fluorine doping, close to metallic conductivity can be achieved (~15 Ω/SQ but as low as 6 Ω/SQ) whilst still retaining transparency.[3] FTO has also found use as a solar control coating for low-emissivity glass owing to its high infra-red reflectivity. This has been exploited by Pilkington NSG in its TEC™ range of coatings consisting of fluorine-doped tin oxide.

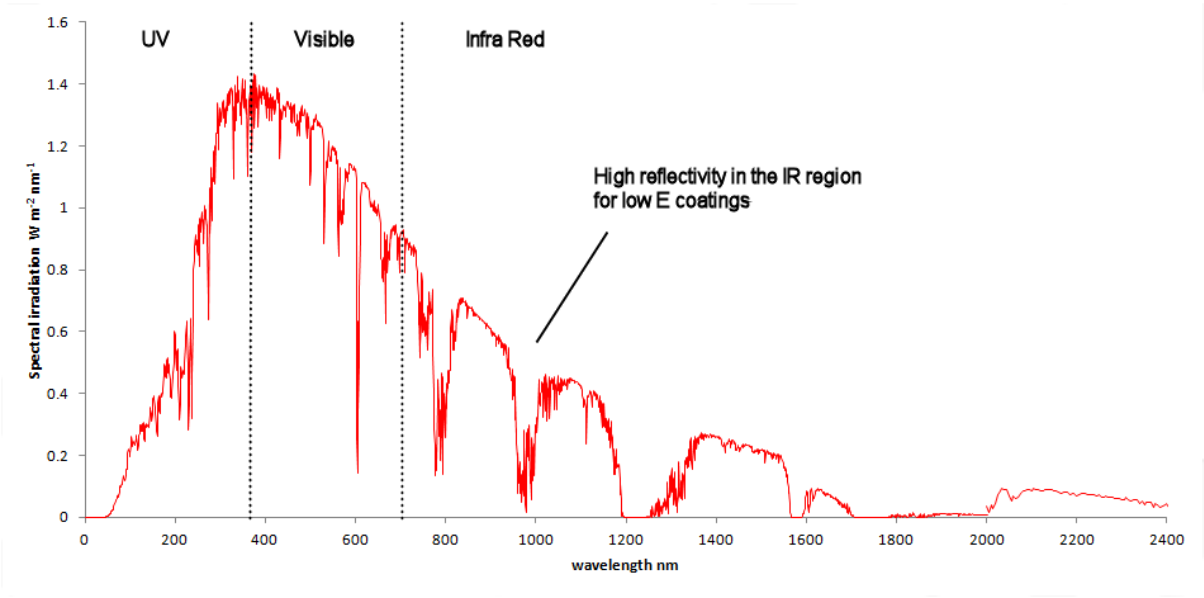

Figure 3.2: Solar irradiation spectrum and properties required for low E coatings.

Solar control coatings or low-E glass such as K-glass selectively allow shorter visible wavelength solar radiation though the window as the coating is not particularly reflective at these wavelengths. Some energy is absorbed which heats the glass, whilst the majority passes through and is absorbed by everyday objects inside such as carpets and furniture, further heating the interior. This warmth is radiated in the form of a longer wavelength IR radiation which the glass coating on the inner pane is particularly reflective to. Now the longer wavelength radiation can be reflected back inside as well as pass through, with a net warming effect inside. Figure 3.3 shows four SEM images of FTO films from the literature, while figure 3.4 illustrates the workings of a solar control coating.

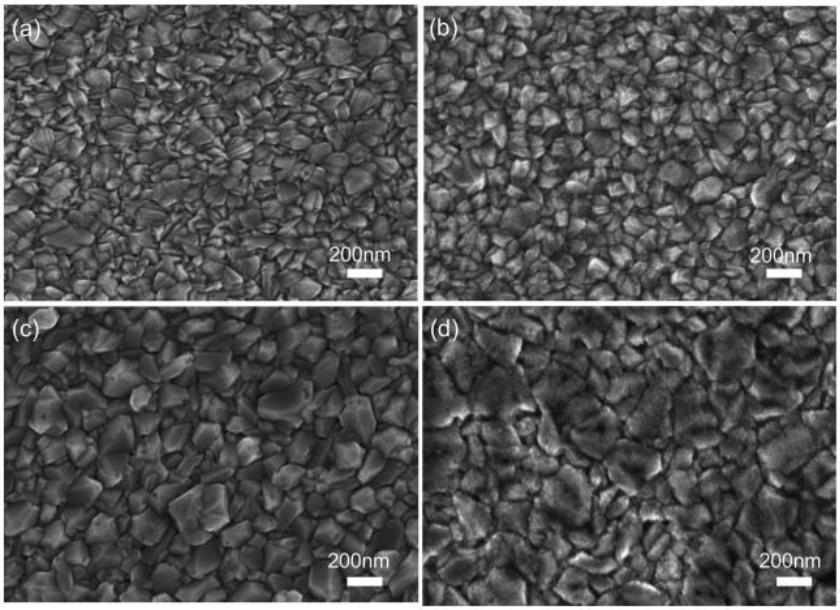

Figure 3.3: Literature SEM micrographs of FTO particles in deposited in the presence of H_2O (a), O_2 (b), EDTA (c), Acac (d).[4]

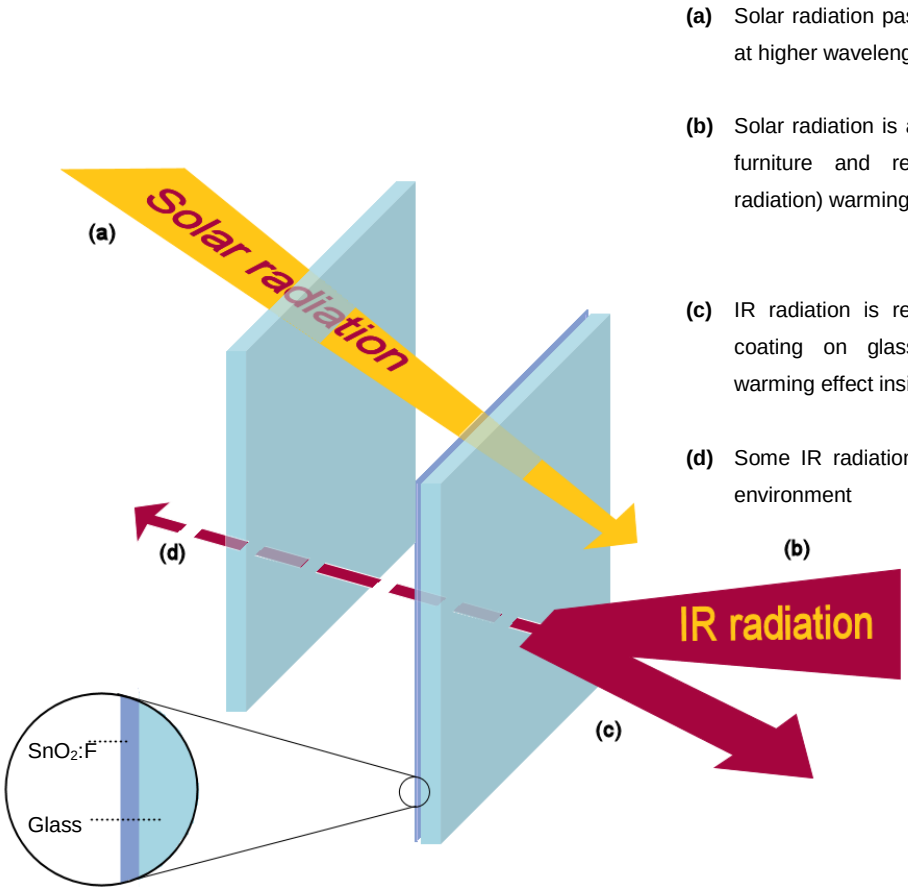

(a) Solar radiation passes through the window at higher wavelengths

(b) Solar radiation is absorbed by carpets and furniture and re-emitted as heat (IR radiation) warming up the interior

(c) IR radiation is reflected by solar control coating on glass surface with a net warming effect inside

(d) Some IR radiation escapes back into the environment

Figure 3.4: Illustration of how solar control coatings on a double glazed unit operate

3.2. Precursors to SnO_2 thin films

3.2.1. Existing processes - advantages and disadvantages.

Existing routes to doped SnO_2 thin films include the atmospheric pressure CVD of:

- $SnCl_4$ and O_2 [5]
- $Sn(Bu)_2(ac)_2$ and O_2, $SbCl_3$ [6]
- $Sn(Bu)_2(ac)_2$ and O_2, CCl_3CF_3 [6]
- $Sn(CF_3CO_2)_2$ [7]
- $Sn(Me)_4$ and O_2, CF_3Br [8,9]
- $SnCl_4$ and O_2, NH_4F [10,11]
- $SnCl_4$ and O_2, F_2 [12]
- SnR_4, where R = various perfluoroalkyls. [13]

F-doped SnO_2 films have also been deposited by the aerosol-assisted CVD of:

- $(Bu)SnCl_3$ and NH_4F [14]

Upon inspection of the aforementioned precursors problems arise. Firstly and perhaps most importantly, many alkyl-tin(IV) species are highly toxic, both to animal and plant life. This poses a significant problem in terms of worker and environmental safety, as well as a safe waste disposal challenge.

Furthermore, tin(IV) chloride and organotin-chlorides are air and moisture sensitive, releasing HCl vapour if exposed to an ambient atmosphere. Such properties require careful air-free handling and synthesis which can be time-consuming and expensive on an industrial scale. In addition, use of a moisture-sensitive precursor inherently rules out the use of water as a solvent in an AACVD process, either in synthesis or deposition. This necessitates the use of dry organic solvents which are costly, and flammable.

A further drawback of using organic ligands and solvents is the resultant carbon contamination in the resulting thin-films, potentially leading to decreased conductivity and optical transmission.

In this respect, it is desirable to use tin oxide precursor systems which are:

1) Air and water compatible
2) Non-toxic to animals or the environment
3) Incorporating little or no carbon in the resultant films

3.2.2 Tin nitrates

Marks *et al* have reported the fabrication of zinc-doped tin oxide and tin-doped indium oxide (ZTO and ITO respectively) by the solution processing (spin-coating) of $SnCl_2$, NH_4NO_3, urea, and $Zn(NO_3)_2.6H_2O$ or $In(NO_3)_3.2.85H_2O$ for ZTO or ITO respectively in a 2-methoxyethanol solvent.[15] This novel fabrication technique uses the concept of combusting a metal-containing oxidising agent such as a tin nitrate, and a fuel such as urea or acetylacetonate. Upon heating, the fuel is burnt, thereby providing a localised source of energy to drive the reaction, leaving the desired metal oxide.

The literature regarding the formation of tin nitrate complexes is limited, especially with thought to them as precursors to tin oxide materials. This is due to their thermodynamic instability and problematic synthesis and isolation. What little does exist usually requires Schlenk and/or drybox techniques. Table 3.1 details a few of the explored tin(IV) and tin(II) nitrate species.

Indeed, the structure of the simple dinitrato,dimethyl-tin(IV) compound was difficult to ascertain in 1973 as decomposition caused X-ray crystallographers problems due to a drop in reflection intensity. The compound's instability was so great that a second crystal had to replace the first for the second half of data collection.[16]

The only tin(II) nitrate in the literature that has been isolated in a pure state is that of $Sn_3(OH)_4(NO_3)_2$ which was prepared by slow addition of hydrous tin(II) oxide into concentrated nitric acid.[17] Donaldson and Moser reported a white crystalline solid that decomposed in water, and was explosive when "rubbed, struck or heated above 100°C". The subsequent formation of tin oxide is of interest from a materials perspective, despite its violent reaction. It was also remarked upon that the oxidation potential of the nitrate ion is heavily pH dependent – being more oxidising in acidic than neutral solutions.

Table 3.1: Selected tin-IV and tin-II nitrate complexes.

Compound	Reaction scheme	Diagram	Physical Properties	Ref.
$Sn(NO_3)_4$	$SnCl_4 + N_2O_5$	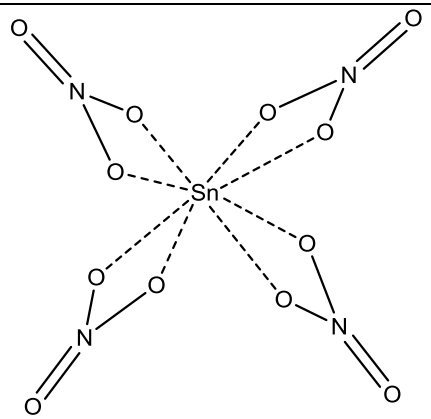	White crystalline solid, highly volatile. Extremely hygroscopic. Decomposes explosively in air and moisture.	[18]
$Me_2Sn(NO_3)_2$	$Me_4Sn + N_2O_4$	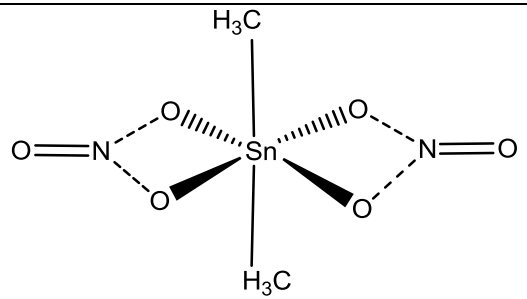	Extremely hygroscopic, explosive on heating, rapid thermal decomposition. Contains carbon.	[16]
$Sn_3(OH)_4(NO_3)_2$	$3SnO.H_2O + HNO_3$	Solid state structure unknown	Highly explosive, decomposes rapidly in air	[17]

It was decided to investigate the process described in Chapter 2, with tin(II) nitrate precursor synthesised *in situ* – scheme 3.1

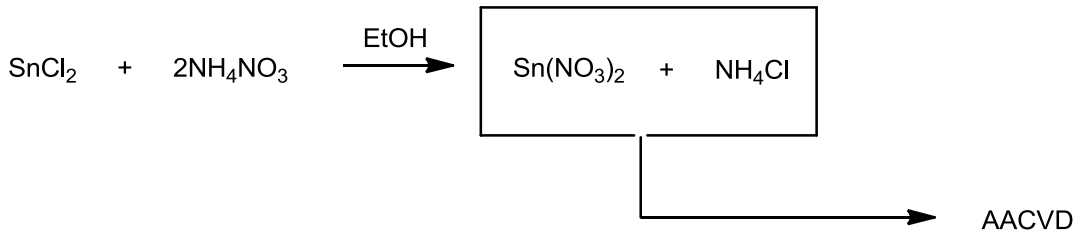

Scheme 3.1: *In situ* generation of tin (II) nitrate precursor and subsequent AACVD

3.3. Results and discussion

Table 3.2 displays the tin oxide and fluorine-doped tin oxide samples that have been deposited from a tin(II) nitrate precursor.

Table 3.2: Sample labels and deposition parameters for tin oxide and fluorine-doped tin oxide films deposited from tin(II) nitrate

Deposition #	Appearance	Precursor	Dopant	Solvent	Concentration (mol dm^{-3})	Substrate Temp. (°C)	Deposition Time (min)	Comments
DS102-300	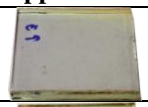	$SnCl_2.2H_2O$, NH_4NO_3	-	EtOH	0.1	300	30	Transparent, insulating
DS103-350	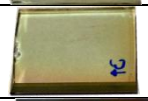	$SnCl_2.2H_2O$, NH_4NO_3	-	EtOH	0.1	350	30	Transparent, conducting
DS104-400		$SnCl_2.2H_2O$, NH_4NO_3	-	EtOH	0.1	400	30	Transparent, conducting
DS105-450		$SnCl_2.2H_2O$, NH_4NO_3	-	EtOH	0.1	450	30	Transparent, conducting
DS106-500		$SnCl_2.2H_2O$, NH_4NO_3	-	EtOH	0.1	500	30	Transparent, conducting
DS180-350		$SnCl_2.2H_2O$, NH_4NO_3	NH_4F	EtOH	0.1	350	30	Transparent, slightly conductive
DS180-400		$SnCl.2H_2O$ $_2$, NH_4NO_3	NH_4F	EtOH	0.1	400	30	Transparent, highly conductive
DS180-450		$SnCl_2.2H_2O$, NH_4NO_3	NH_4F	EtOH	0.1	450	30	Transparent, highly conductive
DS180-500		$SnCl_2.2H_2O$, NH_4NO_3	NH_4F	EtOH	0.1	500	30	Transparent, highly conductive
DS263-500		$SnCl_2.2H_2O$, NH_4NO_3	NH_4F	H_2O	0.1	500	30	Transparent, highly conductive

3.4. AACVD of tin oxide and FTO from $Sn(NO_3)_2$

3.4.1. Deposition conditions for AACVD of $Sn(NO_3)_2$ precursor

Table 3.3: Experimental conditions used for tin oxide depositions using *in situ* generated tin(II) nitrate precursor

Variable	Value
Substrate temperature	300-500 ^{o}C
Precursor concentration	0.1 M
NH_4F dopant concentration	0 – 0.1 M
Bulk flow rate (aerosol)	20 ml/hr
Pressure	137.9 kpa
Deposition time	30 minutes

3.4.2. Film analysis

3.4.2.1. Morphological analysis

Tin oxide films appeared transparent to the naked eye with visible interference fringes. Wherever possible, samples were cut and analysed such that the same distance into the reactor could be compared between substrates. A typical tin oxide micrograph is shown in figure 3.5. Micrographs of tin oxide deposited between 300 and 500 °C and a fluorine-doped tin oxide sample grown at 500°C are shown in figure 3.6.

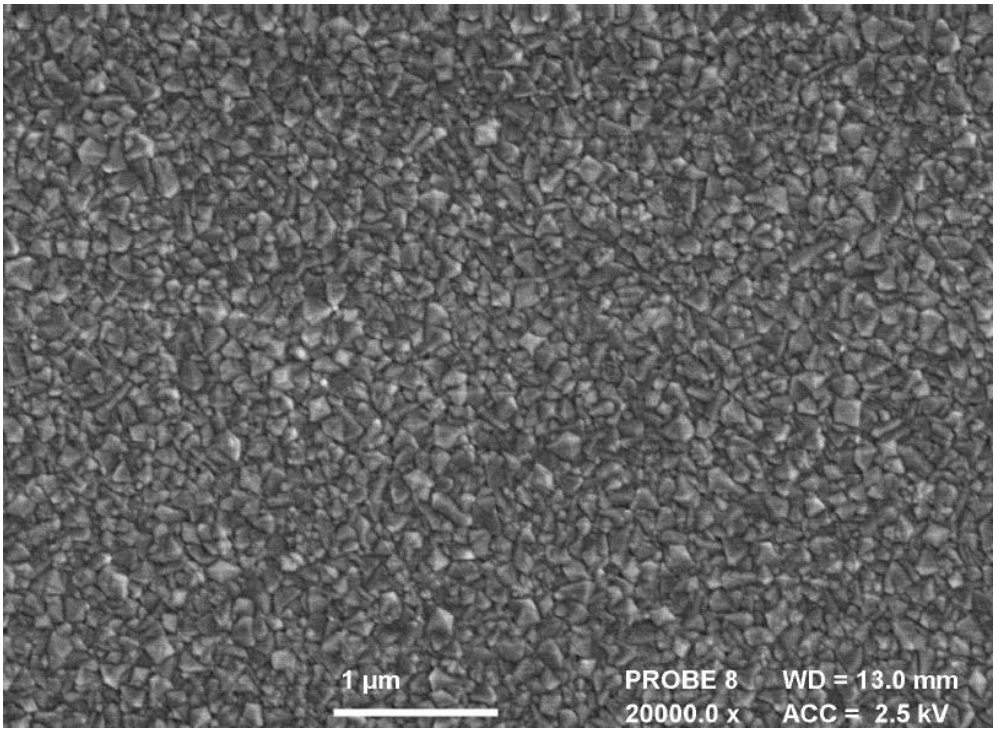

Figure 3.5: SEM micrograph of tin oxide film deposited onto float glass at 400 °C at 20,000x magnification

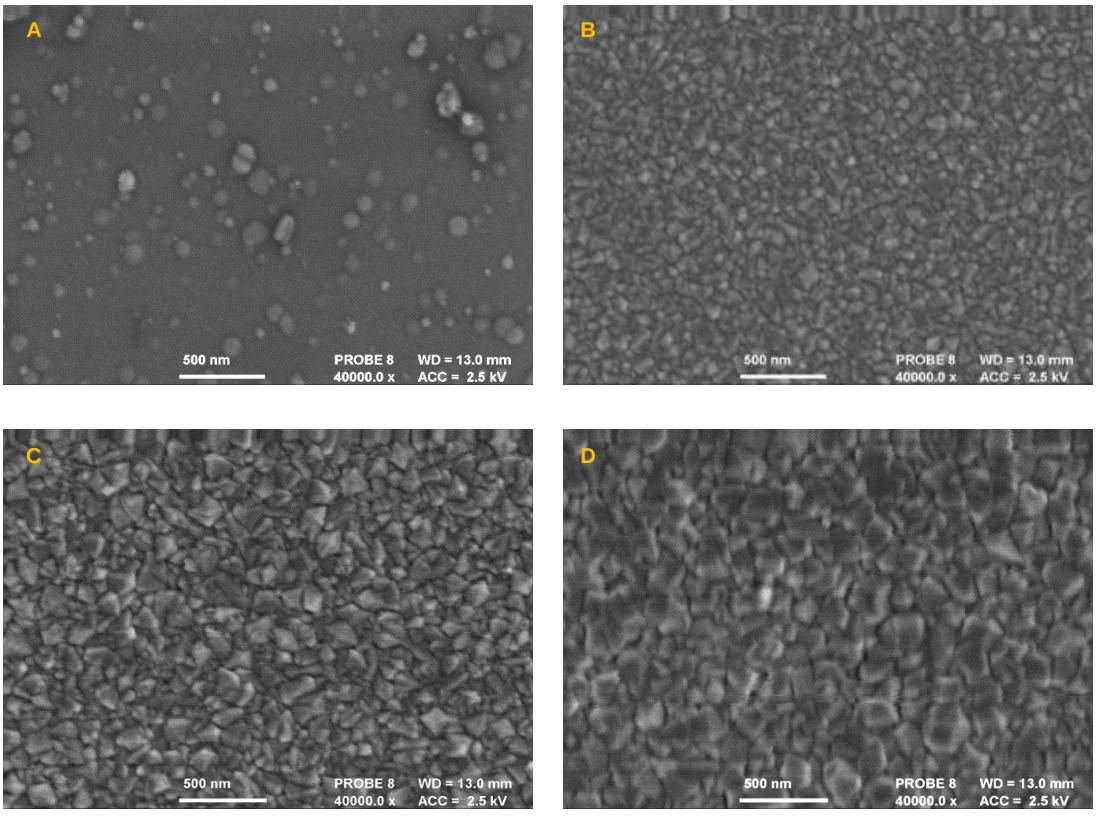

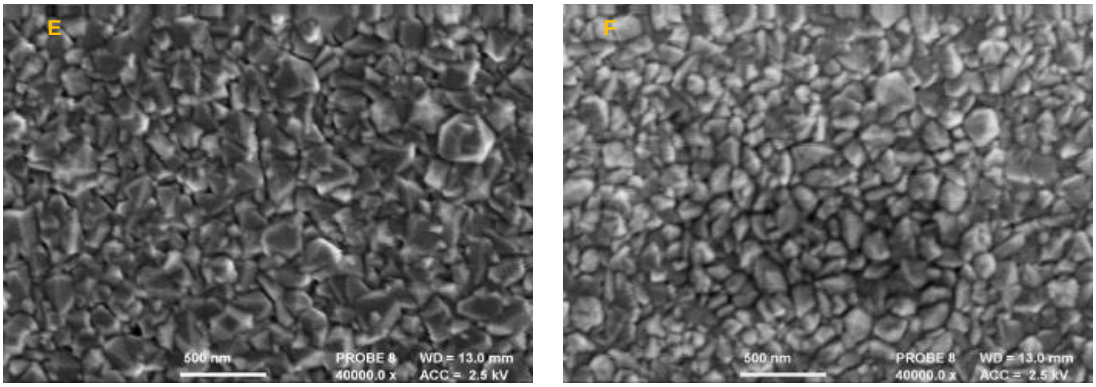

Figure 3.6: SEM micrographs at 40,000 x magnification of undoped tin oxide films deposited at 300, 350, 400, 450, 500°C **(A – E)** and a fluorine doped tin oxide film deposited at 500°C **(F)**.

SEM analysis clearly shows complete and uniform coverage of the growing film to the substrate with the exception of (A). The lowest deposition temperature (300°C) resulted in a surface sparsely covered by rounded particles of varying size, the largest around 100 nm in diameter. This suggests a slower growth rate, and insufficient energy for crystalline material to form. At higher temperatures, all subsequent films take on more angular shape, with many square bipyramidal crystallites visible. The morphology compares well with literature micrographs of fluorine-doped tin oxide.[4]

Films deposited at 350°C had a mean crystallite diameter of 84nm. Unsurprisingly, above this temperature these were significantly larger at 148, 150 and 157nm for 400, 450 and 500°C respectively due to increased growth rate and annealing effects. While the fluorine-doped tin oxide film deposited at 500 °C exhibited a smaller mean particle size (129nm) than its un-doped counterpart, a correlation between increasing crystallite size and temperature was also observed.

3.4.2.2 Compositional/microstructural analysis

EDS analysis was obtained for all samples on glass and (where possible) silicon. The use of silicon substrates is desired to eliminate unwanted signals from the glass that make quantitative measurements difficult. Pilkington float glass contains significant proportions of Ca, Na, K, Mg, Al, and Fe which can all contribute to noise especially when looking for lighter elements such as fluorine. Analysis revealed that films grown on silicon wafers between 300 and 500 °C

contained tin and oxygen as well as silicon which is associated with the substrate. A typical example of an undoped SnO_2 film is shown in figure 3.7.

Full quantitative results are shown in table 3.4. In all samples, the measured atomic weight % Sn : O ratio was consistently 1 : 2 as expected for SnO_2 films. Overall concentrations of tin and oxygen both increased with substrate temperature indicating a faster growth rate and therefore thicker film. Despite a low accelerating voltage (15 kV) the relatively thin nature of the film results in significant amounts of substrate being detected. This is mainly observed in the thinnest film grown at 300°C where high levels of silicon are detected. For the fluorine-doped samples grown between 350 and 500°C, fluorine was detected at levels between 0.7 – 1.2%, with a positive correlation between fluorine concentration and substrate temperature.

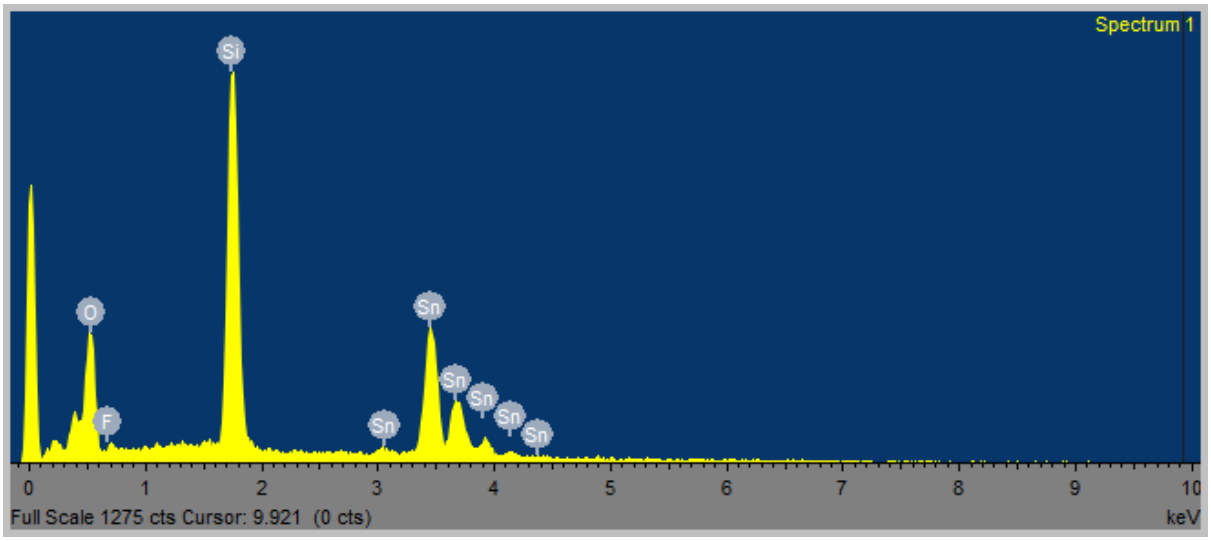

Figure 3.7: EDS spectrum of F-doped SnO_2 grown at 500°C on silicon wafer

Table 3.4: Elemental analysis for tin oxide and fluorine-doped tin oxide films deposited from tin(II) nitrate determined by EDS

	At. %			
Sample [Temp, °C]	**Sn**	**O**	**Si**	**F**
SnO_2 [300]	25.3	54.7	20.0	-
SnO_2 [350]	28.1	60.2	11.7	-
SnO_2 [400]	28.8	61.7	9.5	-
SnO_2 [450]	30.0	64.7	5.3	-
SnO_2 [500]	29.9	65.1	5.0	-
SnO_2:F [350]	18.3	39.4	41.6	0.7
SnO_2:F [400]	29.8	63.6	5.6	1.0
SnO_2:F [450]	28.5	61.5	8.9	1.1
SnO_2:F [500]	30.0	64.4	4.4	1.2

Films grown on glass substrates were analysed by XRD to ascertain their crystallographic orientation. Samples deposited between 300°C and 500°C for the undoped SnO_2 films are detailed in figure 3.8. The film grown at 300°C was amorphous while all films grown above this temperature could be indexed to crystalline tetragonal SnO_2 – cassiterite. Films show increasing crystallinity with increasing temperature, with the film grown at 500 °C exhibiting the most intense diffraction pattern. Of interest is the seemingly preferred orientation in the (2,0,0) plane for the sample grown at 400°C. This may indicate an effect of the substrate to seed a particular orientation before further more normal deposition occurs on top. Above this temperature, this behaviour disappears and the pattern becomes identical to literature patterns.

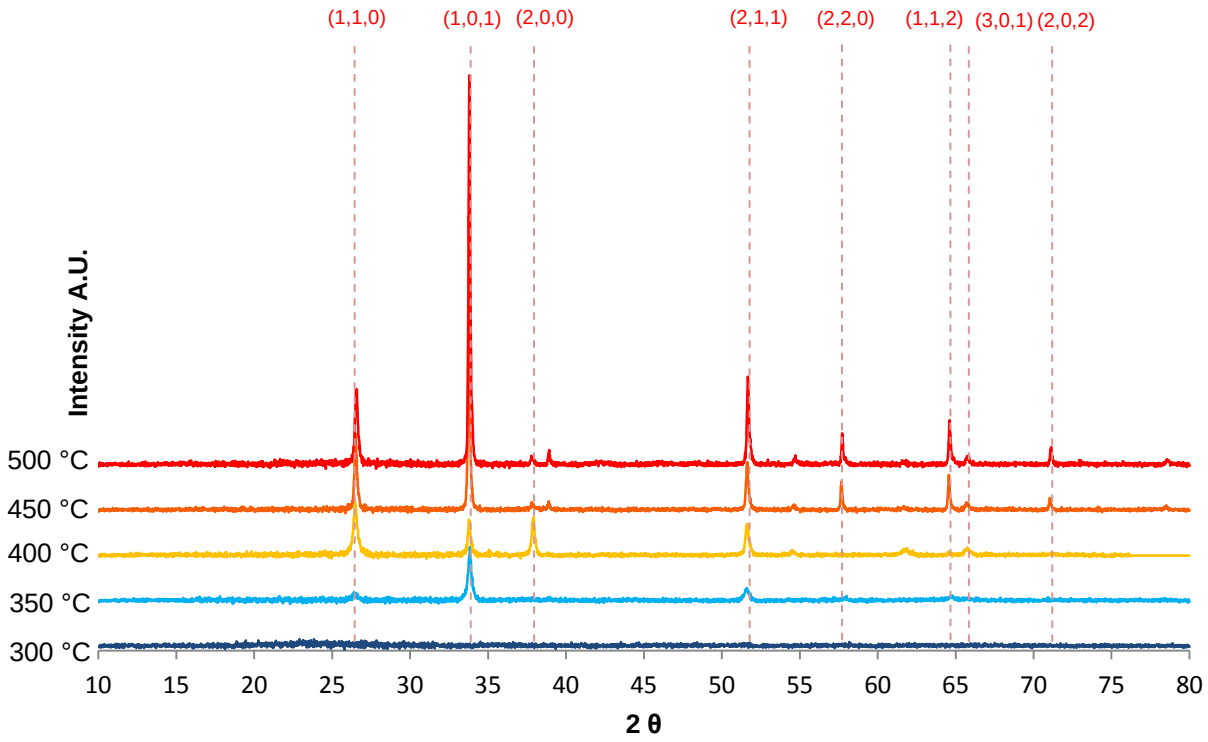

Figure 3.8: An XRD overlay of tin oxide films grown on glass substrates

The diffraction patterns of F-doped samples deposited at temperatures between 350°C and 500°C are shown in figure 3.9. Most obviously, the fluorine-doped tin oxide films are significantly less crystalline than their un-doped counterparts. Another notable feature is the apparent lack of crystallinity of the sample grown at 350 °C. This is in contrast to the undoped sample which did show some crystallinity at the same growth temperature. Whilst SEM and EDS analysis confirm the presence of tin and oxygen-containing particles completely covering the surface at this temperature, the resulting film is either amorphous or too thin to yield a suitable diffraction pattern. Samples deposited at 400, 450 and 500°C, however, can be indexed to tetragonal SnO_2, cassiterite. The (1,0,1) and (2,1,1) peaks become visible at 400°C with the (1,1,0), (2,0,0) and (3,0,1) becoming more pronounced at higher temperatures. The most intense pattern is observed for the tin oxide deposited at 500°C. It is notable that the (1,0,1) and (2,1,1) reflections for samples 400°C and 450°C are more intense than the most crystalline film, perhaps indicating some preferred directional growth along the (1,0,1) plane at lower temperatures.

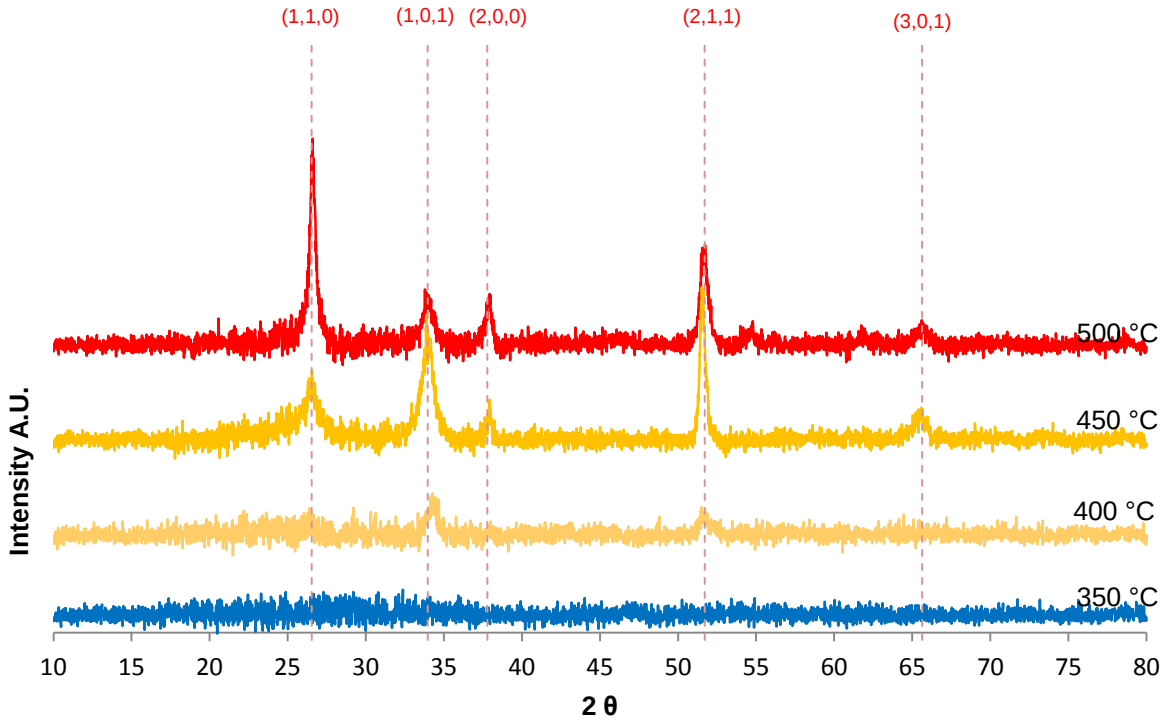

Figure 3.9: An XRD overlay of fluorine-doped tin oxide films grown on glass

The Scherrer equation can be used for further information about the size of the crystallites as follows:

$$T = \frac{K\,\lambda}{\beta\,Cos\,\theta}$$

Where T is the mean crystalline size;

K is the shape factor, 0.9 for unknown shape;

λ is the wavelength of incident radiation, in this case 1.5418 Å

β is the line broadening in radians at full width and half maximum height (FWHM)

θ is the Bragg angle

Crystallite sizes were estimated using the (1,0,1) and (1,1,0) peaks and are listed in table 3.5. Predicted crystallite sizes were smaller than those observed by SEM for all un-doped samples by around 50 nm. For the F-doped samples, predicted crystallite sizes were much smaller than the observed value.

Table 3.5: Crystallite size estimated from the Scherrer formula.

Sample	Estimated crystallite size (nm)
DS102	55.03
DS103	60.66
DS104	64.98
DS105	68.23
DS106	82.11
DS180-350	20.98
DS180-400	23.29
DS180-450	26.12
DS180-500	28.65

Raman spectroscopy was used for further characterisation. Cassiterite is a well studied material and as such data is widely available from a variety of sources.[19] Figure 3.10 shows the Raman spectrum of tin oxide grown at 500 °C under 532 nm (green) laser illumination. Glass notoriously exhibits strong fluorescence in Raman spectra, however the strongest signal associated with the A_{1g} vibrational mode is visible at 632 cm^{-1}.

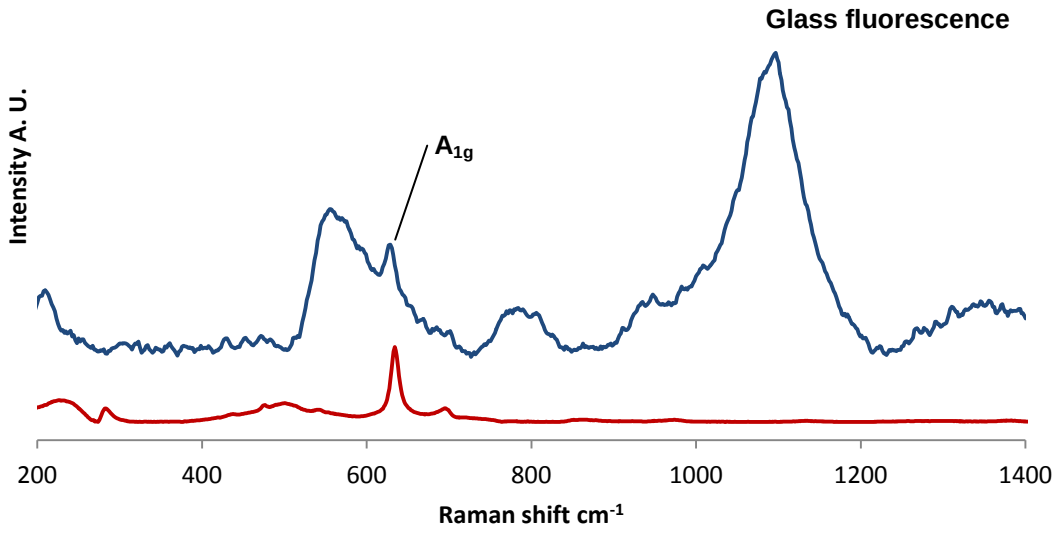

Figure 3.10: Raman spectrum of un-doped tin oxide thin film grown at 500 °C on glass substrate (blue) and literature spectrum of cassiterite[19] SnO_2 (red)

3.4.2.3 Optical properties

A typical UV/Vis sprectrum of a tin oxide thin film on glass is shown in figure 3.11. Films were transparent and colourless to the naked eye. Transmitted light varied between 77 – 89% in the visible region.

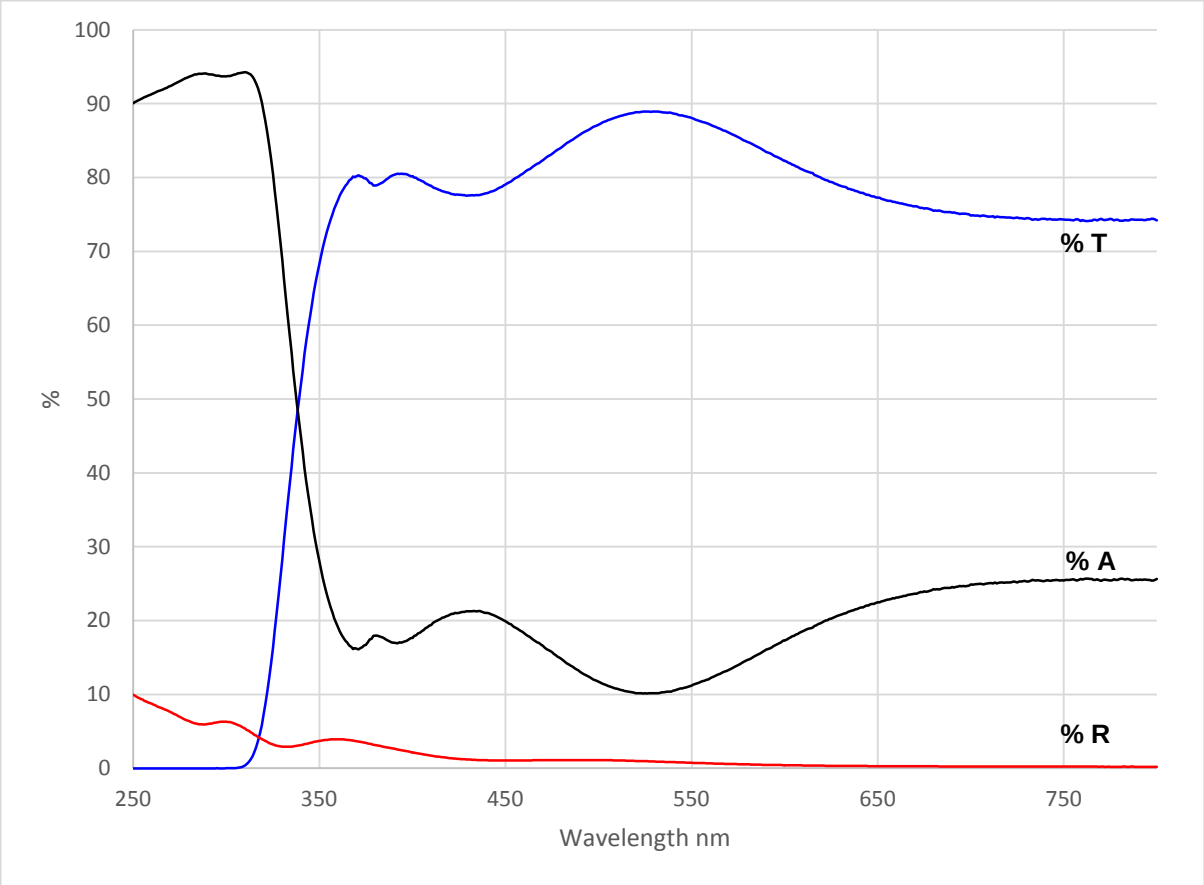

Figure 3.11: UV-vis spectrum of fluorine-doped tin oxide thin film grown on glass at 500 °C.

NB: A broad spectrum scan is required to acquire data on the IR reflectance of these films. A scan range of 200 – 2400 nm is recommended (see figure 3.2).

3.4.2.4 Contact angle measurements

The contact angles of a droplet of distilled water on deposited tin oxide films were determine to assess any unusual surface effects such as those of hydrophobic copper particles discussed in chapter 2. Contact angles are given in table 3.6.

Table 3.6: Contact angle data for tin oxide and FTO thin films (rounded to the nearest degree)

Sample-Temp (°C)	**Contact angle (°)**
SnO_2 -300	64
SnO_2 -350	73
SnO_2 -400	71
SnO_2 -450	68
SnO_2 -500	62
FTO -350	77
FTO -400	69
FTO -450	79
FTO -500	57

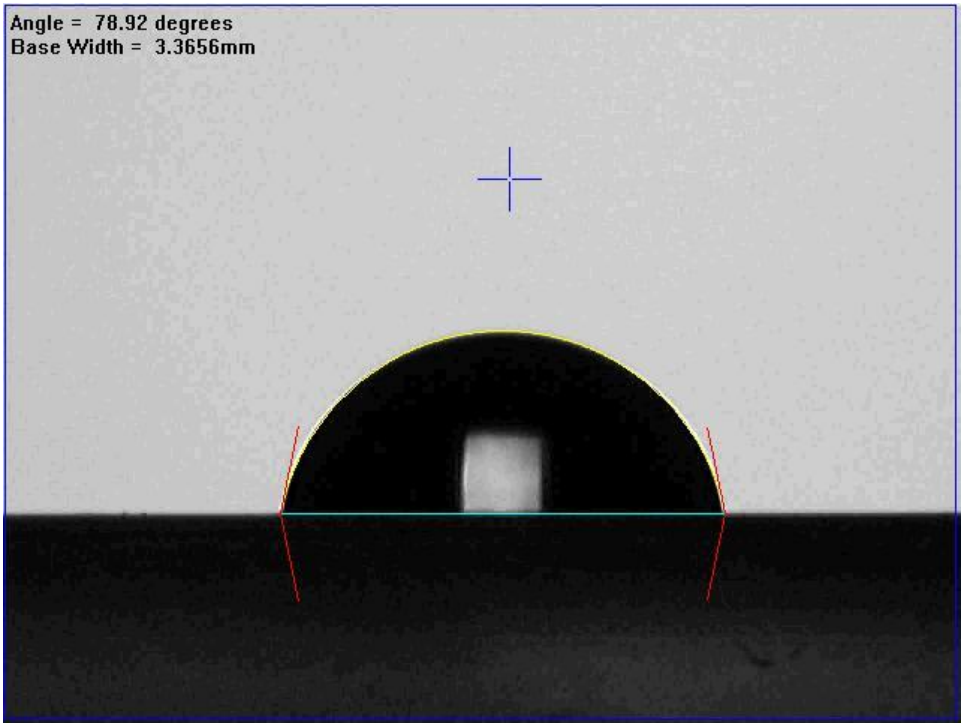

Figure 3.12: Contact angle of water on fluorine-doped tin oxide film deposited at 450 °C

3.4.2.5 Conductivity measurements

Table 3.7 shows the 4-point probe measurements for the tin oxide films and includes the commercially available TEC-15 FTO. Un-doped tin oxide films showed high sheet resistances, with the deposition at 300 °C unable to register a measurement. The lowest sheet resistance of any undoped tin oxide film was 312 Ω / SQ for a deposition temperature of 400 °C. Upon doping with fluorine, sheet resistance becomes notably lower, as illustrated in figure 3.13. In the case of fluorine-doped tin oxide films deposited at 400, 450 and 500 °C, the same order of magnitude for sheet resistance as commercially produced TEC-15 was achieved.

Table 3.7: 4-point probe measurements for undoped and fluorine-doped tin oxide thin films

Sample	Material	Deposition Temperature °C	Avg. sheet resistance Ω/SQ
DS102-300	SnO_2	300	-
DS103-350	SnO_2	350	517.69
DS104-400	SnO_2	400	312.66
DS105-450	SnO_2	450	409.99
DS106-500	SnO_2	500	723.91
DS180-350	SnO_2:F	350	106.04
DS180-400	SnO_2:F	400	41.06
DS180-450	SnO_2:F	450	46.79
DS180-500	SnO_2:F	500	40.84
TEC-15	SnO_2:F		15.13

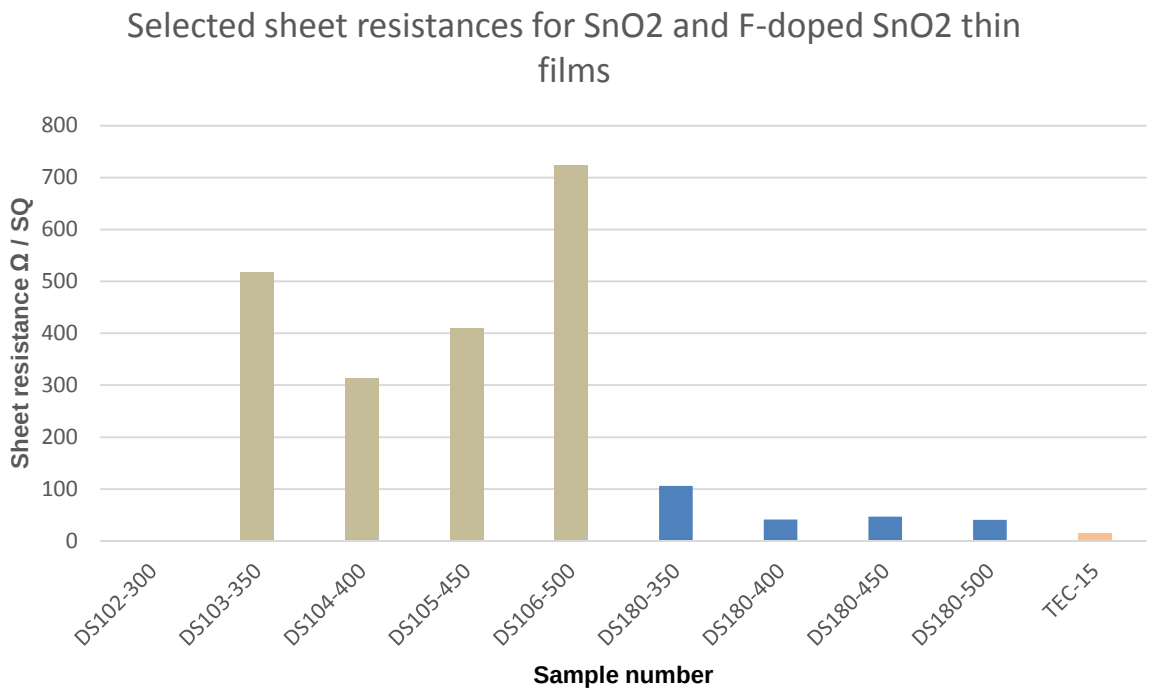

Figure 3.13: Bar chart displaying comparison of sheet resistances of un-doped and fluorine-doped tin oxide thin films grown using a tin (II) nitrate aerosol process and commercially available TEC-15 FTO

3.5. AACVD of FTO with water solvent

Work is continuing in the group to optimise the AACVD of FTO from tin (II) nitrate in water solvent. Recently, work has become the subject of a joint patent titled “Metal Oxide Deposition” application between Pilkington NSG and the University of Bath.[20]

Films have been deposited via the same method as described in section 3.4, with the exception of water in place of ethanol as the aerosol solvent.

To demonstrate the ability of the tin(II) nitrate precursor to deposit via AACVD in a water solvent, a number of depositions were made. Sample DS236 is an example of a fluorine-doped tin oxide coating on glass deposited at 500°C and is analysed below.

3.4.1 Film analysis

3.4.1.1. Morphological analysis

The sample deposited from tin(II) nitrate in water solvent was analysed by SEM at 10,000x and 50,000x magnifications. Figure 3.14-A (80° tilt, IM – 10,000x) showed a uniform coating that completely covered the glass surface. There were some individual particulates at the surface of the specimen that appeared to be of the same material as the coating. A higher magnification image of this region, shown in figure 3.14-B (50,000x) showed that the features were incorporated into the coating surface and were the same coating material. The coating surface consisted of a number of pyramidal peaks. Figure 3.14-C (80° tilt, IM – 50,000x) at the fracture edge, showed the amorphous SiCO base layer and the crystalline growth of the top layer. The coating was arranged in vertical pillars ~40 nm wide. Measurements taken from Figure 3.14-D (90 tilt, IM – 50,000x) showed that the crystalline top layer was typically 408 – 443nm thick with high points up to 502nm.

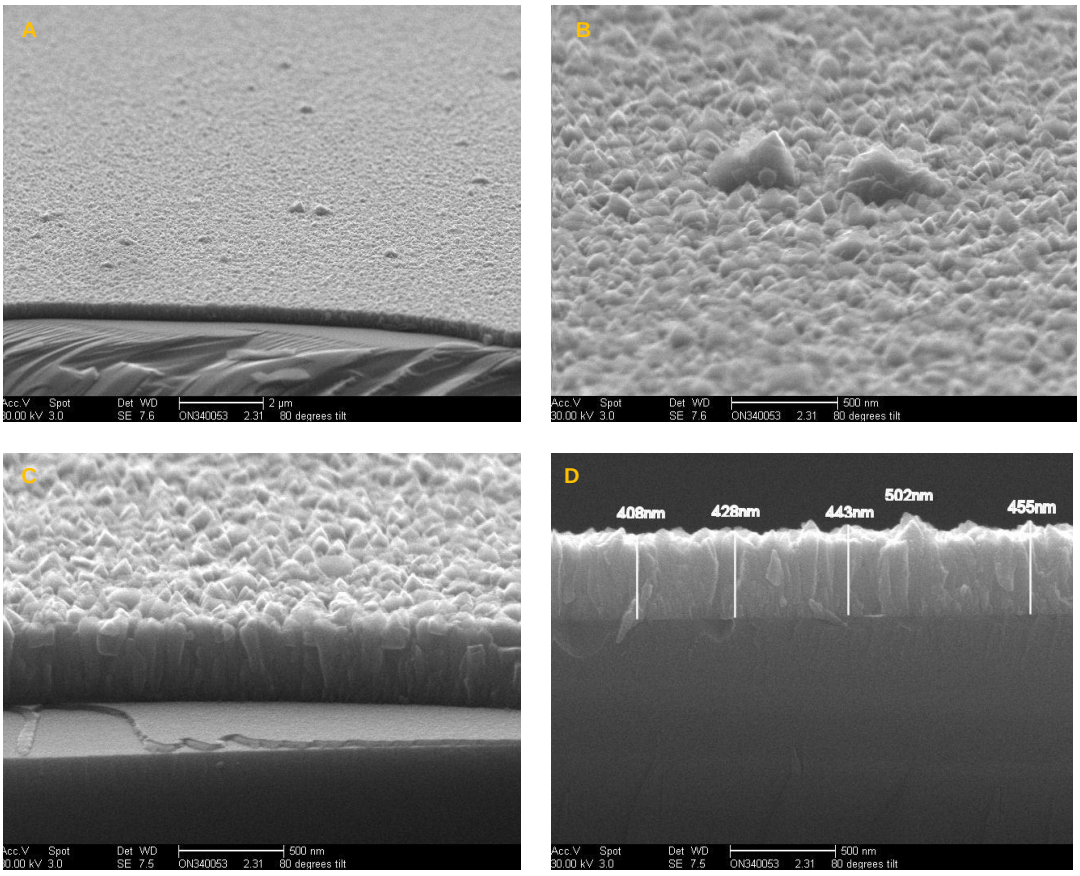

Figure 3.14: SEM micrographs of sample DS236, fluorine-doepd tin oxide on glass substrate at 10,000x magnification (A), and 50,000x magnification (B-D) at 80° tilt (A-C) and 90° tilt (D).

3.4.1.2 Compositional/microstructureal analysis

Sample DS263 was analysed by EDS to obtain elemental analysis. All elements associated with both the coating and substrate were observed, as well as some carbon and nitrogen contamination. Fluorine was detected at ~1%, however since this was around the limits of detection, quantitiative analysis could not be achieved.

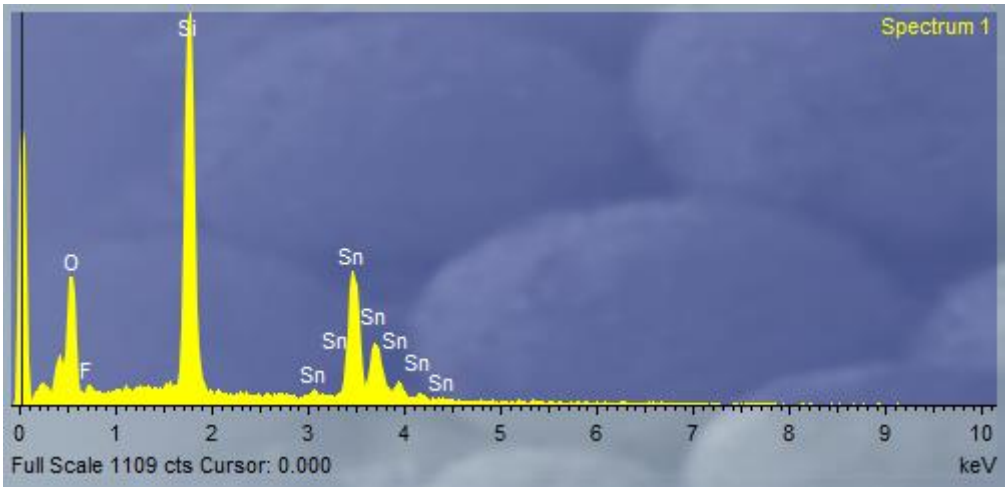

Figure 3.15: EDS spectrum of sample DS236

A depth-profile of Sample 236 was measured by XPS. Fluorine was detected in the tin oxide coating at a concentration of 1.3%. The depth profile is shown in figure 3.16

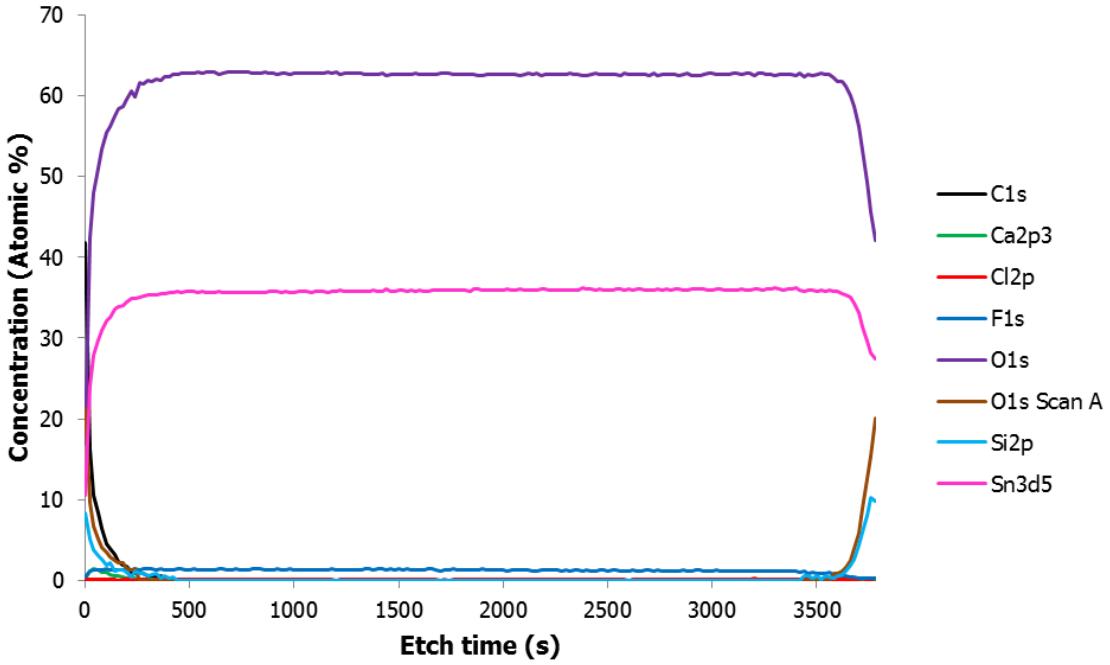

Figure 3.16: Depth profile for sample 236, FTO coating on glass substrate as determined by XPS.

3.6. Conclusions

Previous studies have described a variety of tin(IV) complexes available for use as single- or dual-source precursors to tin oxide type materials. Many of these are alkyl- or halogenated tin(IV) species which are toxic and/or include carbon in the resulting films. Furthermore, their chemistry is such that they often require careful handling under inert atmosphere conditions which makes the process hazardous, expensive and time consuming as well as providing complications for scale-up into industrial applications.

The work detailed in this chapter has provided a new process to allow the growth of tin(IV) oxide and fluorine-doped tin oxide thin films, by the *in-situ* generation of tin(II) nitrate solution in ethanol and subsequent AACVD. It has shown to be possible to use this technique to produce uniform, crystalline and conductive films of FTO material which may be of use to industries such as Pilkington NSG.

What is remarkable, is that any deposition of tin(IV) oxide occurred at all. The literature describes the necessity of a fuel e.g. acetylacetonate or urea in the precursor solution to supply the energy to drive the reaction to completion. Clearly, tin(II) has been oxidised to tin(IV) but seemingly in the absence of any such fuel. Some attempt has been made to explain the process below:

Metal nitrate solutions can deposit the corresponding metal oxide if the reduction potential

$$M^{n+} + ne \rightarrow M$$

is less positive than the standard reduction potential for nitrate reduction. In aqueous solution for a 3 electron reduction in water this is

$$NO_3^- + 4H^+ + 3e \rightarrow NO + 2H_2O \qquad +0.96V$$

Sn^{2+} in the presence of excess nitrate ion will always be oxidised to Sn^{4+} (providing SnO_2); i.e. in acidic solution such as AACVD of tin oxide

$$Sn^{4+} + 2e \rightarrow Sn^{2+} \qquad +0.15V$$

In this case, $E_{cell} = E_{red} – E_{ox} = +0.96 – (+0.15) = + 0.81V$ i.e. as $\Delta G = -nFE$ this process is exothermic and spontaneous.

It should be noted that this does not take into account deposition conditions such as temperature and solvent effects which may alter these values significantly.

XRD and Raman spectroscopy confirm the crystal structure of the materials deposited from tin(II) nitrate precursor to be cassiterite SnO_2 oriented in the (1,0,1) and the (1,1,0) directions. As expected, deposition temperature has an effect on the crystallinity of the films, becoming more crystalline at increasing temperatures. It would be of use to continue further studies at increased temperature

The concentration of F in the films has been found to be around 1% - whether deposited from ethanol or water solvent. Commercially available TEC-15 has around 5% F concentration. In order to achieve this figure, the concentration of NH_4F must be increased.

Commercially available TEC-15 glass is part of a stack of FTO with a reflection suppressing layer and has an optimised visible light transmission between 82 – 84 %. Whilst samples grown using the tin(II) nitrate method were also deposited onto a SiCO layer, there was no such optimisation for maximum transmission so comparison to TEC-15 can only be loose. Samples exhibited transmission over a broader range, 77 – 89 % indicating some refinement in the deposition process is necessary to make this value more consistently above 80% T.

3.7. Further work

EDS analysis has been conducted on SnO_2 and F-doped SnO_2 films both at the university of Bath which confirms a Sn : O ratio of 1 : 2. Fluorine was detected, however quantitative measurement was difficult due to the comparatively low detector sensitivity to fluorine over tin. The XPS data carried out by Pilkington is in good agreement with this Sn : O ratio. Furthermore, this confirms beyond doubt the presence of F in samples where F-doping was desired. In addition, F is present at a constant level throughout the depth of the entire film, which implies uniform film growth for the duration of deposition. A further benefit to using water

as a solvent, is the extreme solubility of NH_4F, the fluorine source. It should be noted, that the metal : dopant stoichiometry in the precursor solution is not reflected in the film itself i.e. a Sn : F ratio of 1 : 1 relates more to a F doping of ~1 mol %. Further study into the effects of precursor concentration and if “aging” of the precursor solution influences film growth is ongoing. Upon addition of NH_4F, a small amount of white precipitate is formed, possibly some SnF_2. In our experiments, this necessitates the addition of a few drops of nitric acid, HNO_3 to fully dissolve the precursor. This may be a small, but important detail in the experimental details.

Also of interest is the doping of tin oxide with other metals such as antimony which are known to yield blue coatings.[21] This work has developed into the process patent B15003 in conjugation with Pilkington NSG.[20]

3.8. References for chapter 3

1. Ellmer, K., *Journal of Physics D: Applied Physics* **2001,** *34*, 3097.
2. G, W. R. W., *Crystal Structures* **1963,** *1*.
3. NSG, P., Global Glass Handbook 2012. In *Architectural Products*, NSG, P., Ed. Pilkington: http://www.pilkington.com/products/bp/downloads/byproduct/specialapplications/default.htm, 2012; pp 208 - 211.
4. Wang, J. T.; Shi, X. L.; Liu, W. W.; Zhong, X. H.; Wang, J. N.; Pyrah, L.; Sanderson, K. D.; Ramsey, P. M.; Hirata, M.; Tsuri, K., *Sci. Rep.* **2014,** *4*.
5. Kojima, M.; Kato, H.; Imai, A.; Yoshida, A., *Journal of Applied Physics* **1988,** *64*, 1902-1905.
6. Bélanger, D.; Dodelet, J. P.; Lombos, B. A.; Dickson, J. I., *Journal of The Electrochemical Society* **1985,** *132*, 1398-1405.
7. Maruyama, T.; Tabata, K., *Journal of Applied Physics* **1990,** *68*, 4282-4285.
8. Borman, C. G.; Gordon, R. G., *Journal of The Electrochemical Society* **1989,** *136*, 3820-3828.
9. Ghandhi, S. K.; Siviy, R.; Borrego, J. M., *Applied Physics Letters* **1979,** *34*, 833-835.
10. Fang, T.-H.; Chang, W.-J., *Applied Surface Science* **2003,** *220*, 175-180.
11. Fang, T.-H.; Chang, W.-J., *Applied Surface Science* **2005,** *252*, 1863-1869.
12. Ma, H. L.; Zhang, D. H.; Win, S. Z.; Li, S. Y.; Chen, Y. P., *Solar Energy Materials and Solar Cells* **1996,** *40*, 371-380.
13. Stanley, J. E.; Swain, A. C.; Molloy, K. C.; Rankin, D. W. H.; Robertson, H. E.; Johnston, B. F., *Applied Organometallic Chemistry* **2005,** *19*, 644-657.
14. Noor, N.; Parkin, I. P., *Journal of Materials Chemistry C* **2013,** *1*, 984-996.
15. Kim, M. G.; Kanatzidis, M. G.; Facchetti, A.; Marks, T. J., *Nat. Mater.* **2011,** *10*, 382-388.
16. Hilton, J.; Nunn, E. K.; Wallwork, S. C., *Journal of the Chemical Society, Dalton Transactions* **1973**, 173-175.
17. Donaldson, J. D.; Moser, W., *Journal of the Chemical Society (Resumed)* **1961**, 1996-2000.

18. Schmeisser, M., *Angew. Chem.* **1955,** *67*, 493.

19. Downs, R. T., Cassiterite. In www.rruff.info, 2006.

20. Stanton, D.; Catherall, A., B15003, *Metal Oxide Deposition*.(pending acceptance) 31st May 2015.

21. Haireche, S.; Boumeddiene, A.; Guittoum, A.; El Hdiy, A.; Boufelfel, A., *Materials Chemistry and Physics* **2013,** *139*, 871-876.

Chapter 4:

Spinels and ceria

4.1. Introduction

This chapter details the combustion synthesis of a number of metal oxide materials from simple metal nitrate precursors. It should be made clear that a true combustion requires the burning of the precursor which is not in fact happening in the AACVD systems described before. With the facile deposition of metals and simple metal oxides including Cu, Ni and Sn detailed in chapters 1 and 2, the natural progression was to explore more complicated materials. A particular emphasis was put on materials that could be useful as functional coatings on glass, such as coloured coatings or catalysts.

4.1.1. Cobalt aluminate

$CoAl_2O_4$ is the chemical formula for the well characterised “cobalt-blue” pigment. As has been discussed in chapter 1, the pigment has found historical use as a colourant in ceramic glazes, paints and glass. Furthermore, the material also finds applications as a component in gas sensors or catalysis owing to its high thermal stability and hydrophobicity.[1]

$CoAl_2O_4$ is a binary metal oxide with a normal spinel-type structure, $A^{2+}B^{3+}{}_2O_4$, and is typically synthesised by the reaction of CoO and Al_2O_3 at temperatures in excess of 1000°C for many hours.[2] Sub-micron $CoAl_2O_4$ particles have been synthesised by sol-gel methods through reaction of $CoCl_2.6H_2O$ and $AlCl_3.6H_2O$,[3] or $CoOH(OOCCH_3)$ and $AlOH(OOCCH_3)$,[4] with fabrication temperatures seen to reduce around 600°C. More recently $CoAl_2O_4$ nanoparticles have been synthesised at temperatures as low as 200°C by the reaction of $Co(OOCCH_3)_2$ and $Al(O^iPr)_3$ in benzyl alcohol.[5] Selected methods are shown in scheme 4.1.

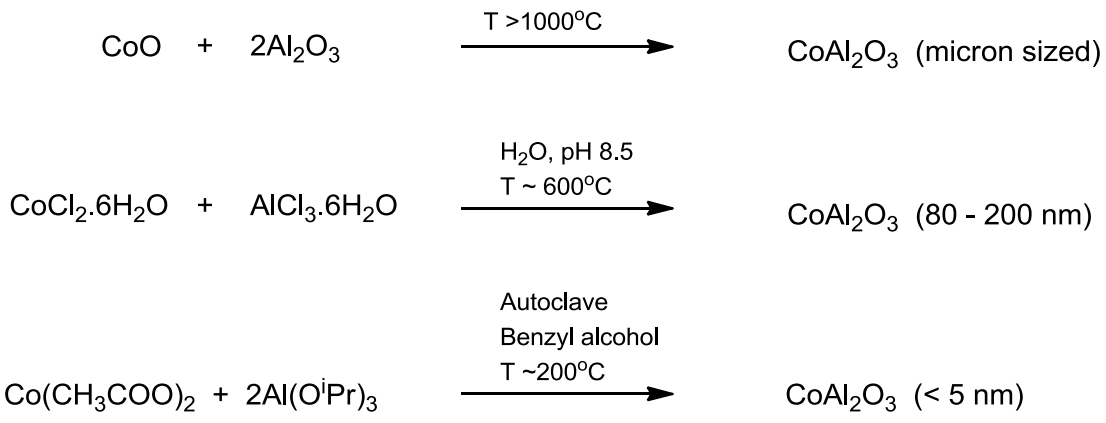

Scheme 4.1: Selected synthetic methods to $CoAl_2O_4$.

The majority of literature regarding $CoAl_2O_4$ deals either with bulk powder synthesis or colloidal suspensions of nanoparticles with relatively little relevant to thin film generation. What does exist focuses on spin coating of either solutions of preformed nanoparticles, or a sol gel with subsequent high heat treatment (>800°C).[6] Clearly a thin layer of the blue pigment could be much more advantageous if applicable by CVD methods.

The only reported CVD routes to $CoAl_2O_4$ thin films involve the dual-source MOCVD of $CoCp_2$ and $[AlMe_2(O^iPr)]$,[7] and single-source MOCVD of $Co[Al(O^iC_3H_7)_4]_2$.[8] The former method was found to deposit individual CoO and Al_2O_3 phases and require heat treatment at 1200°C to affect a blue colouration – similar to traditional manufacture, scheme 4.2. In this chapter the use of metal-nitrate and urea systems are explored for the generation of $CoAl_2O_4$ films by AACVD.

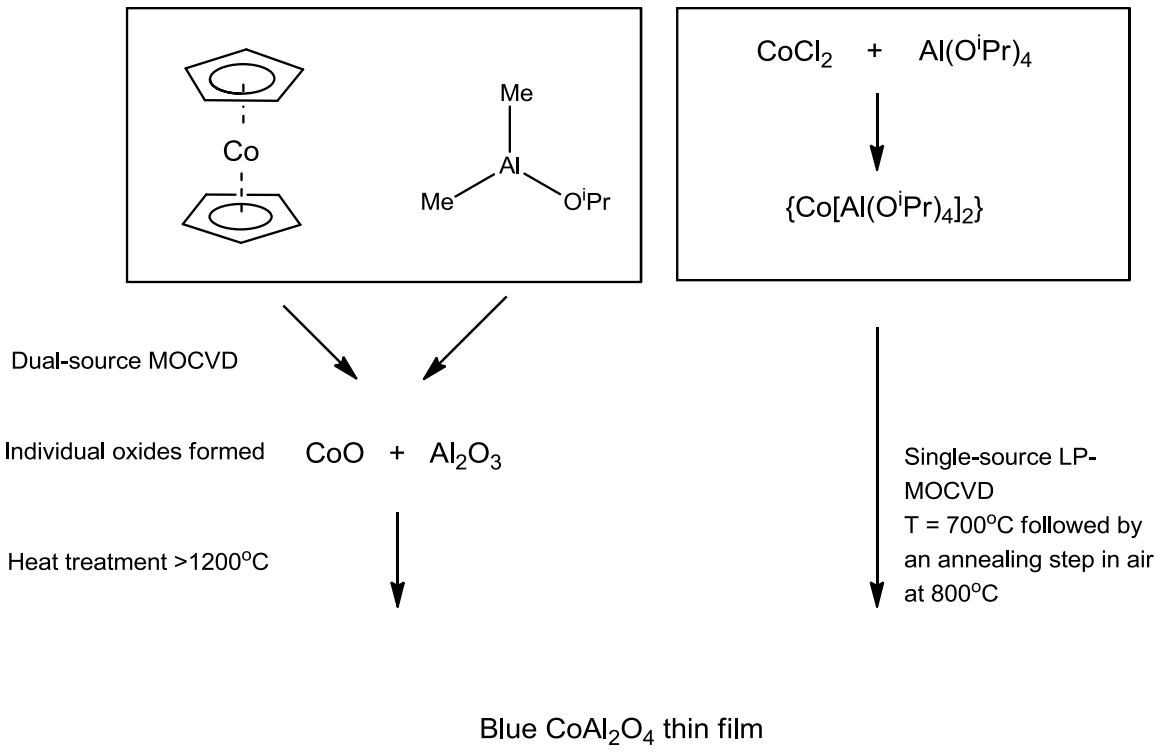

Scheme 4.2: CVD routes to $CoAl_2O_4$ thin films.[7, 8]

4.1.2. Cobalt titanate

"Cobalt titanate" may refer to ilmenite $CoTiO_3$, or spinel-type $CoTi_2O_4$, both of which are green pigments, "Shepherd green G08", and "Shepherd Sherwood Green G09" respectively.[9]

$CoTiO_3$ is one of a number or titanates that have applications in dye sensitised solar cells,[10] photocatalytic water splitting,[11] and in humidity sensors.[12] As with the synthesis of $CoAl_2O_4$, the main method for producing bulk cobalt titanate is from the analogous reaction of CoO or Co_3O_4 and TiO_2 at high temperatures (>1000°C).[13] Thin films of $CoTiO_3$ have been deposited at significantly lower temperatures by a variety of techniques including sol-gel,[14] magnetron sputtering,[15] AACVD,[16] ALD,[17] and spin-coating.[12]

4.1.3 Cobalt chromite

Cobalt chromite, $CoCr_2O_4$ is a spinel-type material belonging to the cubic F*d*3*m* space group.[18] As with other normal cobalt-spinels, Co^{2+} occupies tetrahedral A sites, while in this case, Cr^{3+} occupies all of the octahedral B sites. Co^{2+} and Cr^{3+} have electronic configurations of $3d^7$ and $3d^3$ respectively. Again, this Co^{2+} configuration leads to intense blue-green colouration and, as such, cobalt chromite has found use in pigments, along with other cobalt-containing materials.[19] In addition to pigmentation, $CoCr_2O_4$ has found use as a catalyst for gas purification, magnetic materials and even as substrates for thin-film growth.[20-23]

The majority of the literature regarding $CoCr_2O_4$ relates to nanoparticle synthesis, either for catalysis or pigmentation. The applications of thin films of $CoCr_2O_4$ are sparse in the literature, with most relating to the use of the material as a substrate for directed growth of other cubic materials.[24, 25] Because of its relatively facile solution-based synthesis, the material warrants investigation as a coloured coating by CVD techniques. High purity $CoCr_2O_4$ thin-films have previously been fabricated by pulsed-laser deposition at temperatures of 800°C.[25, 26]

Table 4.1: List of samples detailed in this chapter.

Deposition number	Appearance	Material	Substrate	Deposition method	Deposition conditions					Comments
					Precursors	Conc (mol L^{-1})	Solvent	Temp (°C)	Duration (min)	
DS150		$CoAl_2O_4$	Glass	Spin-coated	$Co(NO_3)_2.6H_2O$ + $Al(sec\text{-}OBu)_3$	0.4	2-methoxy ethanol	600	30 (anneal)	Green, transparent
DS151		$CoAl_2O_4$	Glass	AACVD	$Co(NO_3)_2.6H_2O$ + $Al(sec\text{-}OBu)_3$	0.1	2-methoxy ethanol	450	30	Initially brown/dark green. Annealed in air at 600°C for 60 min required to affect green colour
DS152	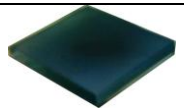	$CoAl_2O_4$	Glass	Spray-coated	$Co(NO_3)_2.6H_2O$ + $Al(NO_3)_3.9H_2O$	0.1	Toluene	150°C	5 (spray)	Preformed nanoparticles sprayed via airbrush onto heated glass substrate
DS155		$CoTiO_3$	Glass	Spin-coated	$Co(NO_3)_2.6H_2O$ + $Ti(O^iPr)_4$	0.4	EtOH	300 – 500	60 (anneal)	Brown/black, upon annealing becomes green, transparent
DS156	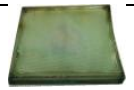	$CoCr_2O_4$	Glass	Spin-coated	$Co(NO_3)_2.6H_2O$ + $Cr(NO_3)_2.9H_2O$	0.1	EtOH	300 – 500	60 (anneal)	Brown before annealing. Green, transparent post annealing.
DS160		CeO_2	Glass	Spin-coated	$Ce(NO_3)_3.6H_2O$ + Urea	0.4	EtOH	140	-	
DS161		CeO_2	Glass	Spin-coated	$Ce(NO_3)_3.6H_2O$ + Urea	0.4	EtOH	300	60 (anneal)	
DS162		CeO_2	Glass	Spin-coated	$Ce(NO_3)_3.6H_2O$ + Urea	0.4	EtOH	400	60 (anneal)	
DS163		CeO_2	Glass	Spin-coated	$Ce(NO_3)_3.6H_2O$ + Urea	0.4	EtOH	500	60 (anneal)	

4.2. Combustion synthesis of $CoAl_2O_4$

The combustion-synthesis by a metal-nitrates method was employed in the formation of $CoAl_2O_4$. Thin films were grown, both by spin-coating and AACVD, and nanoparticles were synthesised by a modified literature method, changing Co and Al precursors to $Co(NO_3)_2.6H_2O$ and $Al(NO_3)_3.9H_2O$ respectively.[5] The spin-coated film, and film grown by AACVD (DS150 and DS151) were both dark brown/green. Upon annealing at 600°C in air, the films turned a green colour. In contrast, the preformed nanoparticles (DS152) were intensely blue in colour.

For the spin-coated films, a 0.4 M (Co conc.) precursor solution of $Co(NO_3)_2.6H_2O$ and Al(*sec*-OBu)$_3$ in 2-methoxyethanol was used, with a Co:Al ratio of 0.5. A similar solution was used for AACVD but diluted to 0.1 M. For the nanoparticle synthesis, $Co(NO_3)_2.6H_2O$ and $Al(NO_3)_3.9H_2O$ were used in a ratio of 0.3 : 1 in benzyl alcohol.

4.2.1. Microstructural/compositional analysis

Due to significant warping of the glass during annealing of DS150, an XRD pattern could not be achieved. A pattern was achieved for DS151 – a thin, green film deposited by AACVD. Although the pattern was of very low intensity, it could tentatively be indexed to crystalline $CoAl_2O_4$, figure 4.1.

Flat-plate XRD indicated DS152, (sprayed on nanoparticles) was amorphous, even on a long scan. TEM results (figure 4.5) indicated there was crystallinity within the sample, but most likely with particles that were too small to yield a conventional pXRD pattern.

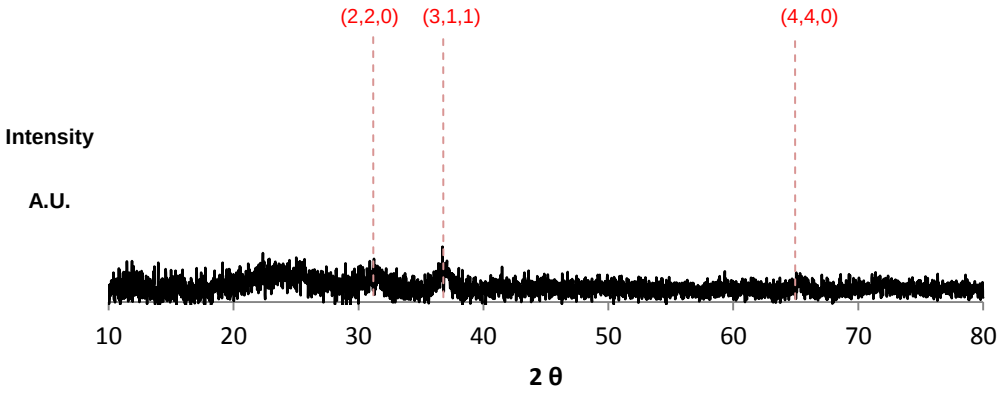

Figure 4.1: XRD pattern of DS151, $CoAl_2O_4$ thin film deposited by AACVD.

For samples DS150 and DS151 all elements present with film and glass substrate were detected. For the spin-coated film (DS150) the Co : Al ratio was 0.8, far higher than the expected value of 0.5. The film grown by AACVD showed a Co : Al ratio of 0.64. No carbon was detected at appreciable levels.

EDS results revealed the particles contained Co, Al and O as well as significant levels of C shown in table 4.2. The ratio of Co : Al was 0.43, close to the expected value of 0.5. The ratio of Co : O was 0.15, lower than the expected value of 0.25.

Table 4.2: Quantitative elemental analysis for DS150, DS151 and DS152, $CoAl_2O_4$ samples as determined by EDS

Sample	Material	At. %							
		O	Na	Mg	Al	Si	Ca	Co	C
DS150	$CoAl_2O_4$	62.33	3.60	1.07	8.51	15.94	1.71	6.85	-
DS151	$CoAl_2O_4$	63.19	3.41	1.23	9.18	15.66	1.42	5.91	-
DS152	$CoAl_2O_4$*	53.9	-	-	19.54	-	-	8.32	18.24

* Preformed $CoAl_2O_4$ nanoparticles applied by airbrush onto heated glass substrate.

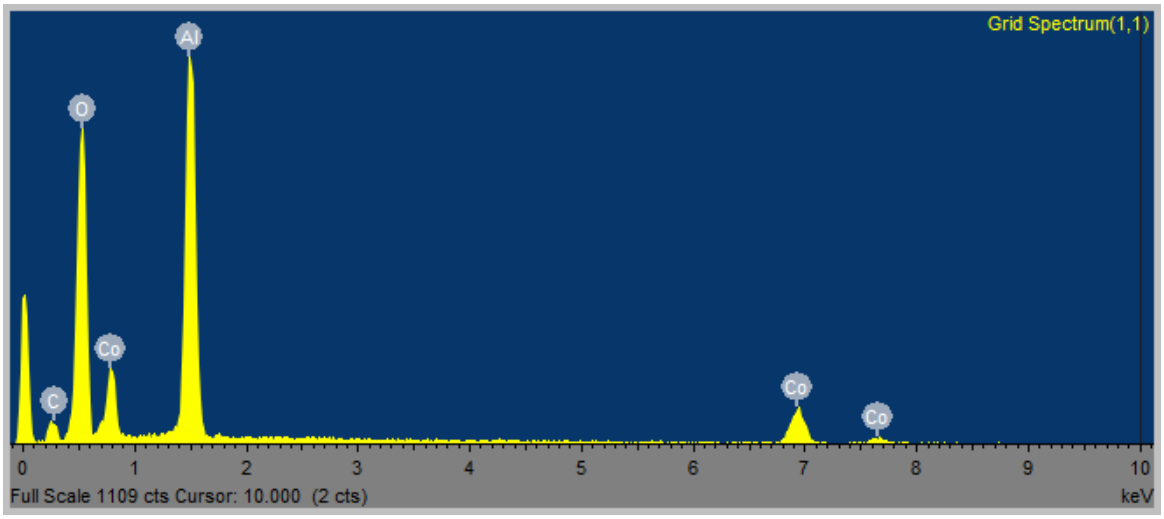

Figure 4.2: EDS spectrum for DS152 – $CoAl_2O_4$ nanoparticles

4.2.2. Morphological analysis

SEM analysis of DS152, at an instrument magnification of 100x, (Figure 4.3-A) showed the film surface consisted of many large particles between 10 – 25 microns in diameter. At 500x magnification the particles were revealed to be large agglomerations of material that were separated by cracks that were around 1 micron in width (Figure 4.3-B).

Figure 4.3-C and -D at instrument magnifications of 2,500x and 5,000x respectively, show smaller, rounded particles of between 0.5 and 1 micron in diameter. It was not possible to determine if the particles were single crystallites or composed of smaller particles due to significant charging of the substrate.

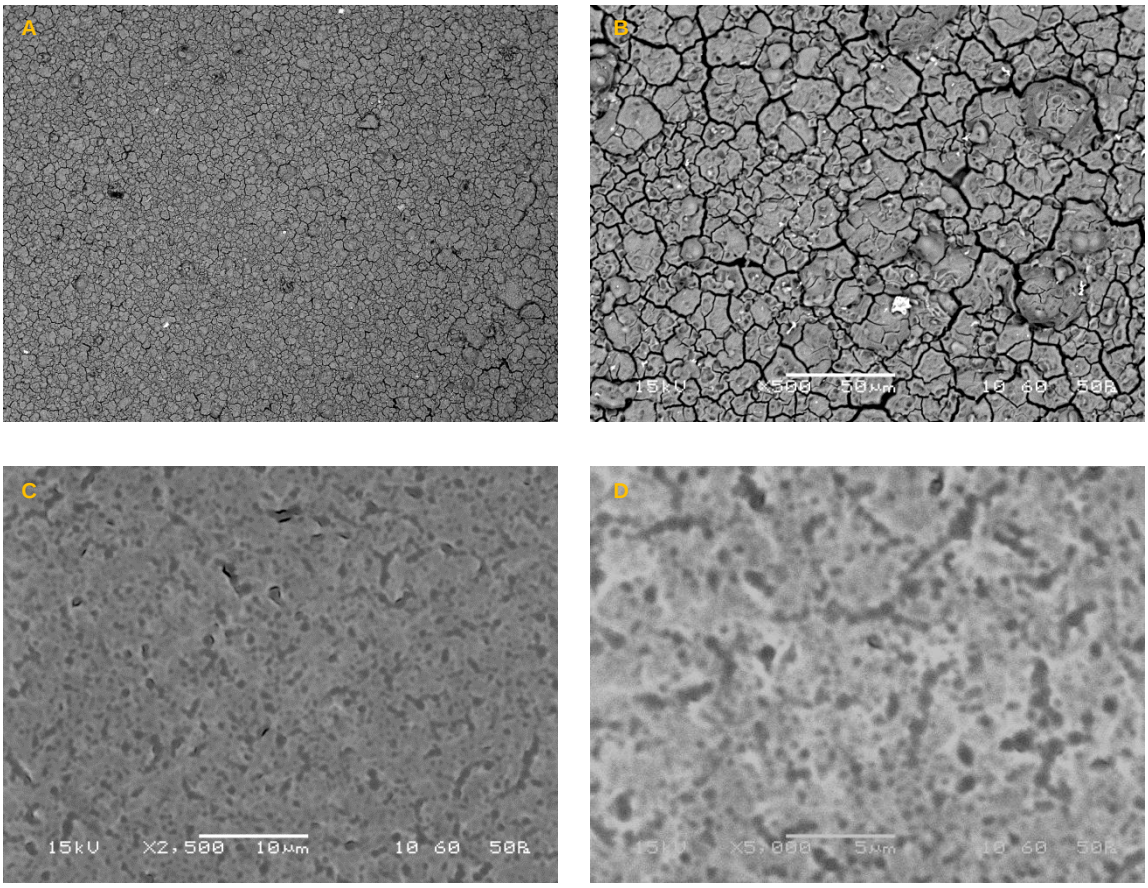

Figure 4.3: SEM micrographs of DS152, $CoAl_2O_4$ nanoparticles sprayed onto glass substrate at 100x magnification **(A)**, 500x magnification **(B),** 2500x magnification **(C)**, and 5000x magnification **(D)**.

Because the SEM analysis of sprayed $CoAl_2O_4$ could not give an indication of particle size, TEM was also used. Particles were scraped from the film surface

and sonicated in ethanol and the solution dripped onto a copper grid. Figure 4.4-A at an instrument magnification of 50,000x, revealed many small particles that were agglomerated into larger clusters. The black area of the image is where many particles had clustered together and EDS revealed it was also carbon-rich which can be attributed to solvent (either ethanol from the sample preparation or benzyl alcohol from synthesis).

Figure 4.4-B revealed that the clusters were made up of individual nanoparticles with a mean diameter of 26.88 nm though particles as small as 5 nm or large as 40 nm could be observed. Selective area electron diffraction (SAED) also revealed a powder diffraction pattern, indicating that the particles were crystalline (figure 4.5).

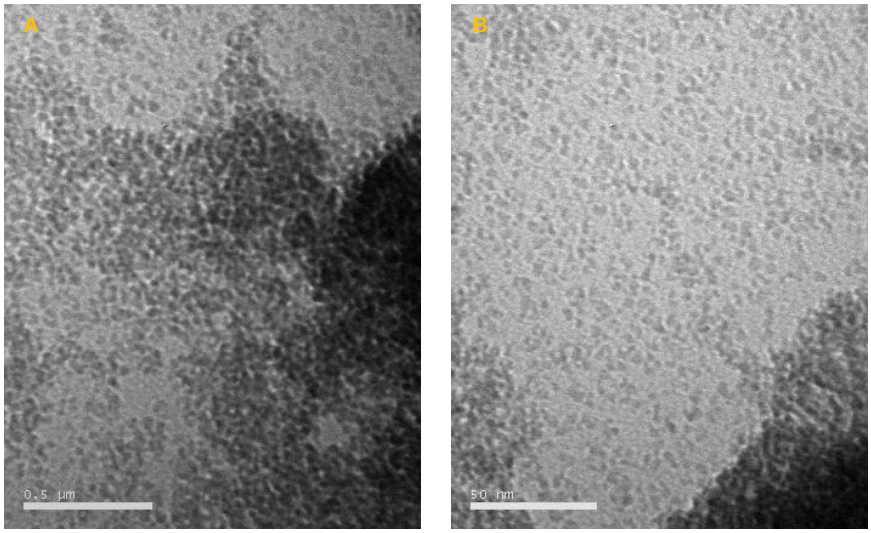

Figure 4.4: TEM micrographs of DS152, $CoAl_2O_4$ nanoparticles sprayed onto glass substrate at 50,000 x magnification (A) and 500,000 x magnification (B).

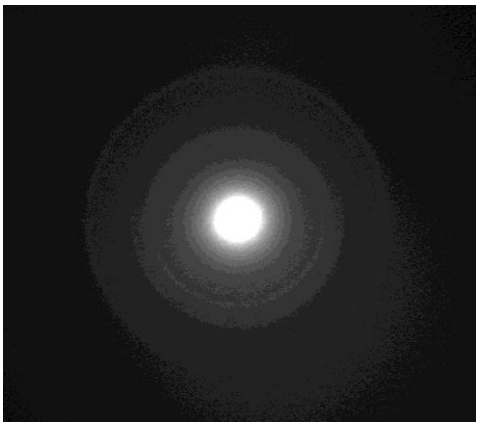

Figure 4.5: Selective area electron diffraction of $CoAl_2O_4$ nanoparticles.

4.2.3. Optical properties

UV/Vis spectroscopy was used to determine the transmission, reflectance and absorbance spectra of sample DS151, deposited by AACVD. The sample absorbed strongly in the violet and blue parts of the visible spectrum (84% at 380 nm). Absorbance reached a minimum of 40% at 545 nm . Absorption between 550 and 750 nm reached a maximum of 53% at 645 nm. Zayat and Levy have attributed the intense colouration at this wavelength due to a number of spin-allowed CT transitions, in particular the $^4A_2(F) \rightarrow {}^4T_1(P)$ and $^4A_2(F) \rightarrow {}^2T(G)$ which correspond to wavelengths of 543 and 630 nm.[27] This results in the intense green colouration of the film.

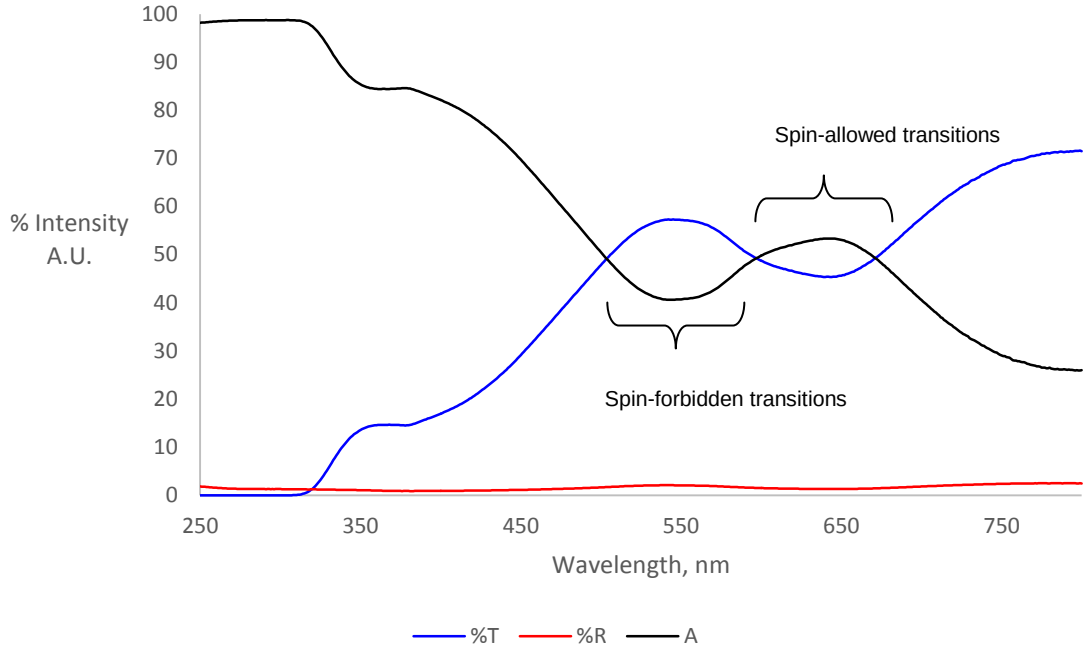

Figure 4.6: UV/Vis spectra for sample DS151, $CoAl_2O_4$ on glass substrate. Shown are transmission (blue), reflectance (red) and absorbance (black) spectra.

4.3. Combustion synthesis of $CoTiO_3$

Utilising the concept of combustion synthesis, cobalt nitrate and titanium isopropoxide were combined in ethanol solvent to form the precursor. The assumption was that the isopropoxide ligand provided the fuel source .

$$2\ Ti(OC_3H_7)_4 + 2\ Co(NO_3)_2(H_2O)_6 + 32\ O_2 \longrightarrow 2\ CoTiO_3 + 28\ H_2O + 24\ CO_2 + 2\ N2$$

A 0.4 M solution of $Co(NO_3)_2.6H_2O$ and $Ti(O^iPr)_4$ in ethanol was spin-coated onto a glass substrate and heated to 140°C. After 5 spin-coat/heat treatment cycles, the brown film was annealed in air at 600°C for one hour. After cooling, an intense green colour was observed in the film.

4.3.1. Microstructural/compositional analysis

The sample DS155 was analysed by XRD to determine the crystallographic phase of the material. Figure 4.7 shows the pattern of the sample after annealing at 500°C in air. Analysis showed strongest intensity for the (1,0,4), (0,1,2,) and (1,1,0) reflections. The pattern was indexed to rhombohedral $CoTiO_3$.[28]

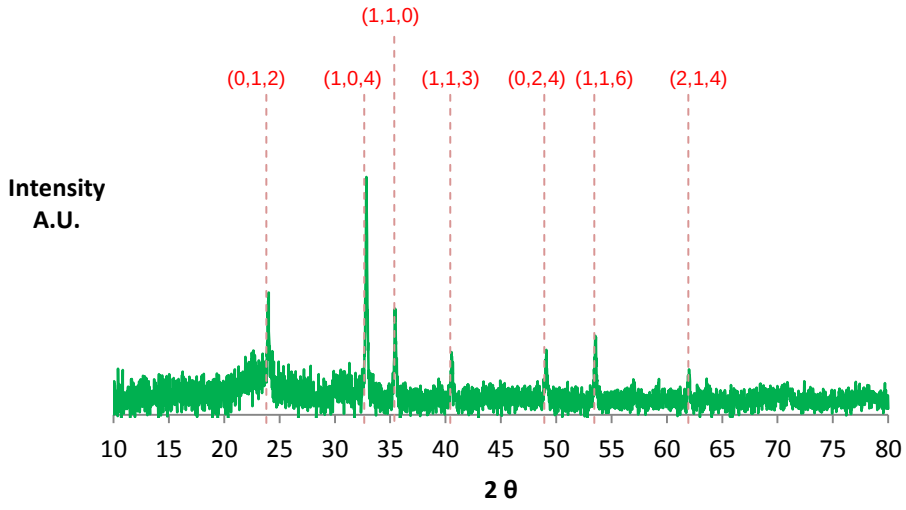

Figure 4.7: XRD pattern of DS155, $CoTiO_3$ film on glass substrate.

EDS analysis was used to determine the elemental composition of the sample, both pre- and post-annealing. The spectrum for the sampled that was annealed at

500°C is shown in figure 4.8, while quantitative elemental results are shown in table 4.3.

Analysis revealed that the sample contained Co and Ti in a ratio of 1:1 as expected for $CoTiO_3$. The ratio of Co : O was 1 : 4.0 and 1 : 2.5 for the pre- and post-annealed samples respectively if it was assumed that all other elements were bound to oxygen in their standard oxidation states (except carbon).

Table 4.3: Quantitative elemental analysis for $CoTiO_3$ thin films determined by EDS.

		At. %							
Sample	**Material**	**O**	**Na**	**Mg**	**Si**	**Ca**	**Ti**	**Co**	**C**
DS155 pre-anneal	$CoTiO_3$	63.55	5.68	1.55	22.64	2.29	2.14	1.92	0.23
DS155 annealed at 500°C	$CoTiO_3$	62.15	6.1	1.61	23.77	2.51	1.95	1.82	0.05

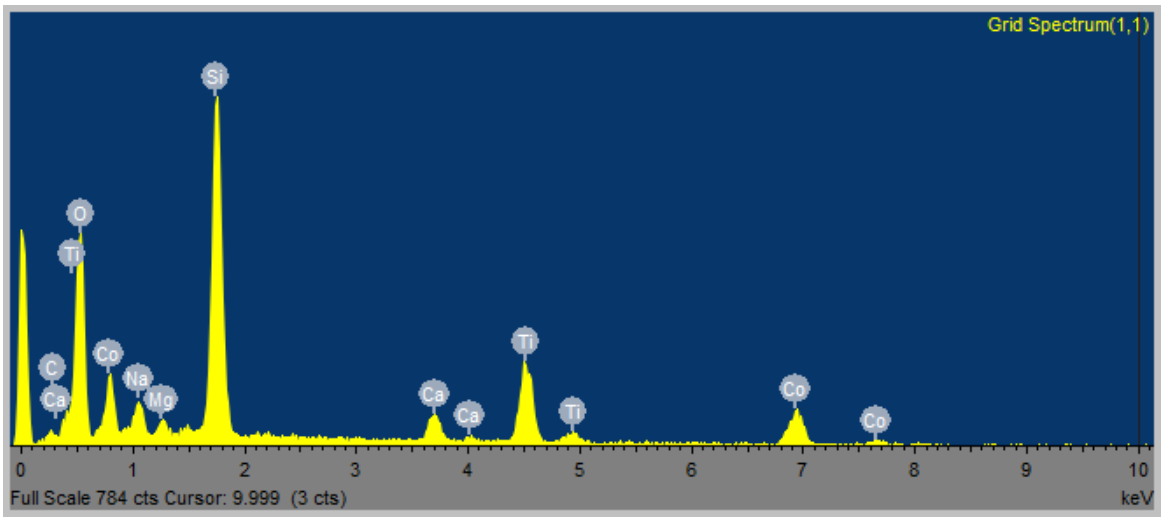

Figure 4.8: EDS spectrum of DS155, $CoTiO_3$ on glass substrate.

4.3.2. Optical properties

UV/Vis spectroscopy was used to determine the transmission, reflectance and absorbance spectra of the sample both pre- and post-annealing at 500°C. The pre-annealed sample absorbed at 70% at the lower visible range between at 390 nm, which decreased to 25% absorbance at 530 nm. Absorption between 550 and 790 nm reached a maximum of 31% at 655 nm. This matches well with the observed brown, transparent appearance. Upon annealing the absorbance reaches a minimum at 22% at 490 nm. A strong absorbance of 35% at 620 nm matches well with the observed spin-allowed crystal field transition for Co^{2+} and is the reason for the observed green colouration of the film.[29] The sample was not particularly reflective, reaching a maximum of 6% at 500 nm.

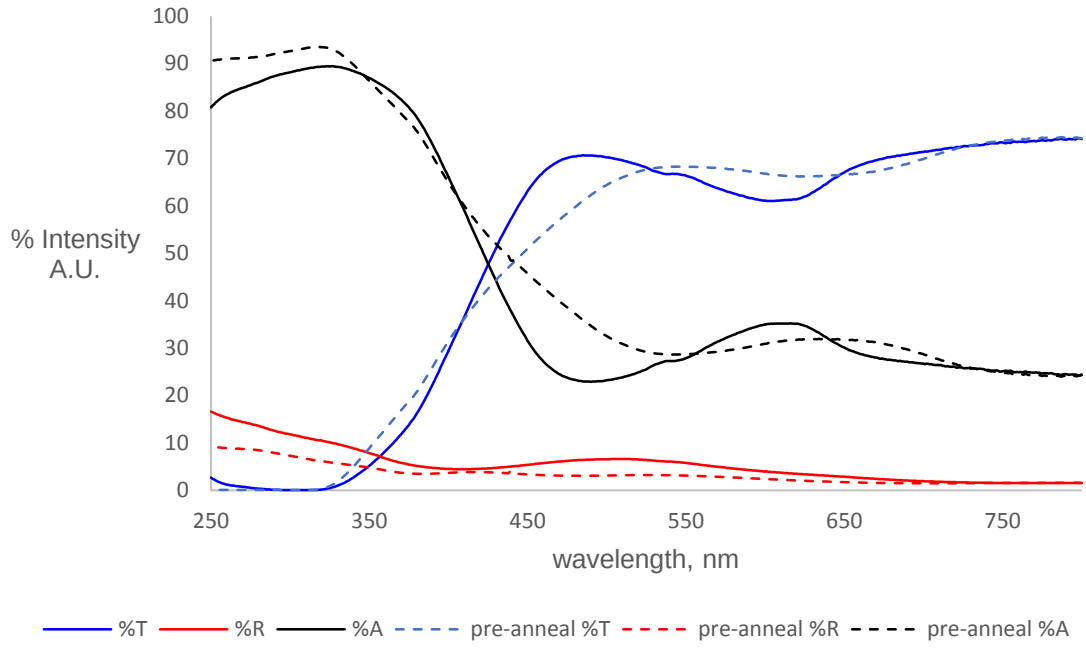

Figure 4.9: UV/Vis spectra for sample DS155, $CoTiO_3$ on glass substrate. Shown are transmission (blue), reflectance (red) and absorbance (black) spectra for pre-annealed (dashed line) and post-annealed sample (solid line).

4.3.3. Morphological analysis

SEM analysis was achieved for the post-annealed sample (DS155) and micrographs are shown in figure 4.10. Figure 4.10-A at an instrument magnification of x 1000 shows the surface of the film to consist of many "cauliflower" like crystallites on the surface. These crystallites ranged between 0.5 – 1 micron in diameter and appeared to have grown on top of another, with a flatter layer beneath. Figure 4.10-B, at an instrument magnification of 80,000 x, shows a large cubic structure 205 nm in diameter on top of the film. It was not possible to determine the composition of this structure, though significant charging indicated it was not the same material as the background film. It is possible this could be a small particle of cubic $CoTi_2O_4$. The image also shows the film to be made up of a number of agglomerations of particles ranging between 32 nm and 102 nm in diameter.

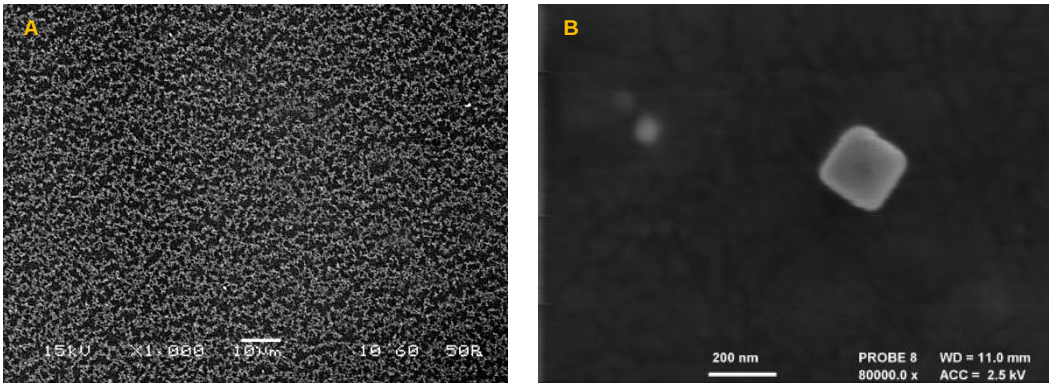

Figure 4.10: SEM micrographs of DS155, $CoTiO_3$ thin film on glass substrate at 1,000 x magnification **(A)** and 80,000 x magnification **(B)**

.

4.4. Combustion synthesis of $CoCr_2O_4$

Thin films of $CoCr_2O_4$ were investigated as potential coloured coatings on glass. Utilising the combustion synthesis method described previously, $Co(NO_3)_2.6H_2O$ and $Cr(NO_3)_3.9H_2O$ were mixed with a urea fuel source in ethanol.

$$3\ Co(NO_3)_2.6H_2O + 6\ Cr(NO_3)_3 9H_2O + 20\ OCN_2H_4 \longrightarrow 3\ CoCrO_4 + 32N_2 + 20\ CO_2 + 112\ H_2O$$

Therefore a Co : Cr ratio of 1 : 2 was used with a Co : urea ratio of 1 : 6.6. A 0.1 M solution was spin-coated onto a glass substrate and heated to 140°C. After five spin-coat and heat treatment cycles the sample was annealed in air at 500°C for one hour. The initially brown/black film became a transparent green colour.

4.4.1 Microstructural/compositional analysis.

The sample (DS156) was analysed by XRD to determine the crystallographic phase of the material. Figure 4.11 shows the diffraction pattern from sample DS156 after annealing in air at 500°C. Analysis showed a preferred orientation in the (3,1,1) direction, with the (1,1,1), (2,2,0) and (4,0,0) reflections all visible. The pattern was indexed to cubic $CoCr_2O_4$.[30]

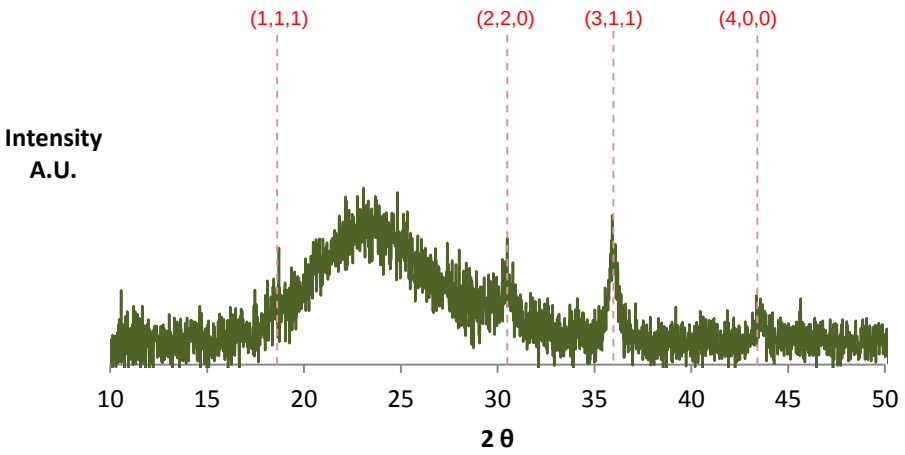

Figure 4.11: XRD pattern of DS156, $CoCr_2O_4$ thin film on glass substrate after annealing at 500°C.

EDS analysis was used to determine the elemental composition of the sample, both pre- and post-annealing. The spectrum for the sampled that was annealed at 500°C is shown in figure 4.12, while quantitative elemental results are shown in table 4.4.

Analysis revealed that the pre-annealed sample contained Co and Cr in a ratio of 1 : 1.2 far lower than the expected 1 : 2. Similarly for the annealed sample, the Co : Cr ratio was also 1 : 2. Carbon was detected at 0.31 % for the pre-annealed sample, and much lower for the annealed sample, at 0.09%.

Table 4.4: Quantitative elemental analysis for sample DS156 as determined by EDS.

		At. %							
Sample	**Material**	**O**	**Na**	**Mg**	**Si**	**Ca**	**Cr**	**Co**	**C**
DS156 pre-anneal	$CoCr_2O_4$	63.22	5.82	1.54	22.69	2.41	2.19	1.82	0.31
DS156 annealed at 500°C	$CoCr_2O_4$	61.98	6.10	1.61	23.77	2.51	2.15	1.79	0.09

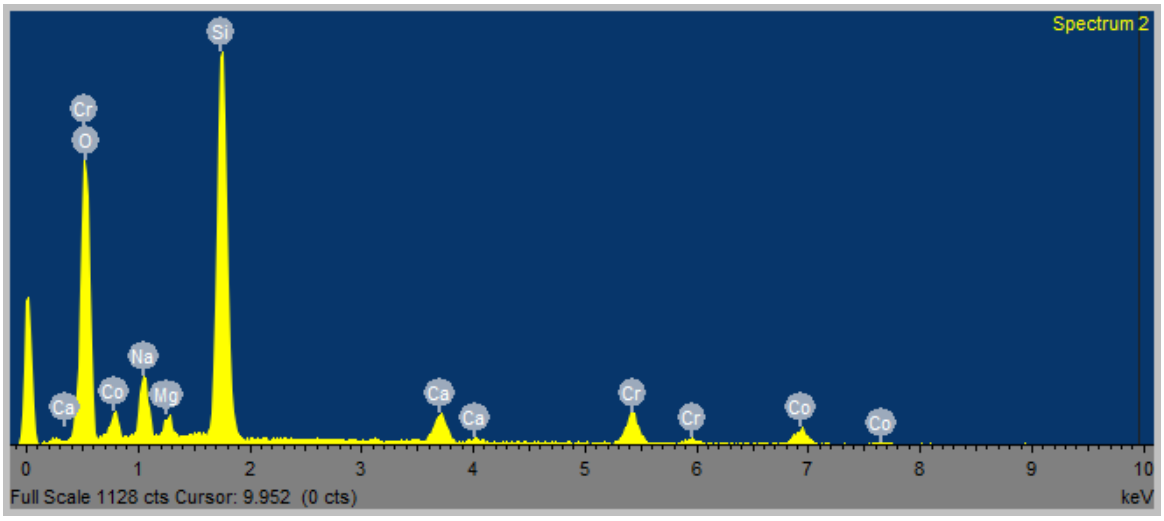

Figure 4.12: EDS spectrum for DS156, $CoCr_2O_4$ on glass substrate.

4.4.2. Optical properties

UV/Vis spectroscopy was used to determine the transmission, reflectance and absorbance spectra of the sample both pre- and post-annealing at 500°C. Before annealing, the absorbance spectrum is unremarkable, with an absorbance of 23% between 520 – 800 nm rising to 50% at 380 nm, and as such the film appears brown. As with the other Co^{2+} -containing materials investigated in this chapter, the intense absorption band between 550 – 750 nm is observed. Previous literature studies have attributed this to the $^4A_2(F) \rightarrow {}^4T_1(P)$ (v_3) transition.[30] The strong absorption of red – yellow wavelengths results in the green-blue colour of the film. The sample exhibits very low reflectance both pre- and post-annealing.

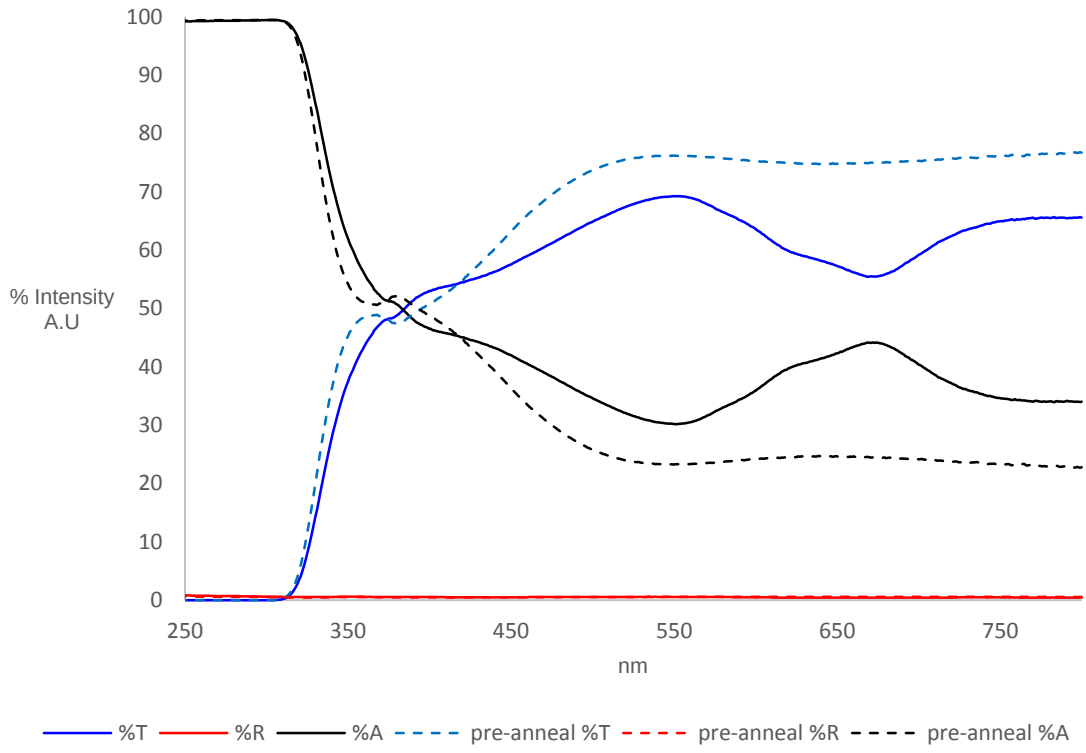

Figure 4.13: UV/Vis spectra for sample DS156, $CoCr_2O_4$ on glass substrate. Shown are transmission (blue), reflectance (red) and absorbance (black) spectra for pre-annealed (dashed lines) and post-annealed sample (solid lines).

4.4.3. Morphological analysis.

Figure 4.14-A, at an instrument magnification of 20,000x, showed some a number of crystallites covering the surface of the film. It could not be determined if these particles were “sat” on the surface of the glass substrate or an amorphous layer of the film. Figure 4.14-B at an instrument magnification of 35,000 x showed the particles to be faceted and appeared either pyramidal or bipyramidal in shape. The particles had a mean diameter of 167 nm.

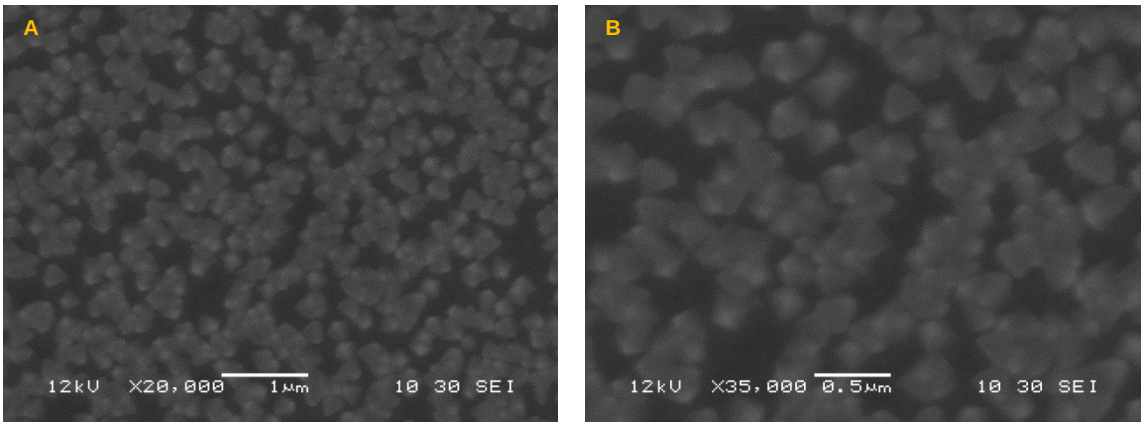

Figure 4.14: SEM micrographs of DS156, $CoCr_2O_4$ on glass substrate at 20,000 x magnification **(A)** and 35,000 x magnification **(B)**.

4.5. Combustion synthesis of CeO_2 from $Ce(NO_3)_3.6H_2O$ and urea

A 0.4 M precursor solution of $Ce(NO_3)_3.6H_2O$ and urea was spin-coated onto float glass substrates. The materials deposited in this section give rise to samples DS160 – DS163.

4.5.1. Deposition conditions

Table 4.5: Conditions used for spin-coating of $Ce(NO_3)_3.9H_2O$

Variable	Value
Precursor concentration	0.4 M
Solvent	EtOH,
Dispense volume	1 ml
Spin speed	2500 rpm
Anneal temperature	300-500 ^oC

Samples appeared mostly transparent after spin-coating, with some areas of opaque white material. Where the film was transparent, interference fringes could be seen. Upon annealing, films had a yellow colour which disappeared on cooling to room temperature. All films had a pearlescent reflectance.

4.5.2. Microstructural/compositional analysis

Films were analysed by XRD to determine their crystallographic orientation. Figure 4.15 shows the pattern for the unannealed film, DS160, while figure 4.16 shows an overlay of the XRD patterns for samples DS161, DS162 and DS163 which correspond to annealing temperatures of 300, 400 and 500°C respectively. DS160, the unannealed film, shows a very intense pattern that can be indexed to $Ce(NO_3)_3.6H_2O$. While all samples were heated to 140°C in between individual spin-coats, this was clearly not sufficient for decomposition of the precursor. Figure 4.16 shows an increasing in intensity with increasing temperature. The strongest reflections areprovided by the (1,1,1) and (2,0,0) peaks which were

visible in all annealed samples, along with the (2,2,0) and (3,3,1) peaks. The (4,0,0) reflection only becomes observable in the sample annealed at 500°C.

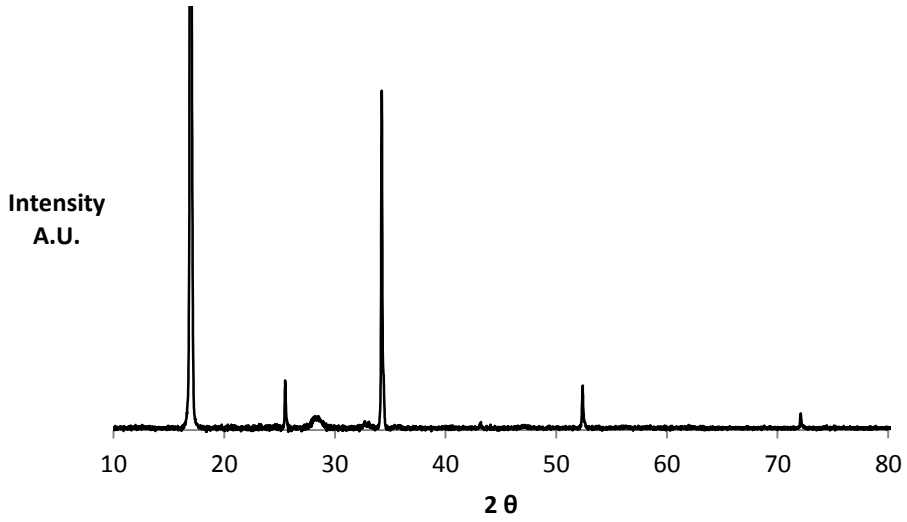

Figure 4.15: XRD pattern for DS160, $Ce(NO_3)_3.6H_2O$ on glass substrate.

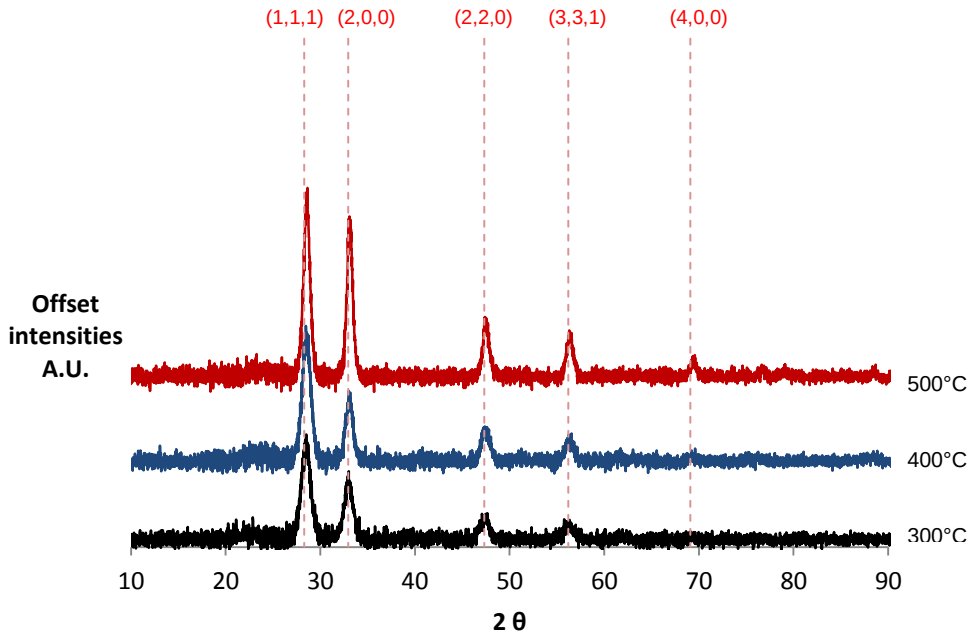

Figure 4.16: Overlayed XRD patterns for CeO_2 samples DS161 (black), DS162 (blue) and 163 (red) which correspond to annealing temperatures of 300, 400 and 500°C respectively.

Application of the Debye-Scherrer formula gives the crystallite sizes as 11, 16, and 18 nm for samples annealed at 300, 400 and 500°C respectively.

Ceria samples were analysed by Raman spectroscopy under green (532 nm) laser illumination. Figure 4.17 shows an overlay of Raman spectra for samples DS161, DS162, and DS163 which correspond to annealing temperatures of 300, 400 and 500°C respectively. The only visible peak in all samples corresponds to the F_{2g} vibrational mode at 452 cm^{-1}, which corresponds well with literature values. [31] The peak increases in intensity with increasing temperature, indicating a further conversion to CeO_2 at higher temperatures.

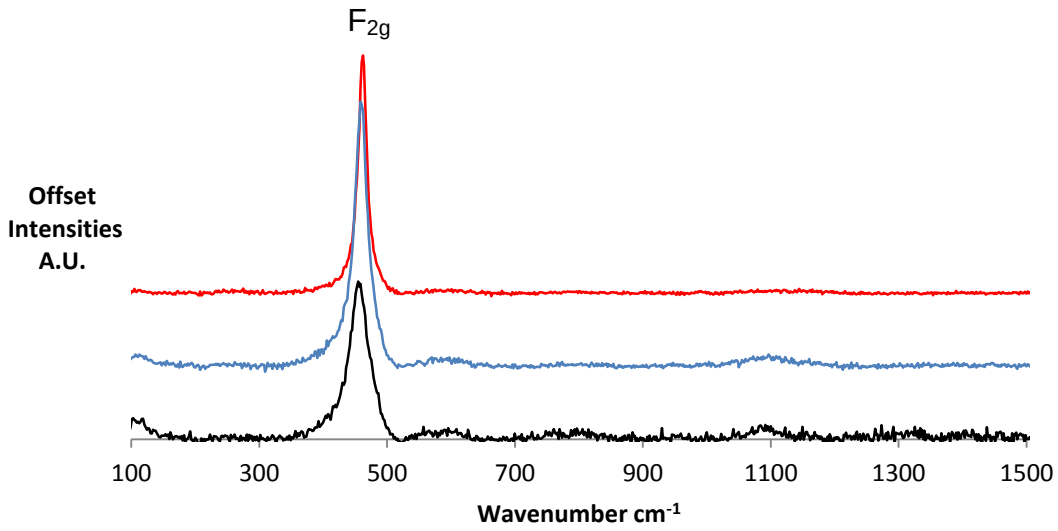

Figure 4.17: Overlayed Raman spectra for CeO_2 films annealed at 300 (black), 400 (blue) and 500°C (red).

EDS analysis was obtained for CeO_2 samples spin-coated onto glass that were un-annealed and annealed at 500°C (DS160 and DS163 respectively). All elements associated with both film and glass substrate were detected and in the case of the un-annealed film, trace amounts of nitrogen and carbon were detected. The EDS spectrum of the CeO_2 coating that was annealed at 500°C (DS163) is shown in figure 4.18 while quantitative elemental analysis is shown in table 4.6.

Quantitative analysis shows atomic percentages of cerium to be 6.32 and 5.18% for DS160 and DS163 respectively. This may indicate a loss of some material when heated to high temperatures. The ratio of Ce : O was approximately 1 : 2 in both samples assuming all other elements present in the glass were in their natural oxidation states and bound to oxygen.

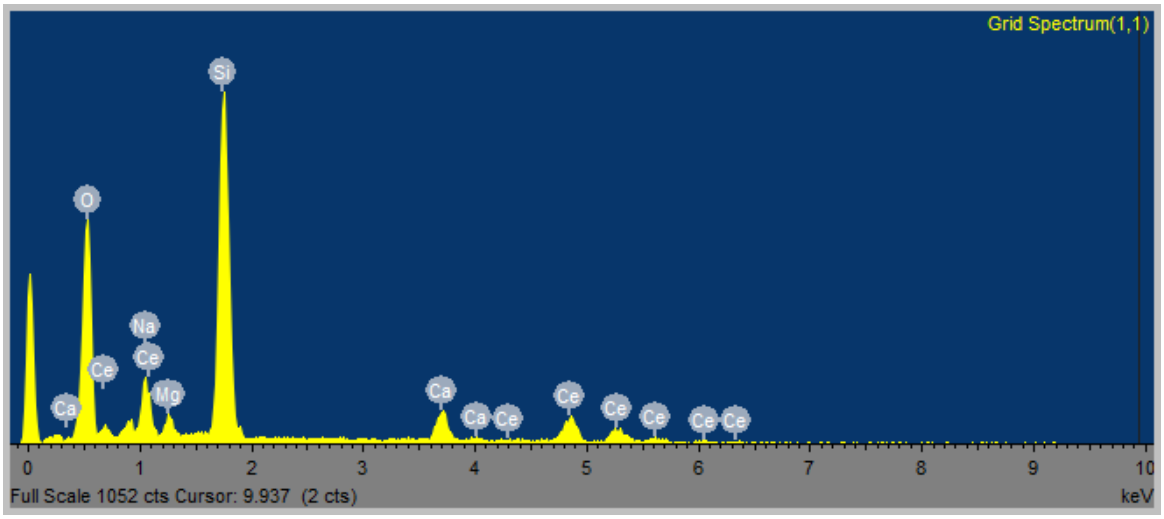

Figure 4.18: EDS spectrum of DS163 – CeO_2 film deposited from $Ce(NO_3)_3.6H_2O$

Table 4.6: Quantitative elemental analysis for DS160 and DS163 as determined by EDS.

	At. %					
Sample	**O**	**Na**	**Mg**	**Si**	**Ca**	**Ce**
DS160	63.19	5.35	1.27	22.77	2.25	5.16
DS163	62.27	5.68	1.41	23.74	2.66	4.24

4.5.3. Morphological analysis.

An SEM micrograph of sample DS160, at an instrument magnification of 20,000x, showed some large ridges and many small rounded particles on the surface (Figure 4.19-A,). There were also some cracks running across the film surface. Figure 4.19-B, at 40,000 x magnification shows many small, rounded particles ranging from 50 – 100 nm in diameter. Larger debris consistent with a spin-coating deposition were also observed.

An SEM micrograph of sample DS163, at instrument magnification of 2,500 shows a large number of cracks that break up the film into pieces between 1-2 microns in diameter. Some of the pieces had delaminated from the substrate which made it difficult to focus the electron beam on (Figure 4.19-C). Figure 4.19-D at 10,000 x magnification shows a large amount of particulate material on the film surface. The cracked surface is also visible.

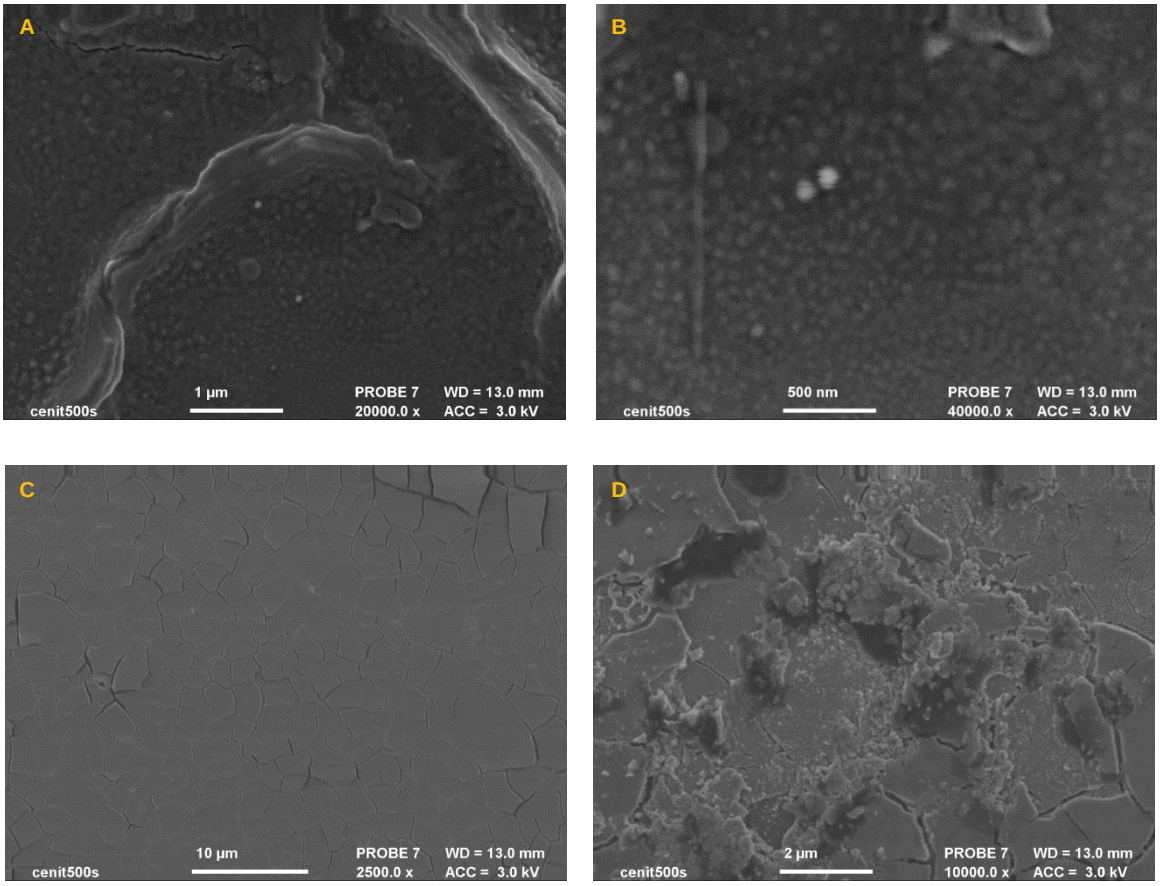

Figure 4.19: SEM micrographs of DS160 unannealed **(A – B)** and DS163, annealed at 500°C **(C - D)** spin-coated CeO_2 films.

4.6. Conclusions

The work in this chapter has detailed the formation of three coloured coatings based on materials containing Co^{2+} ions. $CoAl_2O_4$ is the most studied of these, and while this has been explored as a thin film by MOCVD, practical application remains difficult. The aerosol-assisted deposition of this material has been demonstrated to produce green films at 600°C from simple $Co(NO_3)_2.6H_2O$ and $Al(OBu^{sec})_3$ precursors.

Similar methods involving $Co(NO_3)_2.6H_2O$ and either $Ti(O^iPr)_4$ or $Cr(NO_3)_3.9H_2O$ have also yielded green thin-films in the form of $CoTiO_3$ and $CoCr_2O_4$ respectively. Investigation into other cobalt-containing pigments such as $ZnCo_2O_4$ or Co_2SnO_4 (cerulean) is also recommended.

The apparent lack of characteristic blue colouration in the cobalt aluminate sample can be attributed entirely to the annealing temperature. Studies have shown that increased temperature leads to increased conversion of Co^{2+} ions from octahedral into tetrahedral sites. It may be stated with some confidence that full conversion to $CoAl_2O_4$ could be achieved by increasing the annealing temperature. Although the glass substrate would be unlikely to survive this treatment, it is possible that introduction of precursor onto the surface of glass that was still molten (i.e. during formation on an industrial float line) may produce a blue film. Currently coatings can be applied while the glass is in the tin bath, namely the SiCO barrier layer. A $CoAl_2O_4$ coating could feasibly be applied at this stage also, and would not necessarily require a barrier layer present. To apply onto the surface of molten glass may achieve a thin layer of “body tinting” at the very surface that could be turned on/off as required, although this is largely speculative.

Additionally, the combustion synthesis technique has been successfully employed in the deposition of crystalline cerium oxide thin films. The next step is to introduce the precursor via an aerosol to attempt the AACVD of CeO_2 from the simple metal salt.

4.7. Further work

In addition to the coatings described in this, and previous chapters, it is realised that simple precursor systems such as metal-nitrates are excellent solution-based precursors. Coupled with an aerosol-assisted CVD technique, the potential for a vast range of materials becomes apparent. What is not fully realised yet are the limits of this technique, and further investigation in to more complex materials are recommended.

By way of example, addition of simple thiourea, $SC(NH_2)_2$ to $Ni(NO_3)_2.6H_2O$ yields the hexakis(thiourea) adduct, $Ni(NO_3)_2.6(SC(NH_2)_2)$. e.g:

$$Ni(NO_3)_2.6H_2O + 6SC(NH_2)_2 \longrightarrow Ni(NO3)2.6(SC(NH2)2) + 6H_2O$$

This nickel-thiourea (TU) complex has been shown to decompose to NiS_2 upon heating (figure 4.20), although pure NiS and Ni_3S_4 phases have previously been obtained from the same precursor.[32]

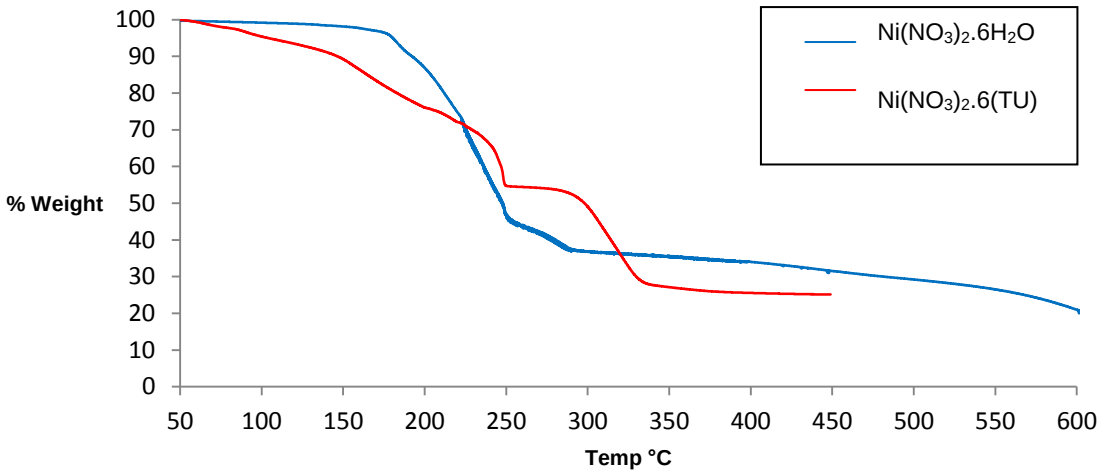

Figure 4.20: TGA plot of $Ni(NO_3).6H_2O$ (blue) and $Ni(NO_3)_2.6(S(NH_2)_2)$

Literature reports the use of this complex for bulk or nanoparticle synthesis of NiS materials,[32] but its application as a precursor for AACVD remains unexplored. Preliminary studies involving spin-coating a 0.1 M solution of this complex in ethanol onto a glass substrate have highlighted its candidacy as a thin-film precursor. Figure 4.21 shows selected SEM and EDS analysis, although detailed characterisation and further study could not be achieved due to time constraints,

the presence of Ni and S were confirmed through EDS. The fact that the sample precursor was decomposed in air indicates a surprising preference for the sulphide phase.

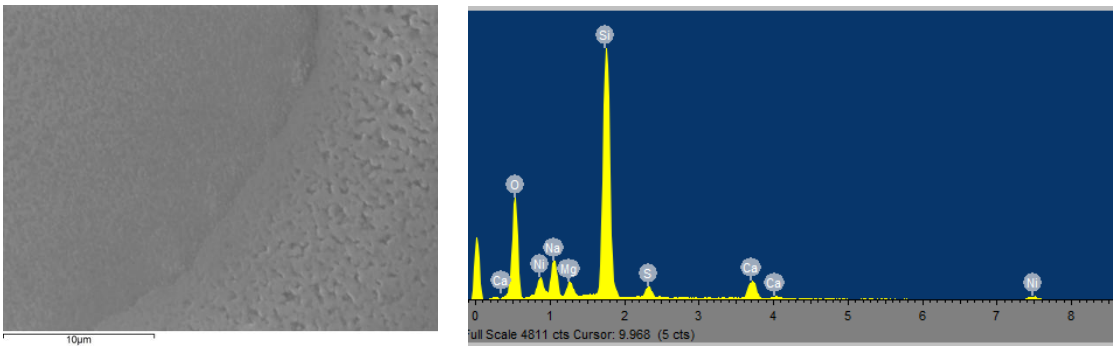

Figure 4.21: SEM micrograph at 2,500 x magnification and corresponding EDS spectrum of film deposited from $Ni(NO_3)_2.6SC(NH_2)_2$.

For future data regarding colour measurements, the LAB colour model is recommended. By attributing a lightness, L, and red, green, blue colour dimensions to A and B, a precise measurement of colour can be achieved which is often used in industry.

4.8. References

1. Ji, L.; Tang, S.; Zeng, H. C.; Lin, J.; Tan, K. L., *Applied Catalysis A: General* **2001,** *207*, 247-255.
2. Rangel, E. R., **2010**, 207--213.
3. Chen, Z.; Shi, E.; Li, W.; Zheng, Y.; Zhong, W., *Materials Letters* **2002,** *55*, 281-284.
4. Merikhi, J.; Jungk, H.-O.; Feldmann, C., *Journal of Materials Chemistry* **2000,** *10*, 1311-1314.
5. Karmaoui, M.; Silva, N. J. O.; Amaral, V. S.; Ibarra, A.; Millan, A.; Palacio, F., *Nanoscale* **2013,** *5*, 4277-4283.
6. Lavrenčič Štangar, U.; Orel, B.; Krajnc, M., *Journal of Sol-Gel Science and Technology* **2003,** *26*, 771-775.
7. Carta, G.; Casarin, M.; El Habra, N.; Natali, M.; Rossetto, G.; Sada, C.; Tondello, E.; Zanella, P., *Electrochimica Acta* **2005,** *50*, 4592-4599.
8. El Habra, N.; Crociani, L.; Sada, C.; Zanella, P.; Casarin, M.; Rossetto, G.; Carta, G.; Paolucci, G., *Chemistry of Materials* **2007,** *19*, 3381-3386.
9. Levinson, R. B., Paul.Akbari, Hashem. Lawrence Berkeley National Laboratory Pigment Database. http://coolcolors.lbl.gov/LBNL-Pigment-Database/database.html
10. Choi, H.; Kim, Y. J.; Varma, R. S.; Dionysiou, D. D., *Chemistry of Materials* **2006,** *18*, 5377-5384.
11. Gracia, F.; Holgado, J. P.; Caballero, A.; Gonzalez-Elipe, A. R., *The Journal of Physical Chemistry B* **2004,** *108*, 17466-17476.
12. Yadav, B. C.; Yadav, R. C.; Singh, S.; Dwivedi, P. K.; Ryu, H.; Kang, S., *Optics & Laser Technology* **2013,** *49*, 68-74.
13. Anjana, P. S., *Journal of the American Ceramic Society* **2006,** *89*, 2114--2117.
14. Chuang, S.H., *Journal of the Chinese Chemical Society* **2010,** *57*, 1022--1026.
15. Lu, J.; Huang, J.; Cao, L.; Wu, J.; Zhao, D. Method for preparing cobalt titanate thin film using dual target magnetron sputtering. 2010.
16. Ehsan, M. A., *Applied Organometallic Chemistry* **2012,** *26*, 493--498.

17. Pore, V.; Dimri, M.; Khanduri, H.; Stern, R.; Lu, J.; Hultman, L.; Kukli, K.; Ritala, M.; Leskelä, M., *Thin Solid Films* **2011,** *519*, 3318-3324.
18. Dutta, D. P.; Manjanna, J.; Tyagi, A. K., *Journal of Applied Physics* **2009,** *106*, 043915.
19. Cui, H.; Zayat, M.; Levy, D., *Journal of Sol-Gel Science and Technology* **2005,** *35*, 175-181.
20. Eliziário, S. A.; de Andrade, J. M.; Lima, S. J. G.; Paskocimas, C. A.; Soledade, L. E. B.; Hammer, P.; Longo, E.; Souza, A. G.; Santos, I. M. G., *Materials Chemistry and Physics* **2011,** *129*, 619-624.
21. Duffy, J. A., *Journal of Non-Crystalline Solids* **1996,** *196*, 45-50.
22. Jankowski, J.; Thomas, G.; Camby, L. P., *Solid State Ionics* **1997,** *101–103, Part 2*, 1321-1326.
23. Kim, K. J.; Park, Y. R., *Solid State Communications* **2003,** *127*, 25-28.
24. Hu, G.; Choi, J. H.; Eom, C. B.; Suzuki, Y., *MRS Online Proceedings Library* **1999,** *603*, null-null.
25. Liu, X.; Kareev, M.; Cao, Y.; Liu, J.; Middey, S.; Meyers, D.; Freeland, J. W.; Chakhalian, J., *Applied Physics Letters* **2014,** *105*, 042401.
26. Varela, F. S., *Nanotechnology* **2005,** *16*, 190.
27. Zayat, M.; Levy, D., *Chemistry of Materials* **2000,** *12*, 2763-2769.
28. *Acta Crystallographica* **1964,** *17*, 240--242.
29. Lin, Y.-J.; Chang, Y.-H.; Yang, W.-D.; Tsai, B.-S., *Journal of Non-Crystalline Solids* **2006,** *352*, 789-794.
30. Gingasu, D.; Mindru, I.; Culita, D. C.; Patron, L.; Calderon-Moreno, J. M.; Osiceanu, P.; Preda, S.; Oprea, O.; Parvulescu, V.; Teodorescu, V.; Walsh, J. P. S., *Materials Research Bulletin* **2015,** *62*, 52-64.
31. Sullivan, J. A.; Dulgheru, P.; Atribak, I.; Bueno-López, A.; García-García, A., *Applied Catalysis B: Environmental* **2011,** *108–109*, 134-139.
32. Kumar, N.; Raman, N.; Sundaresan, A., *Journal of Solid State Chemistry* **2013,** *208*, 103-108.

Chapter 5:

Experimental

5.1. General experimental techniques, procedures and instrumentation

Solvents

All solvents were purchased from Sigma-Aldrich and dried over activated alumina and molecular sieve columns using an Innovative Technology, Inc. PS-400-7 purification system and freeze-thaw degassed prior to use in any air sensitive reactions.

SEM

Scanning electron microscopy and energy dispersive X-ray spectroscopy was performed on a JEOL JSM6480LV SEM or JEOL FESEM6301F FE-SEM at the Microscopy and Analysis Suite, University of Bath, or at the Material Properties and Surface Analysis department at the Pilkington-NSG Technical Centre, Lathom. Specimens were taken from each sample, mounted onto aluminium stubs in cross section and ultrasonically cleaned in methanol for 10 seconds. The cleaned specimens were coated with a thin layer of platinum or chromium (which provides a uniform conductive surface) prior to examination using a scanning electron microscope (SEM). Secondary electron (SE) images were captured at various instrument magnifications using 80° specimen tilt including 2,000x, 10,000x and 50,000x and at an instrument magnification of 50,000x using 90°specimen tilt. The accelerating voltage used was 20 kV.

XRD

Micro-X-ray diffraction (Micro-XRD) were performed on a Bruker D8 Advance diffractometer utilising copper kα radiation (1.5418Å). Analysis was used to determine the crystalline phases. X-ray diffraction (XRD) is performed under ambient conditions of temperature and pressure by directing a collimated X-ray beam onto a specimen, which is diffracted by the regularly repeating atomic structure of the crystalline phases within the specimen. This produces reflection patterns, which are captured on an image plate and converted into a diffractogram. Each crystalline phase in the diffractogram is identified by search matching using a database of 300,000 reference patterns. In micro-XRD

individual particles and small volumes of powder are analysed using a collimated X-ray beam of between 30 and 800 μm in size. Each coating sample was illuminated by an 800 micron X-ray beam for 30 minutes for phase identification. Peak search-match software was used to identify the crystalline components present in each sample.

XPS

XPS was carried out at the Thin Film Technology & Analytical Science section at Pilkington-NSG Technical Centre with Chris Weekes and Mark Farnworth. The instrument was a Thermo Scientific K Alpha. Samples are illuminated with Aluminium K-Alpha X-rays which interact with surface atoms generating photoelectrons with energies characteristic of the atoms from which they originated. The photoelectrons enter an energy analyser that separates the electrons according to their energies. An energy spectrum is produced containing peak intensities that are proportional to the concentrations of the atoms that they represent. Sensitivity factors are applied to the peak intensities to produce quantified compositional data in atom%. An argon ion etching system is used to remove atomic layers at controlled rates. Analysis inside the developing craters allows elemental concentrations to be measured with depth. XPS depth profiles were obtained for all of the samples using Scan Mode. The argon ion etch beam was operated at 3keV(high) producing a beam current of 3.95 microamps. For each sample, 80 levels of etching were used with an etch time of 30 seconds per level. The Crater Size Mode was set to Auto and the X-ray beam size was set to 400μm.

ToF-SIMS

ToF-SIMS was carried out with Mark Farnworth at the thin film technology and analytical science section of the Pilkington-NSG Technical Centre, Lathom. A pulsed beam of bismuth ions is directed to a sample surface. The ions liberate neutral and charged elemental and molecular species from the surface. The positive and negatively charged ions can be selectively extracted and detected using a Time-of-Flight system in which ions are separated according to their mass. A separate, rastered beam of caesium ions is used to remove material from the surface over a defined area. Analysis at the centre of the crater is

carried out using the bismuth beam. The analysis/etch process is repeated every second or so until the coating has been penetrated and the glass substrate reached. The ION-TOF 5 Time of Flight Secondary Ion Mass Spectrometry (ToF-SIMS) instrument was used to obtain a positive ion depth profile. The analysis beam was Bi_3^+ and the sputter beam was 1keV Cs^+ with a beam current of 74.7 nA. The sputter beam was rastered over a 200 x 200 micron area and the bismuth analysis beam was rastered over a 51 x 51 micron area at the centre of the sputtered region. Caesium forms positive and negative ion clusters with neutral species that are sputtered from the surface. The signal level of CsM^+ clusters are less matrix dependent than from M^+ ions and are the ion species of choice, taking into account other factors such as peak intensity and peak overlaps.

Substrate preparation

Pilkington SiCO-coated float glass was the preferred target substrate for both AACVD and spin-coating but in some depositions silicon wafer was used for easier analysis. Substrates were thoroughly cleaned in a 1.5 w% hellmanex solution, acetic acid, isopropanol and distilled water. Samples were cleaned in an oxygen plasma using a Diener Zepto plasma generator 1 – 2 days before deposition.

4-point probe measurements

Selected sheet resistance measurements were performed with TEC-15 FTO as a reference. Measurements were carried out on a Guardian Model SRM – 232 surface resistivity meter which houses a 4-point probe. Measurements were taken at the same thickness for each sample as determined by visible interference fringes, and an average of three measurements was made.

X-Ray crystallography

Solid state molecular structures were obtained using a Nonium Kappa CCD diffractometer fitted with an area detector and Oxford cryostream. Structure solution was followed by full-matrix least squares refinement and was performed with the WinGX-1.70 suite of programmes.

Thermogravimetric analysis

Thermogravimetric analyses were performed using a Perkin Elmer TGA 4000^{TM} quartz microbalance instrument and spectra were analysed using PYRIS Version 10.1 Instrument managing and analysis software. Samples were sealed into pre-weighed aluminium pans and unless stated otherwise, TGAs were run using a standardised method. Under a continuous furnace purge rate of 20 mLmin^{-1} of N_2, the furnace was heated to an initiation temperature of 40 ^{o}C, at which point mass measurements were recorded every second. Temperature was increased at a ramp-rate of 5 ^{o}C min^{-1} until a pre-designated maximum temperature. Mass was recalculated back to a measure of percentage, according to the initial mass of the sample.

Determination of photoactivity

A solution of resazurin photocatalyst intelligent ink was prepared according to the method previously described by Mills *et al*.[1] by mixing 3 g of a 1.5 wt % aqueous solution of hydroxyethyl cellulose, 0.3 g of glycerol and 4 mg of resazurin in a small round bottom flask. The dye was used fresh, however upon storage, the vial was wrapped in aluminium foil to prevent unwanted light-catalysed reaction. 0.1 ml was pipette onto the surface to be tested and covered with a glass coverslip. The dye was left for 10 minutes to spread out under capilliary action and A visible-light spectrum recorded. The sample was then irradiated with 254 nm UV light for 15 minutes with the visible absorbance spectrum recorded every minute.

5.2. Chapter 2 experimental

AACVD of Cu, Cu_2O and CuO from $Cu(NO_3)_2.2.5H_2O$

To produce Cu films, $Cu(NO_3)_2.2.5H_2O$ (2.33 g, 10 mmol) was dissolved in 100 ml degassed ethanol to form a 0.1 M solution. The solution was transferred to a stainless steel bubbler and sealed shut. The bubbler was attached to a TSI 3076 constant output atomizer and purged with nitrogen for 10 minutes to remove any oxygen. The furnace was heated to temperatures between 300 - 500°C and baked out for 20 minutes under a flow of nitrogen prior to each deposition. The nitrogen pressure was set to 20 psi. To start the run, the bypass valve was closed

and both inlet and outlet valves to the bubbler were opened. Deposition lasted 30 minutes. To end the run, the inlet and outlet valves to the bubbler were closed, the bypass valve was opened, and the furnace switched off. Samples were left to cool below 100°C before being removed from the reactor.

To produce Cu_2O films, 10 % O_2 was added to the reactor and deposition carried out at temperatures of 300 – 350°C.

To produce CuO films, 10% O_2 was added to the reactor and deposition carried out at temperatures off 500°C.

AACVD of Ni and NiO from $Ni(NO_3)_2.6H_2O$

For metallic Ni films, $Ni(NO_3)_2.6H_2O$ (2.91 g, 10 mmol) was dissolved in 100 ml degassed ethanol to form a 0.1 M solution. The solution was transferred to a stainless steel bubbler and sealed shut. The bubbler was attached to a TSI 3076 constant output atomizer and purged with nitrogen for 10 minutes to remove any oxygen. The furnace was heated to temperatures between 300 - 500°C and baked out for 20 minutes under a flow of nitrogen prior to each deposition. The nitrogen pressure was set to 20 psi. To start the run, the bypass valve was closed and both inlet and outlet valves to the bubbler were opened. Deposition lasted 30 minutes. To end the run, the inlet and outlet valves to the bubbler were closed, the bypass valve opened, and the furnace switched off. Samples were left to cool below 100°C before being removed from the reactor.

For NiO films, metallic Ni films were deposited as above. Samples were then annealed in air at 500°C for one hour.

AACVD of TiO_2 photoactive layer

$Ti(OEt)_4$ (2.07 ml, 10 mmol) was dissolved in 100 ml dried and degassed toluene to form a 0.1 M solution. The solution was transferred to a stainless steel bubbler in a dry box and sealed shut. The bubbler was attached to a TSI 3076 constant output atomizer. The furnace was heated to 500°C (for anatase phase) and baked out for 20 minutes under a flow of nitrogen prior to each deposition. The nitrogen pressure was set to 20 psi. To start the run, the bypass valve was closed and both inlet and outlet valves to the bubbler were opened. Deposition lasted 5

minutes owing to the high growth rate of titania. To end the run, the inlet and outlet valves to the bubbler were closed, the bypass valve opened, and the furnace switched off. Samples were left to cool below 100°C before being removed from the reactor.

Synthesis of $Cu(NO_3)_2.4(OCN_2H_4)$ ***(1)***

$Cu(NO_3)_2.2.5H_2O$ (2.33 g, 10 mmol) and urea (2.40 g, 40 mmol) were dissolved in 20 ml ethanol and stirred for 30 minutes in a large beaker. The pale blue solution was left to evaporate in a fume cupboard for 24 hours from which blue crystals formed.

Synthesis of $Cu(NO_3)_2.4(MU)$ ***(2)***

$Cu(NO_3)_2.2.5H_2O$ (2.33 g, 10 mmol) and N-methylurea (2.96 g, 40 mmol) were dissolved in 20 ml ethanol and stirred for 30 minutes in a large beaker. The pale blue solution was left to evaporate in a fume cupboard for 24 hours from which blue crystals formed.

Synthesis of $Cu(NO_3)_2.4NNDMU$ ***(3)***

$Cu(NO_3)_2.2.5H_2O$ (2.33 g, 10 mmol) and N,N'-dimethylurea (3.52 g, 40 mmol) were dissolved in 20 ml ethanol and stirred for 30 minutes in a large beaker. The pale blue solution was left to evaporate in a fume cupboard for 24 hours from which blue crystals formed. Analysis found (calc. for $C_{12}H_{32}N_{10}O_{10}Cu$): C 28.04 (26.69), H 7.92 (5.97), N 26.88 (25.94)% (m.p. 110 – 112 dec.).

Synthesis of $Co(NO_3)_2.6NNDMU$ ***(4)***

$Co(NO_3)_2.6H_2O$ (2.91 g, 10 mmol) and N,N'-dimethylurea (3.52 g, 40 mmol) were dissolved in 20 ml ethanol and stirred for 30 minutes in a large beaker. The purple solution was left to evaporate in a fume cupboard for 24 hours from which purple crystals formed.

Synthesis of $Ni(NO_3)_2(H_2O)_6.4NNDMU$ ***(5)***

$Ni(H_2O)_6.6H_2O$ (2.90 g, 10 mmol) and N,N'-dimethylurea (3.52 g, 40 mmol) were dissolved in 20 ml ethanol and stirred for 30 minutes in a large beaker. The green

solution was left to evaporate in a fume cupboard for 24 hours from which pale green crystals formed.

5.3. Chapter 3 experimental

AACVD of SnO_2 and F:SnO_2 from $Sn(NO_3)_2$ precursor

$SnCl_2$ (1.89 g, 10 mmol) and NH_4NO_3 (1.80 g, 20 mmol) were dissolved in 100 ml degassed ethanol. For the undoped films, the precursor was used as described. For the F-doped films, NH_4F (0.37 g, 10 mmol) was added to the precursor solution and a small amount of white precipitate formed. HNO_3 was added drop-wise until the precipitate redissolved. The solution was left stirring for one hour prior to deposition. The solution was transferred to a stainless steel bubbler and the head-space flushed with nitrogen. The precursor was deposited onto Pilkington SiCO glass (and where stated Si) substrates which had been washed in isopropanol and distilled water. Substrates were heated to the desired temperature under a flow of nitrogen for 30 minutes prior to deposition to equilibriate. Deposition was carried out at temperatures of 300 – 500°C at 50°C intervals. After each run, the furnace was switched off and substrates allowed to cool to room temperature before removal from the reactor. This method can also be used with water solvent in place of ethanol.

5.4. Chapter 4 experimental

Spin-coating of $CoAl_2O_4$ films

$Co(NO_3)_2.6H_2O$ (1.16 g, 4 mmol) and Al(*sec*-OBu)$_3$ (2.04 ml, 8 mmol) were dissolved in 10 ml 2-methoxyethanol to form a 0.4 M solution. The purple solution was stirred for 30 minutes prior to spin coating. Pilkington SiCO glass substrates were cut in 30 x 30 mm squares and thoroughly cleaned in isopropanol followed by oxygen plasma treatment to aid wettability of the surface. The substrate was mounted on a circular stub in a Laurell 6NPP/Lite spin coater and precursor pipetted onto the glass to completely cover the surface (~0.5 ml). The substrate was spun at 2500 rpm for 30 seconds on each spin cycle. After spinning the substrate was transferred to a hot plate and heated to 140°C for 5 minutes in a fume cupboard. After gasses had stopped evolving from the surface, the spin-coat cycle was repeated 5 times. The brown/green film was then annealed in air at 600°C for one hour to yield a green coloured film.

AACVD of $CoAl_2O_4$

$Co(NO_3)_2.6H_2O$ (2.91 g, 10 mmol) and Al(O*sec*-Bu)$_3$ (5.1 ml, 8 mmol) were dissolved in 100 ml 2-methoxyethanol to form a 0.1 M solution. The solution was transferred to a stainless steel bubbler in a dry box and sealed shut. The bubbler was attached to a TSI 3076 constant output atomizer. The furnace was heated to 500°C and baked out for 20 minutes under a flow of nitrogen prior to each deposition. The nitrogen pressure was set to 20 psi. To start the run, the bypass valve was closed and both inlet and outlet valves to the bubbler were opened. Deposition lasted 5 minutes owing to the high growth rate of titania. To end the run, the inlet and outlet valves to the bubbler were closed, the bypass valve opened, and the furnace switched off. Samples were left to cool below 100°C before being removed from the reactor. The resulting green/brown films were annealed in air at 600°C for one hour to yield green films.

Synthesis of $CoAl_2O_4$ nanoparticles

The synthesis followed the procedure previously described by Karmaoui *et al* [2] with the exception that Co and Al precursors were changed to $Co(NO_3)_2.6H_2O$ and $Al(NO_3)_3.9H_2O$ respectively. $Co(NO_3)_2.6H_2O$ (0.72 g, 2.5 mmol) and $Al(NO_3)_3.9H_2O$ (1.87 g, 5 mmol) were suspended in 15 ml benzyl alcohol. The suspension was transferred to a stainless-steel autoclave and screwed shut. The vessel was heated in an oven to 300°C for 12 hours and left to cool. Caution: gases were evolved during the nanoparticle synthesis so great care is required when opening the vessel. Isopropanol was added to the resulting blue solution to precipitate the particles. The solution was then centrifuged at 8,000 rpm for 10 minutes and remaining solution discarded. The blue precipitate was washed and sonicated in more isopropanol to fully clean the particles of benyl alcohol. The nanoparticles were then dried in an oven at 180°C overnight. Because the autoclave was so small, nanoparticles were synthesised in batches to produce a sufficient amount of product.

Spray-coating of $CoAl_2O_4$ nanoparticles.

$CoAl_2O_4$ nanoparticles (0.44 g, 2.5 mmol) were dissolved in 25 ml toluene to yield a 0.1 M solution. The solution was transferred into a Master Airbrush and sprayed evenly onto Pilkington SiCO float glass that had been heated to 150°C. This was undertaken in a fume cupboard to avoid spreading of nanoparticles. The spray was applied evenly across the substrate surface for 10 seconds and the solvent allowed to evaporate. This cycle was repeated until all 25 ml of the precursor solution was used up. The resulting blue opaque film was left to cool to room temperature before further analysis.

Spin-coating of $CoTiO_3$ thin films

$Co(NO_3)_2.6H_2O$ (1.16 g, 4 mmol) and $Ti(O^iPr)_4$ (1.18 ml, 4 mmol) were dissolved in 10 ml ethanol to form a 0.4 M solution. The purple solution was stirred for 30 minutes prior to spin coating. Pilkington SiCO glass substrates were cut in 30 x 30 mm squares and thoroughly cleaned in isopropanol followed by oxygen plasma treatment to aid wettability of the surface. The substrate was mounted on a circular stub in a Laurell 6NPP/Lite spin coater and precursor pipetted onto the

glass to completely cover the surface (~0.5 ml). The substrate was spun at 2500 rpm for 30 seconds on each spin cycle. After spinning the substrate was transferred to a hot plate and heated to 140°C for 5 minutes in a fume cupboard. After gasses had stopped evolving from the surface, the spin-coat cycle was repeated 5 times. The brown/green film was then annealed in air at 500°C for one hour to yield a green coloured film.

Spin-coating of $CoCr_2O_4$ thin films

$Co(NO_3)_2.6H_2O$ (0.58 g, 2 mmol) and $Cr(NO_3)_3.9H_2O$ (1.6 g, 4 mmol) and urea (0.79 g, 13.2 mmol) were dissolved in 20 ml ethanol to form a 0.1 M solution. The dark purple solution was stirred for 30 minutes prior to spin coating. Pilkington SiCO glass substrates were cut in 30 x 30 mm squares and thoroughly cleaned in isopropanol followed by oxygen plasma treatment to aid wettability of the surface. The substrate was mounted on a circular stub in a Laurell 6NPP/Lite spin coater and precursor pipetted onto the glass to completely cover the surface (~0.5 ml). The substrate was spun at 2500 rpm for 30 seconds on each spin cycle. After spinning the substrate was transferred to a hot plate and heated to 140°C for 5 minutes in a fume cupboard. After gasses had stopped evolving from the surface, the spin-coat cycle was repeated 10 times. The brown/green film was then annealed in air at 500°C for one hour to yield a green coloured film.

Spin-coating of CeO_2 thin films

$Ce(NO_3)_3.6H_2O$ (3.47 g, 8 mmol) and urea (1.1 g, 18.4 mmol) were dissolved in 20 ml ethanol to form a 0.4 M solution. The clear solution was stirred for 30 minutes prior to spin coating. Pilkington SiCO glass substrates were cut in 30 x 30 mm squares and thoroughly cleaned in isopropanol followed by oxygen plasma treatment to aid wettability of the surface. The substrate was mounted on a circular stub in a Laurell 6NPP/Lite spin coater and precursor pipetted onto the glass to completely cover the surface (~0.5 ml). The substrate was spun at 2500 rpm for 30 seconds on each spin cycle. After spinning the substrate was transferred to a hot plate and heated to 140°C for 5 minutes in a fume cupboard. After gasses had stopped evolving from the surface, the spin-coat cycle was repeated 10 times. The white/hazy film was then annealed in air between 300-500°C for one hour to yield pearlescent, white films.

5.5. References for chapter 5

1. Mills, A.; Wang, J. S.; Lee, S. K.; Simonsen, M., *Chemical Communications* **2005**, 2721-2723.
2. Karmaoui, M.; Silva, N. J. O.; Amaral, V. S.; Ibarra, A.; Millan, A.; Palacio, F., *Nanoscale* **2013,** *5*, 4277-4283.

Chapter 6

Appendices

6.1. Crystallographic refinement data

Table 6.1 Crystal data and structure refinement for **(3)**.

Identification code	k13kcm3
Empirical formula	C12 H32 Cu N10 O10
Formula weight	540.02
Temperature	150(2) K
Wavelength	0.71073 A
Crystal system, space group	Triclinic, P $\bar{1}$
Unit cell dimensions	a = 7.5992(3) A alpha = 96.032(2) deg. b = 8.3741(4) A beta = 109.621(2) deg. c = 10.1452(5) A gamma = 106.528(3) deg.
Volume	568.42(5) A^3
Z, Calculated density	1, 1.578 Mg/m^3
Absorption coefficient	1.031 mm^-1
F(000)	283
Crystal size	0.25 x 0.20 x 0.05 mm
Theta range for data collection	3.00 to 27.48 deg.
Limiting indices	-9<=h<=9, -10<=k<=10, -13<=l<=13
Reflections collected / unique	9725 / 2564 [R(int) = 0.0648]
Completeness to theta = 27.48	98.5 %
Absorption correction	Semi-empirical from equivalents
Max. and min. transmission	0.9503 and 0.7827
Refinement method	Full-matrix least-squares on F^2
Data / restraints / parameters	2564 / 1 / 169
Goodness-of-fit on F^2	1.026
Final R indices [I>2sigma(I)]	R1 = 0.0425, wR2 = 0.0882
R indices (all data)	R1 = 0.0795, wR2 = 0.1016
Largest diff. peak and hole	0.469 and -0.665 e.A^-3

Table 6.2 Crystal data and structure refinement for **(4)**.

Identification code	shelxl
Empirical formula	C18 H48 Co N14 O12
Formula weight	711.63
Temperature	150(2) K
Wavelength	0.71073 A
Crystal system, space group	triclinic, $P\bar{1}$
Unit cell dimensions	a = 7.7164(3) A alpha = 69.322(2) deg. b = 10.6471(4) A beta = 84.552(2) deg. c = 10.8393(4) A gamma = 82.762(2) deg.
Volume	825.30(5) A^3
Z, Calculated density	1, 1.432 Mg/m^3
Absorption coefficient	0.595 mm^-1
F(000)	377
Crystal size	0.25 x 0.20 x 0.20 mm
Theta range for data collection	3.52 to 27.53 deg.
Limiting indices	-9<=h<=10, -13<=k<=13, -14<=l<=14
Reflections collected / unique	13492 / 3751 [R(int) = 0.0969]
Completeness to theta = 27.53	99.1 %
Max. and min. transmission	0.8903 and 0.8655
Refinement method	Full-matrix least-squares on F^2
Data / restraints / parameters	3751 / 0 / 235
Goodness-of-fit on F^2	1.012
Final R indices [I>2sigma(I)]	R1 = 0.0518, wR2 = 0.1153
R indices (all data)	R1 = 0.0950, wR2 = 0.1360
Largest diff. peak and hole	0.492 and -0.717 e.A^-3

Table 6.3 Crystal data and structure refinement for **(5)**.

Identification code	shelxl
Empirical formula	C12 H44 N10 Ni O16
Formula weight	643.28
Temperature	150(2) K
Wavelength	0.71073 A
Crystal system, space group	monoclinic, P $2_1/c$
Unit cell dimensions	a = 8.4215(3) A alpha = 90 deg. b = 13.8484(4) A beta = 97.945(2) deg. c = 12.6817(4) A gamma = 90 deg.
Volume	1464.80(8) A^3
Z, Calculated density	2, 1.458 Mg/m^3
Absorption coefficient	0.744 mm^-1
F(000)	684
Crystal size	0.35 x 0.35 x 0.35 mm
Theta range for data collection	4.06 to 27.50 deg.
Limiting indices	-10<=h<=10, -17<=k<=17, -16<=l<=16
Reflections collected / unique	16298 / 3333 [R(int) = 0.0812]
Completeness to theta = 27.50	99.2 %
Max. and min. transmission	0.7807 and 0.7807
Refinement method	Full-matrix least-squares on F^2
Data / restraints / parameters	3333 / 0 / 221
Goodness-of-fit on F^2	1.215
Final R indices [I>2sigma(I)]	R1 = 0.0626, wR2 = 0.1371
R indices (all data)	R1 = 0.0741, wR2 = 0.1411
Largest diff. peak and hole	0.846 and -0.581 e.A^-3

6.2. Micro-XRD analysis

Below are listed further XRD patterns that could not be included in chapter 2.

DS100A (Cu) [silicon]

DS100A (Cu) [glass]

DS063 (Cu_2O) [silicon]

DS063 (Cu_2O) [glass]

DS053 (TiO_2 on Cu) [glass]

DS055 (TiO_2 on Cu_2O) [glass]

DS058 (TiO_2 on CuO) [silicon]

DS054 (TiO_2 on Cu_2O) [Activ^{TM}]

The diffractogram and phase assignments are shown in Figures 6.1 through 6.10. The identified crystalline phases are shown in Table 1.

Table 6.4: List of samples and assigned crystallographic phases as determined by micro-XRD

Sample	Database Assignment	Chemical Formula	ICDD Pattern
DS100A (Figures 6.1 – 6.2)	Silicon (substrate) Cu Cuprite	Si Cu Cu_2O	01-080-0018 04-002-8854 04-002-0906
DS100A (Figure 6.3)	Copper	Cu	04-002-8854
DS060 (Figures 6.4 – 6.5)	Silicon (substrate) Cuprite	Si Cu_2O	01-080-0018 04-002-0906
DS060 (Figure 6.6)	Cuprite Copper	Cu_2O Cu	04-002-0906 04-002-8854
DS053 (Figure 6.7)	Anatase Copper	TiO_2 Cu	01-084-1285 04-002-8854

	Cuprite*	Cu_2O*	04-002-0906*
DS055 (Figure 6.8)	Anatase Copper Cuprite*	TiO_2 Cu Cu_2O	01-084-1285 04-002-8854 04-002-0906*
DS058 (Figure 6.9)	Silicon (substrate) Anatase Tenorite Copper	Si TiO_2 CuO Cu	01-080-0018 01-084-1285 00-041-0254 04-002-8854
DS054 (Figure 6.10)	Anatase Copper Cuprite*	TiO_2 Cu Cu_2O*	01-084-1285 04-002-8854 04-002-0906*

*Due to overlaps with the other phases present it was difficult to accurately identify if a small amount of Cuprite was or was not present in samples DS053, and DS054.

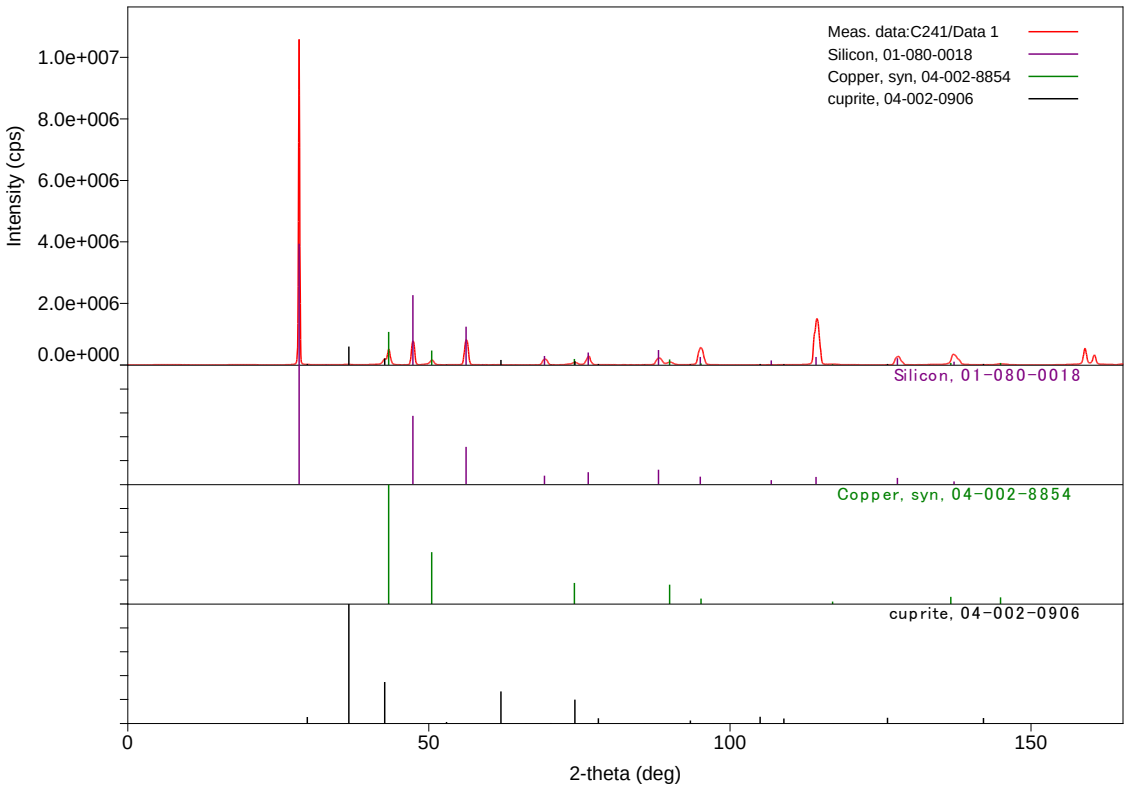

Figure 6.1: DS100A (Silicon)

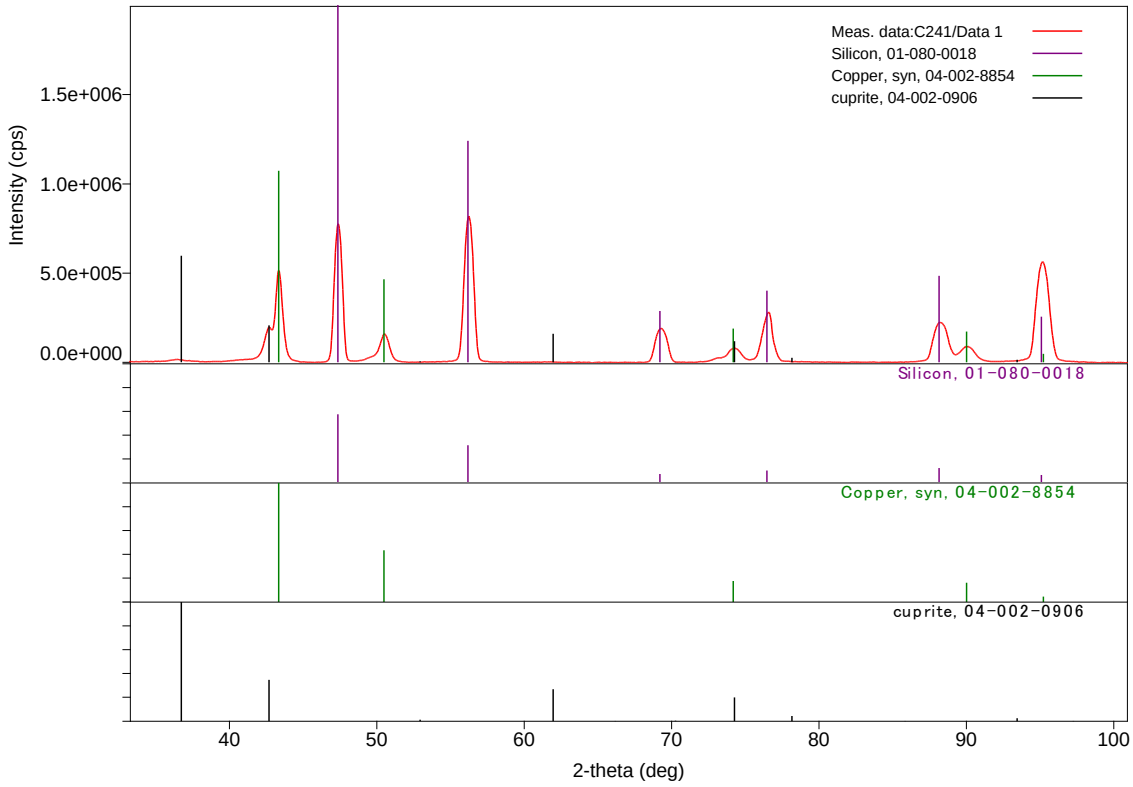

Figure 6.2: DS100A (Silicon) (zoomed to show copper and cuprite)

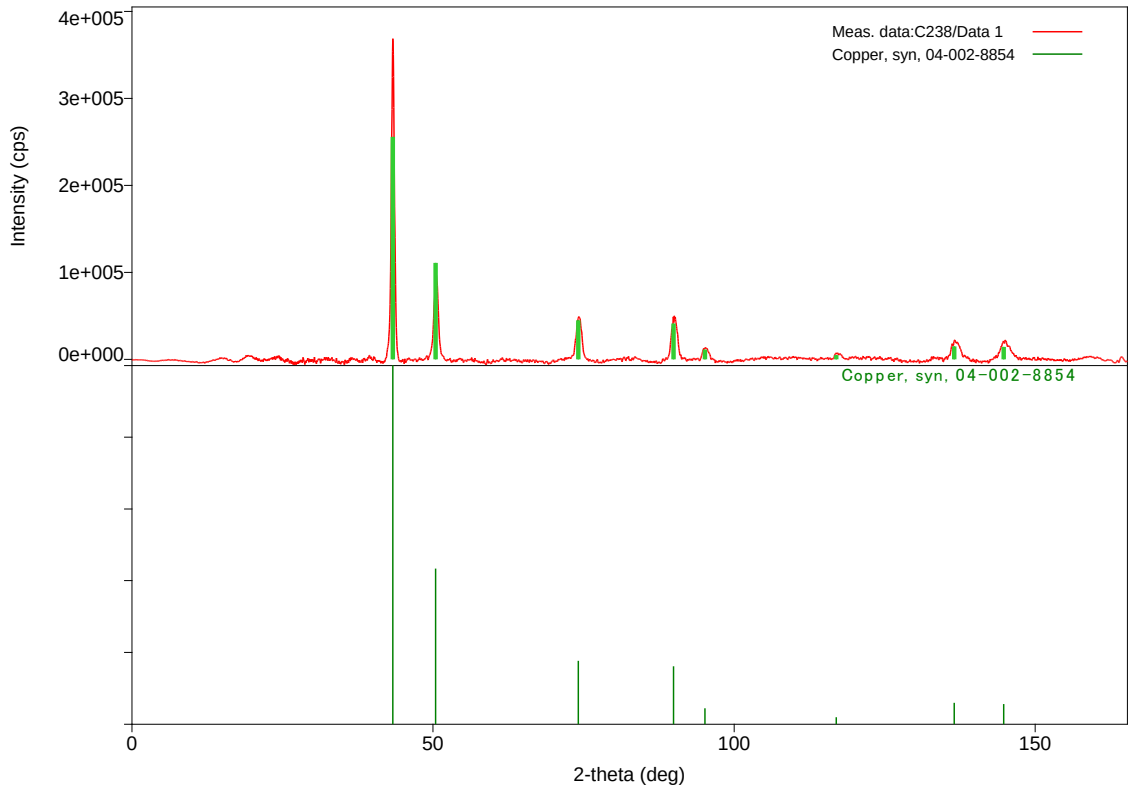

Figure 6.3: DS100A (glass)

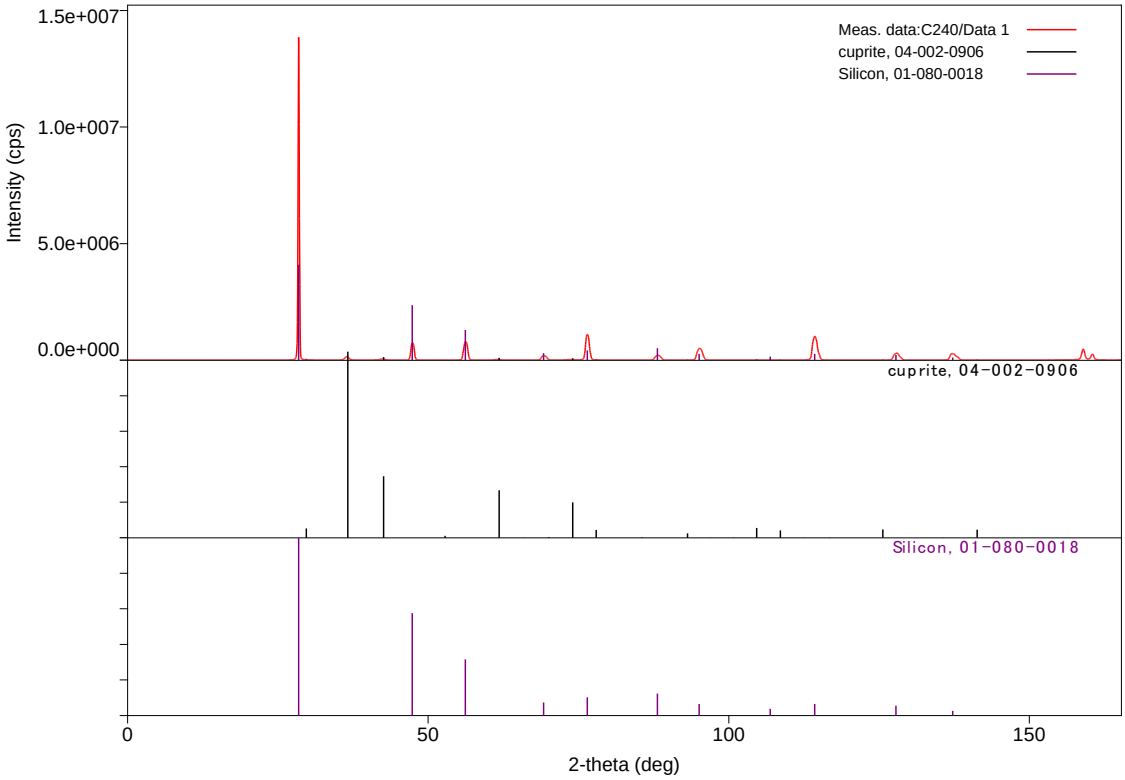

Figure 6.4: DS060 (Silicon)

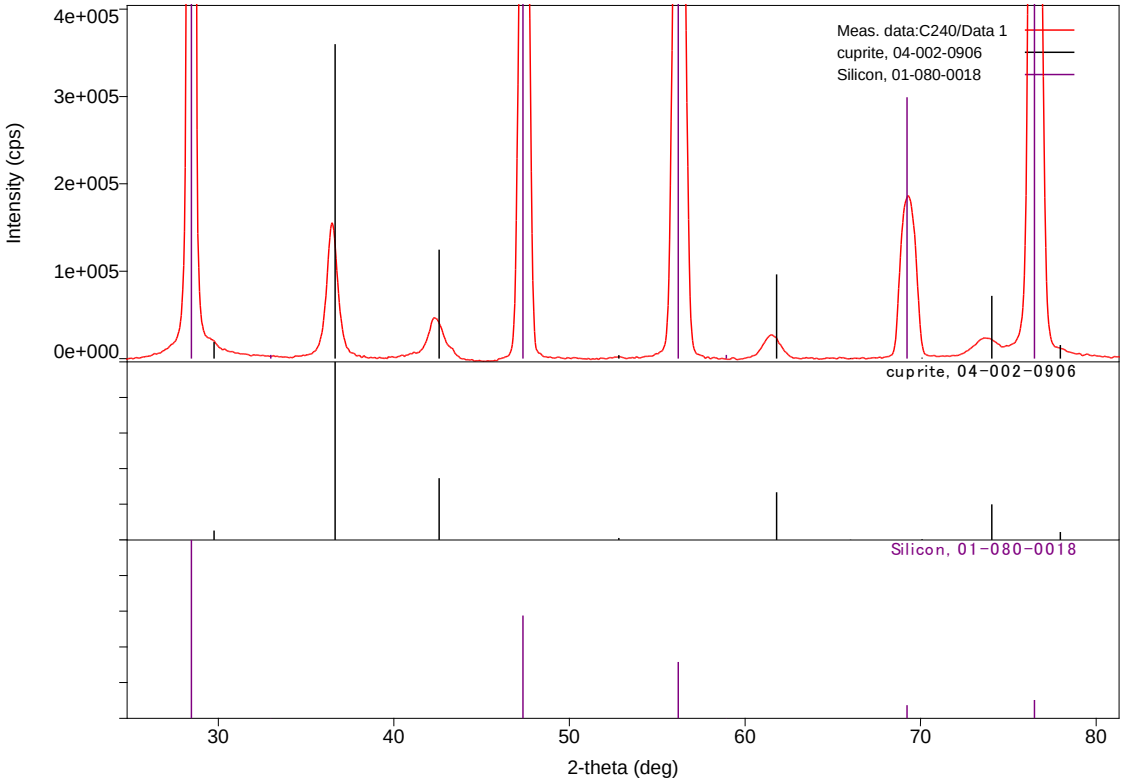

Figure 6.5: DS060 (Silicon) (zoomed to show cuprite peaks)

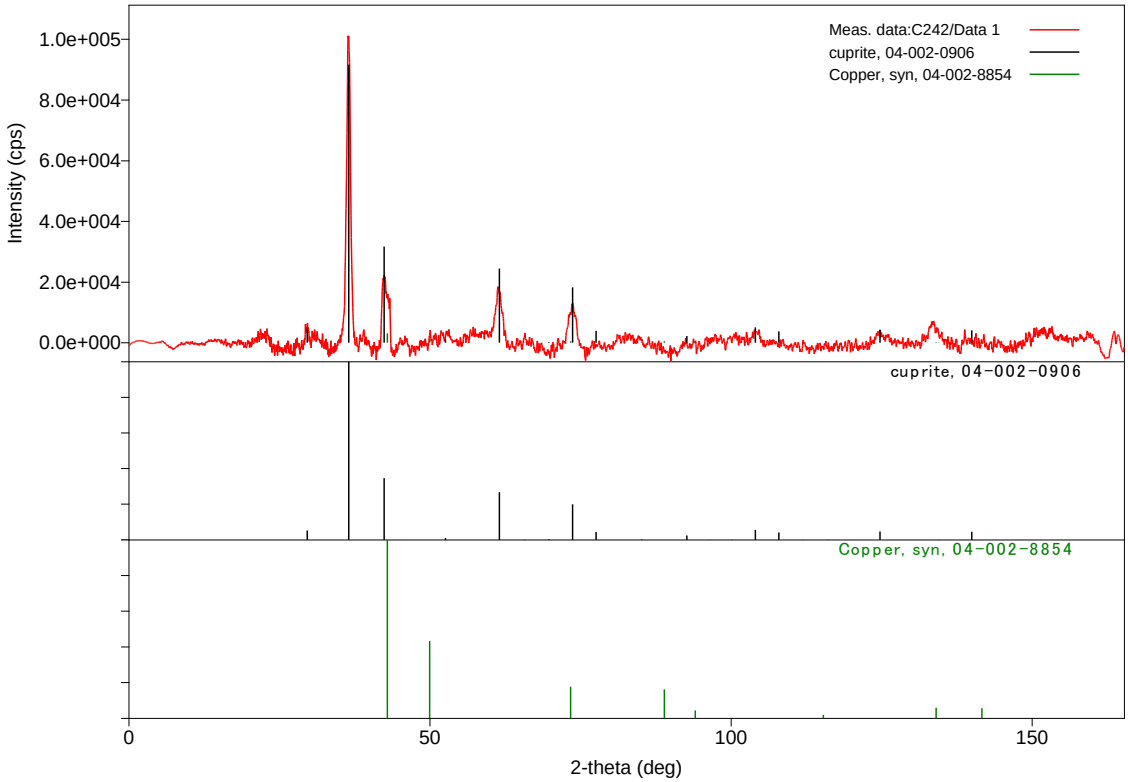

Figure 6.6: DS060 (glass)

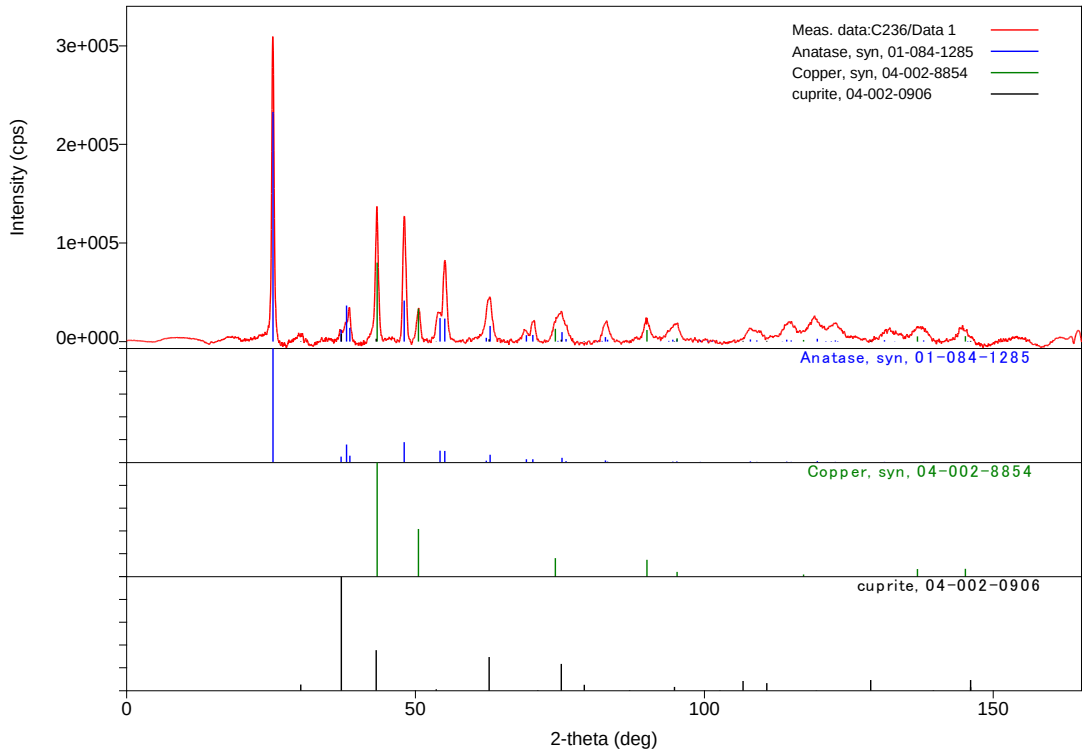

Figure 6.7: DS053 (glass)

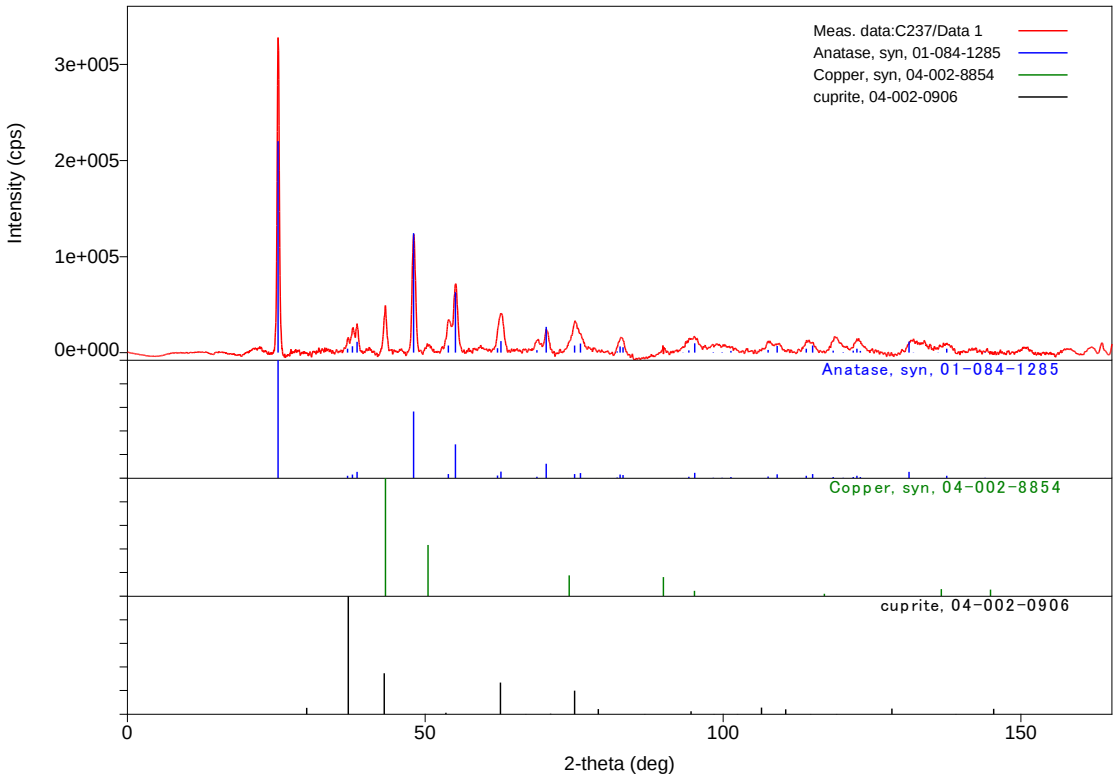

Figure 6.8: DS055 (glass)

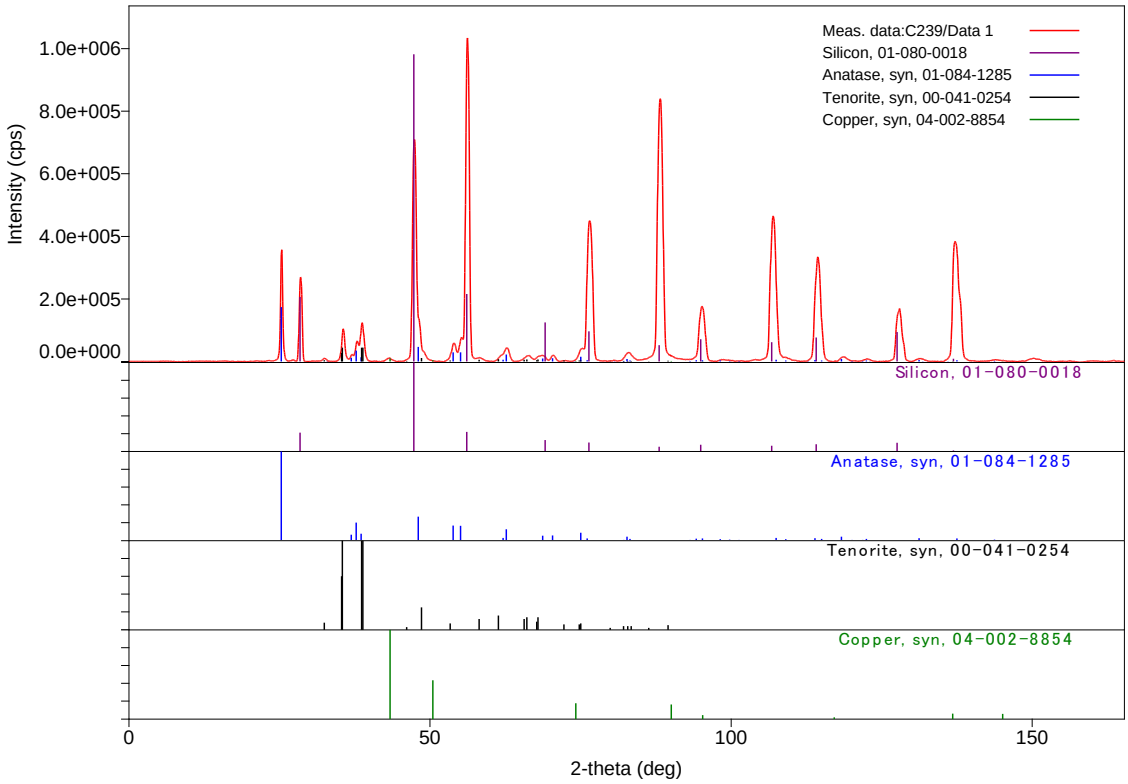

Figure 6.9: DS058 (silicon)

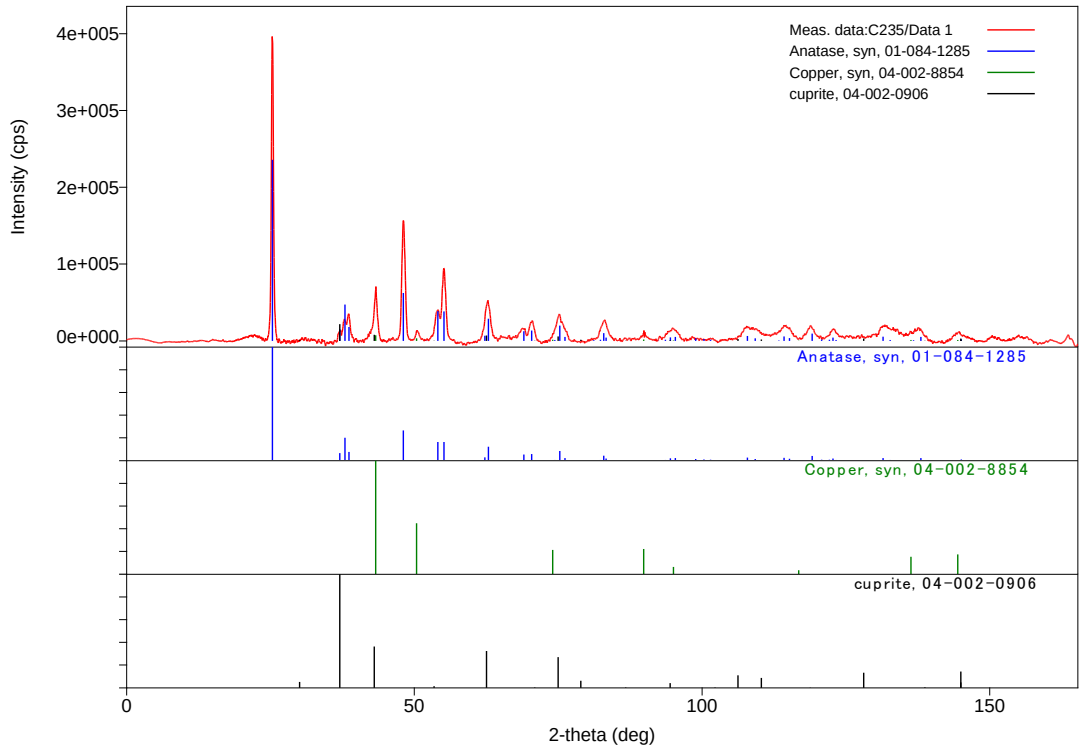

Figure 6.10: DS054 (glass)

6.3. Photographic images

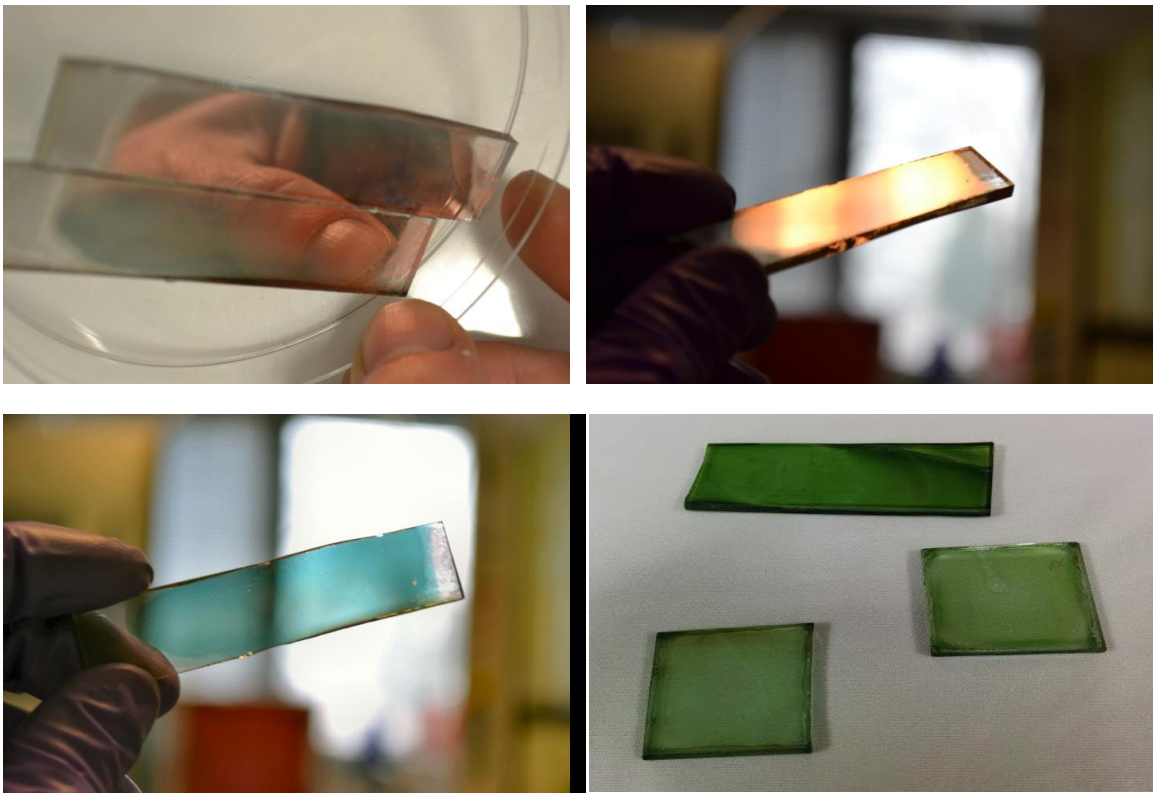

Figure 6.11: Metallic copper films showing reflectance (top left, top right) and blue transmission (bottom left) and green $CoAl_2O_4$ $CoTiO_3$ and $CoCr_2O_4$ thin films.

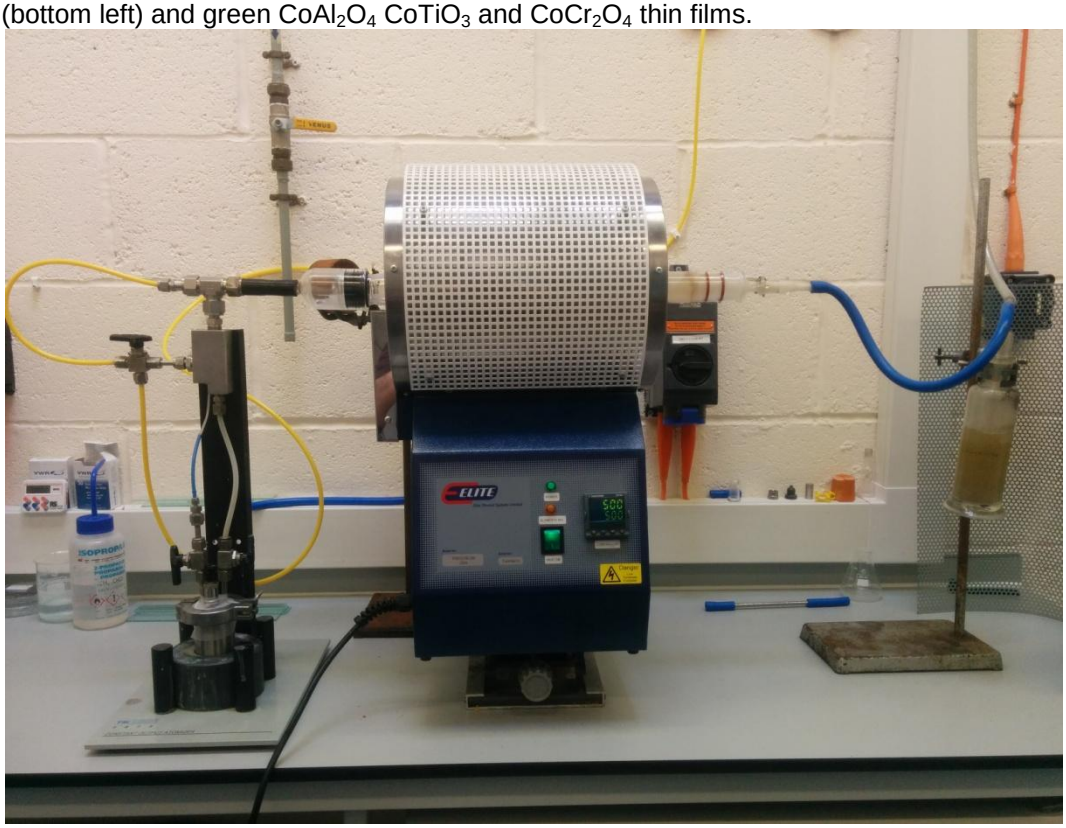

Figure 6.12: Photographic image of the AACVD apparatus used in the formation of thin films detailed in the project.